GENERAL ATOMIC

GA-A14492
UC-77

GAS-COOLED FAST BREEDER REACTOR

QUARTERLY PROGRESS REPORT
FOR THE PERIOD MAY 1, 1977 THROUGH JULY 31, 1977

by
Project Staff

Prepared under
Contract EY-76-C-03-0167
Project Agreement No. 23
for the
San Francisco Operations Office
U.S. Energy Research and Development Administration

General Atomic Project 3228 Date Published: August 1977

DISTRIBUTION OF THIS DOCUMENT IS UNLIMITED

PROGRESS REPORT SERIES

GA-5537	November 1, 1963 through July 31, 1964
GA-6667	August 1, 1964 through July 31, 1965
GA-7645	August 1, 1965 through July 31, 1966
GA-8107	August 1, 1966 through July 31, 1967
GA-8787	August 1, 1967 through July 31, 1968
GA-8895	August 1, 1968 through October 31, 1968
GA-9229	November 1, 1968 through January 31, 1969
GA-9359	February 1, 1969 through April 30, 1969
GA-9639	May 1, 1969 through July 31, 1969
GA-9811	August 1, 1969 through October 31, 1969
GA-9838	November 1, 1969 through January 31, 1970
GA-10517	February 1, 1970 through January 31, 1970
GA-10645	February 1, 1971 through April 30, 1971
GA-A10803	May 1, 1971 through July 31, 1971
GA-A10906	August 1, 1971 through July 31, 1971
GA-A12003	November 1, 1971 through January 31, 1972
GA-A12252	May 1, 1972 through July 31, 1972
GA-A12421	August 1, 1972 through October 31, 1972
GA-A12530	November 1, 1972 through January 31, 1973
GA-A12635	February 1, 1973 through April 30, 1973
GA-A12728	May 1, 1973 through July 31, 1973
GA-A12824	August 1, 1973 through October 31, 1973
GA-A12894	November 1, 1973 through January 31, 1974
GA-A13021	February 1, 1974 through April 30, 1974
GA-A13148	May 1, 1974 through July 31, 1974
GA-A13238	August 1, 1974 through October 31, 1974
GA-A13379	November 1, 1974 through January 31, 1975
GA-A13458	February 1, 1975 through April 30, 1975
GA-A13565	May 1, 1975 through July 31, 1975

GA-A13766	August 1, 1975 through October 31, 1975
GA-A13815	November 1, 1975 through January 31, 1976
GA-A13868	February 1, 1976 through April 30, 1976
GA-A13975	May 1, 1976 through July 31, 1976
GA-A14112	August 1, 1976 through October 31, 1976
GA-A14240	November 1, 1976 through January 31, 1977
GA-A14358	February 1, 1977 through April 30, 1977

ABSTRACT

The tasks of the gas-cooled fast breeder reactor (GCFR) program which are supported by the U.S. Energy Research and Development Administration include development of GCFR fuel, blanket, and control assemblies; development of the pressure equalization system for GCFR fuel; out-of-pile loop facility test programs; fuels and materials development; fuel, blanket, and control rod analyses and development; nuclear analysis and reactor physics for GCFR core design; shielding requirements for the GCFR; reactor engineering to assess the thermal, hydraulic, and structural performance of the core and the core support structure; plant systems control; systems engineering; development of reactor components, including reactor vessel, control and locking mechanisms, fuel handling equipment, core support structure, shielding assemblies, main helium circulator, steam generator, and auxiliary circulator; development of a helium circulator test facility; reactor safety, environment, and risk analyses, including planning and support of an in-pile and out-of-pile safety test program; nuclear island engineering design; and development of a reliability data bank.

CONTENTS

PROGRESS REPORT SERIES iii

ABSTRACT v

1. INTRODUCTION 1-1

2. CORE ASSEMBLY DEVELOPMENT (189a No. 00582) 2-1

    2.1. Core Assembly Thermal-Hydraulic Analysis 2-1

        2.1.1. Introduction 2-1

        2.1.2. Fuel Assembly Analysis 2-1

        2.1.3. Control Assembly Analysis 2-9

        2.1.4. Blanket Assembly Analysis 2-10

    2.2. Core Assembly Mechanical Analysis 2-11

    2.3. Core Assembly Structural Design Criteria 2-13

    2.4. Core Assembly Mechanical Testing 2-21

        2.4.1. Rod-Spacer Interaction Tests 2-24

        2.4.2. Spacer-Grid Mechanical Test 2-24

    2.5. Heat Transfer and Fluid Flow Testing 2-25

    References 2-27

3. PRESSURE EQUALIZATION SYSTEM FOR FUEL (189a No. 00582) 3-1

    3.1. Core Assembly and PES Seals 3-1

        3.1.1. Static Adhesion Tests 3-1

        3.1.2. Fuel Assembly Ring Seal Leakage Tests 3-2

        3.1.3. PES Vent Assembly Seal 3-4

    3.2. Analysis, Models, and Code Development 3-9

    3.3. Plateout and Plugging 3-15

        3.3.1. High-Pressure Loop 3-15

    3.4. Fission Product Release and Transport 3-15

    3.5. Monitor Station and Instrumentation 3-16

        3.5.1. Monitor Station Layout 3-16

        3.5.2. Monitor for PES and Sweep Gas Irradiation Experiment Evaluation 3-19

    3.6. PES Program Planning 3-20

    References 3-20

4. CORE FLOW TEST LOOP PROGRAM (189a No. 00582) 4-1

4.1. Program Planning 4-2

4.1.1. Program Modification 4-2

4.1.2. RECS Planning 4-2

4.1.3. Quality Assurance Program 4-2

4.2. Test Analysis and Prediction 4-3

4.2.1. Transient Heat-Up of a Bundle After Depressurization 4-3

4.2.2. Radiant and Natural Convection Heat Loss from a Single Heater Rod 4-3

4.2.3. Heat Loss From a Test Bundle 4-5

4.2.4. Thermal Radiation Correction for an Outlet Thermocouple 4-7

4.2.5. Status of Transient Thermal-Hydraulic Analysis Methods 4-8

4.2.6. Method of Locating Cladding Thermocouple in a Test Bundle 4-10

4.3. Test Specification 4-11

4.4. Test Bundle Design and Fabrication 4-13

4.4.1. Blanket Test Section 4-13

4.4.2. Roughening of Fuel Rod Simulators 4-13

4.5. Liaison with ORNL 4-13

4.6. GCFR Prototype Assembly Test Planning 4-13

References 4-19

5. FUELS AND MATERIAL ENGINEERING (189a No. 00583) 5-1

5.1. Oxide Fuel, Blanket, and Grid Plate Shielding Materials Technology 5-1

5.2. Cladding Technology 5-5

5.2.1. Mechanical Testing Program at Argonne National Laboratory 5-5

5.2.2. Helium Loop Test Program at Pacific Northwest Laboratory 5-6

5.3. F-1 Fast Flux Irradiation Experiment 5-7

5.4. F-3 Fast Flux Irradiation Experiment 5-11

5.5. F-5 Prototype Irradiation Experiment 5-11

5.5.1. Modification of Shroud Tube Design 5-17

5.5.2. Development of the MONSTR Code 5-21

5.6. GB-10 Vented Fuel Rod Experiment 5-28
5.7. HEDL Cladding Irradiations 5-29
References 5-29
6. FUEL ROD ENGINEERING (189a No. 00583) 6-1
6.1. Fuel, Blanket, and Control Rod Analytical Methods 6-1
6.1.1. A Theory of Radioactive Fission Gas Release and Its Application to Fuel Rod Analysis 6-1
6.1.2. Revision of the LIFE Gas-Cooled Version 6-11
6.2. Analysis of Irradiation Tests 6-11
6.3. Rod Analysis and Performance 6-11
6.3.1. Parametric Study of Mixed-Carbide Fuel Centerline Temperature 6-11
6.3.2. Dependence of Rod Diameter on Fuel Temperature and Linear Power for Metallic Thorium and Uranium Fuels 6-16
6.3.3. Fuel-to-Cladding Gap Size Between Vented and Sealed Rods 6-18
6.4. Rod Mechanical Testing 6-27
References 6-30
7. NUCLEAR ANALYSIS AND REACTOR PHYSICS (189a No. 00584) 7-1
7.1. Phase II GCFR Critical Assembly Analysis 7-1
7.1.1. Analysis of U-238 Doppler Coefficient in a Steam-Flooded Environment 7-1
7.1.2. Studies of Heterogeneity Corrections 7-4
7.1.3. Evaluation of Steam Worth With Improved Methodology 7-6
7.1.4. Evaluation of B_4C Rod Worths in Dry and Wet Cores 7-12
References 7-15
8. SHIELDING REQUIREMENTS (189a No. 00584) 8-1
8.1. Revised Upper Axial Shield 8-1
8.2. Lower Shield 8-2
8.3. Methods Development 8-5
References 8-7
9. SYSTEMS ENGINEERING (189a No. 00585) 9-1
9.1. Core Thermal-Hydraulic Performance 9-1
9.2. System Integration 9-12

9.3. Documentation Management 9-15
References 9-15
10. COMPONENT DEVELOPMENT (189a No. 00586) 10-1
10.1. Reactor Vessel 10-1
10.2. Control and Locking Mechanisms 10-11
10.3. Fuel Handling Development 10-12
10.4. Core Support Structure 10-12
  10.4.1. Seismic Structural Analysis of GCFR Core Support Structure With Effects of Core Assemblies 10-13
  10.4.2. Grid Plate Thermal Analysis 10-13
  10.4.3. Thermal Stress Analysis of the Grid Plate . . . 10-13
10.5. Reactor Shielding Assemblies 10-14
  10.5.1. Design Criteria 10-14
  10.5.2. Inner Shield Design 10-14
10.6. Main Helium Circulator, Valve and Service System 10-15
  10.6.1. Series Flow Turbine Drive 10-22
  10.6.2. Conventional Steam Turbine Drives for the Main Helium Circulator 10-24
  10.6.3. Electric Motor Drive 10-25
  10.6.4. Circulator Accident Conditions 10-30
  10.6.5. Circulator Shaft, Bearings, and Seals 10-30
  10.6.6. Main Loop Isolation Valve 10-39
10.7. Steam Generator 10-39
10.8. Auxiliary Circulator, Valve and Service System 10-41
  10.8.1. Core Auxiliary Heat Exchanger Conceptual Design 10-41
  10.8.2. Alternative Auxiliary Circulator Drive System and Components 10-41
  10.8.3. Core Auxiliary Cooling System Simulation Project 10-42
10.9. Helium Processing Components 10-42
References 10-42
11. PLANT DYNAMICS (189a No. 00638) 11-1
11.1. Control Systems 11-1
11.2. Seismic Engineering 11-1
11.3. Flow and Acoustic Vibrations 11-4
References 11-7

12. REACTOR SAFETY, ENVIRONMENT, AND RISK ANALYSIS (189a No. 00589) 12-1

12.1. Reactor Safety Program Coordination 12-2

12.2. Probabilistic Accident and Risk Analysis 12-2

12.2.1. Introduction 12-2

12.2.2. Residual Heat Removal Reliability Analysis . . 12-3

12.2.3. Containment Event Analysis 12-5

12.3. Accident Consequence Analysis 12-6

12.3.1. Introduction 12-6

12.3.2. Analysis of Loss of Decay Heat Removal Accident 12-7

12.4. Postaccident Fuel Containment 12-12

12.4.1. High-Temperature Crucible 12-12

12.4.2. Heavy Metal Bath 12-17

12.4.3. Decay Heat Analysis 12-23

12.5. Licensing Support and Integration 12-29

12.6. Engineering Reliability Integration 12-29

12.6.1. Introduction 12-29

12.6.2. Methods Identification 12-30

References 12-30

13. GCFR SAFETY TEST PROGRAM (189a No. 00588) 13-1

13.1. GRIST-2 Program 13-1

13.2. Duct Melting and Fallaway Test Program 13-2

14. GCFR NUCLEAR ISLAND DESIGN (189a No. 00615) 14-1

14.1. General Arrangement and Systems 14-1

14.2. Structural Design 14-2

Reference 14-2

15. GAS-COOLED REACTOR RELIABILITY DATA BANK (189a No. 00617) . . . 15-1

15.1. Expansion of Data Base for Gas-Cooled Reactors 15-1

15.2. Common Mode Failure Data 15-2

15.3. Documentation of Reliability Data 15-2

References 15-3

FIGURES

2-1. Peak temperature difference across edge rod vs edge spacing 2-4

2-2. Maximum cladding temperature axial location; power = 3%, flow (vertically upward) = 1% 2-7

2-3. Maximum cladding temperature axial location; power = 3% flow (horizontal) = 1% 2-8

2-4. Assembly numbering scheme for interaction study 2-12

2-5. Core profile prior to refueling 2-14

2-6. Core profile after refueling 2-15

2-7. Assembly interaction forces at outlet end due to bowing . . . 2-16

2-8. Variation of maximum stress intensity with time; fuel rod subject to radial gradient from 60% spacing edge channel . . 2-20

2-9. Stress intensities of the seventh-row duct vs axial position 2-22

2-10. Seventh-row fuel assembly hoop stress, temperature, and flux vs axial position 2-23

2-11. Test arrangement 2-26

2-12. Inlet and grid pressure loss coefficients 2-28

3-1. Typical coated specimens 3-3

3-2. GCFR core assembly piston ring seal test (Dover seal SN 13923-3-3) 3-5

3-3. GCFR core assembly piston ring seal test (Stein seals SN 5609-1, SN 5609-2, and SN 5609-3) 3-6

3-4. Summary of results of room temperature tests of Stein and Dover piston rings 3-7

3-5. PES vent assembly port seal test 3-8

3-6. Comparison of line flow rates using boundary conditions from a three-node model 3-13

3-7. Diffusion runs for Kr-85 in helium 3-17

3-8. Diffusion runs for Kr-85 in helium 3-18

4-1. CFTL transient temperature rise after depressurization . . . 4-6

4-2. Blanket rod simulator 4-16

4-3. Blanket bundle test section 4-17

5-1. Effect of oxygen/metal ratio on cladding attack 5-3

5-2. Fuel region retention as a function of oxygen/metal ratio . . 5-10

5-3. COBRA-IV thermal-hydraulic model of F-5 shroud tube assembly 5-16

FIGURES (Continued)

5-4. CRASIB models for F-5 rod bowing studies 5-18

5-5. Original shroud tube dimple configuration 5-19

5-6. Modified shroud tube dimple configuration 5-20

5-7. F-5 MONSTR code results for case 2 5-23

5-8. F-5 MONSTR code results for case 3 5-24

5-9. F-5 MONSTR code results for case 4 5-25

5-10. F-5 MONSTR code results for case 5 5-26

5-11. Reference geometry rib form 5-30

6-1. Equivalent fuel sphere model 6-3

6-2. Fuel rod geometry 6-10

6-3. Fuel centerline temperature at a linear power of 820 W/cm and a fuel-cladding gap of 0.11 mm 6-15

6-4. Cladding inner radius for metallic thorium and uranium fuels 6-19

6-5. Lifetime cladding temperature/pressure history for hot rod in fuel assembly No. 8 at equilibrium and plant expected operating conditions 6-20

6-6. Plenum pressure of sealed rod 6-22

6-7. Fast flux profile at core centerline 6-24

6-8. Power profile at core centerline 6-25

6-9. Steady-state fuel-cladding radial gap at X/L = 0.375 6-26

7-1. Steam flooding worth in unrodded phase II GCFR assembly . . . 7-11

7-2. Steam flooding worth in phase II GCFR assembly with eight B_4C rods in a 59.4-cm-radius core 7-13

8-1. Revised upper axial shield configuration 8-3

8-2. Nuclear shielding model of proposed core catcher model No. 1 8-4

8-3. Nuclear shielding model of proposed core catcher model No. 2 8-6

9-1. 300-MW(e) GCFR core assembly (120-deg summetry) with assembly identification numbers 9-3

9-2. Core and radial blanket power distribution at beginning and end of first cycle 9-4

9-3. Core and radial blanket power distribution at beginning and end of second cycle 9-5

9-4. Core and radial blanket power distribution at beginning and end of third cycle 9-6

FIGURES (Continued)

9-5. Ideal diameter sizes for core and radial blanket assemblies during first cycle 9-7

9-6. Ideal diameter sizes for core and radial blanket assemblies during second cycle 9-8

9-7. Ideal diameter sizes for core and radial blanket assemblies during third cycle 9-9

9-8. Maximum cladding temperature and helium outlet temperature at beginning of first cycle (time = zero) for scheme A . . . 9-10

9-9. Reactor mixed-mean outlet temperature and pressure drop as a function of time between refueling 9-11

9-10. Maximum cladding temperature and helium outlet temperature at beginning of first cycle (time = zero) for scheme B . . . 9-13

9-11. Maximum cladding temperature and helium outlet temperature at beginning of first cycle (time = zero) for scheme C . . . 9-14

10-1. PCRV configuration C-2 (with nonresuperheat steam generator) 10-2

10-2. PCRV configuration C-3 (with resuperheat steam generator) . . 10-3

10-3. PCRV configuration D-1 10-5

10-4. Routing of primary coolant ducts for configuration D-1 . . . 10-6

10-5. Plan view of configuration D-1 10-7

10-6. PCRV configuration D-2 10-8

10-7. Plan view of configuration D-2 10-9

10-8. Schematic of integral design series flow circulator 10-16

10-9. External drive with series flow two-stage turbine 10-17

10-10. Multistage condensing turbine installation 10-19

10-11. Electric motor drive 10-20

10-12. High-pressure barrel type turbine installation 10-23

10-13. Electrically driven circulator vertically submerged in cavity closure plug 10-27

10-14. Bearing and seal system 10-33

10-15. Bearing and seal assembly 10-35

11-1. Seismic model of GCFR 11-2

12-1. Relative timing of steel melt buildup and axial duct melting during a loss of decay heat removal accident 12-9

12-2. Relative timing of circumferential duct melting and steel spillover as a function of steel freezing location 12-10

12-3. Reference core catcher 12-13

12-4. Fuel pool temperature vs thickness 12-16
12-5. Proposed heavy metal bath core catcher 12-18
12-6. Final core retention configuration 12-21
12-7. Total decay heat vs time 12-24
12-8. Fission and breeding product decay heat vs time 12-27
12-9. Distribution of PAFC fission product group vs time 12-28

TABLES

2-1. Trial application of design criterion 2-18
2-2. Design limit summary 2-19
4-1. Heat loss by radiation and natural convection 4-4
4-2. Recommended minimum priority one test series 4-12
4-3. CFTL priority one test series summary 4-14
4-4. CFTL priority one test verification matrix 4-15
5-1. Cladding attack in fuel rods irradiated in the F-1 (X094) experiment 5-2
5-2. Distribution of cesium isotopes in F-1 fuel rods 5-8
5-3. Dimensional and density measurement results for shield samples removed from the F-3 fast flux experiment at a burnup of 4.3 TJ/kg and a fluence of $\sim 3.5 \times 10^{22}$ n/cm^2 . . . 5-12
5-4. Summary of results of axial shield irradiation 5-13
5-5. F-5 experiment parameters 5-15
5-6. F-5 bowing: final MONSTR analysis results 5-27
6-1. Operating conditions 6-23
6-2. Room-temperature tensile test results 6-28
7-1. Measured Doppler worths in the phase II GCFR critical assembly compared with GA calculations 7-3
7-2. Heterogeneity effects determined by different cell models and codes 7-5
7-3. Selected results of 28-group DTFX runs for heterogeneity factors for phase II core 7-7
7-4. Comparison of steam worth analyses using various methods for resonance shielding and cell-heterogeneity adjustments 7-8

TABLES (Continued)

7-5. 10-group analysis of phase II steam worths using DTFX heterogeneity factors 7-9

7-6. 28-group analysis of phase II steam worths using DTFX heterogeneity factors 7-10

7-7. Comparison of measured and calculated worths of B_4C rods in phase II core for dry and flooded environments 7-14

10-1. Influence of bearing lubricants 10-31

10-2. Journal bearing data 10-37

10-3. Journal bearing design 10-38

12-1. Results of molten fuel heat transfer 12-15

12-2. Elements in PAFC groups 12-26

1. INTRODUCTION

The various tasks of the gas-cooled fast breeder reactor (GCFR) program for the period May 1, 1977 through July 31, 1977 sponsored by the U.S. Energy Research and Development Administration (ERDA) are discussed in this quarterly progress report. The GCFR utility program, which is sponsored by a large number of electric utility companies, rural electric cooperatives, and General Atomic (GA), is primarily directed toward the development of a GCFR demonstration plant. The utility-sponsored work and the ERDA-sponsored work are complementary.

Analytical, experimental, and fabrication development is being accomplished under the core assembly development task to establish the basis for the design of GCFR fuel, blanket, and control assemblies. Methods development for structural, thermal-hydraulic, and mechanical analyses is discussed, and the results of structural analysis of the fuel assembly components and thermal-hydraulic analysis of the blanket assembly during low power are presented. Current progress on rod-spacer interaction tests, fuel assembly seismic and vibration test planning, and development of assembly fabrication techniques is also presented. The various subtasks of core asembly development and the work accomplished during this reporting period are discussed in Section 2.

The technology to support the design and construction of the pressure equalization system (PES) for GCFR fuel is being developed. This includes (1) the development of analytical models and computer codes which will be verified by test programs and testing of materials and seals and (2) the development of fabrication processes for the PES. These are discussed in Section 3.

To demonstrate the ability of GCFR fuel, control, and blanket assembly designs to meet design goals and verify predictions of analytical models, a series of out-of-pile simulation tests will be performed. The emphasis of the tests will be on obtaining thermal-structural data for steady-state, transient, and margin conditions using electrically heated rod bundles in a dynamic helium loop. These are discussed in Section 4.

In the fuels and materials development program, thermal flux and fast flux irradiation programs are being conducted to establish conditions and design features specific to GCFR fuel rods, such as vented fuel, fission product traps, and surface-roughened cladding. In addition, a test program of smooth and surface-roughened GCFR cladding specimens is being conducted to determine how materials behave under irradiation. The fuels and materials tests, the analytical studies, and the results to date are presented in Section 5.

Under the fuel rod engineering task, performance of the fuel and blanket rods under steady-state and transient conditions is being evaluated to determine performance characteristics, operating limits, and design criteria. In addition, surveillance of the fuel rod and blanket rod technology of other programs is being carried out. These studies are presented in Section 6.

The objectives of the nuclear analysis and reactor physics task are to verify and validate the nuclear design methods which will be applied to the GCFR core design. Data from a critical assembly experimental program on the ZPR-9 facility at Argonne National Laboratory (ANL) are being used for this purpose. Critical assembly design, analysis, and methods development are discussed in Section 7.

Verification of the physics and engineering analytical methods and the data for design of the GCFR shields is being conducted under the shielding requirements task along with an evaluation of the effectiveness of various shield configurations. The results of radial shield analyses and the work being done on structural analysis are presented in Section 8.

Section 9 discusses systems engineering for the GCFR. This includes systems integration; coordination of interface requirements between plant systems; development and implementation of effective documentation management; and assessment of the thermal-hydraulic performance of the core.

Section 10 presents the evaluation and development of the main components of the GCFR which are currently in progress, including reactor vessel, control and locking mechanisms, fuel handling, core support structure, shielding assemblies, main helium circulator, steam generator, auxiliary circulator, and helium processing components.

Development of control systems and assessment of seismic- and flow-induced vibration behavior for the GCFR demonstration plant are discussed in Section 11.

The reactor safety task, which is discussed in Section 12, includes (1) maintenance of liaison between GA and other organizations and integration of the overall GCFR safety analysis effort; (2) formulation and review of a GCFR safety program plan; (3) performance of detailed safety, environmental, and risk analyses of the GCFR; (4) evaluation of the postaccident fuel containment (PAFC) capability of the GCFR; (5) integration of the results of ERDA safety studies into the licensing reviews; and (6) evaluation of probabilistic design methods for use in the GCFR program.

Section 13 discusses the safety test program, which involves quantification of fuel and cladding behavior during accidents leading to core damage and identification of safety test information required for licensing and commercialization of the the GCFR. The GRIST-2 and duct melting and fallaway test programs are also examined.

Section 14 discusses the nuclear island. The purposes of this task are to accomplish engineering design work on the nuclear island portion of the demonstration plant and to resolve the interface requirements of major nuclear steam supply (NSSS) and balance of plant (BOP) systems.

Section 15 is concerned with the procurement, supplying, and storage of reliability data and estimates in support of probabilistic analyses of accident events being analyzed for gas-cooled reactors.

2. CORE ASSEMBLY DEVELOPMENT (189a No. 00582)

2.1. CORE ASSEMBLY THERMAL-HYDRAULIC ANALYSIS

2.1.1. Introduction

Experimental data are being evaluated to develop the analytical basis for the design and development of the GCFR fuel, control, and blanket assemblies. Because complete prototype in-pile tests cannot be conducted, a strong analytical base supported by development tests is required to design the core assemblies. The current effort is devoted to the development of an adequate steady-state and transient analysis capability in the areas of thermal-hydraulic and structural analyses to provide a basis for assembly design criteria and specific test requirements. The main efforts have focused on improvement of thermal-hydraulic correlations and development of methods for applying the correlations to the design and analysis of GCFR core assemblies.

2.1.2. Fuel Assembly Analysis

2.1.2.1. Verification of Inverse Stanton Number Transformation for Edge Channel Analysis. Fuel assembly friction factor and Stanton number transformation procedures and transformed data correlation procedures have been developed and described in Ref. 2-1. Reference 2-1 explains the need for the technique for determining the inverse of the friction factor correlation, which is required for edge channel analysis. This technique was checked (Ref. 2-1) by inputting test geometry and Reynolds number values into a system of equations, calculating the radius of zero shear (r_o), the transformed friction factor (f_1), and the Reynolds number (Re_1), and performing the inverse of the transformation to obtain the friction factor for the test condition. As expected, the calculated annulus friction factors compared very well with the measured values (±3%).

A similar procedure was used to check the Stanton number equations. After r_o was determined, f_1 and transformed Stanton number (St_1) were calculated, and the Nathan-Pirie equation was used to predict the annulus Stanton number. These results also compared well with values calculated from test measurements. The Nathan-Pirie equation (Ref. 2-3) is given below.

$$\frac{St_1}{St} = \left[\frac{f_1}{f}\,\frac{D_h}{D_{h1}}\right]^{0.5} \left(1.096 - 1.896\,\frac{f_1}{4}\right)\left(1.255 - 0.0432 \log Re_1\right) \quad ,$$

where St = Stanton number,

f = Darcy friction factor,

Re = Reynolds number,

D_h = hydraulic diameter.

The subscript 1 indicates a transformed value.

2.1.2.2. Edge Spacing Design for GCFR Fuel Assembly. A preliminary edge spacing analysis for GCFR fuel assemblies is presented in Ref. 2-3. This analysis has been updated as follows:

1. The inverse Warburton-Pirie (Ref. 2-4) transformation was used to calculate the friction factor in the edge channel.
2. The inverse Nathan-Pirie (Ref. 2-2) transformation was used to calculate the Stanton number in the edge channel.
3. For all channels, the actual solidity factors for spacers were used. The solidity factor for edge channels is higher than that for interior channels.
4. The spacer loss coefficient was considered a function of the Reynolds number (Ref. 2-5).

The updated temperature difference across the edge rod for various edge spacings is shown in Fig. 2-1. This temperature difference is about 25°C smaller than that obtained in the previous analysis (Ref. 2-3). Based on the results of the updated analysis and using the fabrication tolerances described in Ref. 3 it was concluded that the nominal edge spacing for the GCFR fuel assembly be changed from 46.1% (previous design) to 52%.

2.1.2.3. Analysis of Fuel Assembly Edge Rods Following a Depressurization Accident. Previous analyses of the thermal response of fuel assembly edge rods indicate that edge channel effects cause an edge channel temperature which is 140°C higher than the interior channel temperature during a design basis depressurization accident (DBDA). These analyses and the literature have been reviewed, and the following modifications recommended:

1. Edge channel friction factor. Previous analyses use the same correlation for edge channel laminar friction factor and interior channels. As indicated in Ref. 2-6, the friction factor correlation for edge channels is

   $$f \sim 80/\mathrm{Re} \quad .$$

   The friction factor obtained using this correlation is about 20% smaller than the previously obtained factor, and this correlation should be used in the analysis.

2. Interior channel friction factor. Reference 2-7 indicates that laminar friction factor correlations should be increased by the surface to bulk temperature difference by

   $$f = f_{ISO}\left(\frac{T_S}{T_B}\right) \quad .$$

   This increases the friction factor of the interior channels by about 5%. Because of the small surface to bulk temperature

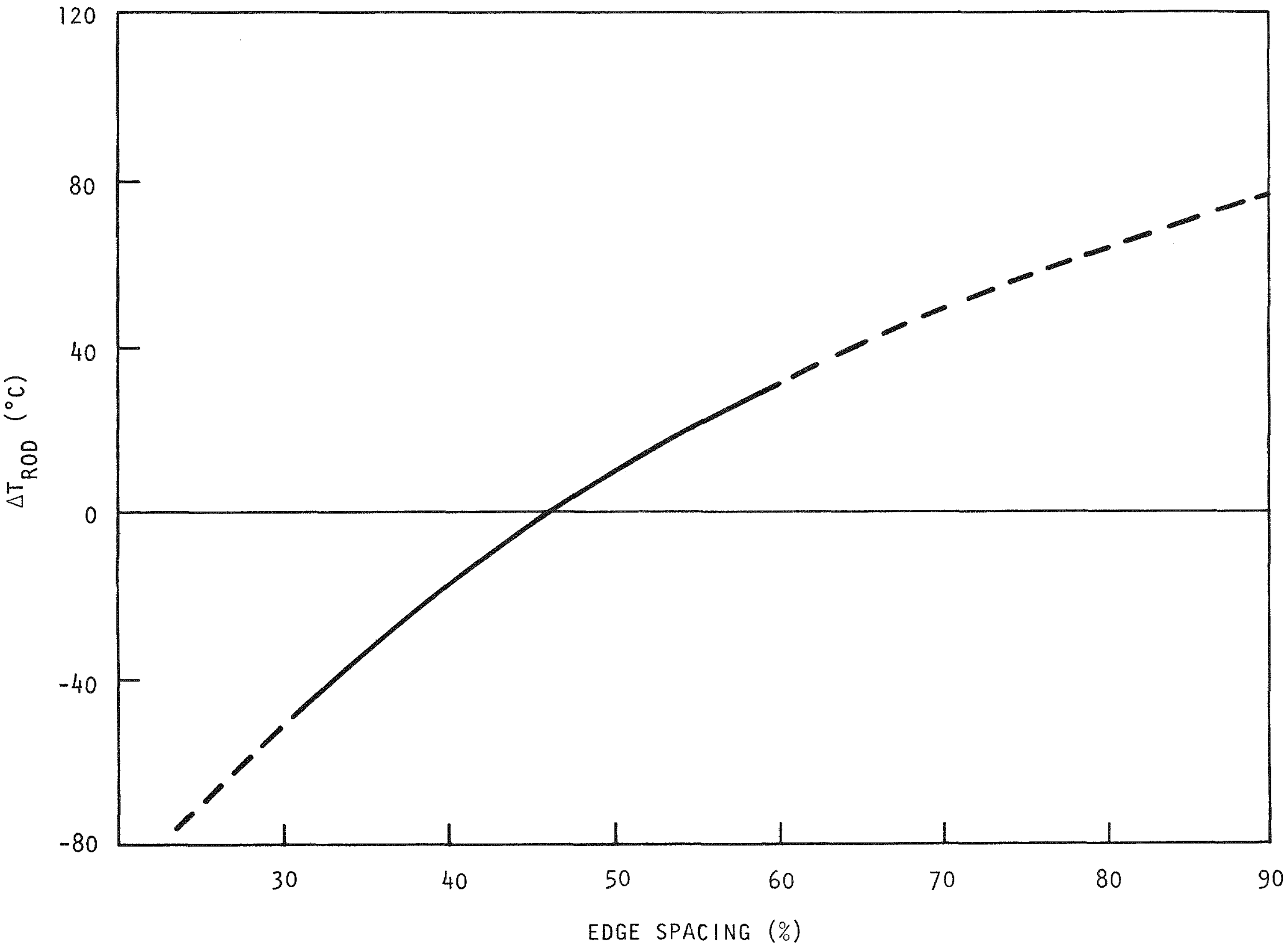

Fig. 2-1. Peak temperature difference across edge rod vs edge spacing (100% spacing = 3.875 mm)

differences in the edge channel, this correction does not affect the edge channel.

3. Channel dimensions. The channel dimensions used for DBDA analysis should be calculated at the actual temperatures of the channels and not at the normal operating temperatures. Because of the considerably high temperature of the duct, the edge channel becomes larger during a DBDA. However, the overall effect of this parameter on the final results is expected to be small.

4. Spacer loss coefficient. The spacer loss coefficient varies with the channel Reynolds number in the following functional form (Ref. 2-5):

   $$K = C_1/Re^{0.5} + C_2 \quad .$$

   Owing to smaller flow Reynolds numbers following a DBDA, the spacer loss coefficients are considerably higher than those during normal full-flow conditions. Thus, the relation given in Ref. 2-5 should be used. The effect of this factor on the overall results is expected to be quite small.

5. Spacer solidities. The spacer loss coefficient is also a function of the solidity of the spacer in the channel. The solidity of the spacer, and hence the spacer loss coefficient, in the edge channel is higher than that in the interior channel, increasing the edge channel temperature under normal operating conditions. This increase in temperature is balanced by increasing the edge channel size. This should be taken into consideration in the analysis.

6. Edge channel spacing. Recent analysis (Section 2.1.2.2.) has shown that about 52% edge spacing is desirable for normal operating conditions. This edge spacing should be used.

7. Coolant flow required for DBDA conditions. The required flow and core auxiliary cooling power necessary for adequately cooling the edge channel must be calculated by using the EDGE-TRAN (Ref. 2-1) or a similar computer code.

Items 1, 2, 3, 6, and 7 are expected to reduce the problem of edge rod cooling; items 4 and 5 will have a small negative effect (i.e., the edge cooling problem will be increased). Overall, the updated analysis will reduce the edge channel cooling problem.

2.1.2.4. SCEPTIC Subchannel Thermal-Hydraulic Analysis Computer Code. The comparison of the COBRA-IV (Ref. 2-8) and SCEPTIC (Ref. 2-9) codes reported in Ref. 2-3 has been extended. New cases were run in the laminar flow regime, and the effect of coolant flow orientation on the flow and temperature distributions within the bundle was examined. For most analyses, the COBRA code is preferred. However, for high power-to-flow ratios, the SCEPTIC code with its conduction and radiation modeling capability is favored.

A 3% power/1% flow case was included in this analysis to check the effects of buoyancy. Since the core inlet pressure is assumed to remain constant, this case more closely represents a loss of coolant flow event rather than a DBDA. At an elevated pressure, the coolant density remains high, and buoyancy effects are more pronounced than they are for the low-pressure DBDA case.

Figures 2-2 and 2-3 present the results of the 3%/1% calculations for coolant flowing in the vertically upward and horizontal flow directions, respectively. Standard laminar bundle flow friction factor and heat transfer correlations were used for these runs, and no distinction was made between edge and interior subchannels. In addition, the turbulent mixing factors were reduced to zero. When there is no conduction and radiation to thermally interconnect the surfaces, SCEPTIC treats this case as a set of parallel pipes within any given axial section. COBRA, with nodal diversion

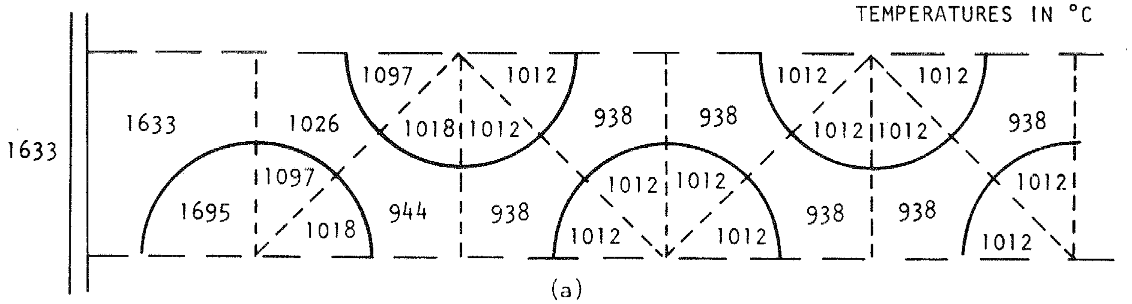

(a)
COBRA

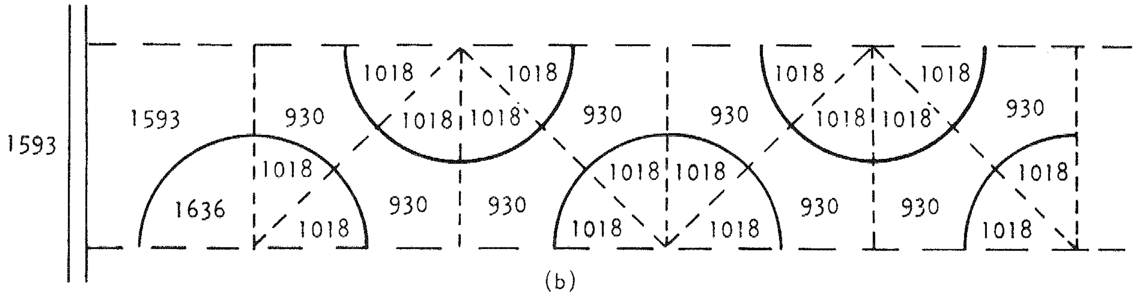

(b)
SCEPTIC WITHOUT CONDUCTION OR RADIATION

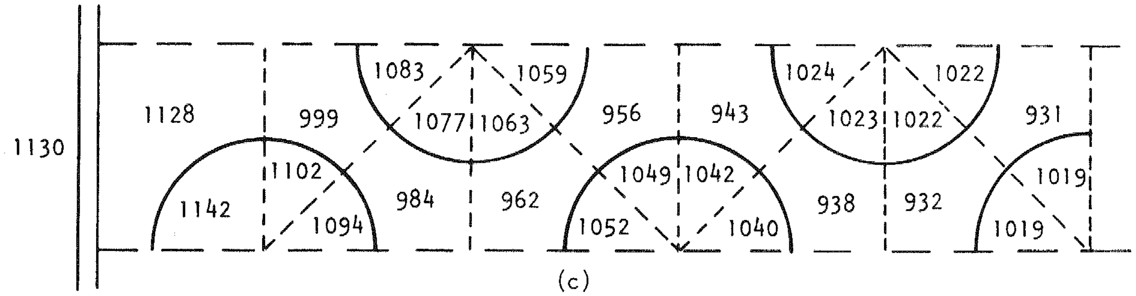

(c)
SCEPTIC WITH CONDUCTION AND RADIATION

Fig. 2-2. Maximum cladding temperature axial location; power = 3%, flow (vertically upward) = 1%

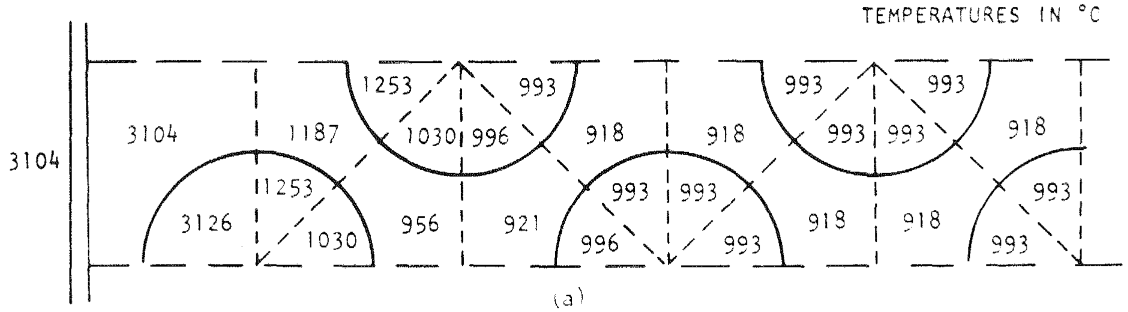

(a)
COBRA

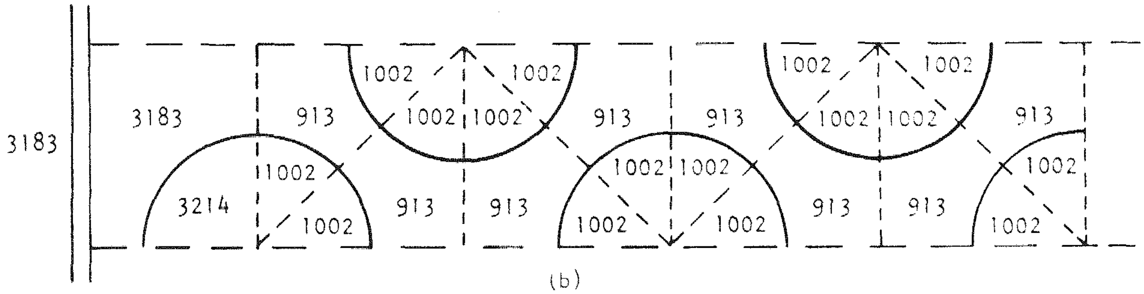

(b)
SCEPTIC WITHOUT CONDUCTION OR RADIATION

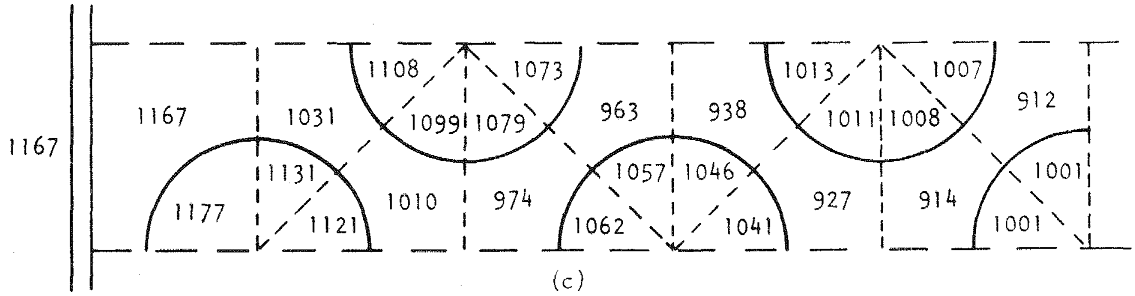

(c)
SCEPTIC WITH CONDUCTION AND RADIATION

Fig. 2-3. Maximum cladding temperature axial location; power = 3%, flow (horizontal) = 1%

cross flow calculations, predicts a more realistic temperature gradient through the bundle. Runs A and B ignored conduction and radiation mechanisms and produced unrealistic results. For the horizontal flow case, the SCEPTIC run included the effects of conduction and radiation and predicted edge channel coolant and cladding temperatures which were 1980°C lower than those calculated by the incomplete analytical models. Vertically upward flow takes maximum advantage of buoyancy effects, resulting in the lowest radial temperature gradients through the bundle.

Attempts were made to run the codes for vertically downward flow, but both codes predicted flow stagnation in the edge channel and were unable to converge. Although the COBRA code could handle this case by imposing a flow transient from a converged steady-state starting point to the 1% flow level, the added effort was not warranted for the simplified model.

The 1% flow case at full pressure (9 MPa) was analyzed to gain additional understanding of the capabilities and limits of the two codes. The flow stagnation observed in the edge channels for 1% flow of fully pressurized helium in a downward-cooled core is not anticipated for GCFR operating or accident modes. The COBRA and SCEPTIC codes provide reasonably similar coolant and cladding temperature predictions. The results tend to diverge with large power-to-flow ratios, requiring the inclusion of conduction and radiation heat transfer models. Therefore, it is proposed that the COBRA code be used for steady-state, "normal" power-to-flow cases, and the SCEPTIC code, with its conduction and radiation models, be used for "off-normal" power-to-flow analyses.

2.1.3. Control Assembly Analysis

There was no effort devoted to the analysis of the control assembly design during this quarter. The thermal-hydraulic design developed during the previous quarter (Ref. 2-3) is being considered for the core design.

2.1.4. Blanket Assembly Analysis

2.1.4.1. COBRA-IV Code Development. Development of a helium-cooled version of the new COBRA-IV subchannel thermal-hydraulic analysis computer code continued during this quarter. This program is particularly useful for the analysis of the GCFR radial blanket because it has a complete model of the wire-wrap spacer system. The COBRA-III code currently in use at GA does not have this capability, and wire-wrap effects have been simulated by increasing the turbulent mixing coefficient.

For wire-wrapped bundles, the COBRA-IV code has been run assuming that the wires have the same start angle on each rod. With this configuration, at any axial location in the bundle, there is never more than one wire at a time crossing the boundaries of a given subchannel. However, the current GCFR radial blanket design is based on start angles of 0, 120, and 240 deg on adjacent rods. In this case, there is one axial location within each wire pitch where three wires simultaneously enter a subchannel. This particular configuration has been programmed into the COBRA-IV model of the blanket assembly and is currently causing a loss of diagonal dominance in the cross flow coefficient matrix. A separate 61-rod model has successfully been run with uniform and 0, 45, and 90 deg start angle configurations.

Two sets of program updates have been received from Battelle Northwest Laboratory (BNWL) and incorporated into the code, and various problems caused by differences in the computer systems at BNWL and GA have been corrected. Sample problems provided by BNWL have been run to verify the performance of the code on the GA system. Portions of the output have been modified to eliminate unused parameters such as coolant quality and to add parameters such as coolant Reynolds number. Other modifications have improved the restart capability after a maximum time exit.

2.1.4.2. Thermal-Hydraulic Analysis. During this quarter, efforts have been directed toward the development of the COBRA-IV code for analysis of helium-cooled wire-wrapped rod bundles. When this version of the code is running properly, a detailed analysis of the radial blanket assembly will be conducted and compared with the COBRA-IIIC results (Ref. 2-1).

2.2. CORE ASSEMBLY MECHANICAL ANALYSIS

Assembly rotation is used to limit interactions of GCFR assemblies as a result of bowing distortion. Recently, Argonne National Laboratory (ANL) used a newly developed version of the NUBOW computer code to address assembly interlocking. ANL used a strip model of inelastic beam elements capable of inelastic interaction and predicted the swelling-induced assembly interference loads during three repeating cycles of an equilibrium core considering assembly rotation and replacement. The equilibrium core concept consists of partially spent assemblies distributed so that no adjacent assemblies are the same age. The assemblies are rotated every 250 full-power days and replaced after 750 full-power days.

During this quarter, the CRASIB code (Ref. 2-10) was used to obtain an approximate basis for fuel handling studies using the most current physics and thermal-hydraulics data and to provide verification of the ANL work. The code was run for each of the eight radial strip locations shown in Fig. 2-4; each location was assumed to be unrestrained. Information on the amount of permanent deformation as a function of time was obtained and separated into 250 full-power-day cycles, and the equilibrium core configurations were analyzed using elastic superposition. The major drawback of this approach is the absence of interaction load relaxation due to creep. However, this approach is conservative and should provide an upper bound on the actual loads.

The beam assembly model consisted of 50 nodes and three cross sections (inlet nozzle, thick upper hexagonal section, thin lower hexagonal section), and the support at the grid plate was a double-pin connection at the top and bottom of the grid plate. Core thermal-hydraulics information was obtained from CALIOP (Ref. 2-11) runs on the medium-pressure-drop core (353°C inlet, ∿554°C outlet). Bending from differential thermal and swelling loads, elastically computed mechanical interaction loads, and

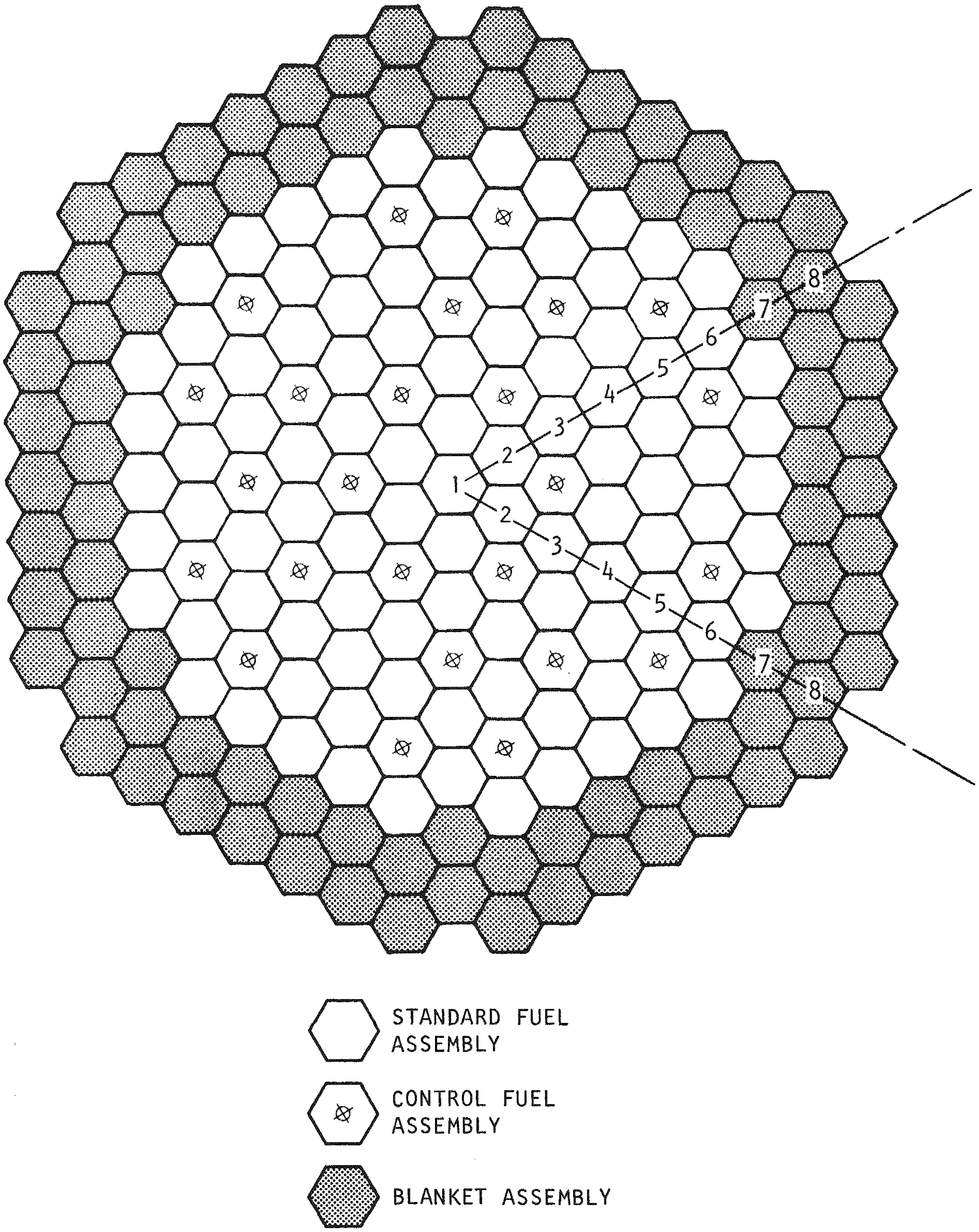

Fig. 2-4. Assembly numbering scheme for interaction study

bowing of the grid plate due to the coolant pressure differential were superimposed.

The major results are presented in Figs. 2-5 and 2-6, which show the four conditions encountered at the end of the worst-case 250 full-power-day cycle: the hot condition prior to shutdown, the cold condition immediately after shutdown, the cold condition after assembly rotation and replacement, and the hot condition at commencement of the following 250 full-power-day operating period. The maximum interaction force of 960 N occurs between assembly rows 5 and 6 in the cold condition before assembly removal. Interaction does not occur after assembly rotation and replacement, and while at power, the blanket assembly is always clear of the fueled assemblies.

Figure 2-7 presents the maximum GA and ANL interaction loads, Q_i and Q'_i, respectively; the subscript i refers to the outer of the two interfering assemblies causing the load. Although the magnitudes of the GA and ANL loads differ; the location of interaction is consistent in both studies. The differences are probably due to variations of core operating conditions and creep relaxation. The following conclusions have been reached:

1. The current fuel management criterion for an equilibrium core is adequate for limiting interactions between assemblies.

2. The maximum load required of the fuel handling machinery will probably not exceed 1000 N in any single direction.

3. Further refinement of the analysis should consider an r-z sector (multiplane interaction) and the effects of manufacturing tolerances.

2.3. CORE ASSEMBLY STRUCTURAL DESIGN CRITERIA

The first stage of the trail application program for the preliminary GCFR core component structural design criteria has been completed. An

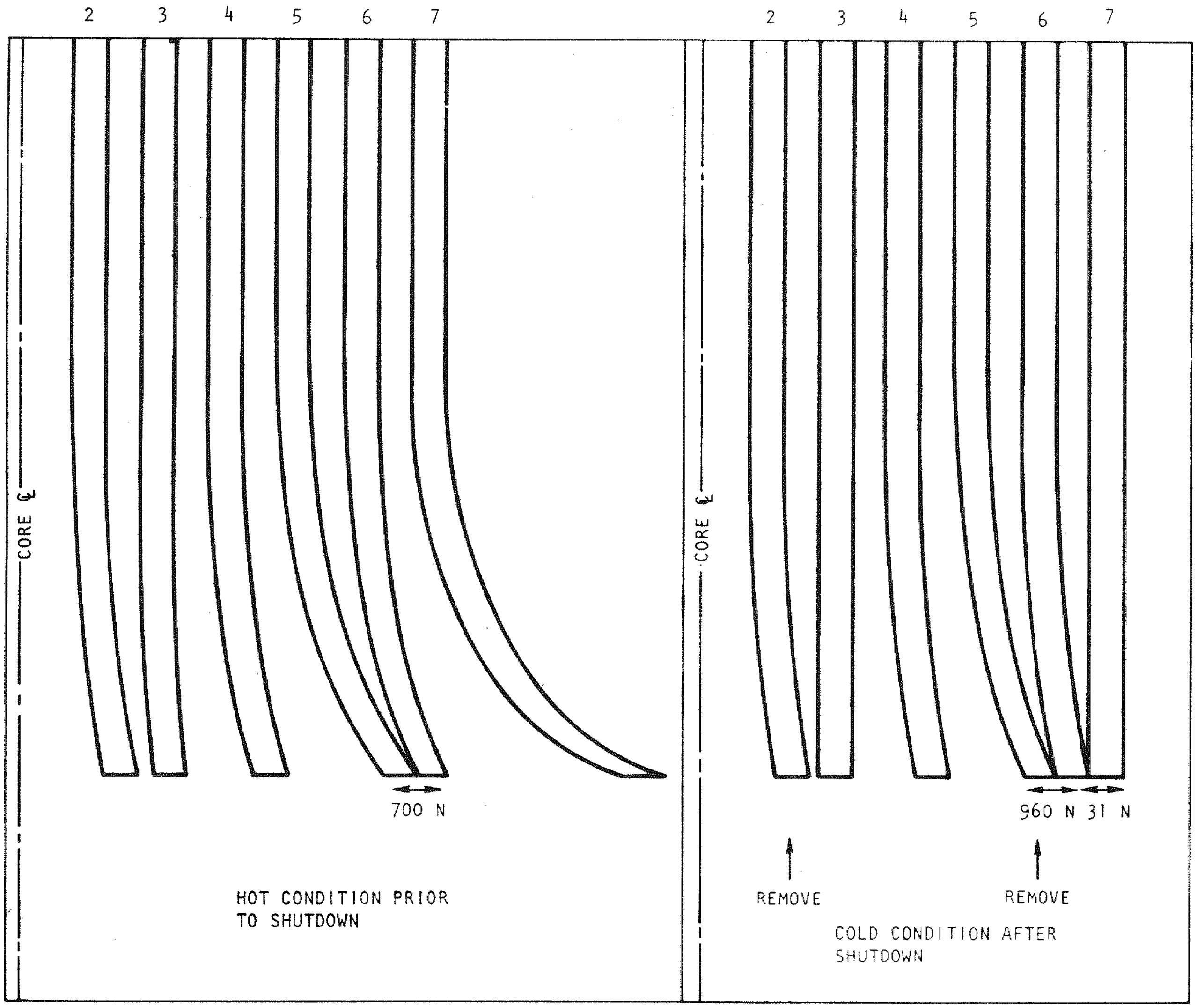

Fig. 2-5. Core profile prior to refueling

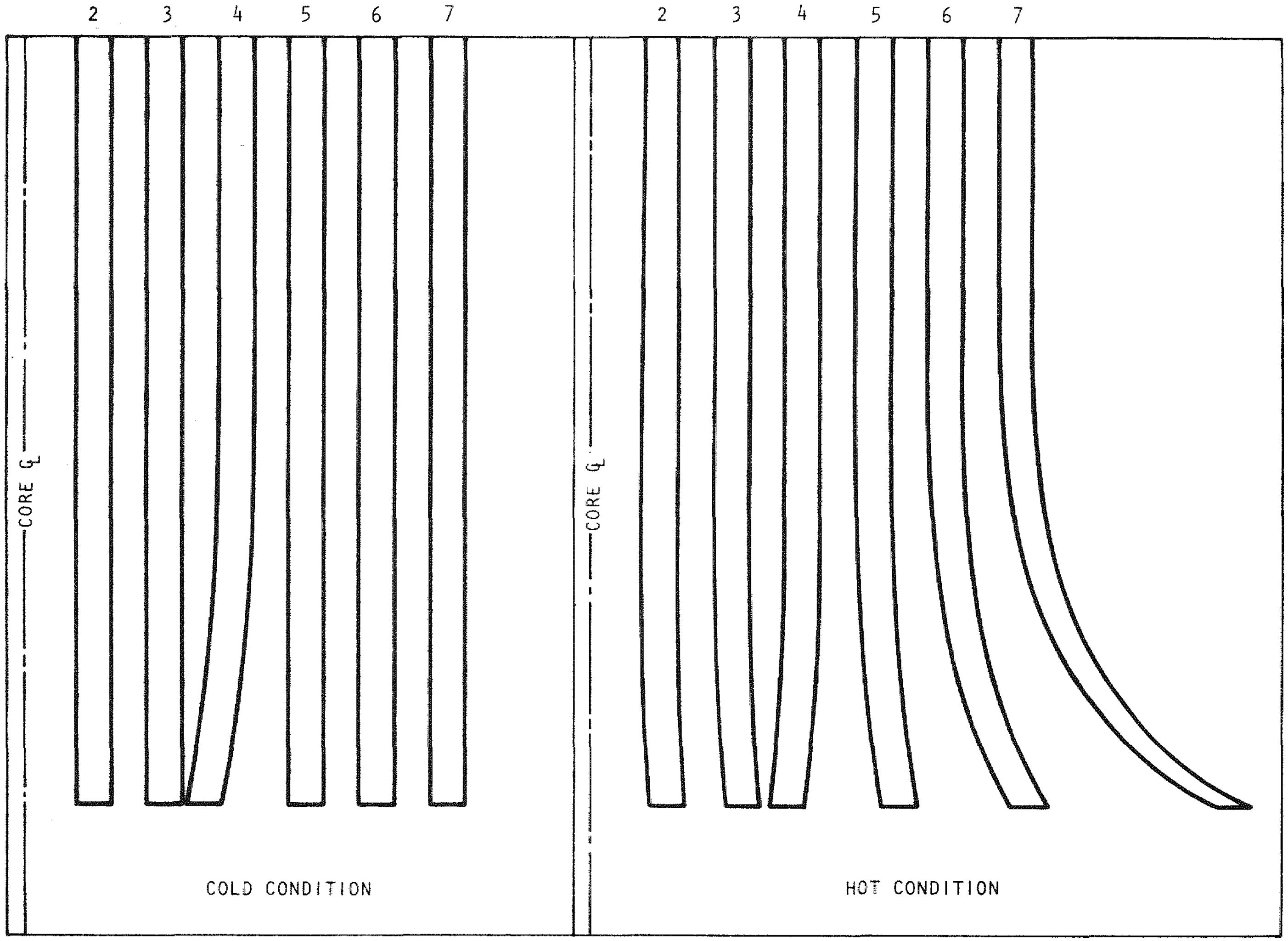

Fig. 2-6. Core profile after refueling

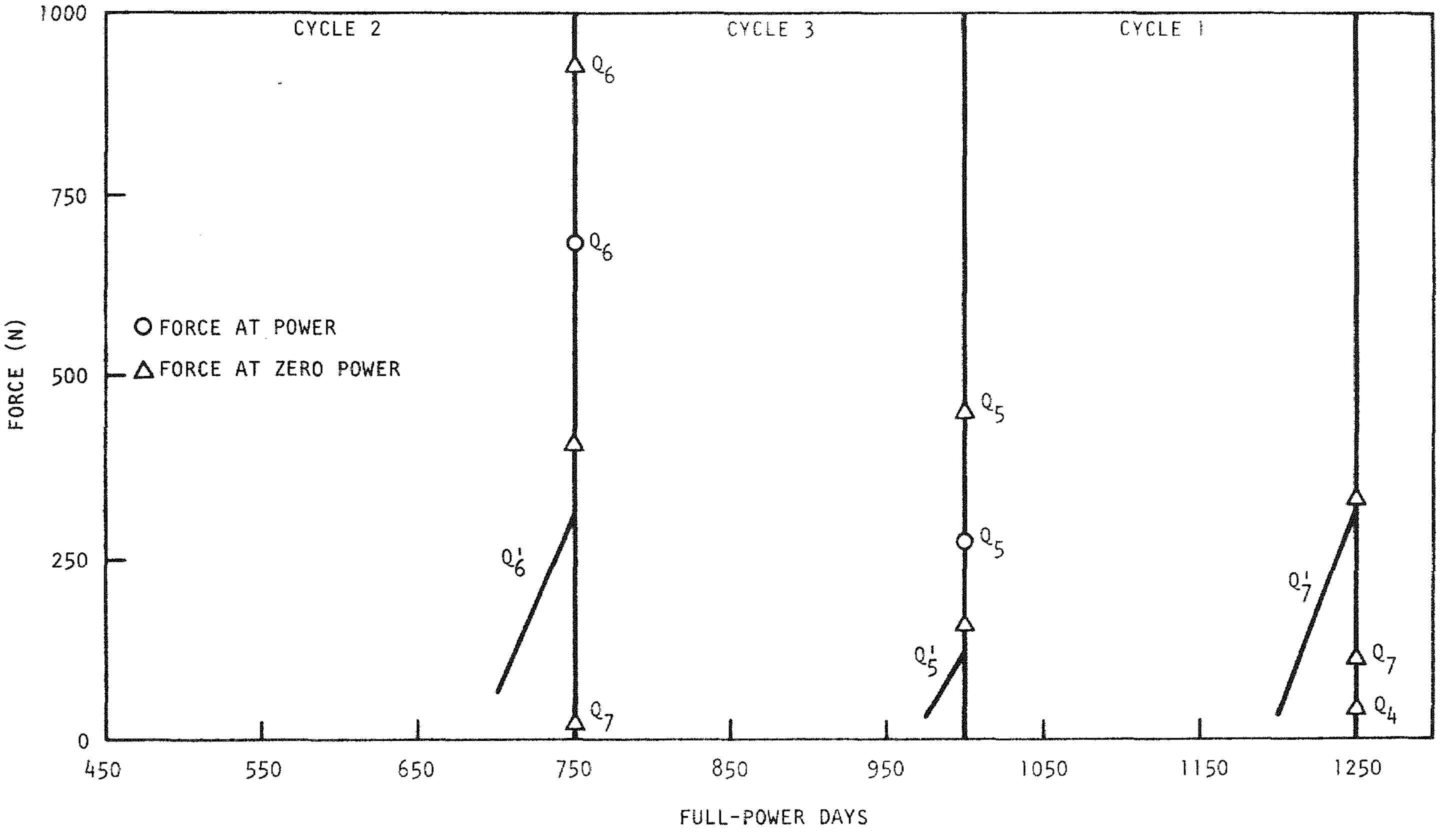

Fig. 2-7. Assembly interaction forces at outlet end due to bowing (thermally-induced and swelling-induced)

assessment was made of the compatibility of the rules of the criteria with available analytic methods and material properties data, and the extent to which new methods and data would be required was studied. The ease of interpretation of the criteria was evaluated. By analyzing proposed or existing hardware, numerical examples could be used as guidelines for future users and as supporting rationale for the criteria.

Two components were analyzed: the central assembly edge channel fuel rod cladding and a seventh-row fuel assembly duct. Both components were subjected to steady-state loading conditions and modeled as an assemblage of beams constrained at particular support locations. Except for the end-of-life (EOL) deformation, both designs satisfied the criterion.

The fuel rod cladding was analyzed using the worst edge channel conditions in the center assembly. The model was constructed for a version of the CRASIB computer code which was modified to calculate the damage and strain fractions required by the criteria. Nominal beginning-of-life (BOL) values for material properties and minimum values of the limit quantities were used; steady-state operation to EOL was assumed, and a 10-grid spacer design was analyzed. The major operating parameters are given in Table 2-1. The thermal loads considered produced primary stresses from cladding-spacer interaction. The analysis included volume swelling, irradiation-enhanced creep, and thermal creep, resulting in time-varying reaction loads, stresses, and deformations. Table 2-2 compares the limit quantities with the computed values. Figure 2-8 shows the more significant stress intensities and deformations. Of particular interest is the ability of the code to predict correctly the various phenomena affecting stress intensity. The initial dip in the curve is the stress relaxation of the elastic thermal stresses due to creep; the secondary rise is due to differential swelling increasing the stresses. The plateau reached during the second half of lifetime is the equilibrium state between the increasing swelling strains and creep relaxation.

A similar structural evaluation was performed on the seventh-row fuel assembly. Steady-state operation throughout lifetime and transverse

TABLE 2-1
TRIAL APPLICATION OF DESIGN CRITERION

Fuel rod operating parameters	
Maximum flux, > 0.1 MeV (n/cm^2-hr)	1.1203×10^{19}
Maximum fluence (n/cm^2)	2.3×10^{23}
Inlet helium temperature (°C)	350
Outlet helium temperature (°C)	535
Helium pressure drop (kPa)	224
Fuel assembly flow duct operating parameters	
Radial position	Seventh row
Maximum flux, > 0.1 MwV (n/cm^2-hr)	3.7728×10^{18}
Maximum flux tilt (% of maximum flux)	12.6
Maximum fluence (n/cm^2-hr)	7.647×10^{22}
Inlet helium temperature (°C)	353
Outlet helium temperature (°C)	523
Helium pressure drop (kPa)	224

TABLE 2-2
DESIGN LIMIT SUMMARY

Limit Quantity	Fuel Rod Cladding		Assembly Duct	
	Limit Value	EOL Value	Limit Value	EOL Value
Primary membrane stress (MPa)	148	0	448	0
Sum of primary local and bending stresses (MPa)	148	30.3	448	85
Secondary stress (MPa)	456	0	931	0
Strain fraction	0.50	0.002	--	--
Functionally adequate deformation (mm)	1.5	2.0	4.5, no interassembly contact	0.1

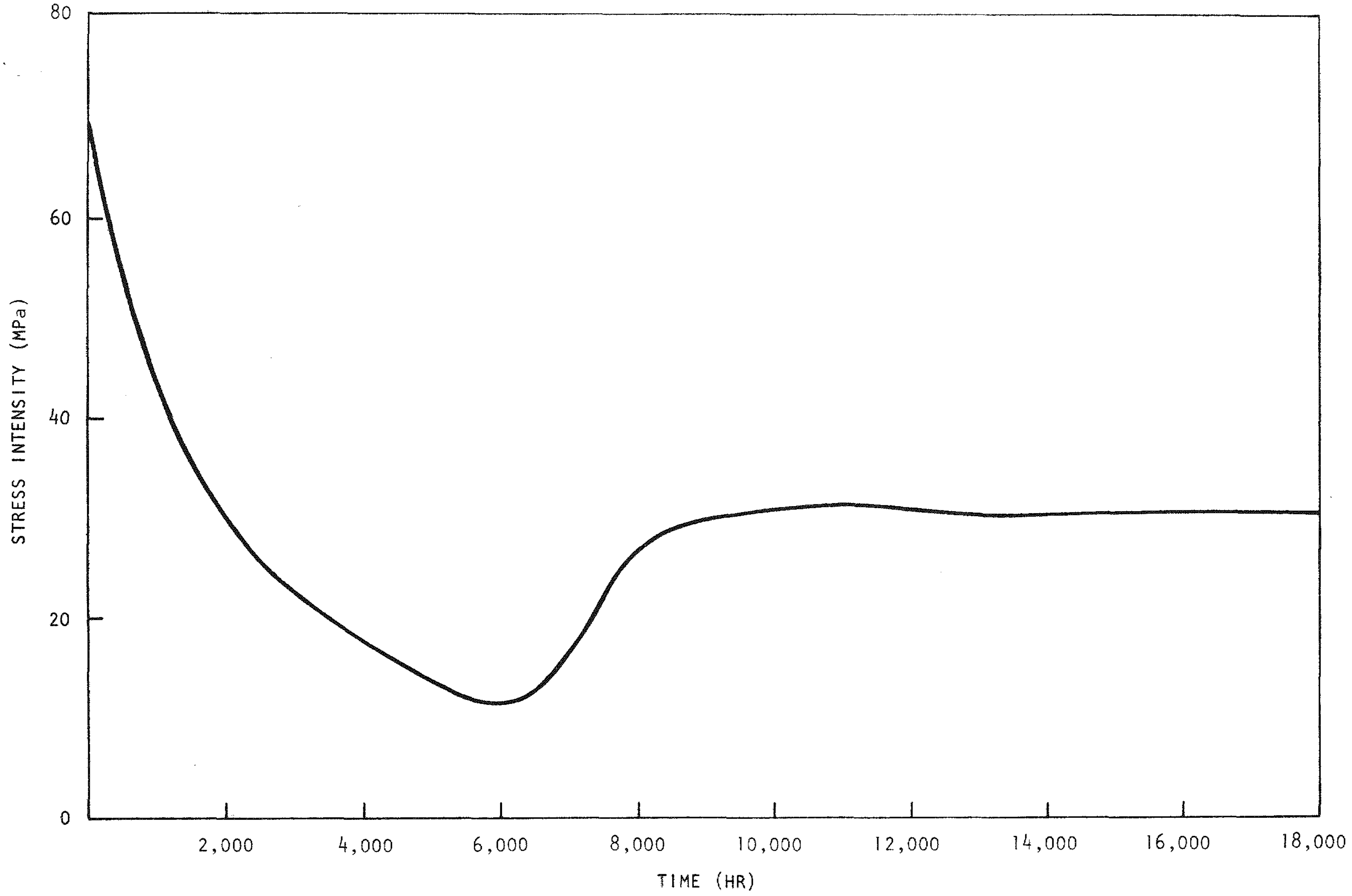

Fig. 2-8. Variation of maximum stress intensity with time; fuel rod subject to radial gradient from 60% spacing edge channel (10 spacers, 160-mm apart)

thermal and fluence gradients were assumed; the model and operating parameters are also given in Table 2-1. Although the core is designed to be unconstrained, this study simulated lower-end contact between a blanket assembly and the core by restraining the lower node to zero displacement. Differential pressure across the duct wall produced dilation distortion. The effects of lower-end contact and dilation distortion were separately computed and linearily superimposed with the bowing results. This was a very conservative approach since the additional relaxation of the bowing stresses from the additional creep due to the dilatation stresses was ignored. The results are summarized in Table 2-1. Figure 2-9 shows the combined stress intensities and their corresponding limits are shown as a function of axial position. The point chosen for application of the design rules was where the limit most closely approached the computed value. Figures 2-9 and 2-10 show the stress intensity deformation from the undisturbed centerline due to dilatation and constrained bowing. The two deformation limits are for bowing and dilatation and constrained bowing. The two deformation limits are for bowing and dilatation deformations; the former cannot be assessed without a core-wide deformation study.

2.4. CORE ASSEMBLY MECHANICAL TESTING

The objective of this task is to conduct mechanical tests of core assembly components and subassemblies to simulate the mechanical loads expected during normal and abnormal reactor operating conditions. The current phase of the assembly mechanical testing program involves testing of fuel assembly components. The preliminary fuel rod/spacer interaction test using single spacer cells and rods was conducted during FY 76. The reproducibility testing of the hexagonal spacer cells was completed, and testing of a new modified hex design is continuing. The design and procurement of blanket assembly components for testing was initiated. Further tests on grid spacers are being planned and designed, and flow-induced vibration test planning is in progress.

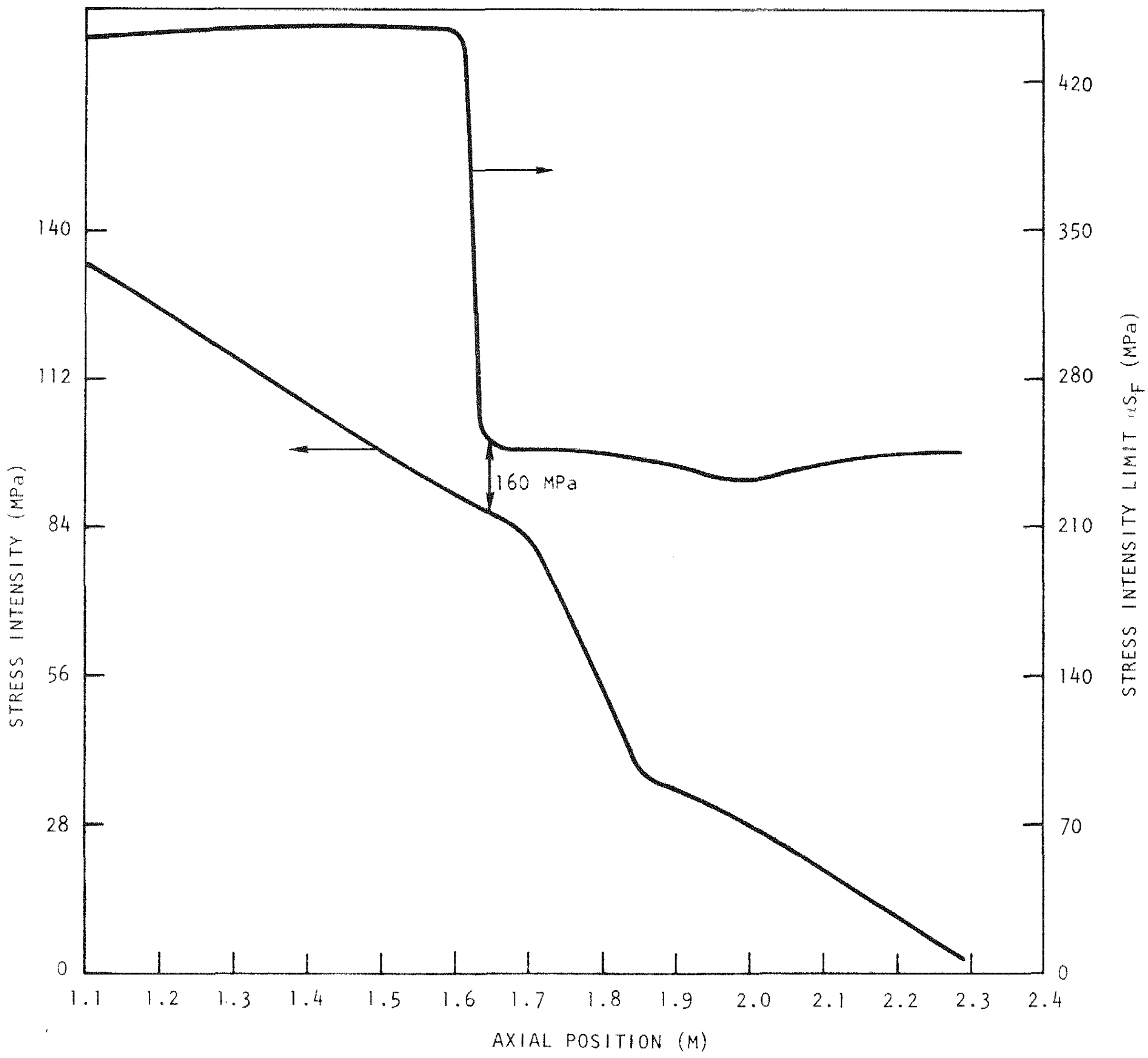

Fig. 2-9. Stress intensities of the seventh-row duct vs axial position

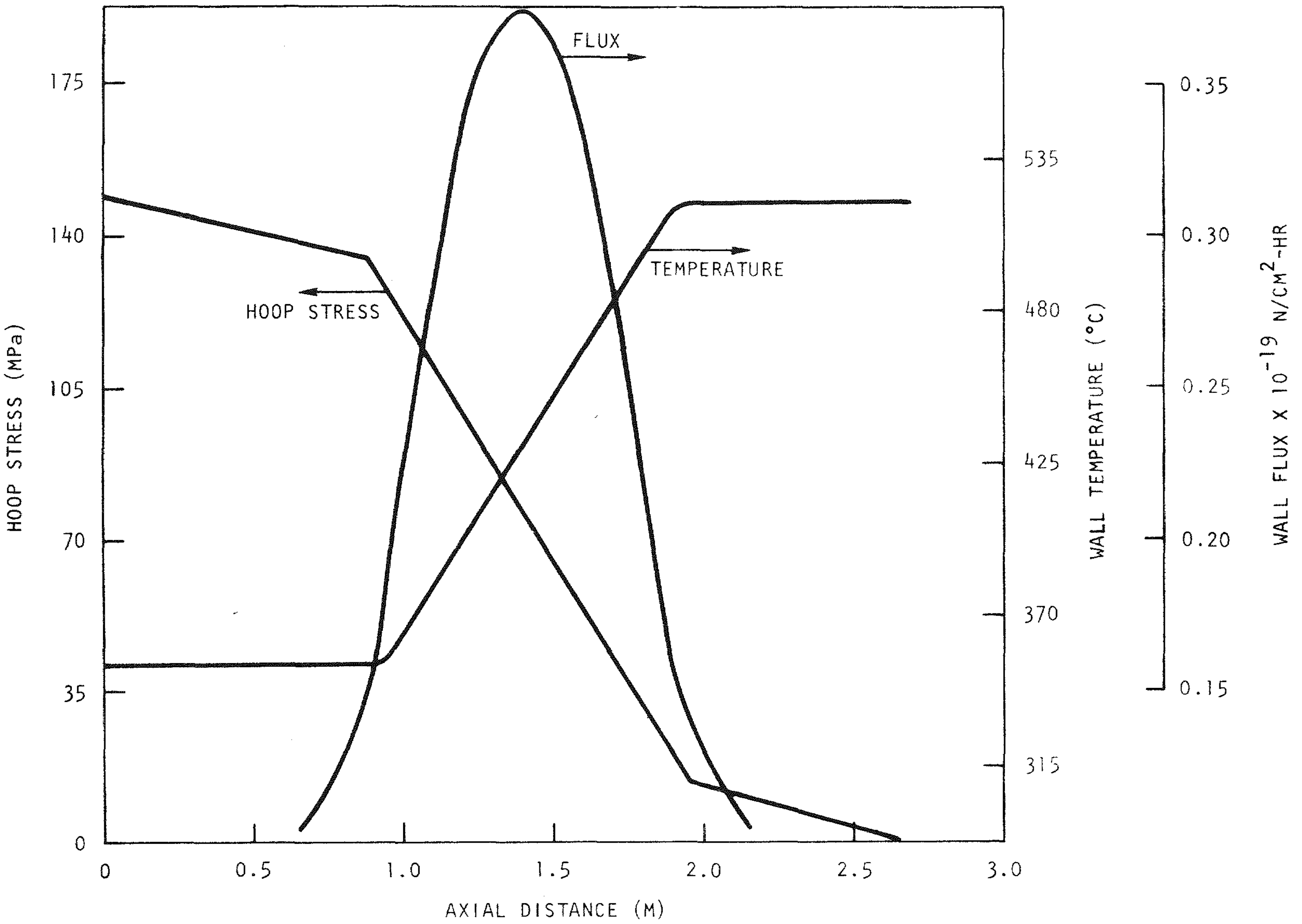

Fig. 2-10. Seventh-row fuel assembly hoop stress, temperature, and flux vs axial position

2.4.1. Rod-Spacer Interaction Tests

The purpose of prior rod-spacer interaction tests was to evaluate the effect of interacting forces between the fuel rod and the spacers under the mechanical and environmental operating conditions expected in the GCFR. The simulated forces are primarily caused by bowing induced by temperature gradients and irradiation-induced swelling. Reactor operational transients cause relative motion of the rod and spacer, which results in frictional forces. The frictional forces and relative motion cause wear of the rod and spacer pad surfaces. The interaction force is simulated by a deadweight load on a spacer cell resting on a fuel rod. The calculated loads due to rod bowing have always been predicted to be of the order of 5 N. The results of the reproducibility tests using a reference design hexagonal rod spacer indicated that there was no problem due to these loads. The bowing load simulation tests are being continued to investigate an improved design called the modified hexagonal spacer.

During this quarter, six additional tests were conducted using the modified hex spacer cells cut from a 37-rod spacer fabricated for the AGATHE 37-rod bundle flow tests. The cells were measured after each step of annealing and cutting, and there were no dimension changes. The cells were tested against ribbed tubes, and the results showed negligible friction and wear for all tests except one, which resulted in a friction coefficient which was 50% higher than the normal coefficient and wear which exceeded 0.1 mm (normal wear is 0.03). A detailed metallurgical examination is being conducted, and additional spacers will be procured and cells cut out for further testing in the rod-spacer test rig.

2.4.2. Spacer-Grid Mechanical Test

A test plan for structural testing of the 37-rod AGATHE spacer has been written and is in review. The data from this testing program will be correlated for use in the design by using finite-element analytical techniques. Three of the 37-rod spacers have been ordered, and the test fixtures for adapting the INSTRON test machine to these tests are being designed.

2.5. HEAT TRANSFER AND FLUID FLOW TESTING

The test specification for the second phase of testing of the fuel assembly inlet nozzle design has been written and is in review. The test assembly design was completed and the parts fabricated and delivered. The test assembly from the phase I test was set up without the inner parts (i.e., annular fission product trap and grid plate shields), and a series of measurements were made to evaluate the inlet and grid manifold pressure loss coefficients.

Figure 2-11 shows the test setup and instrumentation. Manometers were used to measure the inlet and grid pressure drops and venturi flow conditions; all data were recorded by hand. The smooth inlet configuration was installed, and the annular fission trap and shields and the center thermocouple tube were removed. The hole in the inlet center body through which the thermocouple tube is normally inserted was plugged, and the data were put into dimensionless form as a static pressure loss coefficient defined by

$$K = \frac{\Delta p}{\frac{1}{2}\rho \bar{V}^2} = \frac{\Delta p}{\frac{RT}{2p}\left(\frac{\dot{m}}{A}\right)^2} \quad .$$

The static pressure loss coefficients are based on the following conditions:

Parameter	Inlet	Grid
Δp	Static pressure between ambient and station 4	Static pressure between stations 12 and 13
T	Ambient	Ambient
p	Ambient	Downstream of grid (station 13)
A	Minimum inlet area through struts	Area in fuel pin region
$\dot{m}$	Venturi flow rate	Venturi flow rate

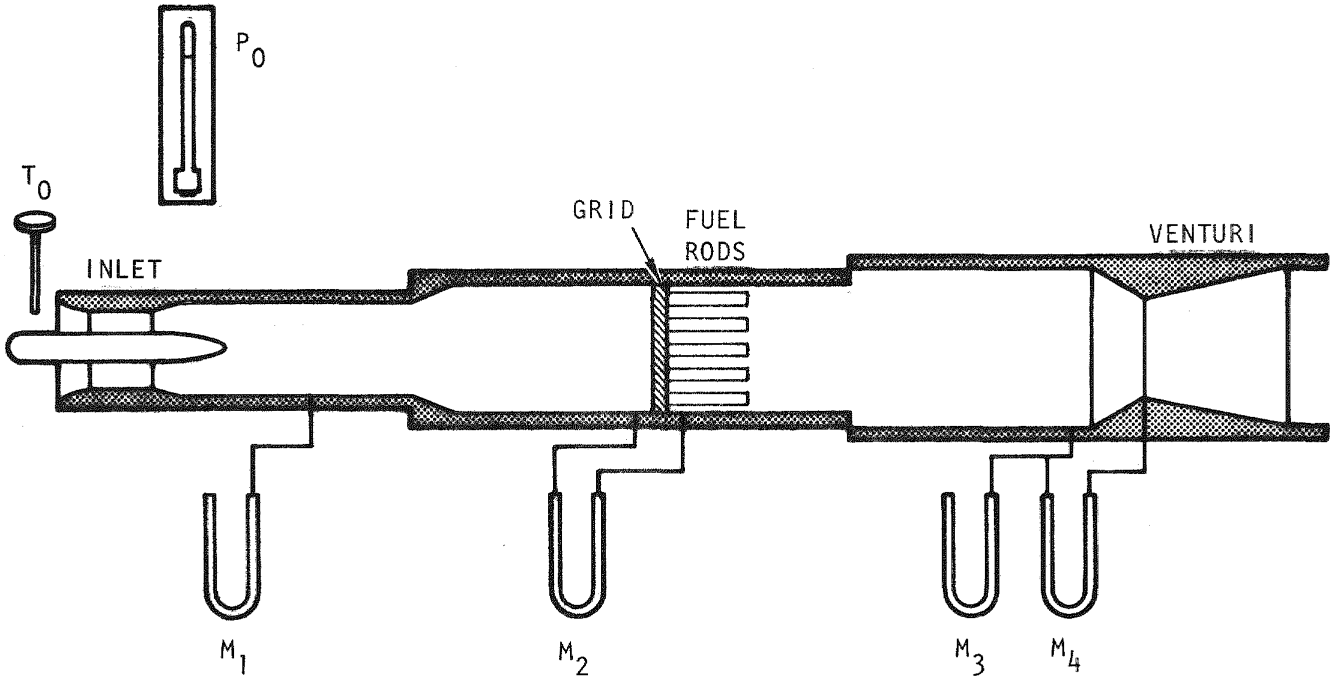

P_0 - BAROMETER
T_0 - WESTON DIAL THERMOMETER
M_1 - MANOMETER - WATER
M_2 - MANOMETER - MERCURY INCLINED
M_3 - MANOMETER - MERCURY
M_4 - MANOMETER - WATER

Fig. 2-11. Test arrangement

Figure 2-12 shows the pressure loss coefficients versus the Reynolds number. The grid loss and inlet loss can be considered constant over the limited Reynolds number range for these measurements. The average inlet loss is $K_I = 0.31$, and the average grid loss is $K_G = 1.07$. The grid pressure loss coefficient for the phase I model is also shown; the average of these data is $K_G = 1.64$. A true comparison of the inlet pressure loss coefficient from phases I and II is not feasible because the inlet during the phase I test was partially blocked to eliminate the acoustic noise phenomena.

The grid pressure loss coefficient is about 33% less when it is measured alone than when it is measured in the fully assembled model. This is because the annular shield upstream of the grid has a flow separation which is equivalent to the flow blockage preceding the grid. Therefore, the effective flow area of the grid is less when the annular shield is installed. These types of flow test measurements will be repeated for phase II flow testing of the new fuel assembly inlet nozzle, and a better comparison of the inlet pressure loss coefficients will be obtained.

REFERENCES

2-1. "Gas-Cooled Fast Breeder Reactor Quarterly Progress Report for the Period February 1, 1977 Through April 30, 1977," ERDA Report GA-A14358, General Atomic, May 1977.

2-2. "Gas-Cooled Fast Breeder Reactor Quarterly Progress Report for the Period November 1, 1976 Through January 31, 1977," ERDA Report GA-A14240, General Atomic, February 1977.

2-3. Nathan, D. I., and M. A. M. Pirie, "On the Interpretation of Heat Transfer and Pressure Drop Tests on Roughened Rods in Smooth Circular Channels," Berkeley Nuclear Laboratories Report CEAB RD/B/N 1370, 1970.

2-4. Warburton, C., and M. A. M. Pirie, "An Improved Method for Analyzing Heat Transfer and Pressure Drop Tests on Roughened Rods in Smooth Channels," ASME Paper 74-WA/MT-56, November 1974.

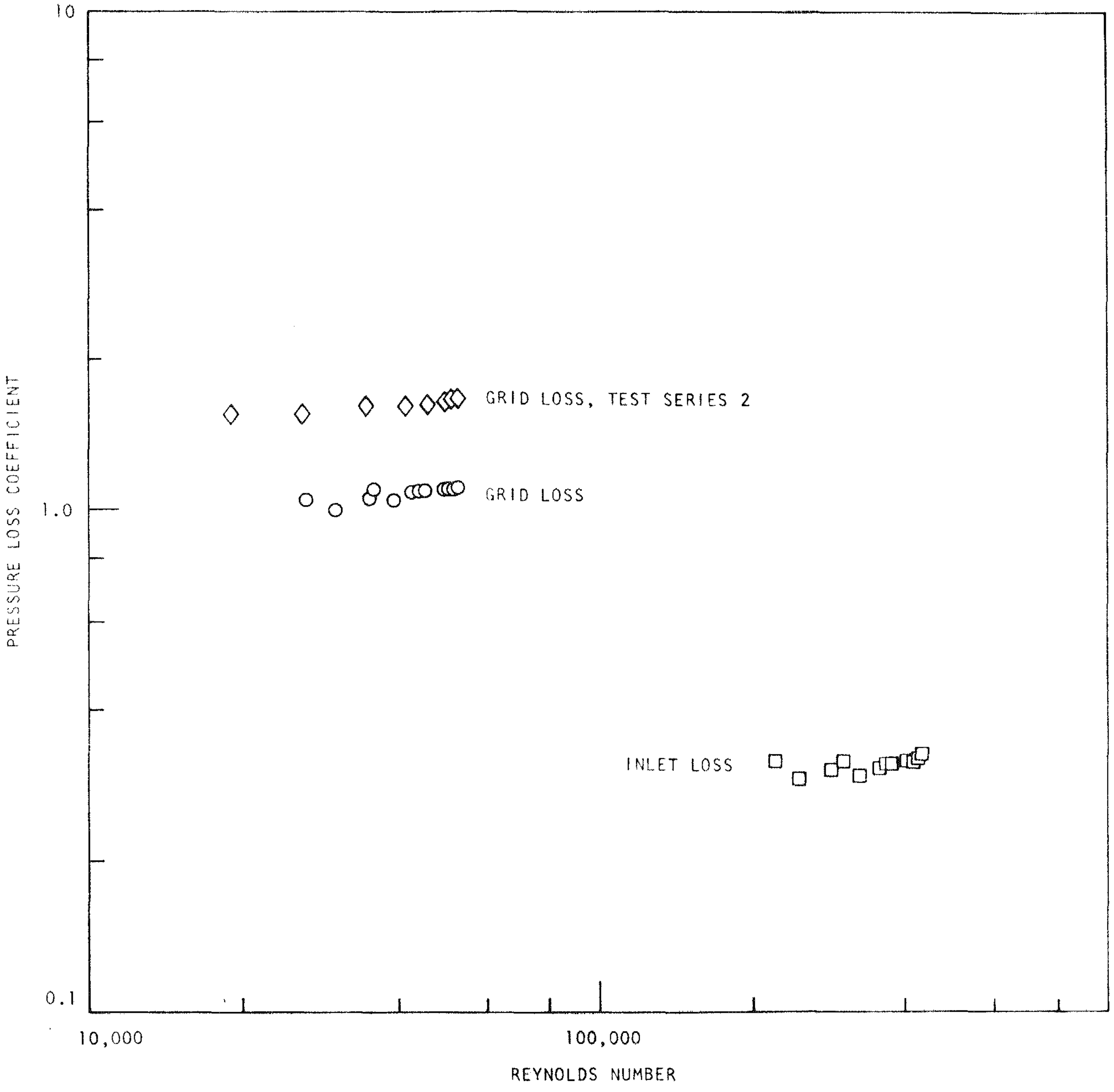

Fig. 2-12. Inlet and grid pressure loss coefficients

2-5. Buettiker, P., "Calculation of the Spacer Drop Coefficient for AGATHE HEX," EIR Report TMIN-550, 1973.

2-6. Rehme, K., "Laminarströmung in Stabbündeen," Chem. Ing. Tech. 17, 962-966 (1971).

2-7. Kays, W. M., Convective Heat and Mass Transfer, McGraw-Hill, New York, 1966.

2-8. Wheeler, C. L., *et al*., "COBRA-IV-I: An Interim Version of COBRA for Thermal-Hydraulic Analysis of Rod Bundle Nuclear Fuel Elements and Cores," Battelle Northwest Laboratory Report BNWL-1962, March 1976.

2-9. Eriksson, S. O., "SCEPTIC, a Fortran IV Computer Program for Temperature Analysis of Gas or Liquid Cooled Flow Passages With Heated Smooth or Roughened Surfaces, A User's Guide," Swiss Federal Institute for Reactor Research Report TM-IN-479, July 16, 1971.

2-10. Rector, J. D., and W. H. Sutherland, "CRASIB Users Guide and Program Manual," Battelle Northwest Laboratory, March 23, 1970.

2-11. Thompson, W. I., "CALIOP -- A Multichannel Design Code for Gas-Cooled Fast Reactors," General Atomic, unpublished data.

3. PRESSURE EQUALIZATION SYSTEM FOR FUEL (189a No. 00582)

3.1. CORE ASSEMBLY AND PES SEALS

The core assemblies (fuel, control, and blanket) in the GCFR are clamped at the conical surfaces of the assemblies to the matching surfaces in the grid plate. The assemblies are cantilevered downward and must be sealed to the grid plate to limit the coolant flow bypassing the assemblies. The assembly PES vents must be connected and sealed to matching gas passages in the grid plate, and the seals must function at the coolant pressure difference between the reactor core inlet and exit plenums. The effectiveness of the seals over the life of the core is uncertain, not only because each assembly may be rotated several times over its useful life, but also because the seals must be effective in a high-purity, high-temperature helium environment while subject to mechanical, vibrational, and thermal effects. Most of the uncertainties are expected to be resolved in a two-part program: (1) a materials screening test program for the study of static adhesion of simulated fuel assembly and grid plate parts clamped together and (2) leakage tests of fuel assembly and vent connection seals to the grid plate. Current progress in these activities is described below.

3.1.1. Static Adhesion Tests

The first set of static adhesion tests was conducted in FY 75 on 316 and 304 stainless steel at various matching cone angles, contact loadings, and surface finishes. This was followed in FY 76 by a second set of tests using materials including couples of Inconel 718 - 316 stainless steel, Inconel 718 - 304 stainless steel, and 304 - 316 stainless steel. The third test phase includes adhesion tests of metal samples coated with hardened surface materials. The simulated grid plate materials are

316 or 304 stainless steel and Stellite-6B tested against simulated fuel assembly samples of 316 stainless steel, Stellite-6B, and coatings of chromium carbide, chromium oxide, aluminum oxide, and Stellite-6. The conical surface angle is limited to a 60-deg included angle, and the static load is 1,333 N (simulating a 13,330-N clamping load for a full-size assembly).

Chromium carbide and chromium oxide coated specimens were received from the Linde Division of Union Carbide. These coatings were made using the detonation gun (D-gun) process, which is a proprietary process qualified for use on fast flux test facility (FFTF) and liquid metal fast breeder reactor (LMFBR) parts. Typical coated specimens are shown in Fig. 3-1.

Because of uncertainties about the delivery of the Linde coatings, a backup coating source was sought. In addition, Linde did not agree to produce Stellite-6 because of the development required. Therefore, coatings of chromium carbide, chromium oxide, and aluminum oxide applied with a plasma spray gun are being procured from Solar Corporation. Specimens will also be hard-faced with Stellite-6 coatings by the weld deposition method. The Solar coated specimens will be included in the static adhesion tests.

3.1.2. Fuel Assembly Ring Seal Leakage Tests

An alternative to the conical metal-to-metal core assembly seal design being developed uses piston rings as static sealing members. The test equipment, test grid parts, and core subassembly parts from the conical seal test have been modified, and ring seal tests are in progress. These tests include two ring designs provided by U.S. vendors (Stein and Dover) and one German design (KWU). The KWU design is being fabricated by KWU and two U.S. vendors for performance test comparisons. The piston ring designs and the room temperature test data for the U.S. vendor designs are described in Ref. 3-1.

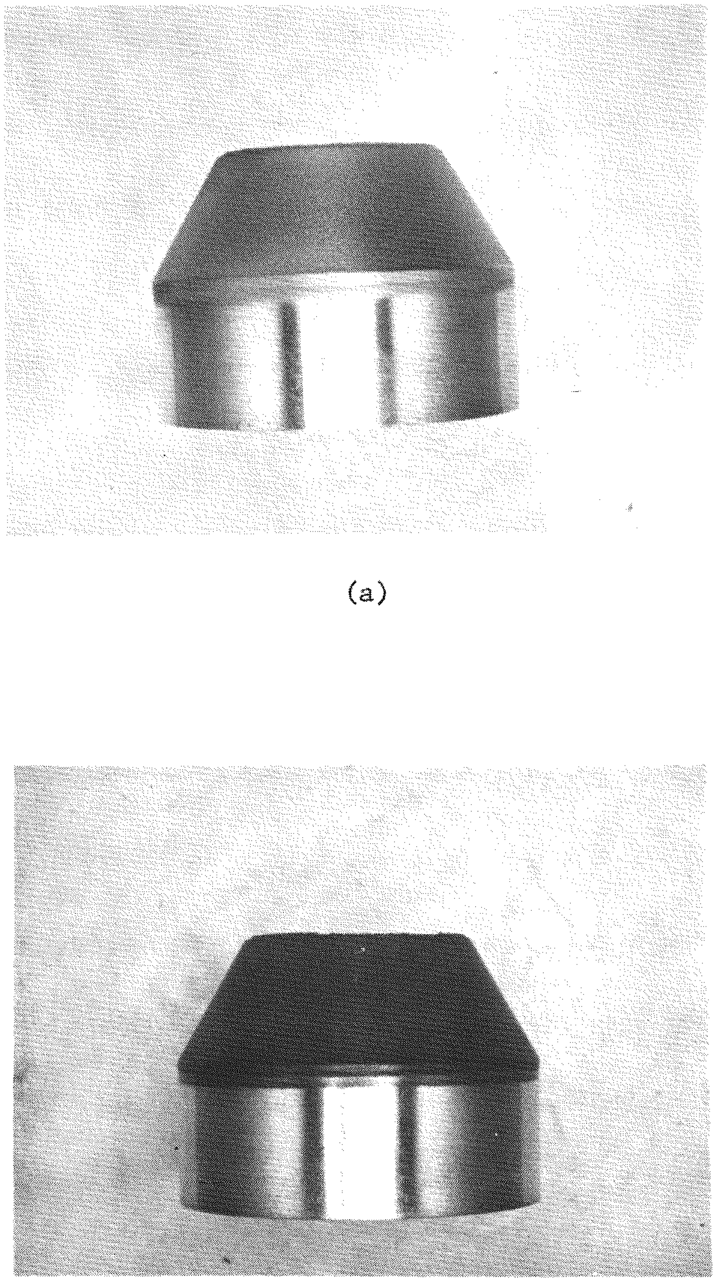

(a)

(b)

Fig. 3-1. Typical coated specimens

Elevated temperature testing of the Dover and Stein seal designs was completed, and the test results are shown in Figs. 3-2 through 3-4. In general, the performance of the two seal designs at elevated temperatures is equivalent to that at room temperature and is within the required leakage specifications. The Stein seal is considered better, not only because of its performance, but also owing to its single-piece design, which is preferred over the complex Dover five-piece design.

A piston ring seal design manufactured by Kraftwerk Union (KWU) has been received, and the test autoclave parts are in the final stages of fabrication.

3.1.3. PES Vent Assembly Seal

The vent assembly design concept being developed for the GCFR and the vent assembly test results are described in Refs. 3-1, 3-2, and 3-5. These results showed that except for port seal leakage, the design performance was satisfactory. This seal must seal the assembly after it is removed from the core grid plate. Since the operation of this port seal is independent of other seal assembly functions, the other functions will be tested separately. The test rig design is shown in Fig. 3-5. The design features being tested are as follows:

1. Contact seal surface shape, i.e., flat or conical.

2. Compliant sealing rings, i.e., O-rings, C-rings, V-rings, and K-rings.

3. Effect of Belleville spring force on seal performance.

The parts for this test are being fabricated, and the tests will be performed during the next quarter.

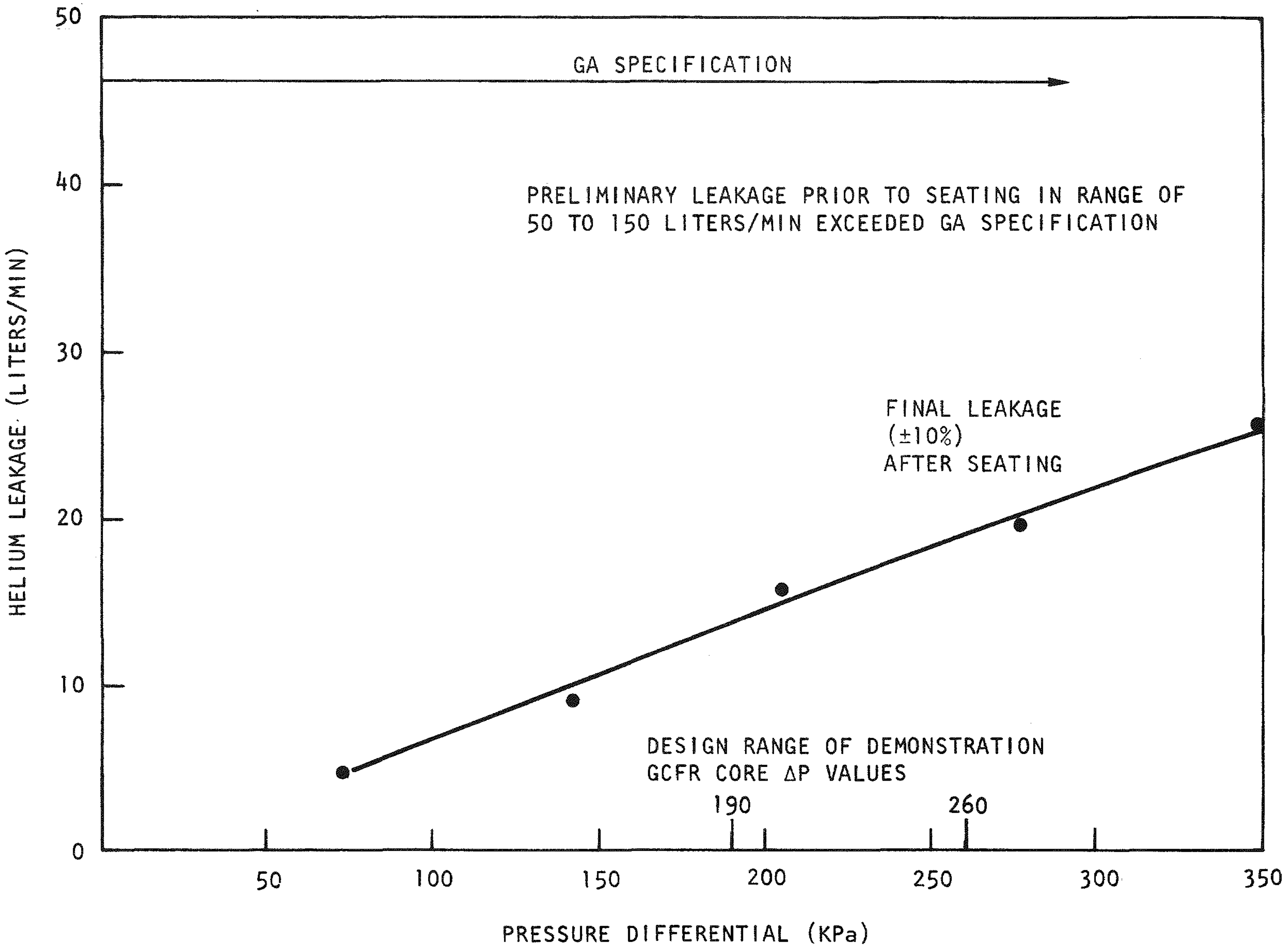

Fig. 3-2. GCFR core assembly piston ring seal test (Dover seal SN 13923-3-3)

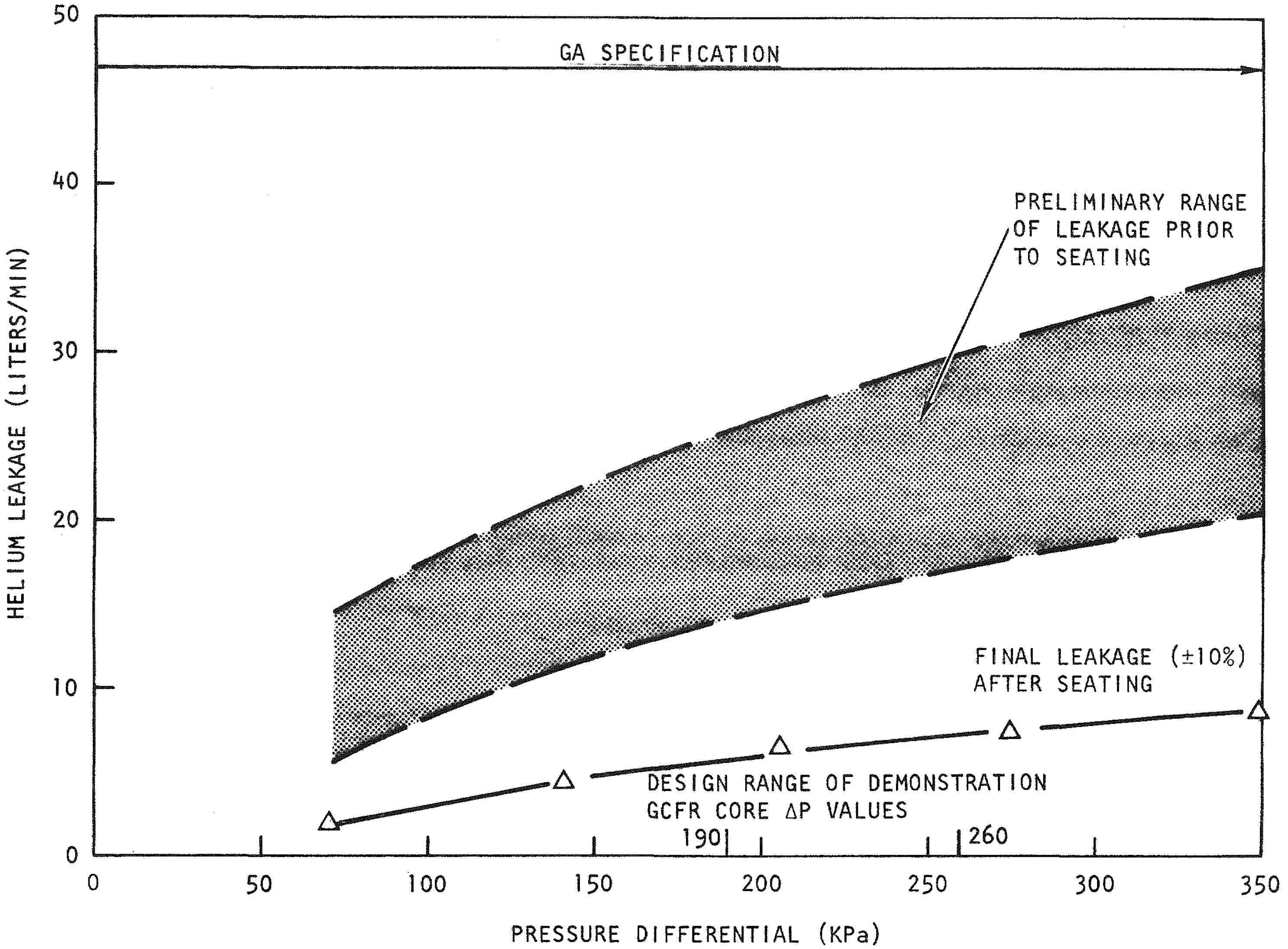

Fig. 3-3. GCFR core assembly piston ring seal test (Stein seals SN 5609-1, SN 5609-2, and SN 5609-3)

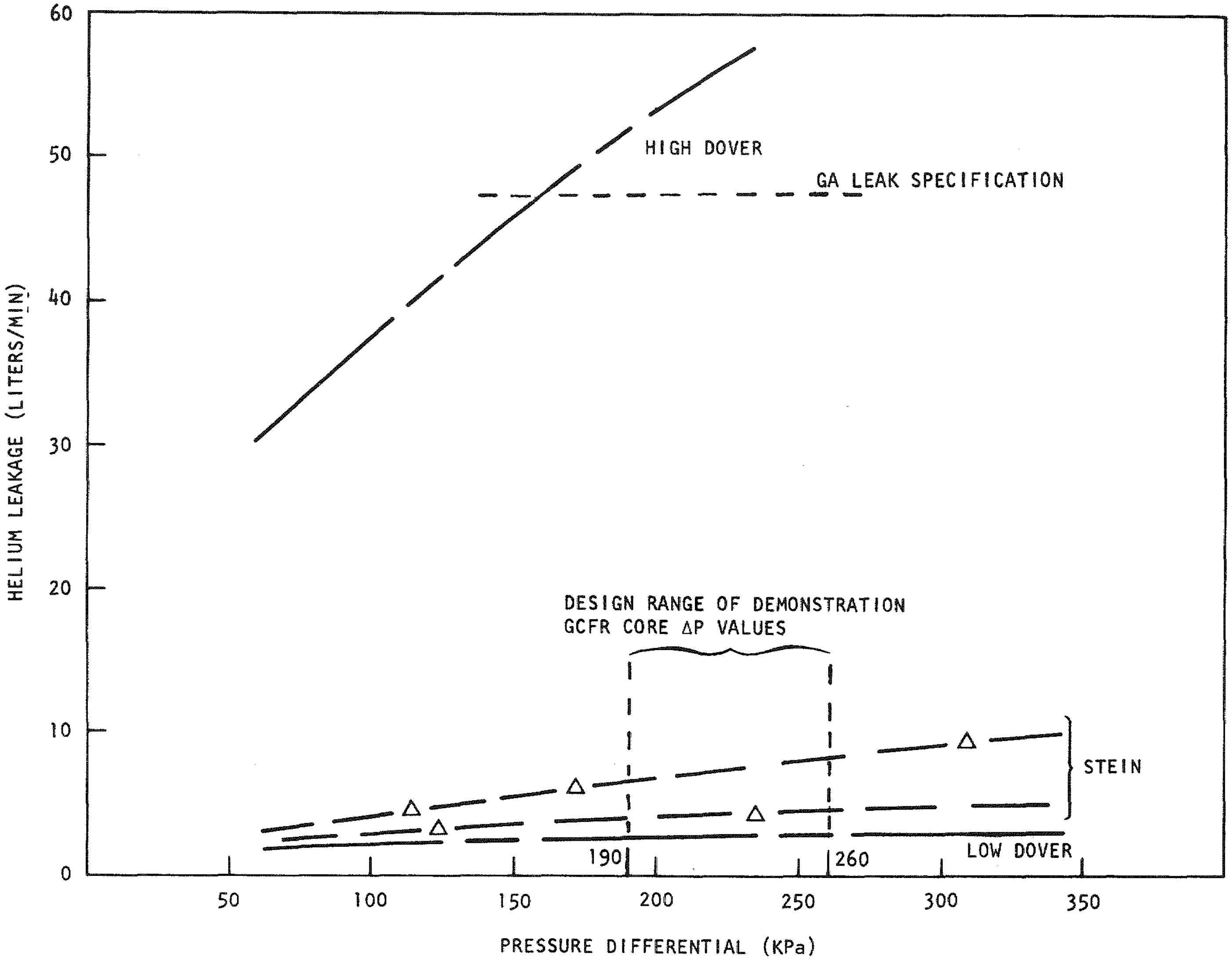

Fig. 3-4. Summary of results of room temperature tests of Stein and Dover piston rings

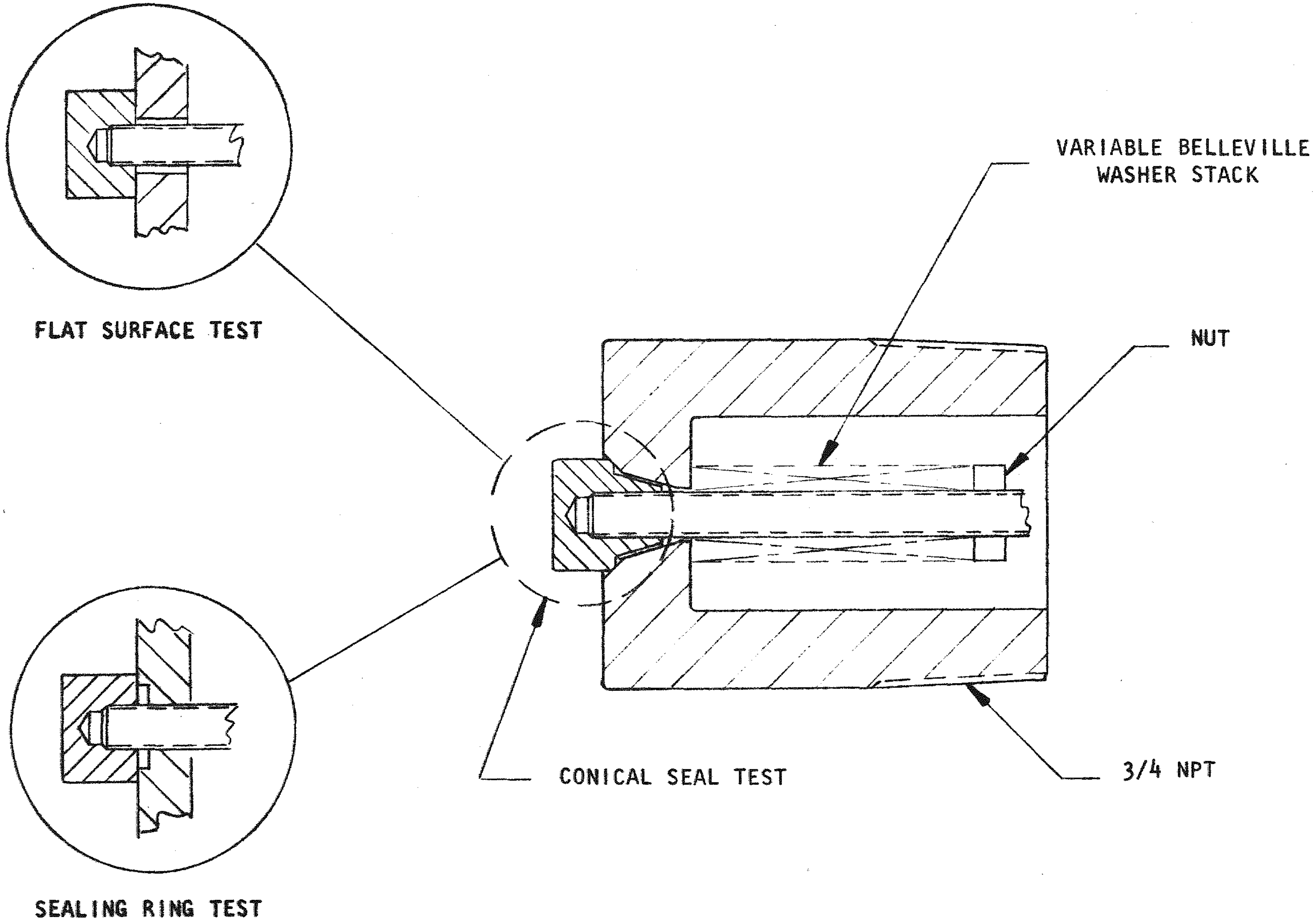

Fig. 3-5. PES vent assembly port seal test

3.2. ANALYSIS, MODELS, AND CODE DEVELOPMENT

Development of a transient flow network code continued during this quarter along with a detailed dimensional analysis of the one-dimensional compressible flow equations derived in Ref. 3-2. The variables of the equations were first made nondimensional by dividing them by reference values (denoted by subscript r). If an asterisk denotes a dimensional variable, then the variables can be written as

$$x^* = x x_r^* \quad ,$$
$$t^* = t t_r^* \quad ,$$
$$G^* = G G_r^* \quad ,$$
$$\rho^* = \rho \rho_r^* \quad ,$$
$$p^* = p \pi_r^* + p_a^* \quad ,$$
$$T^* = T T_r^* \quad ,$$
$$\lambda^* = \lambda \lambda_r^* \quad ,$$
$$q_w^* = q_w q_{wr}^* \quad ,$$

where x, t, G, ρ, p, T, λ, and q_w are the dimensionless axial coordinate, time, mass flux, density, pressure, temperature, friction factor, and heat flux variables, respectively. The pressure p^* was scaled using a reference pressure drop π_r^* and the inlet pressure p_a^* so that the axial pressure gradient has the correct order of magnitude.

Substituting the above variables into Eqs. 3-10 through 3-13 of Ref. 3-2 resulted in the following dimensionless equations (if these equations are compared with Eqs. 3-10 through 3-13, it should be noted that an asterisk was not used to indicate that the variables of Eqs. 3-10 through 3-13 were dimensional):

$$\delta \frac{\partial \rho}{\partial t} + \frac{\partial G}{\partial x} = 0 \quad , \tag{3-1}$$

$$\delta \frac{\partial G}{\partial t} + \frac{\partial (G^2/\rho)}{\partial x} = - \frac{C_L^*}{2}\left(\frac{\partial p}{\partial x} + G^2\lambda/\rho\right) \quad , \tag{3-2}$$

$$\delta \frac{\partial (\rho T)}{\partial t} + \frac{\partial (GT)}{\partial x} = \frac{C_L^*}{2} q_w - \varepsilon \frac{G}{\rho}\left(\delta \frac{\partial G}{\partial t} + \frac{\partial (G^2/\rho)}{\partial x}\right)$$
$$+ \delta\alpha \frac{\gamma - 1}{\gamma}\left(\frac{\partial p}{\partial t} + \frac{t_r^*}{\pi_r^*}\frac{dp_a^*}{dt^*}\right) \quad , \tag{3-3}$$

$$\rho T = p_a + \alpha p \quad , \tag{3-4}$$

where

$$\delta = \frac{x_r^* \rho_r^* / G_r^*}{t_r^*} \quad ,$$

= particle transit time through line/time constant of boundary conditions ,

$\varepsilon = (\gamma - 1)M_r^2$,

M_r = reference Mach number ,

$\alpha = \pi_r^*/p_a^*(o)$

= reference pressure drop/initial inlet pressure ,

$C_L^* = \lambda_r^* x_r^* / D_h^*$,

= reference loss coefficient ,

γ = ratio of specific heats.

The original objective was to integrate Eqs. 3-1 through 3-4 over the length of the line, subject to the following boundary conditions at node a of the inlet and node b of the outlet of the line:

$$p(o,t) = 0 \quad ,$$

$$p(1,t) = \left[p_b^*(t^*) - p_a^*(t^*)\right] \Big/ \pi_r^* \quad ,$$

$$T(o,t) = T_a^*(t^*)/T_r^* \quad .$$

An analytical solution of the equations does not exist; but fortunately, the parameters δ and ε are small for all PES lines under the most severe transient conditions so that approximate analytical solutions were obtained. The parameters were evaluated using the three-node PES model of Ref. 3-2:

	δ	ε	α
Suction hole line	0.0002	0.033	0.23
HPS-to-circulator line	0.028	0.022	6.17

The parameter α in Eq. 3-4 is not small for the 30-m-long helium purification system (HPS) circulator line; however, for adiabatic lines, a solution including α was obtained. The fact that ε and δ are small means that the terms which they multiply in Eqs. 3-1 through 3-3 can be neglected as a first approximation, and an improved solution can be obtained by adding perturbations to that approximation:

$$G(x,t) \sim G_o(x,t) + \delta G_\delta(x,t) + \varepsilon G_\varepsilon(x,t) + \ldots \quad . \tag{3-5}$$

There are similar expansions for pressure, temperature, and density. Such a procedure results in sufficiently accurate solutions of the equations, except at the very beginning of the transient where, on a time scale of $t^* = \delta t_r^* \leq 0.6$ s, the unsteady terms cannot be neglected if the initial part of the transient is important. For the PES application, the first milliseconds of the transient are not so important because the integral transport of fission products is significant, and the initial part of the transient does not contribute much to the integral transport. Thus, the regular expansion, Eq. 3-5, is adequate for the PES application. By substituting Eq. 3-5 into Eq. 3-1 it can be seen that G_o and G_ε are functions of time only, but G_δ is a function of x and t.

For an adiabatic line, the temperature is $T_o(t) = T_a^*(t^*)/T_r^*$. With this temperature Eqs. 3-2 and 3-4 were solved for the first approximation. The result expressed in dimensional variables is

$$p_a^*(t^*) - p_b^*(t^*) \equiv \Delta p^* = \frac{G^*(t^*)^2}{2\bar{\rho}^*(t^*)} \left\{ \lambda^*(G^*) \frac{L^*}{D_h^*} + 2\,\ell n[p_a^*(t^*)/p_b^*(t^*)] \right\}, \quad (3\text{-}6)$$

where $\bar{\rho}^*(t^*) = 1/2[p_a^*(t^*) + p_b^*(t^*)]/[R^*T_a^*(t^*)]$ is the average density, and L^* is the length of the line. Thus, given the boundary conditions $p_a^*(t^*)$, $p_b^*(t^*)$, and $T_a^*(t^*)$ and a friction factor function $\lambda^*(G^*)$, Eq. 3-6 can be iteratively solved for $G^*(t^*)$. For long lines, the ℓn term is negligible and Eq. 3-6 reduces to the usual head loss equation using the average density.

Equation 3-6 was evaluated using the boundary condition from the three-node PES SYSL model (Ref. 3-3) which has an imposed linear reduction in system pressure of 100% to 2% in 20 s (see Ref. 3-2). Figure 3-6 compares the line mass flow $W_o^* = G_o^*A^*$, where A^* is the line flow area to the SYSL output. The results are almost identical for the HPS to circulator line in the upper part of the figure, because for this long line, the ℓn term in Eq. 3-6 is negligible, and SYSL uses the usual head loss formula. For the suction hole line in the lower part of the figure, the ℓn term causes added resistance, so that $|W_o^*|$ is somewhat less than the output from SYSL at $t^* \sim 20$ s.

At $t^* = 22$ s, the imposed system pressure of the model was reduced to 2% but there was still sufficient pressure drop across the suction hole line

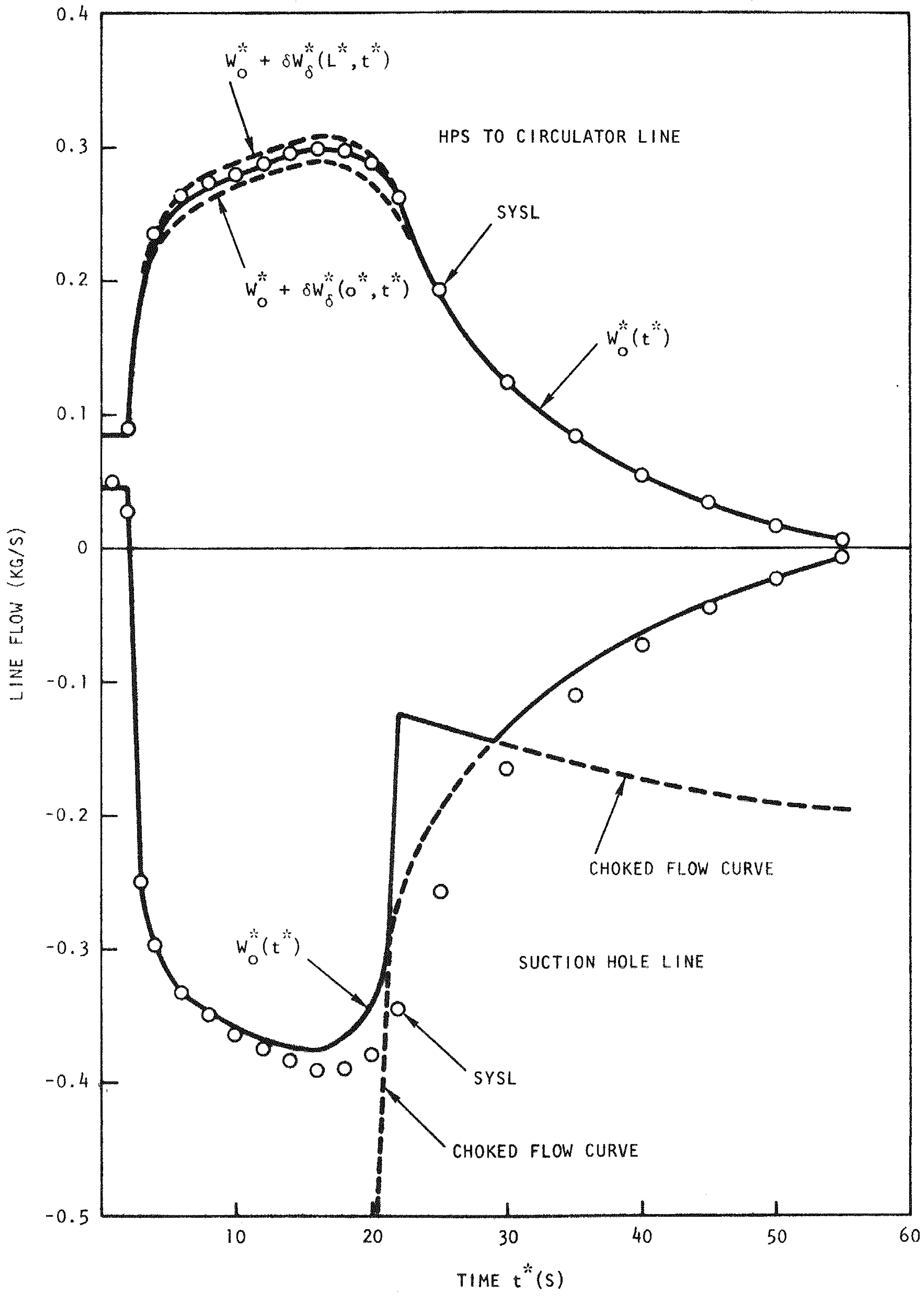

Fig. 3-6. Comparison of line flow rates using boundary conditions from a three-node model

to cause the flow to become choked at the outlet. The maximum velocity at the outlet is sonic velocity:

$$U^*_{max} = \sqrt{\gamma R^* T^*_a} \quad .$$

Thus, the maximum mass flow is given by

$$|W^*_{max}| = \rho^*_b A^* U^*_{max} = p^*_b A^* \sqrt{\gamma / R^* T^*_a} \quad . \tag{3-7}$$

Equation 3-7 is shown as the "choked flow curve" in Fig. 3-6, and the solid line indicates the minimum of $|W^*_o|$ and $|W^*_{max}|$. Equations 3-6 and 3-7 will be included in the PES code being developed.

The function $G_\delta(x,t)$ was also evaluated. It was found that at $x = 0$, where the pressure is higher, $G_\delta(o,t)$ is negative, modeling the compressibility of the gas; at $x = 1$, $G_\delta(1,t)$ is positive because the gas is expanding at the lower exit pressure. This means that the compressibility and inertial effects tend to make the gas flow out of both ends of the line. This effect is shown in Fig. 3-6, where $W^*_\delta = A^* G^*_r G_\delta$ is superposed on W^*_o. Even for the long HPS to circulator line, this compressibility effect is negligible.

It is concluded from this analyses that the flow in all PES lines under all conditions is quasi-steady and not fully transient. This means that the PES flow system becomes a capacitance-resistance network which must be integrated in time. The lines provide the resistances, but the inertia of the gas in the lines is negligible, and the volumes of gas to which the lines are connected provide the capacitances. Consequently, adaptation of the conduction network code SINDA (Ref. 3-4) to the PES flow network is being evaluated.

3.3. PLATEOUT AND PLUGGING

Volatile fission products, particularly cesium and iodine, vented from the core assemblies and produced by gaseous precursor decay of fission products vented from the core assemblies may plate out on the walls of the monitor lines. These fission products are swept through the monitor lines into the HPS traps by helium entering at the core subassembly vent connections. Accumulation of deposited material may constrict the sweep gas flow passages and could potentially lead to plugging of the lines. The conditions under which plateout and plugging of the lines could occur in the GCFR, the means of minimizing or eliminating it, and the methods for removing deposits are being investigated. A small high-pressure loop has been built and is being used for this purpose. Development of components for injection control, and measurement of impurities in the helium (i.e., H_2 and H_2O) and sources for simulating venting of the volatile fission products and their compounds is being examined.

3.3.1. High-Pressure Loop

During two months of continuous high pressure service (9.1-MPa helium) the loop system was leak-free. There were problems with the measurement of trace H_2, O_2, and N_2 impurity levels by helium ionization gas chromatography. Different columns were evaluated when it was found that the apparent sensitivity to oxygen was severely diminished at oxygen concentrations $\leq$ 2 vpm. The problem was finally traced to the exponential dilution flask (EDF) used for calibration purposes. Although the actual cause of the problem in the EDF has not been positively ascertained, a method has been developed to minimize or obviate it altogether.

3.4. FISSION PRODUCT RELEASE AND TRANSPORT

The purpose of the work on this subtask is to obtain experimental data on the interdiffusion and gas phase and the surface back diffusion of gaseous and volatile fission products. The diffusion coefficient data will be used to validate or improve the SLIDER code (Ref. 3-6), a one-dimensional model for fission gas diffusion transport (including radioactivity decay). Surface transport and back diffusion data will be used to establish a model for predicting the importance of these mechanisms to contamination of the reactor coolant system.

It was necessary to modify the original diffusion apparatus to include the dead volume of one of the bellows seal valves as part of the source tube region and remove it from the diffusion tube region. This modification permits establishment of a sharper diffusion front and eliminated what appeared to be a plateau region prior to attainment of equilibrium. This effect is illustrated in Fig. 3-7; the circles represent data from a Kr-85 diffusion run performed prior to the modification (note the plateau in the region where $C/C_\infty \sim 0.8$), and the triangles represent the data obtained after the apparatus had been altered. Figure 3-7 also shows the SLIDER output generated for the updated apparatus using a temperature- and pressure-corrected value of the standard Kr-85 diffusion coefficient ($D_0 = 0.57$ cm^2/s, $T_0 = 273$ K, $P_0 = 0.101$-MPa helium), where $D(P,T) = D_0(T/T_0)^{5/3}\ (P_0/P)$. The agreement between calculations and experiment appears to be excellent.

Figure 3-8 illustrates the data obtained for Kr-85 diffusion in 8.7-MPa helium at temperatures of 306 K, 475 K, and 623 K. Figure 3-8 also gives the SLIDER generated data. The experimental data suggest that the Kr-85 diffusion coefficients are larger than those predicted by theory. This behavior is often indicative of the presence of convective transport, which in effect speeds up the mixing process and results in apparently greater diffusion constants. Consideration is being given to further reduction or elimination of such effects from the experiments.

3.5. MONITOR STATION AND INSTRUMENTATION

3.5.1. Monitor Station Layout

A diverter concept and a mechanical scanner concept have been developed. Other concepts are being considered, but layout and arrangement drawings

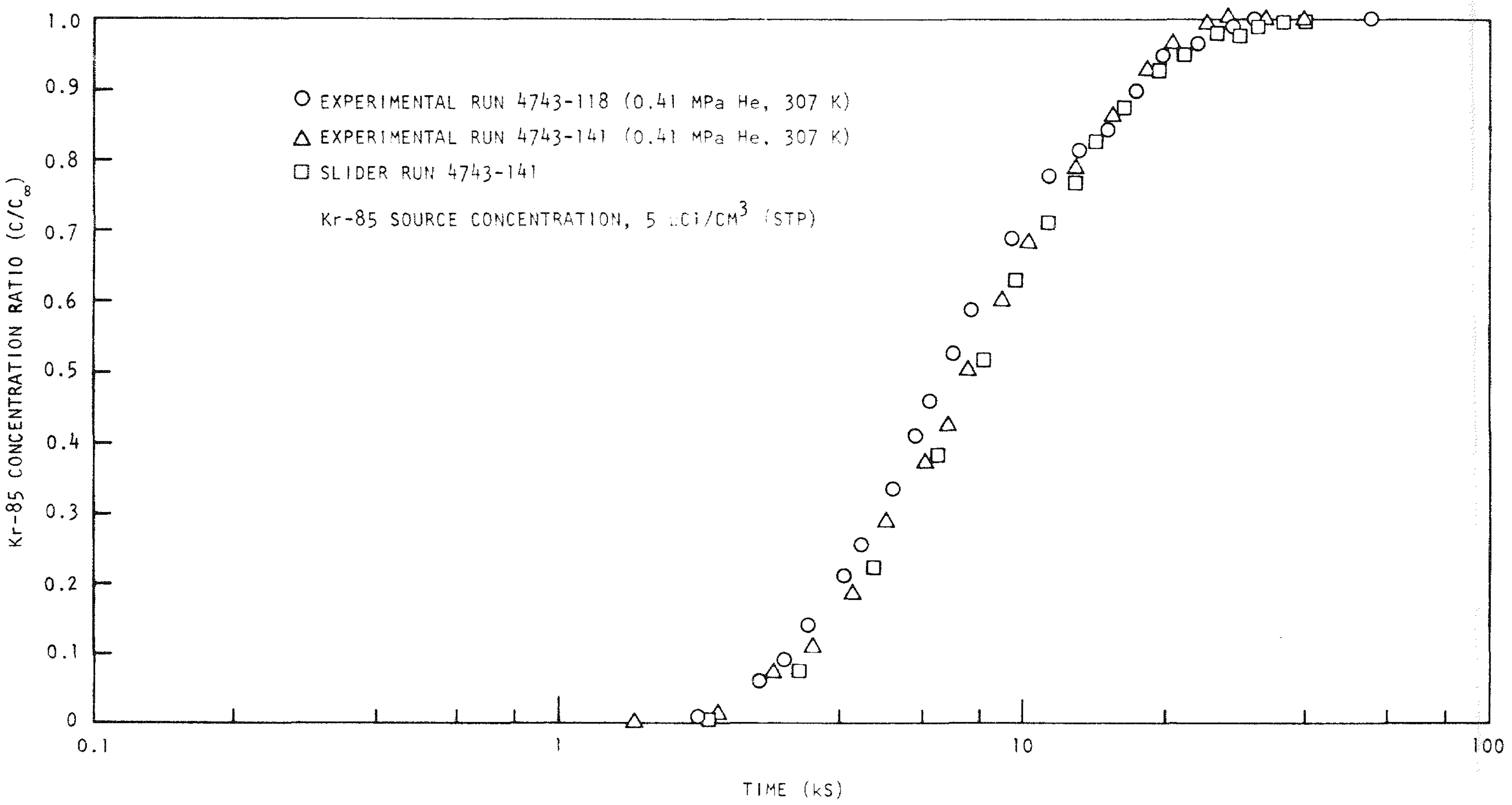

Fig. 3-7. Diffusion runs for Kr-85 in helium

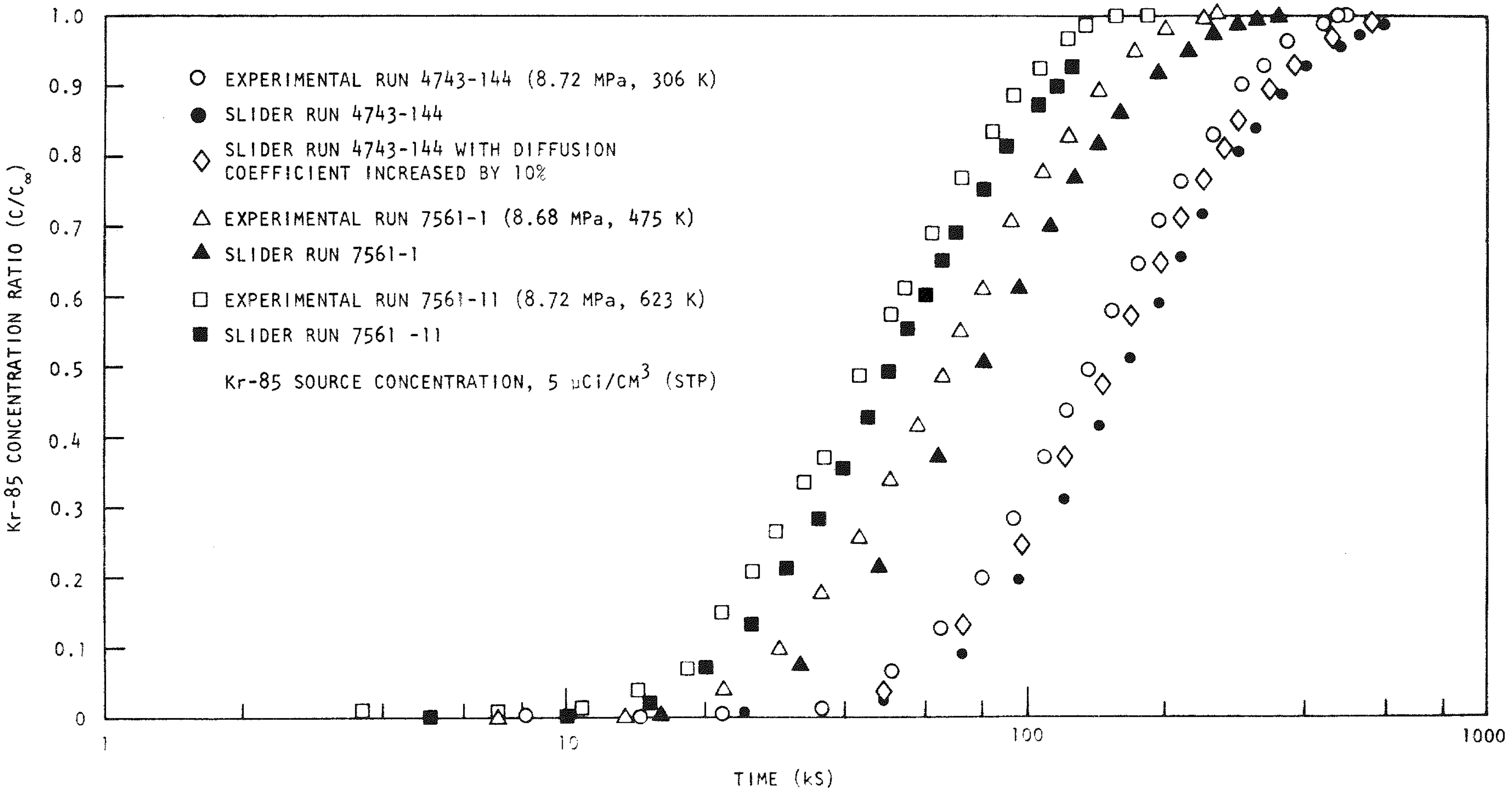

Fig. 3-8. Diffusion runs for Kr-85 in helium

will not be prepared for them because the diverter and mechanical scanner concepts represent the maximum monitor station sizes. One alternate concept is the electronic scanner, where each line is monitored by a separate radiation detector and identification of hot lines is accomplished by electronic switching from line detector to line detector, i.e., by sequential detector scanning. If the cost of maintenance and repair of diverter valves exceeds the cost of the detectors and their electronic channels, then the electronic scanning concept will replace the diverter concept. Investigation of commercially available equipment is in progress and is expected to continue for several years.

3.5.2. Monitor for PES and Sweep Gas Irradiation Experiment Evaluation

Cadmium-telluride semiconductor gamma radiation detectors may be attractive for GCFR monitor station applications. Chlorine-doped [CdTe(Cl)] detectors are commercially available, and indium doped detectors have been used for medical scanning applications and may become commercially available for other applications. The features making these detectors attractive for monitor station applications have been reported by various vendors. These detectors will operate at room temperature with low temperature sensitivity, and have resolutions comparable to those of NaI(Tl), dynamic ranges of six to seven decades, and volumes of only a few cubic millimeters to be shielded. The cost per detector is reasonable ($300 to $500). The high resolution could eliminate the need to divert flow to a separate Ge(Li) cryogenic station, and the 10^6 to 10^7 dynamic range could eliminate the capstan collimator and TRIGA drive positioner. The low expected cost of each detector could eliminate the line scanner. If the attributes of the CdTe(In) were demonstrated to be real, it would probably be possible to reduce the seven monitor stations of the demonstration plant to the small station of relatively simple design. CdTe(In) appears to be preferable because of its reportedly better resolution. Experimental verification of the important properties of CdTe(In) detectors for monitor station use is planned.

3.6. PES PROGRAM PLANNING

Work on the PES design criteria has resumed and is expected to be completed during the next quarter.

REFERENCES

3-1. "Gas-Cooled Fast Breeder Reactor Quarterly Progress Report for the Period November 1, 1976 Through January 31, 1977," ERDA Report GA-A14240, General Atomic, February 1977.

3-2. "Gas-Cooled Fast Breeder Reactor Quarterly Progress Report for the Period February 1, 1977 Through April 30, 1977," ERDA Report GA-A14358, General Atomic, May 1977.

3-3. Estrine, E. A., "SYSL Users Guide," General Atomic, to be published.

3-4. Smith, J. P., "SINDA User's Manual," TRW Systems Group Report 14690-H001-R0-00, April 1971.

3-5. "Gas-Cooled Fast Breeder Reactor Quarterly Progress Report for the Period August 1, 1976 Through October 31, 1976," ERDA Report GA-A14112, General Atomic, November 1976.

3-6. Jadhov, K. B., and B. W. Roos, "SLIDER, A Fortran-V Program for the Computation of Release of Fission Products From One-Dimensional Multi-Layered Fuel Configurations," USAEC Report GA-8566, Gulf General Atomic, August 1969.

4. CORE FLOW TEST LOOP PROGRAM (189a No. 00582)

A series of out-of-pile simulation tests will be performed to (1) demonstrate the ability of the GCFR fuel, control, and blanket assembly designs to meet design goals and (2) verify predictions of analytical models which describe design operation and accident behavior. The emphasis of the tests will be on obtaining thermal-structural data for steady-state, transient, and marginal conditions using electrically heated rod bundles in a dynamic helium loop. Final margin tests will be progressively extended to the highest possible temperature until the heater elements fail. The core flow test loop (CFTL) program plan (Ref. 4-1) describes the requirements for the test program to be conducted in the CFTL, which will be constructed and operated by Oak Ridge National Laboratory (ORNL). The principal work accomplished during this quarter was as follows:

1. Based on an ORNL recommendation, the reference program was reduced from 12 test bundles to 6, with the assurance that the priority one verification requirements will be satisfied.

2. The scope of the specifications for the 6-bundle test program was developed.

3. The preliminary design of the blanket bundle test section was issued.

4. Trial fuel rod simulator roughening demonstrated the need for better quality control of the unroughened rod simulator.

5. The initial trial roughening of a fuel rod simulator was partially successful.

4.1. PROGRAM PLANNING

4.1.1. Program Modification

At a meeting of ERDA, GA, and ORNL, CFTL program activities were ordered according to their technical priority and GA gave recommendations for reducing the reference program. ERDA, GA, and ORNL agreed to the following planned program modifications: (1) reduction of the number of test bundles from 12 to 6, with three fuel bundles, two control bundles, and one blanket bundle; (2) elimination of internal flow blockage tests from the reference program; and (3) establishment of the reference heater components (Nichrome-V heater elements and 4 internal type K thermocouples with Inconel 600 sheaths).

4.1.2. RECS Planning

General Atomic has selected the resource evaluation and control system (RECS) (Ref. 4-2) to integrate the planning, scheduling, cost control, and priority identification for the GCFR program. The CFTL network diagram is given in Ref. 4-3. The initial phase of the total CFTL program input to RECS was completed during this quarter.

4.1.3. Quality Assurance Program

As part of the planning activity, GA has maintained a continuing dialogue with ORNL to assure a consistent set of quality assurance requirements for the CFTL program. During this quarter, GA requested that ORNL observe the requirement that design verification testing be accomplished following the measures described in Part XI, 10CFR50 Appendix B. Other parts of 10CFR50, Appendix B, should be used when applicable.

Adequate quality assurance is particularly important at the GA-ORNL interfaces of the CFTL program, e.g. for roughening of the fuel rod simulator, where ORNL will procure the rods, GA will roughen them, and

ORNL will assemble them into bundles. Initial trial roughening is being carried out. Procedures for handling, roughening, and inspecting were drafted and are being updated. Modifications and additional procedures are being prepared.

4.2. TEST ANALYSIS AND PREDICTION

The effects of the following conditions have been examined: (1) transient heat-up of a bundle after depressurization; (2) radiant and natural convection heat loss from a single rod; (3) heat loss from a test bundle; and (4) thermal radiation correction for an outlet thermocouple. A report was issued (Ref. 4-4) on the status of transient thermal-hydraulic analysis methods. A method for locating cladding thermocouples in a test bundle was developed. This method is based on a random distribution.

4.2.1. Transient Heat-Up of a Bundle After Depressurization

Design basis depressurization in a GCFR is considered to occur in two phases: a depressurization which takes one minute or more and removal of afterheat in the depressurized condition. It is predicted that the core assemblies will approach the damage limit depending on the severity of the assumed conditions. The optimum CFTL simulation is being studied.

4.2.2. Radiant and Natural Convection Heat Loss from a Single Heater Rod

At normal GCFR operating conditions, heat transfer by radiation and natural convection are not significant factors in determining optimal CFTL simulation. This may not be true for extreme transient conditions such as the depressurized phase of the DBDA. Scoping calculations were performed to estimate the heat loss from a single rod inside a pressure vessel with a cold wall temperature of 325°C. Table 4-1 presents the estimated heat loss for various conditions and assumed emissivities. At rod surface temperatures approaching the cladding melting temperature ($\sim$1380°C), heat loss is

TABLE 4-1
HEAT LOSS BY RADIATION AND NATURAL CONVECTION(a)

Surface Temperature (°C)	Heat Loss by Radiation (kW)		Heat Loss by Natural Convection (kW)	
	Rod Emissivity = 1.0	Rod Emissivity = 0.5	Helium Pressure = 8.9 MPa	Helium Pressure = 0.1 MPa
600	0.24	0.12	1.0	0.06
1000	1.1	0.53	2.9	0.17
1400	3.2	1.6	4.8	0.30

(a) Conditions and assumptions: (1) single CFTL fuel rod simulator; (2) 1.13-m length; ambient pressure vessel temperature = 325°C; initial GCFR afterheat ∿2.8 kW/rod.

equal to initial GCFR afterheat. Thus, radiant and natural convection heat loss must be considered when specifying the CFTL simulation for extreme transients.

The actual transient DBDA behavior of a CFTL bundle depends upon fuel rod simulator (heater) thermal characteristics and the time function of power and flow. A scoping calculation of approximate transient behavior after completion of depressurization was accomplished using TSPEC (Ref. 4-5) for power-to-flow ratios of 1, 3, and 6. The calculations assume an isothermal initial condition at simulated reactor inlet temperature followed by rod heat-up without heat loss to the surroundings. The results (Fig. 4-1) illustrate the type of behavior to be expected of the CFTL for the power and flow specified. When heat loss to the surroundings is considered, the time required to approach an equilibrium coolant outlet temperature and reduce the equilibrium maximum cladding temperature will be extended.

The scoping calculations represent a sample of the very large set of possible postdepressurization test conditions and indicate the characteristic performance to be expected from this simulation. Improved simulation test conditions require (1) definition of the specific GCFR transient conditions to be modeled; (2) criteria for optimum simulation; (3) development of a more accurate transient analysis method; and (4) accounting for the performance limitation of the loop and heaters. The effect of heat loss to the surroundings and the feasibility of reducing heat loss by insulation must also be determined.

4.2.3. Heat Loss From a Test Bundle

In the GCFR core, each fuel assembly is surrounded by assemblies at approximately the same temperature, and there is no net heat loss between assemblies. The CFTL assembly is placed in a large duct containing stagnant helium and surrounded by attemperation flow at the inlet temperature (325°C). Convection currents can be set up since there is a cool wall and a heated wall. If the heat loss is significant, insulation will have to be provided to simulate GCFR conditions.

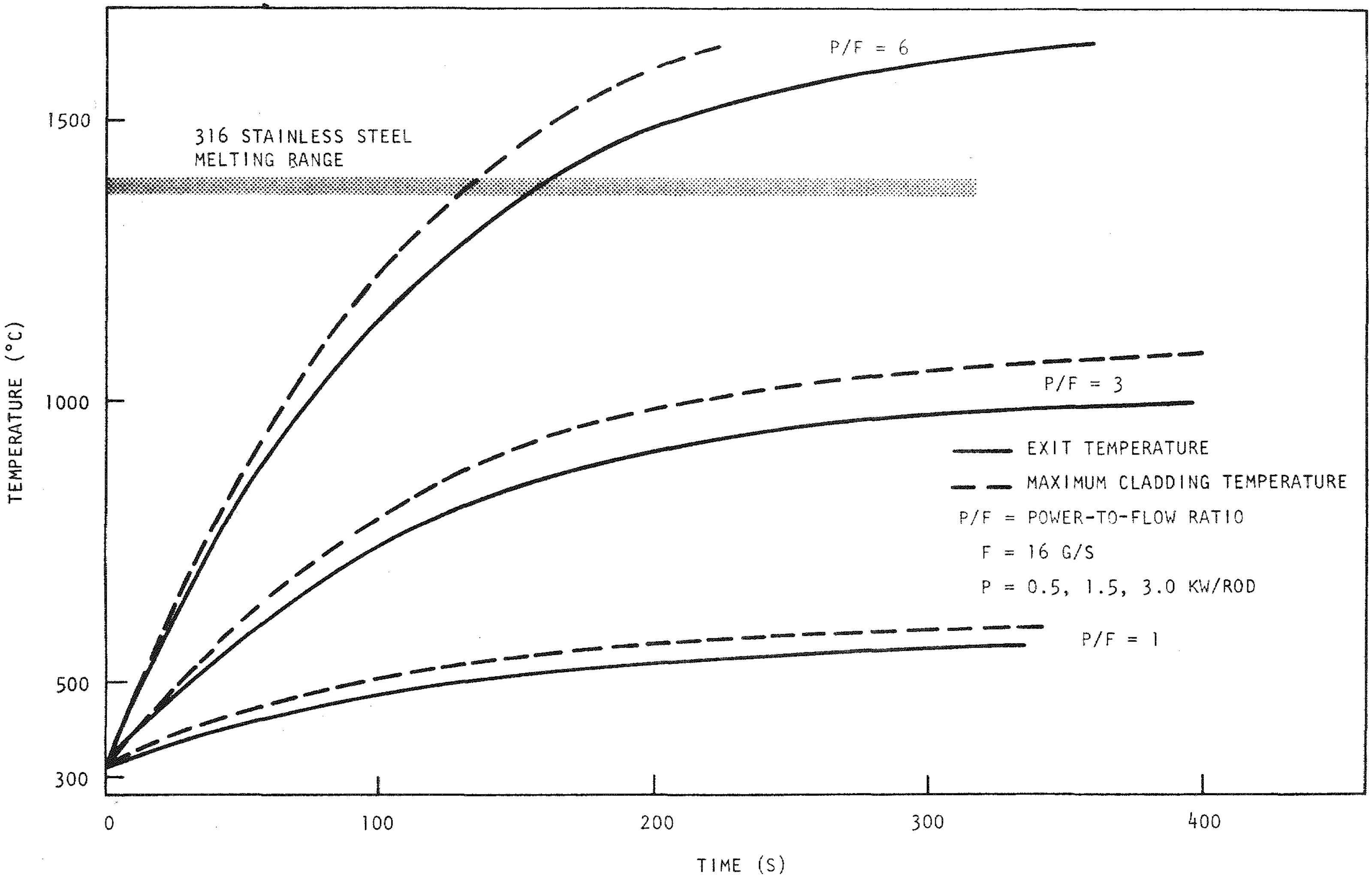

Fig. 4-1. CFTL transient temperature rise after depressurization

The test assembly was assumed to have an equivalent diameter of 74.65 mm inside a duct with a 300-mm diameter. The Grashof number at the average temperature of 436°C is 9500, and the overall heat transfer coefficient U is given by

$$\frac{1}{U} = \frac{1}{h_{hot}} + \frac{b}{k_f} + \frac{1}{h_{cold}} \quad .$$

For one peripheral subchannel, the heat loss q_ℓ is given by

$$q_\ell = UA \times \Delta T_w \quad ,$$

where $U = 2.58\ w/m^2\text{-}°C$,

$A = 0.0129\ m^2$,

$\Delta T = 111°C$,

$q_\ell = 3.69\ w$.

Heat input to the peripheral subchannel q_i at 100% power by one-half a rod is

$$q_i = 1.4 \times 10^4\ w \quad .$$

At 100% power, the heat loss is 0.026% and at 10%, 0.26%. Since the heat loss from the test assembly to the attemperation flow is small, there seems to be no need to insulate the duct walls.

4.2.4. Thermal Radiation Correction for an Outlet Thermocouple

Measurement of the temperature of a gas may be subject to error because of the relatively high gas thermal resistance to heat transfer to the sensor and the potential heat loss via radiation and conduction. For the mixing test with a single heated rod, a thermocouple rake will be used to measure the coolant temperatures of the various subchannels at the bundle exit. Only the central row of subchannels is heated; the rest of the subchannels and the walls are almost at the inlet temperature. An analysis must be done to determine the steady-state temperature which the thermocouple reaches owing to conduction along the thermocouple, convection from the hot gas, and radiant heat transfer between the hot walls, cool walls, and thermocouple.

A resistance network was developed to analyze the heat flows. All three gray surfaces (hot and cold walls and the thermocouple) are assumed to have a potential of r with respect to the potential e of a black surface and a resistance of $(1 - \varepsilon)/A_{\varepsilon}$ between r and e. Resistances 1/AF connect the potential points r, and convection from the hot gas to the thermocouple is defined by the conductance hA; KA/L defines conduction to the thermocouple holder.

A trial and error method was used to evaluate the temperature of the thermocouple. A temperature between that of the hot gas and the cold wall was assumed for the thermocouple. Knowing all three potentials, the flows can be determined. If all flows do not balance at any node, a new temperature is assumed for the thermocouple. It was found that the heat transfer coefficient for helium is sufficiently large, making the corrections small. The correction is less than one-fourth of a degree centigrade for 100% flow and about 1/2°C for 10% flow. This potential source of error is not significant for normal operation.

4.2.5. Status of Transient Thermal-Hydraulic Analysis Methods

A GCFR core must handle transients which involve changes in coolant flow rate, coolant pressure, and power. Depending on the rate of these changes and the time constant of the system, the transients can be defined as slow or fast. The slow transients are (1) normal load changes, (2) start-up and shutdown, and (3) power overshoot. The fast transients are (1) coolant flow system malfunction, (2) DBDA, and (3) reactor trip. For the fast transients, a transient analysis is needed, whereas a quasi-steady-state analysis can be used for the slow transients.

A study has been made of the computer codes available at GA which can be used for the transient analysis of the GCFR and the CFTL rod bundles. These codes are required for design and performance prediction of CFTL rod bundles. The following codes are either operating or under development:

1. COBRA-IV (Ref. 4-6) has the transient capability to analyze fuel and blanket assemblies. It will accept pressure, inlet coolant flow and temperature, and power as forcing functions and is capable of handling reverse flow and recirculation effects. At present, it does not model circumferential cladding conduction and surface-to-surface radiation, both of which are important in low flow/high power cases. GA is negotiating with BNWL for a transient version of COBRA with the improvements listed above; it is expected to be available in the middle of 1978 and verified by early 1979.

2. FLOMAX, used for steady-state bundle analysis, is expected to be able to handle transient bundle analysis by mid-1979.

3. TAC2D and TAC3D (Refs. 4-7, 4-8) solve the diffusion equation and handle power flow and temperature as functions of time. Surface-to-surface radiation can be modeled. TAC2D can be used for axisymmetric models.

4. TSPEC (Ref. 4-5) analyzes the response of an average rod in a bundle on a quasi-steady state basis. Transient behavior is approximated by assuming an exponential time approach to a new steady-state condition.

5. SYSL (Ref. 4-9) is a high-level digital simulation language which may be used to solve systems of coupled, nonlinear differential equations. SYSL has been used to implement two codes: Rod*SIM (Ref. 4-10) which performs transient thermal calculations for isolated CFTL heater rods and GCFR fuel rods, and CFTL*SIM (Ref. 4-11) which performs transient thermal-hydraulic simulation of the CFTL.

6. SINDA (Ref. 4-12) is a three-dimensional thermal-hydraulic network code which is capable of transient analysis. Input and debugging are very time consuming and the code is expensive to run. This code is recommended only for three-dimensional asymmetric geometries.

7. EDGTRN (Ref. 4-13) is used for analysis of the transient response of the peripheral rods in an assembly. The duct wall, coolant, and fuel rods are modeled as slabs.

8. MINGAF, DEPTRN, GAFTRN (Refs. 4-14 through 4-16) are systems analysis codes which handle core response to rod withdrawal accidents, depressurization, scrams, and other reactor transients.

4.2.6. Method of Locating Cladding Thermocouple in a Test Bundle

A realistic evaluation of predicted bundle surface temperature reveals that measured temperatures will vary in a statistical manner from the nominal expected values. The spread of measured values will depend on the uncertainties associated with the input to the predictions, the correlations used in the prediction, and the precision of the temperature measurements. To interpret the temperature measurement results and verify the predicted performance, the statistical nature of the measurements and predictions must be considered in the design of the experiments and the evaluation of the data (Ref. 4-17).

The method suggested for developing the temperature measurement locations considers a random distribution of thermocouples within the test bundle as a base case and approaches the optimum arrangement by moving the thermocouples to positions which increase the total information yield. The advantage of this method is that the base case information can be relatively simply defined. However, further analysis is required to improve thermocouple distribution. Furthermore, the information yield decreases continuously with an increasing number of thermocouples, which is valuable for estimating the cost-effective function. Failure of any particular thermocouple or heater has the smallest possible impact on the results.

The reference 37-rod bundle will contain 31 fuel rod simulators (heater rods) with 4 cladding thermocouples per rod. Thermocouple location will be determined by selecting 124 five-digit random numbers. The first digit will indicate 1 of 10 possible axial locations; the next two digits will indicate 1 of 31 possible rods; the last two digits will indicate 1 of 12 possible initial azimuthal positions. If selection results in more than 4 thermocouples per rod or more than 1 at the same azimuthal position in a rod, then other random numbers will be selected. Ater the initial azimuthal position is selected, other positions are limited to 90, 180, and 270 deg.

For each steady-state test run, the expected values, standard deviations, and hot spot factor-uncertainties at each measurement point will be predicted, assuming a normal distribution. Then the following algebraic sum will be calculated:

$$\sum^{n} \frac{\text{predicted} - \text{measured}}{\text{standard deviation}} .$$

The statistical hypothesis that the measured values are correctly predicted will be accepted to a significance level of 0.05. It is believed that this approach will yield significant, if minimal, information about the validity of the predictive analysis and that the next steps will involve statistical tests of the fine structure and improved locations.

4.3. TEST SPECIFICATION

The draft (Ref. 4-18) of the test specification for priority one preliminary series P-1 and P-2, which applies to the first fuel rod simulator test bundle (37-rod), was updated based on currently available test requirement information and the GA-ORNL-ERDA agreement for using a total of 6 test bundles. Table 4-2 summarizes the test series, bundles, and major test areas for the reduced program. Information on the tests for the total CFTL

TABLE 4-2
RECOMMENDED MINIMUM PRIORITY ONE TEST SERIES

Test Series	Test Series ID	Bundle	Major Test Areas
Preliminary			
37 rods, BOL	P-1	C	Unheated bundle checkout, flow and pressure
	P-2	C	Loop hot flow checkout, normal transients, depressurization margin, steady-state undercooling margin, transient undercooling margin
Fuel bundle			
61 rods, BOL	F-1	H	Size effect, heat transfer verification, normal transients, accident behavior, steady-state undercooling margin, transient undercooling margin
91 rods, BOL	F-4	K	Size effect, heat transfer verification, normal transients, accident behavior, steady-state undercooling margin, transient undercooling margin
Control bundle			
90 rods, BOL	C-1	A	Normal transients, accident behavior, depressurization margin
		B	Transient undercooling margin
Blanket bundle			
61 rods, BOL	B-1	A	GCFR simulation, verification of heat transfer, normal transients, accident transients, steady-state undercooling margin, transient undercooling margin

program was prepared for review by GA, ORNL, and ERDA. Tables 4-3 and 4-4 delineate the priority one test verification series.

4.4. TEST BUNDLE DESIGN AND FABRICATION

4.4.1. Blanket Test Section

Preliminary drawings for the blanket bundle test section and components were issued for test planning purposes. Figures 4-2 and 4-3 are sketches of the blanket rod simulator and bundle test assembly, respectively.

4.4.2. Roughening of Fuel Rod Simulators

The sample fuel rod simulators provided by ORNL to be used for determining the effects of roughening (ribbing) on internal heater and thermocouple integrity were found to be out-of-round and kinked, so that it was impossible to consistently provide a rib height of 0.13 ± 0.01 mm. However, one CFTL and one LMFBR fuel rod simulator were roughened and prepared for final inspection at GA.

4.5. LIAISON WITH ORNL

Coordination and review meetings and a meeting on fabrication of fuel rod simulators (heater rods) were held with ORNL. The GCFR versions of the computer codes FLAC (Ref. 4-17) and COBRA (Ref. 4-19) were sent to ORNL for use in the CFTL analysis. GA and ORNL responsibilities in the CFTL analysis were jointly approved, and the initial development of a computerized task document index was completed.

4.6. GCFR PROTOTYPE ASSEMBLY TEST PLANNING

Program planning for testing of the prototype core assemblies is continuing. The tests will be conducted on full-size core assemblies to ensure that they meet design qualification requirements prior to fabrication of the demonstration plant initial core. The prototype assemblies will be the

TABLE 4-3
CFTL PRIORITY ONE TEST SERIES SUMMARY

	Number of Tests in Each Series					
	Fuel Assembly			Control Assembly		Blanket Assembly
Test Series	37 Rods	61 Rods	91 Rods	54 Rods(a)	90 Rods	61 Rods
Steady-state flow, unheated	29	16	16	--	29	29
Normal transients, unheated	38	3	3	--	1	0
Upset transients, unheated	5	5	5	--	1	0
Emergency transients, unheated	3	0	0	--	0	0
Depressurization transients, unheated	4	0	0	--	0	0
Steady-state, uniform power	45	26	26	--	35	4
Steady-state, skewed power	35	13	13	--	10	24
Steady-state, single heated rod	102	0	0	--	0	184
Normal transients, uniform power	14	0	0	--	8	0
Normal transients, skewed power	24(b)	4(b)	4(b)	--	8(b)	4(b)
Upset transients, uniform power	5	1	1	--	1	0
Upset transients, skewed power	3	1	1	--	1	2
Emergency transients	3	3	3	--	3	0
Depressurization transients	3	2	2	--	2	2
Design margin	40	20	20	--	20	40
Total	353	94	94	--	119	269

(a) Similar test to 90-rod control bundle if analysis indicates need.

(b) 1200 cycles at 140 s/cycle.

TABLE 4-4
CFTL PRIORITY ONE TEST VERIFICATION MATRIX

Information Required	Fuel Assembly			Control Assembly		Blanket Assembly
	37 Rods	61 Rods	91 Rods	54 Rods	90 Rods	61 Rods
Isothermal flow data	1(a)	2	1	2	1	1
Steady-state thermal performance						
Uniform power, heat transfer	1	1	1	2	2	2
Skewed power effects, heat transfer	2	2	1	2	1	1
Verify Swiss, German, and University of California, Santa Barbara results	1	--	--	--	--	2
Verify size extrapolation	1	1	1	1	1	--
Statistical temperature variation, code verification	2	1	1	--	--	1
Thermal distortion interaction	2	2	1	2	1	1
Normal transients, structural behavior	2	2	1	2	1	1
Upset transients, structural behavior	2	2	1	2	1	1
Early life endurance, structural behavior	2	2	1	2	1	1
Emergency transients, structural behavior	2	2	1	2	1	2
Faulted transients, structural behavior DBDA	2	2	1	2	1	2
Design margin testing undercooling	2	2	2	2	2	2
Local flow blockage	2	2	1	2	1	2
Component tests	2	2	2	2	?	?

(a) 1 = primary data; 2 = data for comparison or backup.

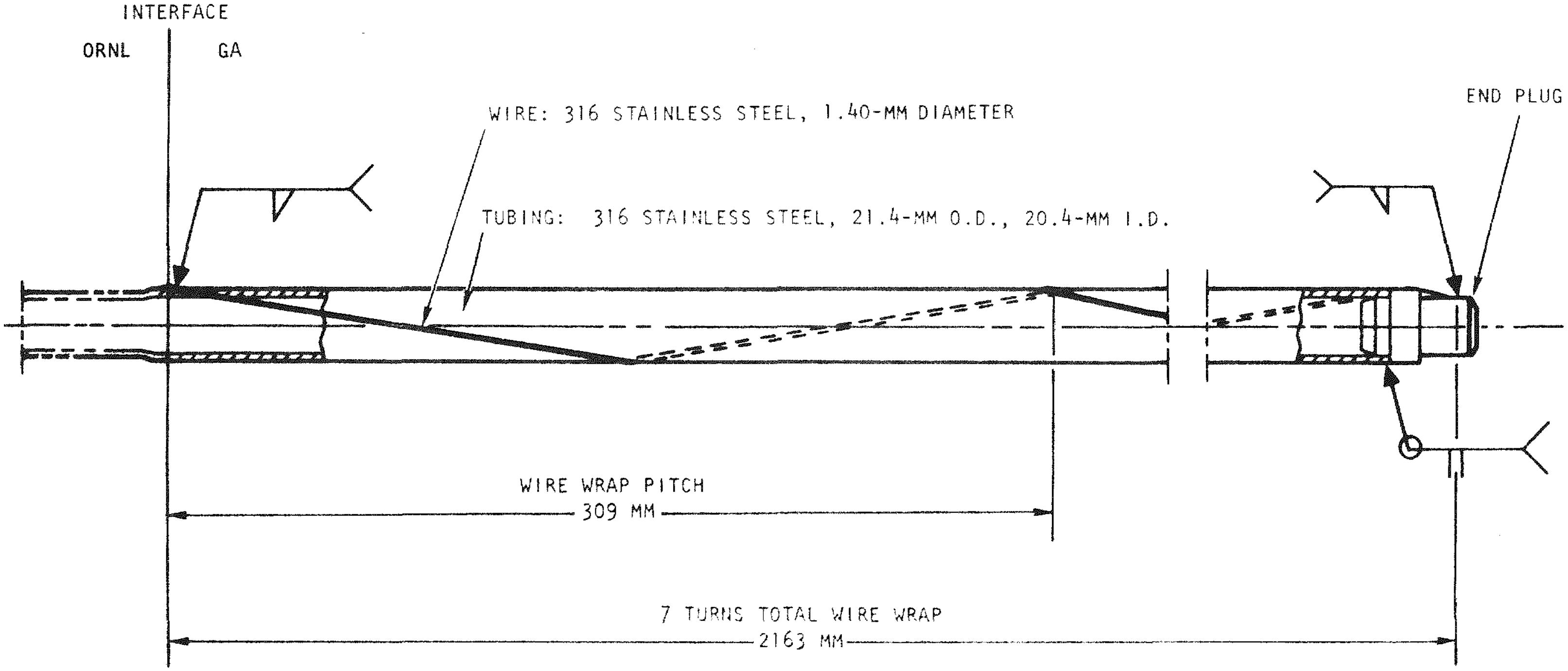

Fig. 4-2. Blanket rod simulator

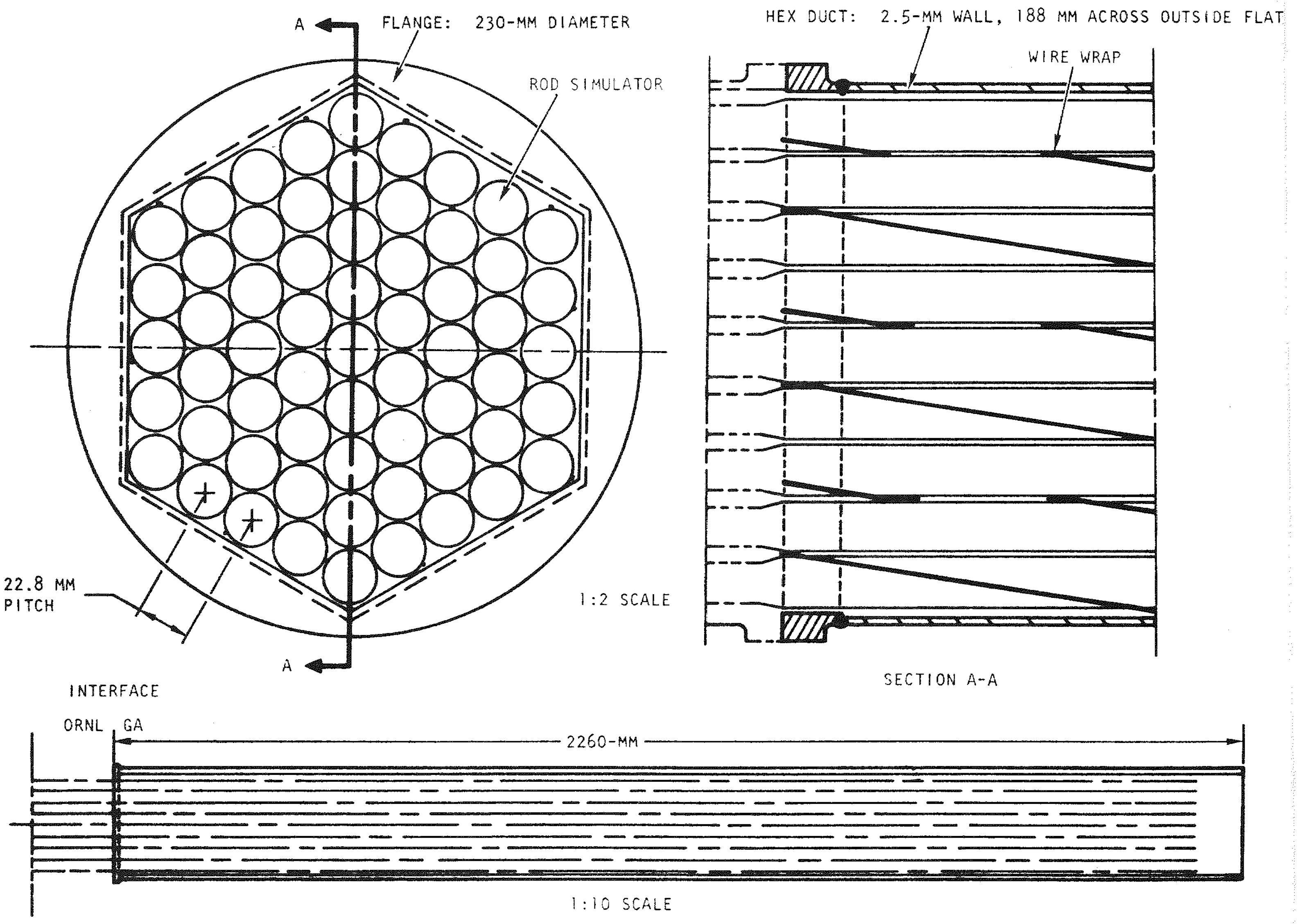

Fig. 4-3. Blanket bundle test section

same as the GCFR demonstration plant core assemblies except that the PuO_2-UO_2 fuel in the rods will be simulated by depleted UO_2. The assemblies will be subjected to maximum GCFR helium flow conditions to closely simulate the reactor core environment; however, there will be no radiation. One assembly of each type (fuel, control, and blanket) will be subjected to the equivalent of approximately 1 yr of reactor operation in a hot helium test loop.

Review of the test loop facility options for the prototype tests has continued. These options include a modification of the EBOR loop at Idaho Nuclear Engineering Laboratory (INEL), the CARMEN 2 loop at Saclay, France, and a new facility which will most likely be situated in Germany. As pointed out in Ref. 4-20, EG&G has completed a preliminary proposal for conducting the prototype tests in the modified EBOR loop. This proposal suggests that the EBOR main blower, which failed during the last operation of the loop in 1966, be inspected, refurbished, and checked out by the blower manufacturer. Lack of funding is holding up this effort. Early determination of the adequacy of the EBOR blower is needed to permit a meaningful evaluation of the EBOR facility option, since the blower is a major component of the facility.

The French representatives had requested that GA prepare a more detailed information package defining the prototype test conditions (Ref. 4-3). This package has been prepared and sent to them to enable them to proceed with their prototype test program study. In addition, the technical and economic feasibility of conducting the prototype tests in the CARMEN 2 loop at Saclay was discussed with the Commissariat à L'Energie Atomique (CEA).

Analysis has continued on whether testing at 450°C rather than 550°C would satisfy the test objectives. This reduction in operating temperature would result in considerable cost savings during facility construction, modification, and testing phases. The initial analysis indicates that from an acoustical, material, and vibration standpoint, the test objectives would be satisfied; an alternate approach being investigated involves conducting the tests at a reduced temperature at the full assembly flow condition and at a reduced flow at the full assembly temperature condition, i.e., 450°C at full flow and 550°C at half-flow. This approach would also substantially reduce the test loop equipment and operating costs. Additional investigation of these alternatives will be made prior to a final commitment to a test section inlet temperature and flow requirements.

REFERENCES

4-1. Hopkins, H. C., Jr., "Program Plan for GCFR Core Flow Test Loop," USAEC Report GA-A13080, General Atomic, August 9, 1977.

4-2. Yensuang, P. K., "Users Guide for Integrated Scheduling Management: RECS - Resource Evaluation and Control System," General Atomic Report GA-A13805, March 1976.

4-3. "Gas-Cooled Fast Breeder Reactor Quarterly Progress Report for the Period February 1, 1977 Through April 30, 1977," ERDA Report GA-A14358, General Atomic, May 1977.

4-4. Rao, S. B., "Status of the Transient Thermal Hydraulic Analysis Methods for the GCFR and CFTL," General Atomic, unpublished data.

4-5. Hopkins, H. C., Jr., "TSPEC - A Computer Program to Predict Approximate Model Performance in the Core Flow Test Loop," ERDA Report GA-A14057, General Atomic, November 1976.

4-6. Wheeler, C. L., et al., "COBRA-IV-I: An Interim Version of COBRA for Thermal-Hydraulic Analysis of Rod Bundle Nuclear Fuel Elements and Cores," Battelle Northwest Laboratory Report BNWL-1962, March 1976.

4-7. Boonstra, R. H., "TAC2D: A General Purpose Two-Dimensional Heat Transfer Computer Code, User's Manual," General Atomic Report GA-A14032, July 15, 1976.

4-8. Petersen, J. F., "TAC3D, A General Purpose Three-Dimensional Heat Transfer Computer Code, User's Manual," USAEC Report GA-9263, Gulf General Atomic, September 1969.

4-9. Estrine, E. A., "SYSL Users Guide," General Atomic, to be published.

4-10. Lee, G. E., "User's Manual for 'ROD*SIM'," General Atomic, unpublished data.

4-11. Lee, G. E., "CFTL*SIM: A Computer Program for Performance of Transient Thermal-Hydraulic Simulation of the GCFR Core Flow Test Loop," General Atomic, unpublished data.

4-12. Smith, J. P., "SINDA User's Manual," TRW Systems Group Report 14690-H001-R0-00, April 1971.

4-13. "EDGTRN: A Computer Program for Determining Thermal-Hydraulic Response of Local Fuel Rods," General Atomic, unpublished data.

4-14. Buttemer, D. R., and B. E. Boyack, "MINGAF - A Computer Program to Evaluate the Transient Thermal-Hydraulic and Neutronic Response of a Gas-Cooled Fast Breeder Reactor (GCFR) Core," General Atomic, unpublished data.

4-15. "DEPTRN: A Computer Program for Analysis of the Overall GCFR System Response to Rapid Depressurization Accidents," General Atomic, unpublished data.

4-16. "GAFTRN: A Computer Program for Analysis of the Overall GCFR System Response to a Broad Range of Normal and Abnormal Plant Conditions Excluding Rapid Depressurization Accidents," General Atomic, unpublished data.

4-17. Marksberry, C. L., "FLAC 73: 1973 Status of FLAC, A Flow Network Analysis Code," General Atomic Report GA-D12942, March 1974.

4-18. "Test Specification for Priority One Preliminary Series P-1 and P-2," General Atomic, unpublished data.

4-19. Rowe, D. S., "COBRA IIIC: A Digital Computer Program for Steady State and Transient Thermal-Hydraulic Analysis of Rod Bundle Nuclear Fuel Elements, "Battelle Northwest Laboratory Report BNWL-1695, March 1973.

4-20. "Gas-Cooled Fast Breeder Reactor Quarterly Progress Report for the Period November 1, 1976 Through January 31, 1977," ERDA Report GA-A14240, General Atomic, February 1977.

5. FUELS AND MATERIAL ENGINEERING (189a No. 00583)

5.1. OXIDE FUEL, BLANKET, AND GRID PLATE SHIELDING MATERIALS TECHNOLOGY

This subtask is concerned with oxide fuel and blanket technology. As a result of the decision to replace ThO_2 with UO_2 as a candidate radial blanket material, differentiation of the axial and radial blanket material has been suspended.

Fuel-cladding chemical interaction data from the F-1 (X094) experiment have been sent to the national Fuel-Cladding Chemical Interaction (FCCI) Steering Group. These data support the correlations being developed at Hanford Engineering Development Laboratory (HEDL) and General Electric (GE).

Cladding attack data from the F-1 fuel rods have been analyzed to determine whether the depth of attack is dependent on the oxygen to metal (O/M) ratio of the fuel. Although the data base is small compared with that of the HEDL P-23 experiment and the cladding temperatures were not constant in all rods of the F-1 subassembly, analysis of the data did show a dependence on O/M ratio. The four fuel rods on which this O/M correlation is based were irradiated to 50 MWd/kg at temperatures between 625° and 750°C. The cladding attack rates (microns/at. % burnup) are given in Table 5-1 and plotted in Fig. 5-1; the numbers on each point indicate the local temperatures at the sections examined metallographically. In developing the O/M dependence of the cladding attack rate, it was necessary to assume that the 735° and 750°C fuel rods formed one data set and the 625°, 630°, and 665°C rods formed a second data set. Straight lines drawn through the points for each data set indicate that the cladding attack decreases by 1.8 microns/at. % burnup per $\Delta 0.01$ in O/M ratio at ~650°C* and

---

*At 50 MWd/kg burnup, this is equivalent to 4.3 microns/100 effective full-power days (EFPD).

TABLE 5-1
CLADDING ATTACK IN FUEL RODS IRRADIATED IN THE F-1 (X094) EXPERIMENT

Pin	Section	Local Temperature (°C)	Irradiation Time (EFPD)	Burnup (At. %)	Cladding Attack (microns)	Fuel O/M	Cladding Attack (microns/At. % Burnup)
G-1	6.75	750	293	5.45	63.5	1.992	11.7
	11.25	745	293	4.33	66.0	1.992	15.2
G-2	6.75	730	293	5.20	25.4	1.971	4.9
	11.25	730	293	4.26	30.5	1.971	7.2
G-6	6.75	665	293	4.70	15.2	1.972	3.2
	11.25	665	293	3.96	25.4	1.972	6.4
G-7	6.75	625	293	(4.7)	25.4	1.984	5.4
	11.25	632	293	(4.0)	33.0	1.984	8.3
G-4		680	588	13.2	76.2	1.983	5.8
G-9		727			0	1.947	0

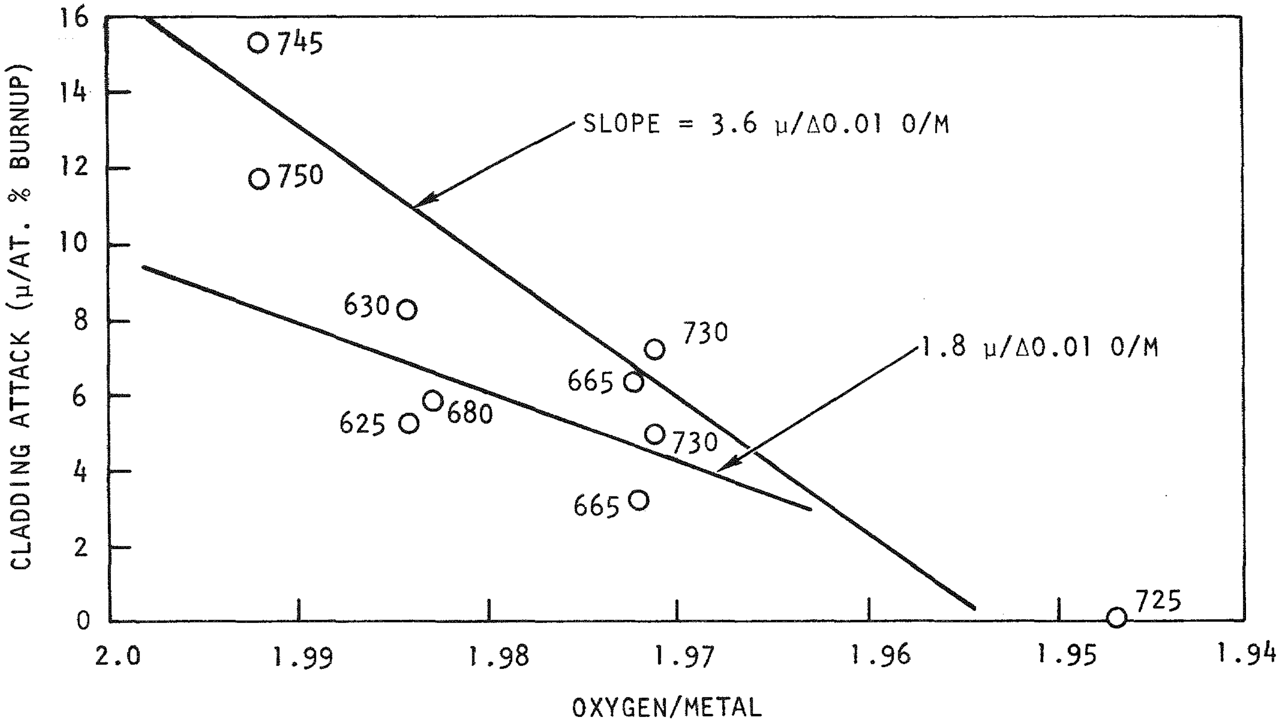

Fig. 5-1. Effect of oxygen/metal ratio on cladding attack

by 3.6 microns/at.% burnup per Δ0.01 in O/M ratio at ∿740°C.* These results were supported by an initial examination of one rod irradiated to 75MWd/kg at a maximum cladding i.d. temperature of 725°C using fuel with an initial O/M of 1.947 (rod G-9).** This rod has shown essentially zero corrosion. Preliminary data from rod G-4, irradiated to 121 MWd/kg at an i.d. cladding temperature of 680°C, indicate a maximum of ∿76 microns of cladding attack and support the slope of the lower temperature line.*** Based on this rather small data base, a conservative decrease in cladding attack rate of 2 microns/at. % burnup for each 0.01 decrease in O/M was recommended.

Postirradiation gamma spectrometry data on F-1 (X094) fuel rods has shown that isotopic fractionation of cesium isotopes occurs during the processes of release from the fuel and deposition in the axial blanket and charcoal traps. Analysis of the data, which is discussed in Section 5.3, was reported to FCCI. Descriptions of the F-1, F-3, and F-5 irradiation experiments have been sent to HEDL in a standardized format for inclusion in their irradiation test description notebooks.

Reference 5-1 states that the cesium transport phenomena in the F-1 fuel rods were reviewed during the design of the modified fuel-blanket interface for the F-5 experiment and the results of the review discussed in Section 5.5. Unfortunately, this discussion was excluded from Ref. 5-1 and is therefore presented below.

Gamma spectrometry data for six rods in the F-1 irradiation experiment have been quantitatively analyzed for their axial isotopic cesium distributions. Based on the analysis of rods G-4, G-8, G-9, G-10, G-11, and G-13 it has been concluded that in the F-5 experiment

1. It is expected that the maximum amounts of cesium transported to the fuel/blanket interface will be 40% of the Cs-137 chain; 15% of the Cs-133 chain; and 15% of the Cs-135 chain.****

---

*At 50 MWd/kg burnup, this is equivalent to 5.6 microns/100 EFPD.

**Indicated by a triangle in Fig. 5-1.

***Indicated by a hexagon in Fig. 5-1.

****Values rounded to the nearest 5%.

2. It is expected that the maximum amounts of cesium transported to the charcoal traps will be ∿30% of the Cs-133 chain; 30% of the Cs-135 chain; and 5% of the Cs-137 chain.*

3. The fuel-blanket interface will be designed to accommodate the cesium fractions given in item 1 in the two special blanket pellets at each end of the fuel column.

5.2. CLADDING TECHNOLOGY

5.2.1. Mechanical Testing Program at Argonne National Laboratory

The objectives of the ANL test program are to determine the effects of the following factors on the behavior and mechanical properties of GCFR ribbed and smooth cladding:

1. Ribs, rib geometry, and fabrication technique.

2. Helium impurity levels typical of the environment expected in the GCFR demonstration plant.

Biaxial creep rupture tests with a hoop to axial tensile stress ratio of 2 are being performed. Two tests at 650°C and a hoop stress of ∿238 MPa in purified helium atmosphere using smooth and ribbed cladding fabricated by various techniques have been completed. In general, the ribs increased the load-carrying ability of the cladding.

The third biaxial creep rupture test on ribbed and smooth cladding was initiated. The specimens for this test include (1) mechanically ground, smooth cladding; (2) mechanically ground, ribbed cladding (KWU); (3) electrochemically ribbed cladding [Swiss Federal Institute for Reactor Research (EIR)]; and (4) as-received smooth cladding. Two different hoop stress levels, i.e., 238 and 262 MPa, are used, and the test is being

---

*Values rounded to the nearest 5%.

performed in a helium atmosphere containing 300 Pa of H_2 and 30 Pa of H_2O. Selective oxidization of chromium is expected under these environmental conditions. The test matrix is given in Ref. 5-1.

During this quarter, two interchangeable test manifolds were used to minimize downtime and maximize data acquisition. Approximately 125 hr of test time have been spent on the smooth test specimens, and over 80 hr of test time have been spent on the ribbed specimens. All the as-received smooth specimens stressed at 262 MPa failed and had an average rupture life of $\sim$45 hr. As-received smooth specimens at 238 MPa also started failing after $\sim$71 hr. Some of the mechanically ground smooth and electrochemically ribbed specimens also failed. Detailed failure data have not yet been received from ANL. Initial cursory analysis of the data indicates nothing unusual. The rupture lives appear to be low compared with LMFBR data but are still higher than the lower 2σ values given in Ref. 5-2. This is a different heat of material which has never been tested before.

WMC Corporation has manufactured eight specimens from ribbed cladding by mechanical grinding. These will be added to the third test along with smooth specimens from the new reference cladding recently purchased from Superior Tubing Company.

5.2.2. Helium Loop Test Program at Pacific Northwest Laboratory

The primary objective of the helium loop test program is to compare the mechanical properties in recirculating helium determined at Pacific Northwest Laboratory (PNL) with those in quasistatic helium determined at ANL. The work scope has been defined, and the loop has been modified for unattended operation. An impurity monitoring system has been installed, and the first test has been initiated. The first 100 hr of testing indicated many significant problems, and efforts to solve these problems are under way.

A calibration setup for the impurity monitoring equipment has been assembled. It is planned to calibrate the Thermox oxygen analyzer and the EG&G dewpoint meter prior to operation of the loop. A water saturator and a refrigeration system will be used to generate the moisture levels for the calibration. Unfortunately, the refrigeration unit procured for this purpose has failed to operate, and a replacement unit is being repaired by the manufacturer and is being shipped to PNL. Calibration will be initiated after the unit is received.

5.3. F-1 FAST FLUX IRRADIATION EXPERIMENT

Postirradiation examination of the encapsulated seven-fuel-rod F-1 (X094) experiment (Ref. 5-3), which received a maximum burnup exposure of ∿13.0 at. % [∿121 MWd/kg (8×10^{22} n/cm^2, 6.1×10^{22} E > 0.1 m/cm^2)], is continuing at Argonne National Laboratory East (ANL-E). Special components such as dosimeters, charcoal traps, and SiC temperature monitors from the F-1 experiment have been received at GA and are being prepared for postirradiation examination.

Postirradiation examination of F-1 rod G-9 (7.7 B.U., O/M = 1.947) at ANL Material Science Division (ANL-MSD) revealed no measurable attack of the cladding in the unetched condition. To date, only a section taken from near the middle of the rod has been etched, and it showed no evidence of attack. However, a section from a similar location in rod G-4 (13.4 at. % burnup, O/M = 1.983) did show measurable attack (Ref. 5-1).

Analysis of postirradiation data obtained on F-1 rods examined at ANL has continued. Distribution profiles for Cs-133 and Cs-137 in the rods have been developed based on gamma spectrometry data. The isotopic distributions for Cs-133 and 137 were based on the integration of peak activity areas for Cs-134 (the neutron activation product of Cs-133) and Cs-137. A summary of the profile analyses is given in Table 5-2, which presents the results of gamma spectrometric assays of cesium plateout in the rods, expressed as percent of the total isotopic yield in each region. This table also gives the F-1 fuel rod irradiation parameters. Several observations can be made:

1. Cs-137 is released from the fuel primarily as a metal vapor species and deposits predominantly in the axial blanket region, close to the fuel end. The Cs-137 vapor condenses and plates out at the temperature gradient at the fuel-blanket interface.

TABLE 5-2
DISTRIBUTION OF CESIUM ISOTOPES IN F-1 FUEL RODS

Rod No.	Burnup (MWd/kg)	Cladding Temperature (°C)	Linear Power (kW/m)	Fuel O/M	Percentage of Isotope in Each Region(a)				
					Lower Charcoal Trap	Lower Axial Blanket	Fuel Region	Upper Axial Blanket	Upper Charcoal Trap
Cs-137									
G-4	121	680	45.6	1.98	0.2	10	80	8	1.4
G-8	96	672	48.6	1.99	(b)	8	86	7	(b)
G-9	71	727	48.0	1.95	5	9	54	22	8
G-10	71	727	48.0	1.97	--	14	68	14	4
G-11	71	729	50.4	1.97	2	6	51	38	2
G-13	71	772	50.4	1.97	2	11	60	21	6
Cs-134									
G-4	121	680	45.6	1.98	23	5	40	6	17
G-8	96	672	48.6	1.99	(b)	14	67	7	(b)
G-9	71	727	48.0	1.95	27	2	46	5	16
G-10	71	727	48.0	1.97	23	4	42	8	16
G-11	71	729	50.4	1.97	27	8	40	14	12
G-13	71	772	50.4	1.97	22	6	41	6	15

(a) Values are rounded and do not necessarily total 100% since small fractions of cesium were deposited on metallic components.

(b) These rods did not contain active charcoal traps.

2. Cs-134, which serves as a monitor for Cs-133, is principally released as the xenon precursor and deposits predominantly in the charcoal traps, beyond the axial blanket regions. The xenon precursor will pressure equilibrate itself throughout the rod and there be concentrated in the cooler charcoal region. Decay of xenon to cesium will enhance the pressure gradient driving force, leading to even greater concentration of Cs-133 (and Cs-134) in the charcoal regions (as indicated below, Cs-135 is expected to behave similarly).

3. Cs-137 release from the fuel region is promoted by either high cladding temperature or low O/M in the fuel. It is not clear which parameter is more important, but the O/M ratio appears to be the more fundamental property since the central fuel temperatures of all rods are similar and high cladding temperatures are obtained by the use of thermal barriers. Figure 5-2 shows fuel region retention is a function of O/M ratio. In contrast, Cs-134 retention is not dependent on O/M ratio. This is expected since Cs-137 is released as the metal whose binding energy is dependent on the oxygen potential of mixed oxide fuel. Cs-134 is released as the inert gas; and this process should not be O/M dependent.

4. Release of cesium from the fuel region is enhanced by charcoal traps in the fuel rod which lowers the chemical potential of cesium in the low-temperature portion of the rod, thus promoting cesium release. However, significant deposition in the traps will not occur in a vented GCFR rod as it does in these sealed irradiation experiments since the xenon precursors will pass through the traps with negligible decay under steady-state conditions.

Because Cs-135 is not a gamma emitter, its profile could not be determined by gamma spectrometry, but it is expected to be similar to that of Cs-133. The half-lives of the iodine precursors of both chains are sufficiently long; so that they can be released from the fuel and contribute

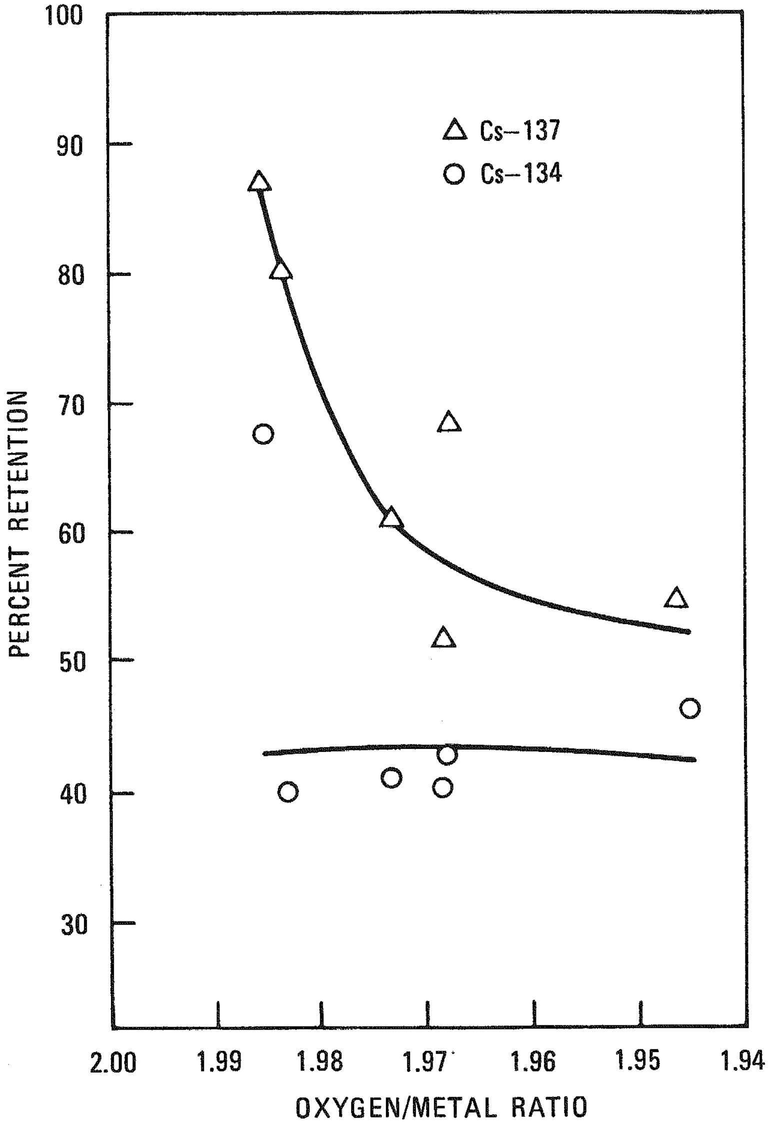

Fig. 5-2. Fuel region retention as a function of oxygen/metal ratio

to transport; the xenon precursors have even longer half-lives and are expected to be the principal contributors to transport. Cs-137 has short-lived iodine and xenon precursors, which are unlikely to be significant contributors to transport. Thus, the only effective contributor is Cs-137.

5.4. F-3 FAST FLUX IRRADIATION EXPERIMENT

The F-3 experiment was irradiated in location 4B3 in EBR-II to an exposure of 4.9 at. % (∿46 MWd/kg); the burnup goal was 100 MWd/kg. The experiment reached an exposure of 46 MWd/kg on February 11, 1976, at which time it was removed from the core for a planned interim examination. It was discovered that nine of the ten rods had failed owing to inadequate capsule sodium bonds. Examination of neutron shield materials from the F-3 experiment has been completed; the results are summarized in Tables 5-3 and 5-4. Postirradiation examination of the components from the F-3 fuel rods has been limited to gamma counting of the dosimeter particles.

5.5. F-5 PROTOTYPE IRRADIATION EXPERIMENT

Design work continued during this quarter, and fabrication of special components for the F-5 prototype design fuel rod experiment was initiated. As previously reported (Ref. 5-4), the F-5 experiment for the study of the performance of fuel rods irradiated under simulated GCFR conditions to high burnups will (1) determine the reliability of the GCFR fuel rod design, (2) discover the failure modes which may exist, and (3) study the effect of a step power increase which simulates the 180-deg rotation of a subassembly at the core-blanket interface in the proposed GCFR demonstration plant.

During the previous quarter, thermomechanical analysis of 19-rod shroud tube type subassemblies for use in the F-5 irradiation experiment, were performed. A design which can achieve the goal burnup of 10.6 at. % was developed, but the analysis cast doubt on whether a shroud tube assembly was suitable for extended burnups beyond 10.6 at. %.

TABLE 5-3

DIMENSIONAL AND DENSITY MEASUREMENT RESULTS FOR SHIELD SAMPLES REMOVED FROM THE F-3 FAST FLUX EXPERIMENT AT A BURNUP OF 4.3 TJ/KG AND A FLUENCE OF ∿3.5 x 10^{22} N/CM^2

	Material/Capsule			
	BeO[a]	Be	$ZrH_{1.62}$	$ZrH_{1.75}$
Percent Dimensional Change From Archives Based on Diameters				
G-14	3.22	-0.04	0.84	0.71
G-19	3.08	0.09	0.84	0.93
G-20	2.14	-0.04	-0.04	0
Percent Density Change From Archive Samples				
G-14	-0.35	-0.36	-2.01	-1.37
G-19	-0.33	-0.34	-2.15	-2.48
G-20	-1.23	-0.31	1.15	-1.04

---

[a] The BeO sample diameter was 20% that of the other samples, resulting in a larger uncertainty in the measurements, and thereby a larger uncertainty in the percent changes.

TABLE 5-4
SUMMARY OF RESULTS OF AXIAL SHIELD IRRADIATION

Fluence exposure = 3.0×10^{22} n/cm, E > 0.1 MeV(a)
Intact Be
Cracked BeO
Intact ZrH_2 except for chipping from handling (also observed in archive samples)
No significant change in dimensional and density measurements
Be and ZrH_2 are adequate backup axial shields (reference is B_4C)

(a) Compared with 6.0×10^{21} n/cm^2 in GCFR demonstration plant core assemblies.

The original concept (Ref. 5-5) for the F-5 experiment was for a 37-position subassembly to be irradiated in the EBR-II reactor. This was later changed (Ref. 5-6) to twin 19-rod subassemblies to enable evaluation of the effect of step power changes on GCFR fuel rods to be more easily accomplished. These 19 pin subassemblies were to be of the shroud tube type, in which each fuel pin would be surrounded and supported by its own flow guide or shroud tube. The shroud tubes were to be assembled into a tightly packed array and enclosed in an insulated hex can, which would provide annular bypass flow to reduce the mixed mean temperature of the sodium coolant leaving the subassembly. Table 5-5 presents the parameters for the F-5 experiment.

Analysis of rod bowing in the F-5 experiment was initiated in April 1977, with the aim of setting the axial pitch between the shroud tube dimples used to center the rod within the shroud tube. Because geometric considerations limited the size of the coolant annulus between the fuel rod and the shroud tube to 1 mm, it was necessary to limit rod bows to a small value to avoid possible failures due to local rod and/or shroud tube overheating. Some failures had already been observed (Ref. 5-7).

Thermal-hydraulics analysis was performed using the computer code COBRA-IV (Ref. 5-8), which allows for cross flow, turbulent mixing, and conduction in the fluid around the rod. Only radial conduction through the cladding was considered. An individual rod cross section was modeled as shown in Fig. 5-3. In the axial direction, the rod was divided into 26 equal length nodes. Nominal and displaced conditions of the rod were modeled in terms of area variation factors applied to the local coolant channels. No account was taken of conduction between adjacent shroud tubes. An analysis to evaluate the effects of conduction between shroud tubes showed that for interior rods, such conduction may lead to a large reduction in rod temperature gradients. However, for rods near the (insulated) periphery of the bundle, the reduction was much less, amounting to only about 20% of the rod ΔT in the adiabatic case. If complete sodium wetting between adjacent shroud tubes were not to occur, conduction between shroud tubes would be negligible.

TABLE 5-5
F-5 EXPERIMENT PARAMETERS

Assembly

Type: MkJ-19B subassembly with shroud tubes
Location: row 5
Inlet temperature: 370°C
Flow rate: 37.5 g/s per rod
Maximum flux (at core midplane, row 5) $\sim 1.6 \times 10^{15}$ n/cm^2-s
Flux profile: axial profile from EBR-11 experimenters guide (Ref. 5-10)
Design burnup: 10.6 at. % (∿16,000 hr)
Extended burnup: 16.5 at. % (∿26,000 hr)

Rod

Type: mixed oxide fuel, 20% cold-worked stainless steel cladding
Cladding root o.d.: 7.2 ± 0.02 mm
Cladding o.d. over ribs: 7.46 ± 0.02 mm
Cladding i.d.: 6.44 ± 0.02 mm
Peak linear power: 39.4 kW/m
Power profile: chopped cosine
Transverse gradient: 0.6% across rod

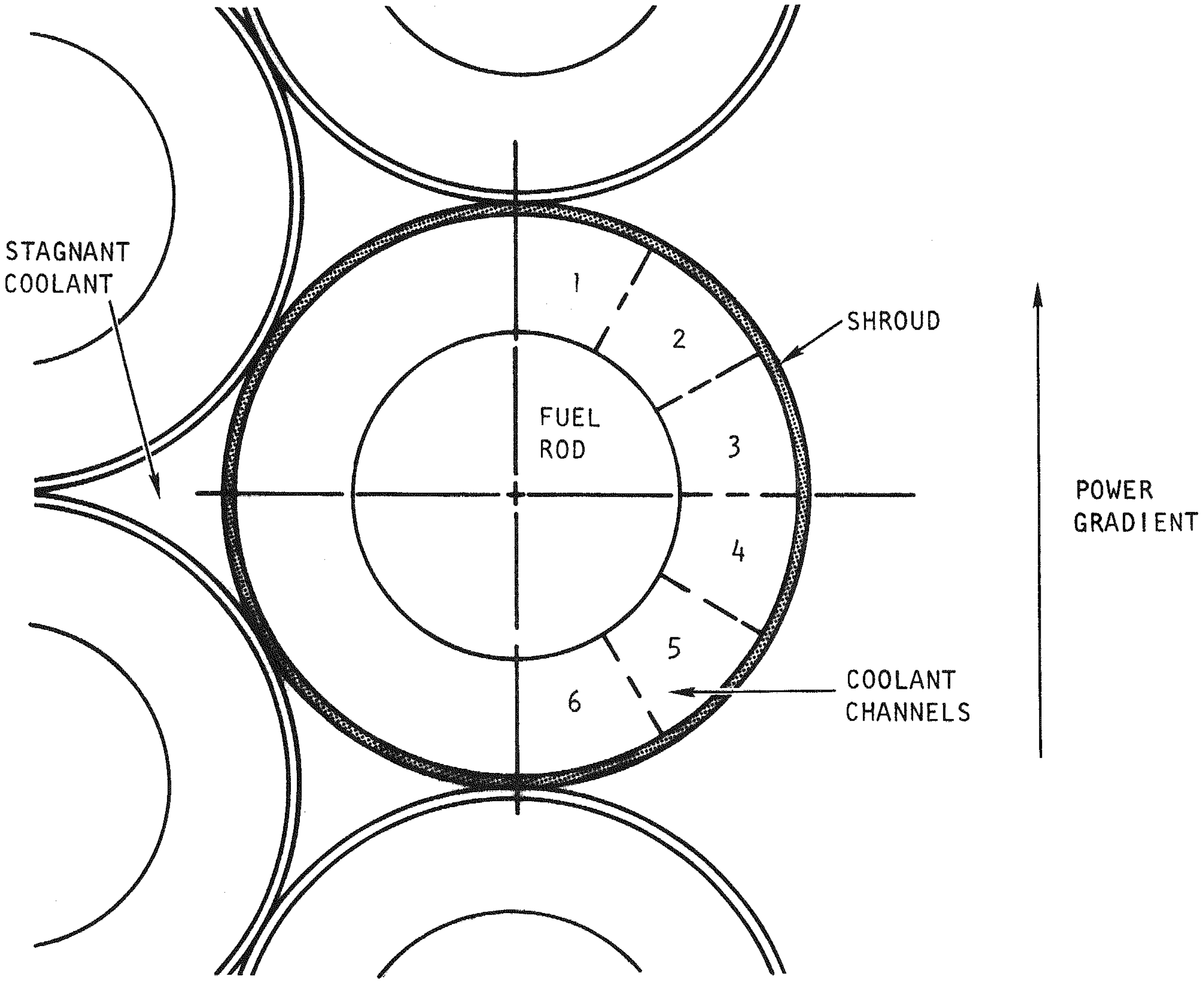

NOT TO SCALE

Fig. 5-3. COBRA-IV thermal-hydraulic model of F-5 shroud tube assembly

The mechanical analysis was performed using the computer code CRASIB (Ref. 5-9), a finite element code which can analyze the irradiation swelling and irradiation and thermal creep of statically indeterminate beams. The rod was modelled using 26 beam elements with an axial nodal layout (Fig. 5-4) which coincides with the COBRA thermal model for ease of data transfer. Dimple locations were modeled by nodes which could rotate or move axially but which were restrained from movement transverse to the rod. Temperature-dependent properties consistent with Ref. 5-2 were employed. The latest nominal creep and swelling correlations were used. The analysis focused on the effect of displacing the rod away from its nominal position, concentric within the shroud tube. With the original dimple arrangement (Fig. 5-5), the rod could be displaced a maximum of 0.12 mm toward the shroud tube wall. Because the annulus available for coolant flow between the rod and the shroud tube was only 1.08 mm wide, this displacement resulted in a significant change in the flow around the rod. The side of the rod nearest the shroud tube was now undercooled, and the side furthest from the shroud tube wall was overcooled. This resulted in substantial temperature gradients across the rod. When these temperature gradients were input to the rod bowing model, rod bows as large as, or sometimes larger than, the inner diameter of the shroud tube resulted.

Two conclusions were reached on the basis of preliminary analyses. First, it was apparent that there was very strong coupling between the thermal-hydraulics and the mechanics of the rod shroud tube system. This would necessitate development of special techniques to properly assess rod bowing. Second, it was felt that a redesign of the dimple arrangement would be required to limit bowing to acceptable values.

5.5.1. Modification of Shroud Tube Design

One of the difficulties with the original shroud tube design was that the original dimple arrangement allowed too much free movement of the fuel rod within the shroud tube. Therefore, the design was changed from three dimples per axial section to four dimples per axial section (Fig. 5-6).

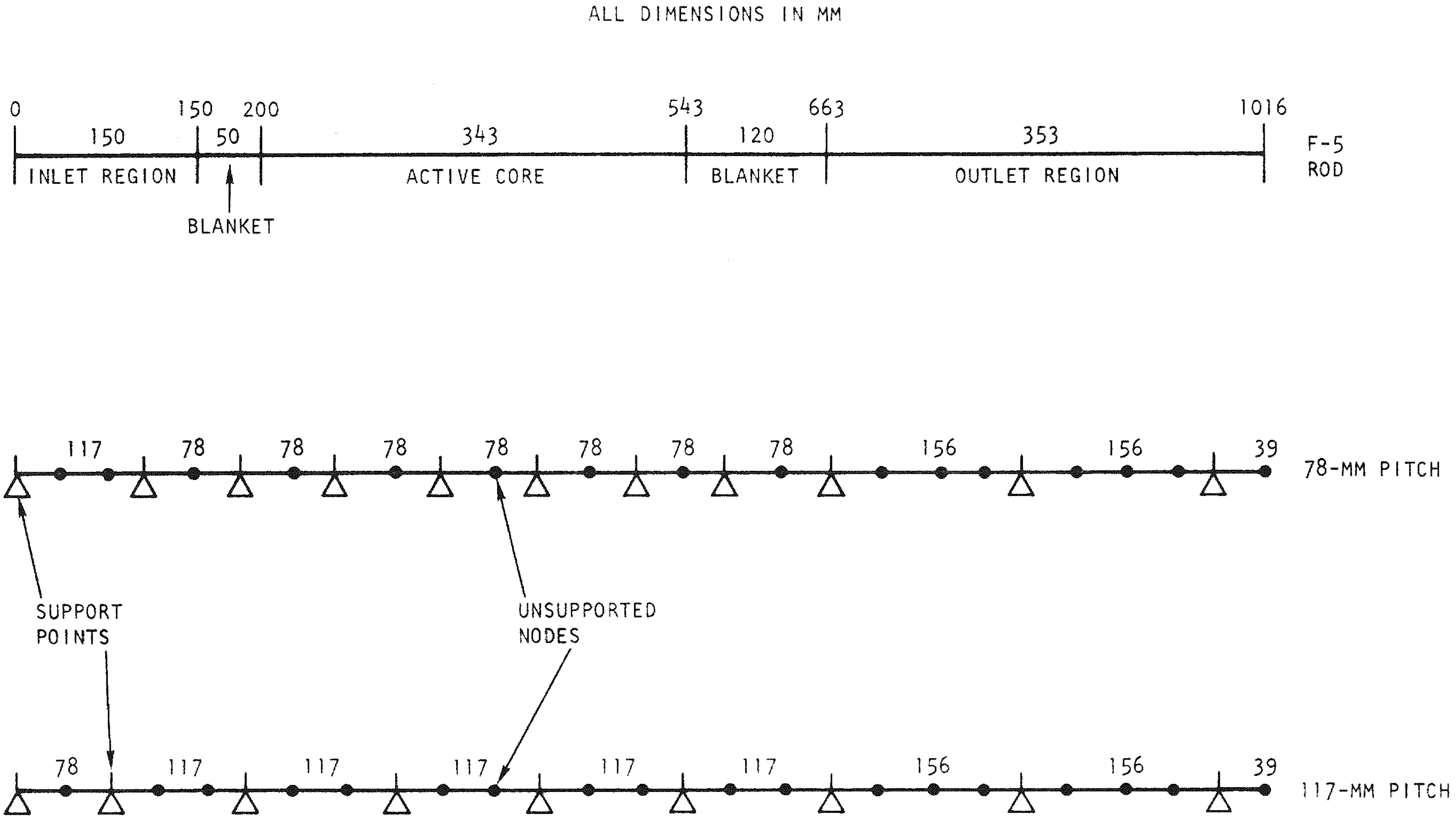

Fig. 5-4. CRASIB models for F-5 rod bowing studies

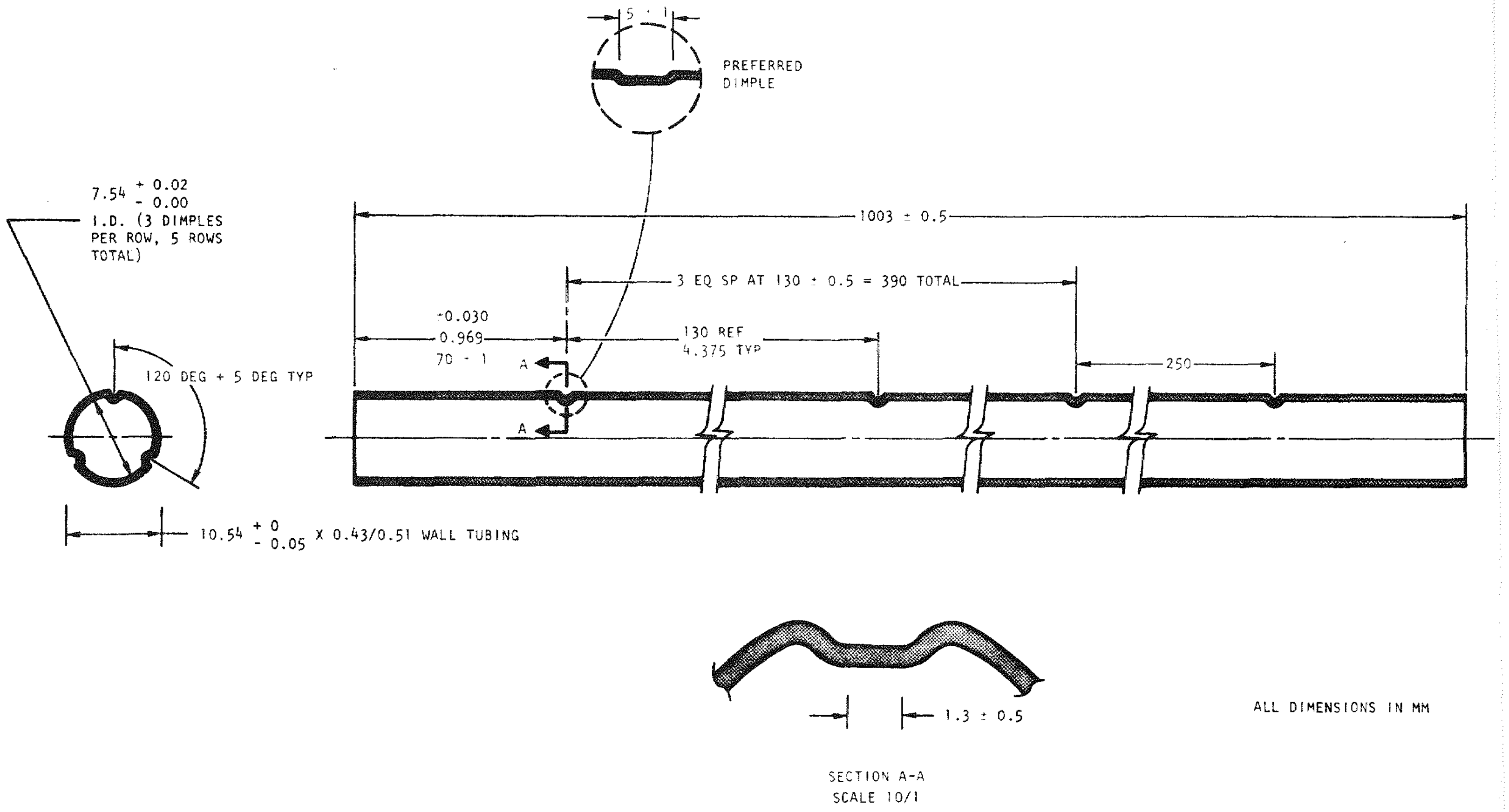

Fig. 5-5. Original shroud tube dimple configuration

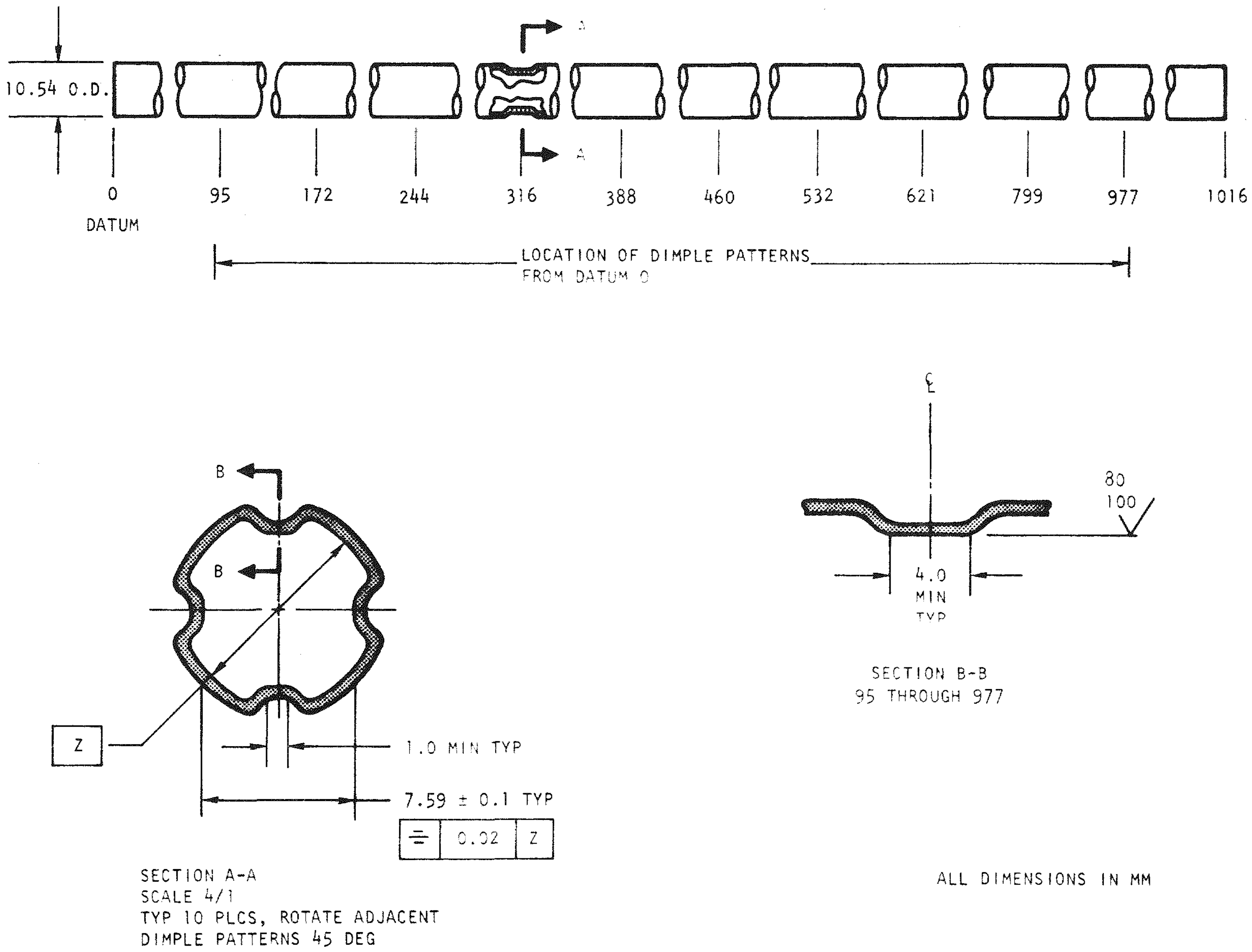

Fig. 5-6. Modified shroud tube dimple configuration

This resulted in approximately a factor of two reduction in the rod's potential free movement. Tolerances for the new arrangement were specified so that a minimum diametral clearance of 0.01 mm existed between the rod and the dimple circle to allow room for differential swelling between the rod and the shroud tube. The potential for rod motion was further reduced by rotating the dimple pattern 45 deg at each elevation.

5.5.2. Development of the MONSTR Code

Because rod bowing significantly altered the thermal gradients imposed on the rod, which in turn significantly altered the rod bowing, it became clear that to determine equilibrium rod shapes with any degree of confidence, it would be necessary to take this into account. The proper way to do this would be to establish correct temperature profiles for the rod at each time step during a rod bowing calculation. However, such an approach would consume considerable computer time and would require a considerable programming effort. In lieu of this, an approximate method was developed which linked the COBRA thermal-hydraulic code with the CRASIB rod bowing code in an iterative scheme. This combined code was called MONSTR. The COBRA and CRASIB models were set up to operate with the same number of nodes and the same nodal locations. COBRA was given an initial geometry which represented the initial configuration of the rod. The rod was typically assumed to be initially straight but uniformly displaced by a specified amount. COBRA then performed the thermal-hydraulic calculations for the given geometry, and the main routine in MONSTR processed the results to obtain cladding temperatures and temperature gradients at each node in the model. The thermal data were then input by MONSTR into the CRASIB code, which calculated rod bowing, assuming that the thermal conditions specified were acting on the rod throughout its lifetime. The main routine then translated the CRASIB rod bowing data into new geometry data for COBRA, and the process was repeated for a specified number of iterations.

In general, the convergence characteristics of the code proved to be quite satisfactory. For the cases analyzed, the code generally either converged to an equilibrium rod configuration in four to five iterations or diverged. It is believed that the cases in which code divergence occurs represent situations in which the actual physical system is thermomechanically unstable. The results obtained are only approximations of the actual results because it was assumed that the EOL thermal conditions acted for the entire life of the rod and (2) constant BOL powers were employed for the analysis. The results are conservative; i.e., the rod bows calculated represent an upper bound to the actual rod displacements.

The final rod bowing results obtained with the MONSTR code are illustrated in Figs. 5-7 through 5-10 and summarized in Table 5-6. Because the small gap between the fuel rod outer diameter and the shroud tube inner diameter is used to carry the sodium which cools the rod, it was necessary to limit rod bowing to extremely small values. It was felt that rod bowing (not counting initial misalignment) of up to 0.25 mm could be tolerated without adverse effects. On this basis, it was concluded that a shroud tube spacing concept would be acceptable from a rod bowing standpoint to a burnup of 10.6 at. %, provided the modified dimple configuration was used and the axial pitch between the shroud tube dimples was maintained at 78 mm or less. Such a design might also be adequate for extended burnup to 16.5 at. %, although this cannot be demonstrated with confidence at this time.

Recent communications with the EBR-II project have made it clear that the F-5 experiment will have to be a 37-rod assembly (31 fuel rods and 6 flow bypass tube positions) so that there is not too large a reactivity burden. A single 31-rod subassembly imposes one-fourth as much of a burden as two 19-rod subassemblies. The shroud tube design was clearly unacceptable for the 37-rod design since it was shown to be marginal even for the 19-rod bundle design.

Analysis of F-5 rod bowing is continuing, with the major emphasis on a grid-spaced assembly. The grid-spaced subassembly design will require fabrication of additional hardware by GA and possibly a change in the design of the bottom end plugs for the final rods. Fabrication of the end plugs has been suspended. Design details have been discussed with ANL,

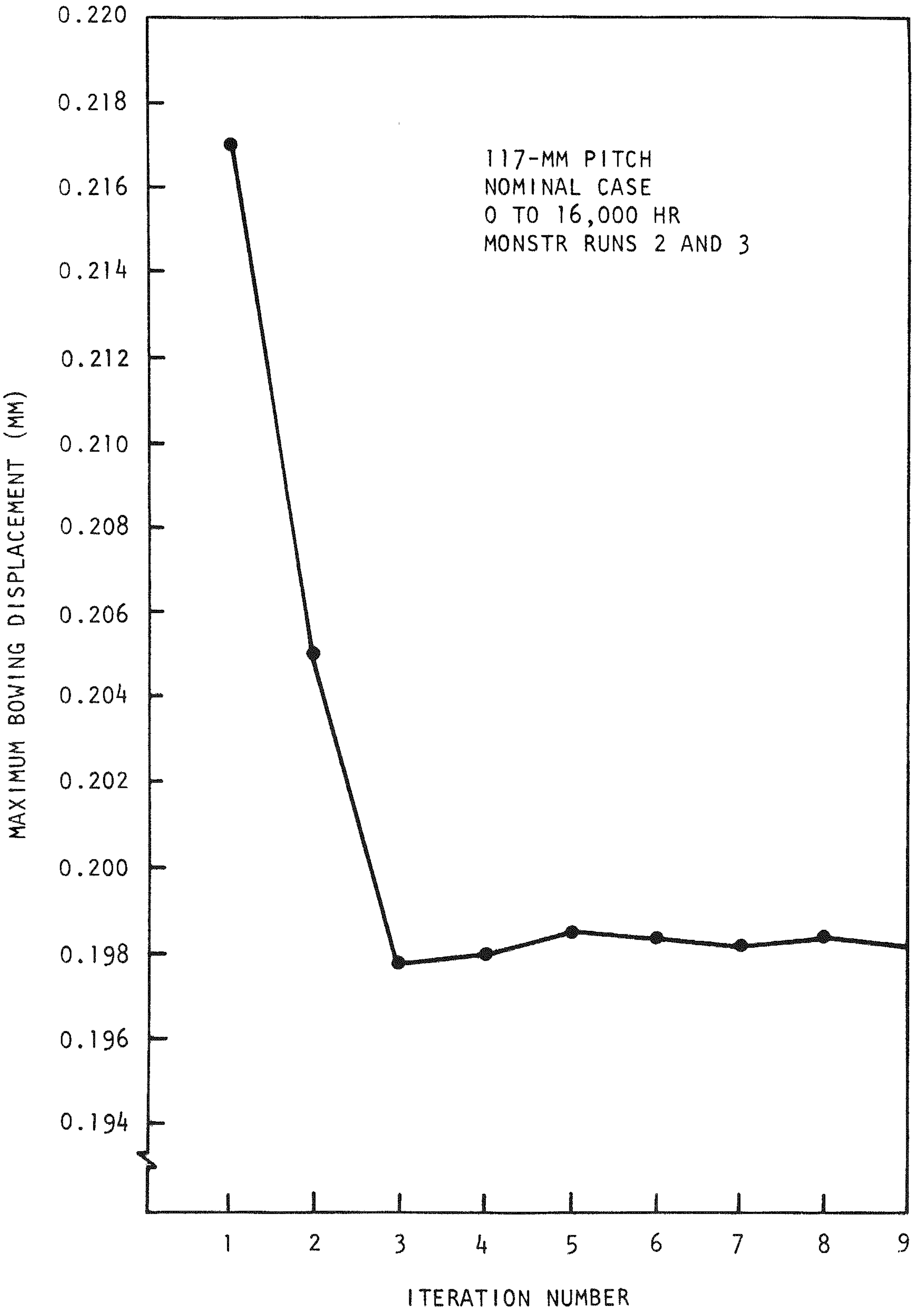

Fig. 5-7. F-5 MONSTR code results for case 2

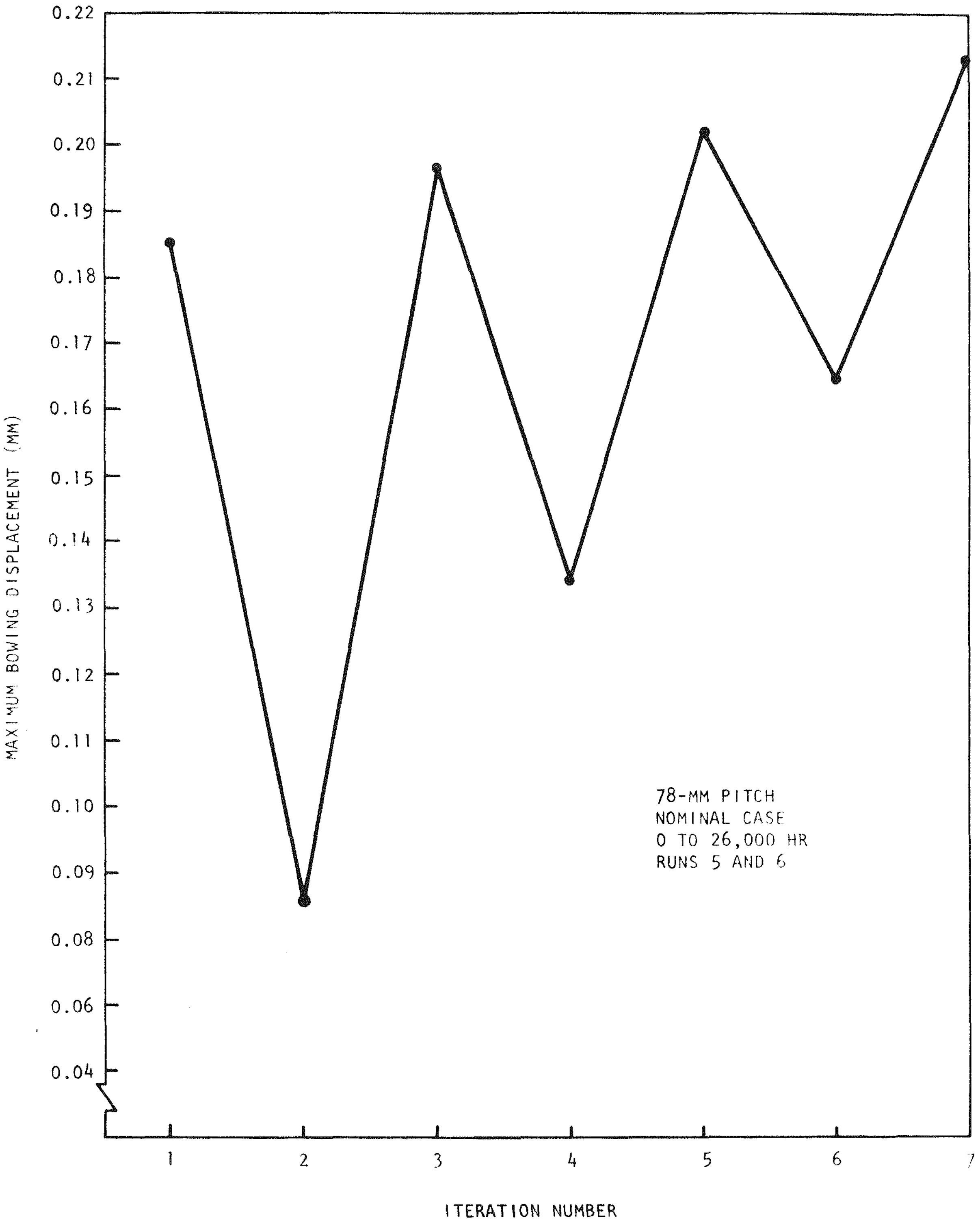

Fig. 5-8. F-5 MONSTR code results for case 3

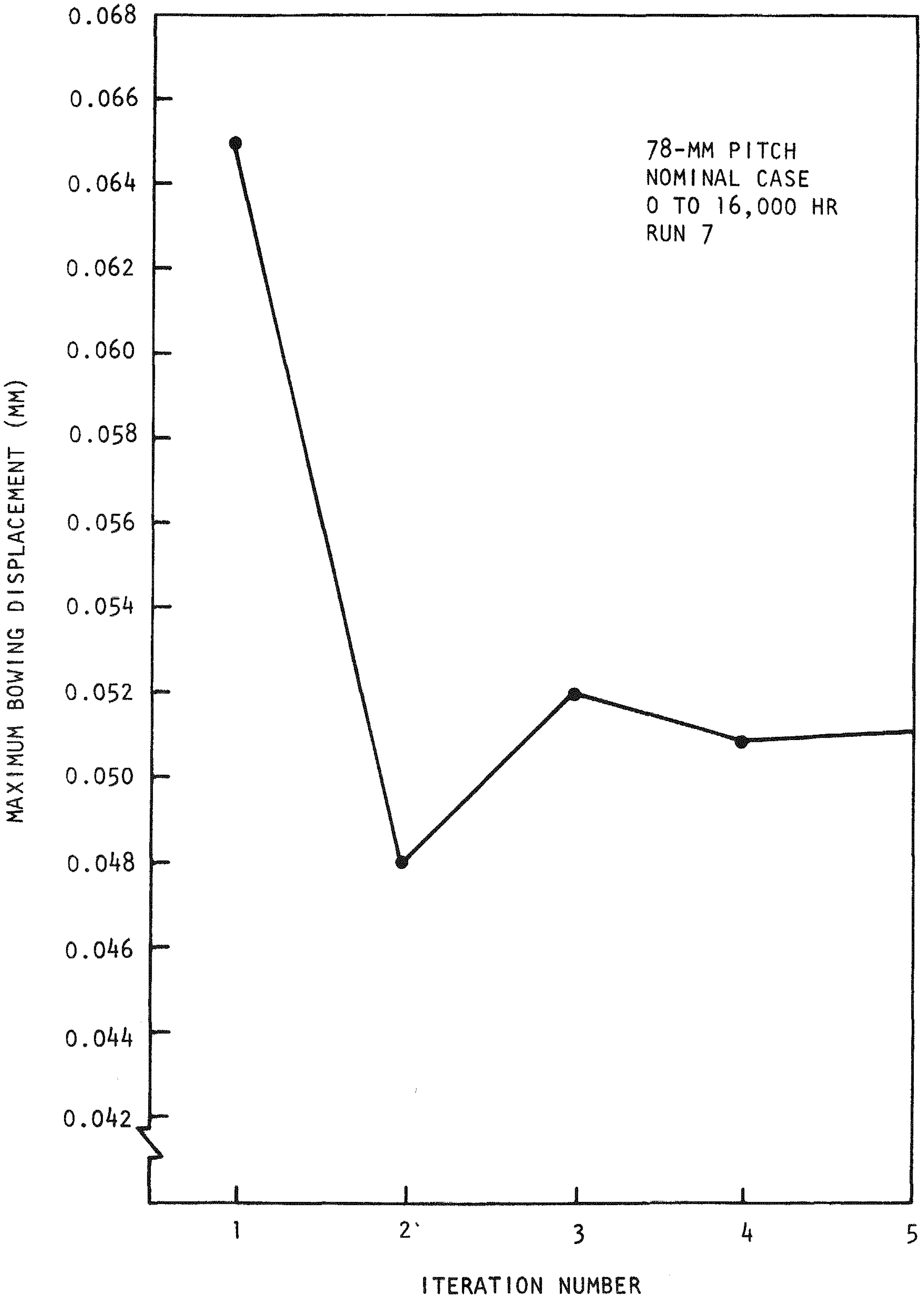

Fig. 5-9. F-5 MONSTR code results for case 4

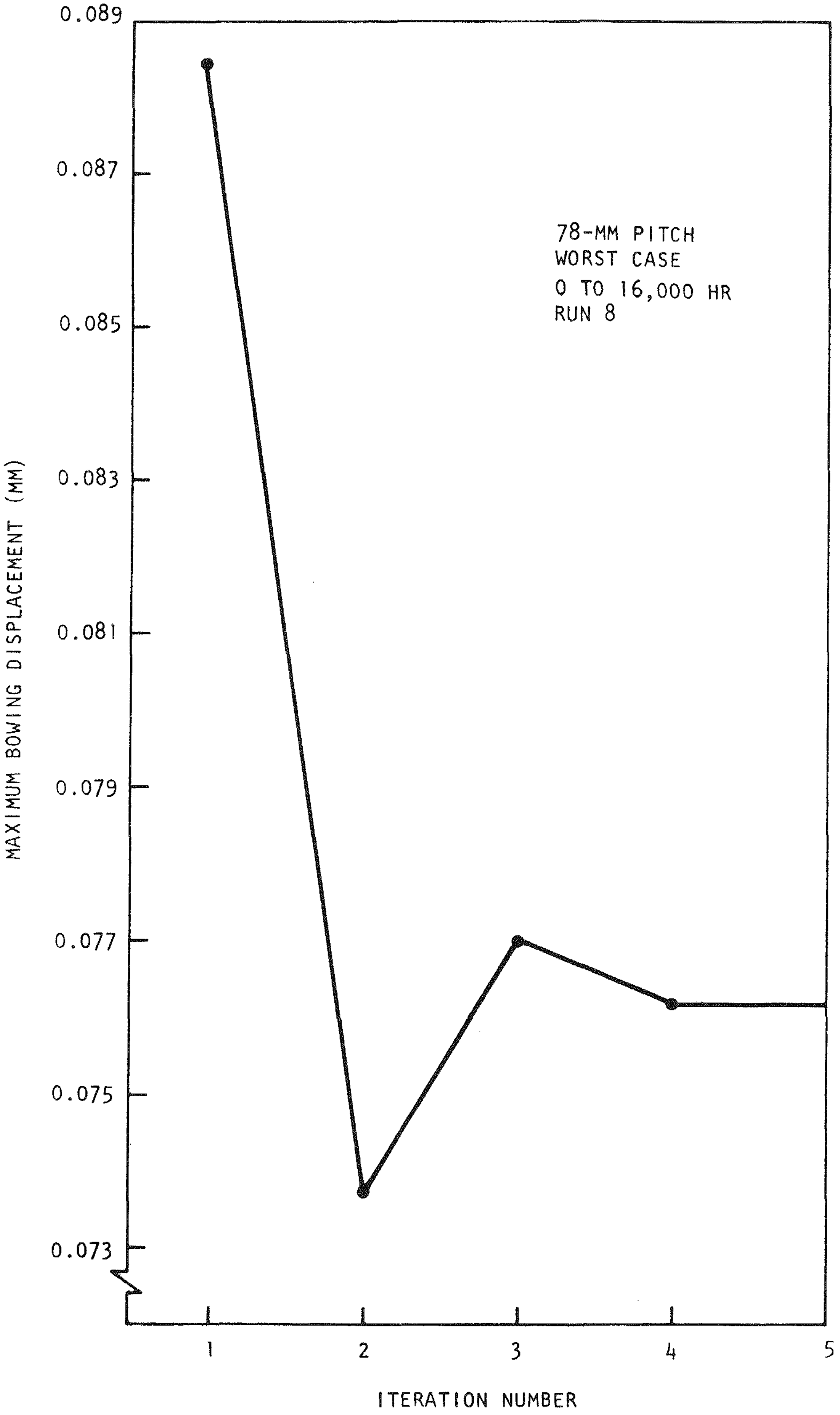

Fig. 5-10. F-5 MONSTR code results for case 5

TABLE 5-6
F-5 BOWING: FINAL MONSTR ANALYSIS RESULTS

	Displacement of Modified Dimple Configuration (mm)			
	78-mm Pitch		117-mm Pitch	
	16,000 hr	26,000 hr	16,000 hr	26,000 hr
Nominal case	$\delta = 0.05, -0.09$ Converges, Fig. 5-9	$\delta = 0.22, -0.65$ Unknown, Fig. 5-8	$\delta = 0.20, -0.33$ Converges, Fig. 5-7	$\delta = 0.74, -1.11$ Diverges
Worst case	$\delta = 0.08, -0.12$ Converges, Fig. 5-10	$\delta^{(a)} = 0.27, -0.33$	$\delta^{(a)} = 0.35, -0.51$	$\delta^{(a)} = 1.29, -2.06$

(a) Indicates estimates from hand iteration.

the tooling for the ribbing has been completed, and the cladding tubing for the F-5 fuel rods has been received. After inspection for shipping damage and cutting to the lengths for ribbing, the cladding will be shipped to WMC Corporation. Ribbing of 60 cladding tubes is expected to take ∿3 weeks.

Sintering of the special UO_2 pellets has been delayed because of a furnace heater burnout. A new sintering furnace is expected to be delivered soon. The dosimetry subcapsules for the F-5 experiment have been completed, and loading of the dosimeters, which will contain U-233/O_2 and Pu-239/O_2 coated particles is in progress at ORNL. Fuel fabrication for the F-5 experiment has been initiated by HEDL, and the engineering test plan will be released.

5.6. GB-10 VENTED FUEL ROD EXPERIMENT

During this quarter, destructive examination of the GB-10 experiment GA-21 vented fuel rod which achieved an exposure of ∿112 MWd/kg in the Oak Ridge Reactor (ORR) was initiated at ANL. Flow testing was performed to determine the location of the apparent flow restriction in the fuel rod. The flow restriction was found to be in the region of the bottom blanket pellets. Following the flow tests, the rod was sectioned for metallographic examination, microprobe scanning, and burnup analyses, and the charcoal trap was removed for analysis.

The final set of flow test measurements were completed on the fuel rod irradiated in capsule GB-10. A new hole was drilled through the cladding at the interface of the Al_2O_3 insulator pellet at the bottom of the rod and the lowest UO_2 blanket pellet. Flow entering the bottom of the rod and exiting through this hole was eight times greater than the flow entering at the bottom and exiting through the hole just above the lower fuel-blanket interface. The constriction is assumed to be in the region of the lower fuel-blanket interface. The major constriction is not caused by the metal ingots located in the central void and is not at the bottom entrance to the fuel rod, as previously conjectured. The cause and mechanism of the constriction will be determined by destructive examination at the completion of flow testing.

5.7. HEDL CLADDING IRRADIATIONS

Tooling has been completed at WMC Corporation for ribbing of the cladding specimens with the current reference geometry (Fig. 5-11). The cladding tube required for the specimens has been received from Superior Tube Company. Upon completion of ribbing and inspection, the ribbed cladding specimens will be sent to ANL-MSD for inclusion in the capsules to be irradiated in EBR-II (Ref. 5-1).

REFERENCES

5-1. "Gas-Cooled Fast Breeder Reactor Quarterly Progress Report for the Period February 1, 1977 Through April 30, 1977," ERDA Report GA-A14358, General Atomic, May 1977.

5-2. Nuclear Systems Materials Handbook, Hanford Engineering Development Laboratory (TID-26666).

5-3. "Gas-Cooled Fast Breeder Reactor Quarterly Progress Report for the Period November 1, 1976 Through January 31, 1977," ERDA Report GA-A14240, General Atomic, February 1977.

5-4. "Gas-Cooled Fast Breeder Reactor Quarterly Progress Report for the Period August 1, 1976 Through October 31, 1976," ERDA Report GA-A14112, General Atomic, November 1976.

5-5. Weeks, R. W., Argonne National Laboratory, private communication.

5-6. Weeks, R. W., Argonne National Laboratory, private communication.

5-7. Lee, G. E., General Atomic, private communication.

5-8. Wheeler, C. L., et al., "COBRA-IV-I: An Interim Version of COBRA for Thermal-Hydraulic Analysis of Rod Bundle Nuclear Fuel Elements and Cores," Battelle Northwest Laboratory Report BNWL-1962, March 1976.

5-9. Rector, J. D., and W. H. Sutherland, "CRASIB Users Guide and Program Manual," Battelle Northwest Laboratory, March 23, 1970.

5-10. "Guide for Irradiation Experiments in EBR-II," Argonne National Laboratory.

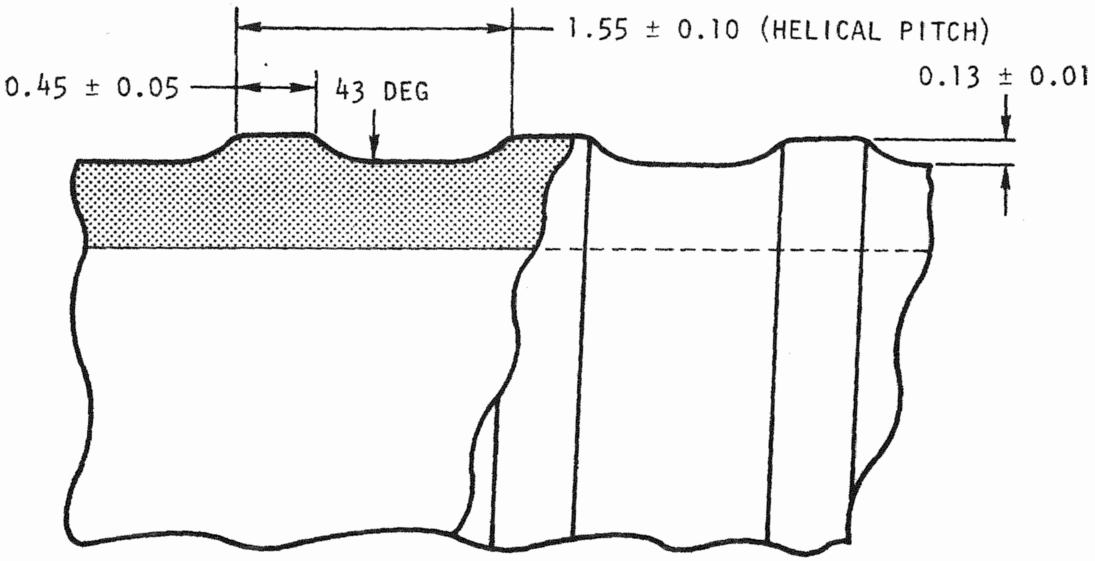

ALL DIMENSIONS IN MILLIMETERS

Fig. 5-11. Reference geometry rib form

6. FUEL ROD ENGINEERING (189a No. 00583)

The objective of this task is to evaluate the steady-state and transient performance of the fuel, blanket, and control rods to determine performance characteristics, operating limits, and design criteria. To this end, analytical tools such as the LIFE-III code (Ref. 6-1) are being adapted and/or developed and applied to the analysis of GCFR prototypical and experimental rods. In addition, continuous surveillance of the LMFBR fuels and materials development program and technology is maintained to maximize the use of development technology and material properties. Support is also given for planning and designing irradiation experiments.

6.1. FUEL, BLANKET, AND CONTROL ROD ANALYTICAL METHODS

6.1.1. A Theory of Radioactive Fission Gas Release and Its Application to Fuel Rod Analysis

Classical diffusion theory was used to describe the behavior of radioactive gases produced in a fuel compact under irradiation. The formulation was based on Booth's concept (Refs. 6-2, 6-3) that the fuel compact is an agglomerate of spheroids. Solutions were obtained for fission gas release rates, fission gas distribution inside the fuel, and amount of fission gas external to the fuel for transient and steady-state conditions. The solutions for short-lived isotopes were obtained from the asymptotic behavior of the general solutions, and the solutions of stable (or long-lived) isotopes were recovered by deletion of the radioactive decay term. Application of the spherical diffusional model to fission gas release of fuel rods under irradiation was formulated, and incorporation of the results into an integral fuel rod thermomechanical analysis code such as LIFE was assumed.

6.1.1.1. *Physical Model.* The simplest explanation for the temperature-dependent fission gas release observed above $\sim$1000 K is that such escape represents lattice diffusion of gas atoms to surfaces which communicate directly with the surroundings. An analytical model describing this physical process of release was first proposed by Booth (Refs. 6-2, 6-3), who made the following assumptions:

1. The entire gas content of the fuel consists of single, freely diffusing atoms.
2. The fuel is an assembly of discrete homogeneous spherical particles (see Fig. 6-1).
3. The surface of each spheroid behaves as a perfect sink for gas atoms.

These assumptions were used in the present analysis, and Booth's steady-state results were generalized to transient problems. In addition, the equivalent sphere model of diffusional release was applied to fission gas release in a fuel rod.

6.1.1.2. *Mathematical Formulation.* The time-dependent spatial distribution of a particular radioactive fission gas isotope in a fuel spheroid (Fig. 6-1) was considered. The balance condition for the differential volume dV is

$$\left(\begin{array}{l}\text{Rate of increase of}\\\text{gas atoms in dV}\end{array}\right) = \left(\begin{array}{l}\text{Rate of gas atoms}\\\text{produced in dV}\end{array}\right)$$
$$-\left(\begin{array}{l}\text{Rate of gas atoms}\\\text{escaping from dV}\end{array}\right) - \left(\begin{array}{l}\text{Rate of gas atoms}\\\text{decayed in dV}\end{array}\right) .$$

Translation of this statement into mathematical terms enables the time-dependent diffusion equation for radioactive fission-produced gas isotopes in a homogeneous medium to be obtained:

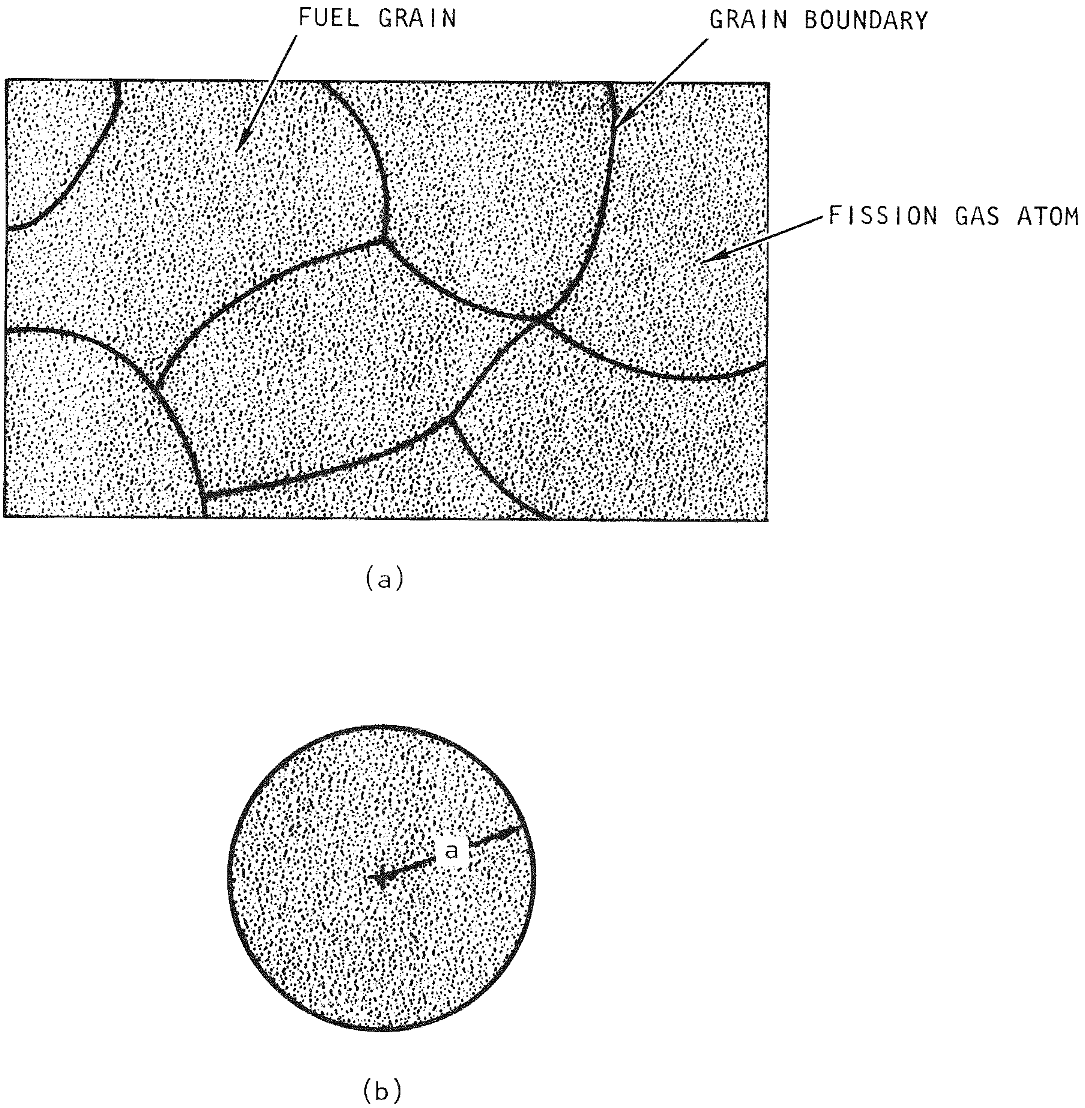

Fig. 6-1. Equivalent fuel sphere model: (a) portion of fuel, (b) equivalent fuel spherical particle

$$\frac{\partial}{\partial t} C(\underset{\sim}{r},t) = y\dot{F} + D\nabla^2 C(\underset{\sim}{r},t) - \lambda C(\underset{\sim}{r},t) \quad , \qquad (6\text{-}1)$$

where $C(\underset{\sim}{r},t)$ = gas concentration at spatial coordinate $\underset{\sim}{r}$ and time t (atoms/cm^3),
y = fission yield (atoms/fission),
$\dot{F}$ = fission rate density (fissions/cm^3-s),
D = diffusion coefficient (cm^2/s),
λ = radioactive decay constant (s^{-1}),
∇^2 = Laplacian operator.

The associated initial and boundary conditions for an in-pile gas release for Eq. 6-1 are

$$C(\underset{\sim}{r},o) = 0 \quad , \qquad (6\text{-}2)$$

$$C(\underset{\sim}{o},t) = \text{finite} \quad , \qquad (6\text{-}3)$$

$$C(\underset{\sim}{a},t) = 0 \quad . \qquad (6\text{-}4)$$

If it is assumed that the fission rate density is uniform throughout the sphere, the problem reduces to a spherical symmetry. Therefore, Eq. 6-1 becomes

$$D \frac{1}{r} \frac{\partial^2}{\partial r^2} rC - \lambda C + y\dot{F} = \frac{\partial C}{\partial t} \quad . \qquad (6\text{-}5)$$

The general solution of Eq. 6-5 subject to the initial and boundary conditions of Eqs. 6-2 through 6-4 is of the form

$$C(r,t) = \frac{y\dot{F}}{\lambda}\left(1 - \frac{a}{r}\,\frac{\sinh\sqrt{\frac{\lambda}{D}}\,r}{\sinh\sqrt{\frac{\lambda}{D}}\,a}\right)$$

$$+ \sum_{n=1} \frac{2y\dot{F}(-1)^n}{\frac{n\pi}{a}\left(\lambda + \frac{n^2\pi^2 D}{a^2}\right)} \exp\left[-\left(\frac{Dn^2\pi^2}{a^2} + \lambda\right)t\right] \frac{\sin\frac{n\pi\gamma}{a}}{r} \quad . \qquad (6\text{-}6)$$

The absolute gas release rate R_{ab} is defined as the number of gas atoms per unit time to cross the boundary of the equivalent sphere. Using Fick's first law of diffusion,

$$R_{ab} = 4\pi a^3 y\dot{F}\left[\sqrt{\frac{D}{a^2\lambda}}\coth\sqrt{\frac{\lambda}{D}}\,a - \frac{D}{\lambda a^2}\right.$$

$$\left. - 2e^{-\lambda t} \sum_{h=1}^{\infty} \frac{1}{\frac{\lambda a^2}{D} + n^2\pi^2} \exp\left(-\frac{Dn^2\pi^2}{a^2}\,t\right)\right] \quad . \qquad (6\text{-}7)$$

The release-to-birth rate R/B is defined as the ratio of the absolute release rate to the fission gas production rate. Bearing in mind that the fission gas production in the fuel sphere is $(4\pi/3)a^3y\dot{F}$,

$$R/B = 3\left[\sqrt{\frac{D}{a^2\lambda}}\coth\sqrt{\frac{\lambda}{D}}\,a - \frac{D}{\lambda a^2} - 2e^{-\lambda t} \sum_{n=1}^{\infty} \frac{1}{\frac{\lambda a^2}{D} + n^2\pi^2}\right.$$

$$\left.\exp\left(-\frac{Dn^2\pi^2}{a^2}\,t\right)\right] \quad . \qquad (6\text{-}8)$$

The total number of gas atoms external to the equivalent sphere N_{ext} at time t is governed by the initial value problem:

$$\frac{dN_{ext}}{dt} = R_{ab} - \lambda N_{ext} \quad ; \qquad N_{ext}(o) = 0 \quad . \tag{6-9}$$

Solving Eq. 6-9 yields

$$N_{ext} = 4\pi a^3 y\dot{F} \left[\left(\sqrt{\frac{D}{a^2\lambda}} \coth \sqrt{\frac{\lambda}{D}}\, a - \frac{D}{a^2\lambda} \right) \frac{1 - e^{-\lambda t}}{\lambda} - \frac{2}{\pi^2} e^{-\lambda t} \sum_{n=1}^{\infty} \frac{1 - \exp\left(- \frac{n^2\pi^2 D}{a^2} t \right)}{n^2 \left(\lambda + \frac{n^2\pi^2 D}{a^2} t \right)} \right] \quad . \tag{6-10}$$

Equation 6-10 is given in Refs. 6-4 and 6-5.*

When the rate of loss of gas atoms due to diffusional escape and radioactive decay is equal to the gas production rate from fissions, the fission gas distribution inside the fuel sphere reaches equilibrium, i.e., the steady-state condition. Therefore, Eqs. 6-1 through 6-5 reduce to a time-dependent boundary value problem:

$$D \frac{1}{r} \frac{d^2}{dr^2} rC^s(r) - C^s(r) + y\dot{F} = 0 \quad , \tag{6-11}$$

where $C^s(o)$ = finite,

$C^s(a) = 0$.

---

*Reference 6-5 contains a sign error.

The general solution to this problem is

$$C^s(r) = \frac{y\dot{F}}{\lambda}\left(1 - \frac{a}{r}\,\frac{\sinh\sqrt{\frac{\lambda}{D}}\,r}{\sinh\sqrt{\frac{\lambda}{D}}\,a}\right) . \tag{6-12}$$

Equation 6-12 can be reproduced from the transient solution (Ref. 6-6) by letting t → ∞. Absolute fission gas release, release-to-birth rate, and total external gas are found using the following equations:

$$R^s_{ab} = 4\pi a^3 y\dot{F}\left(\sqrt{\frac{D}{\lambda a^2}}\,\coth\sqrt{\frac{\lambda}{D}}\,a - \frac{D}{\lambda a^2}\right) , \tag{6-13}$$

$$(R/B)^s = 3\left(\sqrt{\frac{D}{\lambda a^2}}\,\coth\sqrt{\frac{\lambda}{D}}\,a - \frac{D}{\lambda a^2}\right) , \tag{6-14}$$

$$N^s_{ext} = 4\pi a^3 y\dot{F}\left(\sqrt{\frac{D}{\lambda a^2}}\,\coth\sqrt{\frac{\lambda}{D}}\,a - \frac{D}{\lambda a^2}\right) . \tag{6-15}$$

Equation 6-14 has been used to investigate fission gas release in a crushed oxide and single fuel pellet (Ref. 6-6) and in fuel rod irradiation experiments (Ref. 6-7).

Since

$$\lim_{x \to \infty} \coth x = 1 ,$$

Equations 6-13 through 6-15 can be further simplified if

$$\left(\frac{\lambda a^2}{D}\right)^{\frac{1}{2}} >> 1 . \tag{6-16}$$

For example,

$$(R/B)^{s,s} \equiv \lim_{\left(\frac{\lambda a^2}{D}\right) \to \infty} (R/B)^{s} = 3\left(\frac{D}{\lambda a^2}\right)^{\frac{1}{2}} \quad . \qquad (6\text{-}17)$$

Equation 6-17 is applicable to short-lived isotopes because Eq. 6-16 implies that the radioactive decay is much faster than the diffusional decay.

For a long-lived or stable isotope, the radioactive decay term λc can be deleted. Therefore, the steady-state equation becomes

$$D \frac{1}{r} \frac{d^2}{dr^2} rC^{s,1} + y\dot{F} = 0 \quad . \qquad (6\text{-}18)$$

The solution of Eq. 6-18 coupled with the boundary conditions

$$C^{s,1}(o) = \text{finite} \quad ,$$

$$C^{s,1}(a) = 0$$

is given by

$$C^{s,1}(r) = \frac{y\dot{F}}{6D} (a^2 - r^2) \quad . \qquad (6\text{-}19)$$

The fission gas release rates are

$$R^{s,1}_{ab} = \frac{4\pi a^3}{3} y\dot{F} \quad , \qquad (6\text{-}20)$$

$$(R/B)^{s,1} = \frac{R^{s,1}_{ab}}{\frac{4\pi}{3} a^3 y\dot{F}} = 1 \quad . \qquad (6\text{-}21)$$

When the steady state is reached, all stable isotopes produced will be released from the fuel sphere.

6.1.1.3. Application to Fuel Rod Analysis. The fission gas release model derived above can easily be applied to an entire fuel rod analysis. Consider an annular volume element in a fuel rod with a thickness dr and a height dz at (r,z) (Fig. 6-2). The rate of fission gas generated in the volume $2\pi r dr dz$ is $y\dot{F}(2\pi r dr dz)$. The gas release rate from this volume element is therefore $(R/B) \cdot y\dot{F}(2\pi r dr dz)$. Summing this throughout the entire cross section and total length of the fuel column, the fission gas release rate from an entire fuel rod is

$$R_{\text{fuel rod}} = \int_{-L/2}^{L/2} dz \int_{0}^{R} (R/B) \cdot y\dot{F}(2\pi r) dr \quad . \tag{6-22}$$

If $\dot{F}$ is independent of radial coordinate, i.e., there is no flux depression effect,

$$R_{\text{fuel rod}} = 2\pi y \int_{L/2}^{L/2} \dot{F} dz \int_{0}^{R} (R/B) r dr \quad . \tag{6-23}$$

Equation 6-23 can be used to evaluate the fission gas release rate from an irradiated fuel rod for short-lived or stable isotopes at transient or steady-state conditions if R/B is replaced by the corresponding expression derived in the preceding section. However, all the equations for release-to-birth rate contain the parameter of diffusion coefficient D, which is a function of temperature in Arrhenius form:

$$D = D_o e^{-\frac{Q}{KT}} \quad , \tag{6-24}$$

where D_o = pre-exponential factor,

Q = activation energy,

K = Boltzmann's constant,

T = absolute temperature.

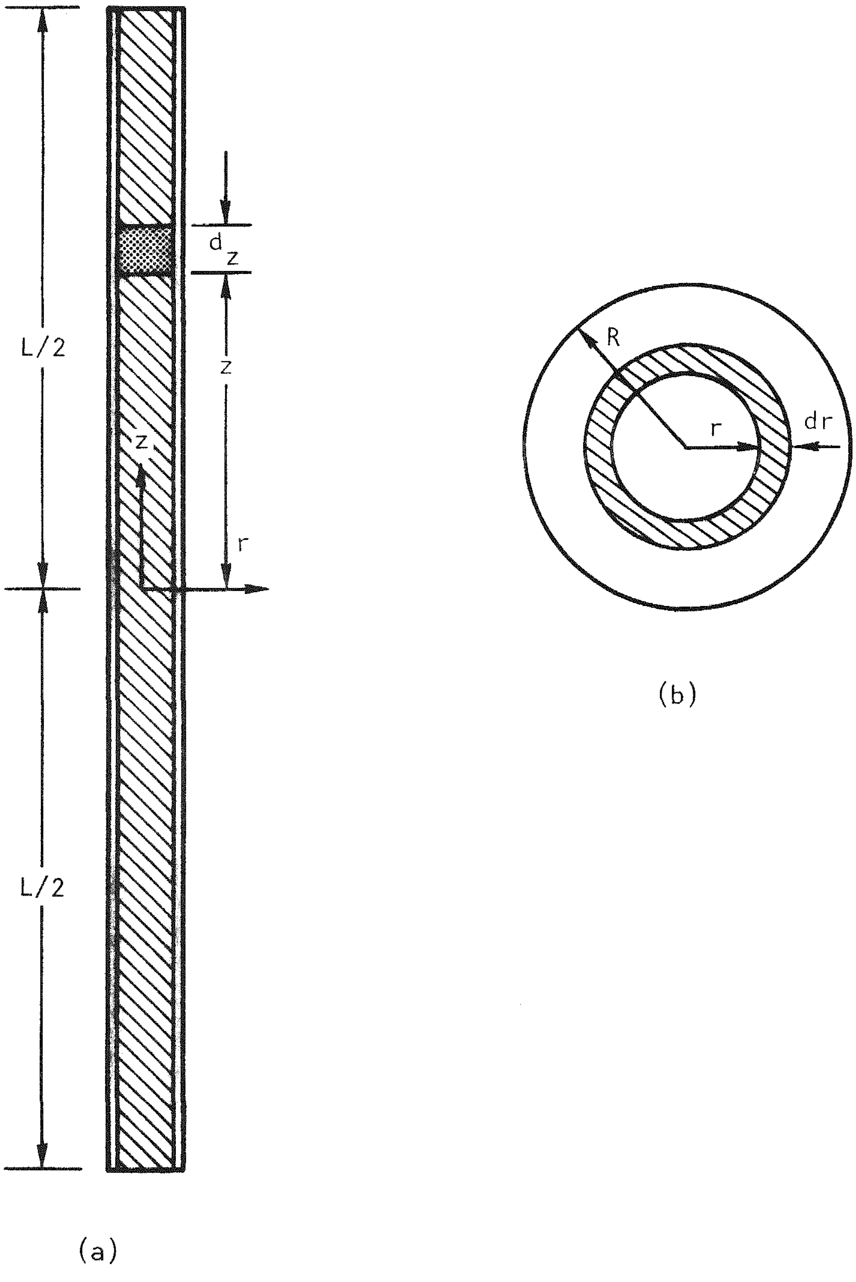

Fig. 6-2. Fuel rod geometry: (a) fuel column, (b) fuel column cross section

Integration of Eq. 6-23 requires knowledge of the temperature distribution of the fuel rod. Even if the temperature distribution function is available, the integral is too complicated to carry out. Therefore, Eq. 6-24 will be incorporated into a fuel rod thermomechanical analysis code such as LIFE for evaluation of fission gas release.

6.1.2. Revision of the LIFE Gas-Cooled Version

Since the gas-cooled version of the LIFE code was implemented in Ref. 6-8, the LIFE code has been updated from LIFE-III to LIFE-IIIA, and a new correlation for Nusselt number has been developed for the heat transfer calculation from the roughened cladding section to the coolant (Ref. 6-9). The gas-cooled version of the LIFE code has been updated to reflect these changes.

6.2. ANALYSIS OF IRRADIATION TESTS

Analysis of the GB-9 and GB-10 capsule tests has been initiated, and work is in progress to set up the fuel rod analysis using the LIFE-IIIA code (the geometry, materials, and operating conditions are being arranged in the input format of LIFE-IIIA). The purpose of the LIFE analysis is to obtain the time history of the temperature in the fuel rod; this time history is needed for fission gas release calculations. The fuel restructuring and cladding deformation information from the LIFE analysis will be useful for comparison with data obtained from postirradiation examination.

6.3. ROD ANALYSIS AND PERFORMANCE

6.3.1. Parametric Study of Mixed-Carbide Fuel Centerline Temperature

Although the mixed oxide of uranium and plutonium $(U,Pu)O_2$ is the current reference fuel, the need to develop advanced fuels, predominantly mixed carbides of uranium and plutonium (U,Pu)C, has long been recognized (Refs. 6-10 through 6-12). Compared with mixed oxides, mixed carbide fuels possess higher metal density, better neutron economics, and greater thermal conductivity. As a result, this fuel exhibits a higher linear power rating with lower centerline temperatures and has a superior breeding capability, which can lower fuel cycle cost. Therefore, a parametric study was performed of the centerline temperature of $(U_{0.8},Pu_{0.2})C$ was performed. The centerline temperature results at BOL varied from 2150° to 2430°C, depending on rod size and cladding i.d. temperature.

6.3.1.1. Fuel Rod Parameters. The major geometric parameters of the fuel rod chosen for the analysis are listed below.

Rod o.d. (mm)	Rod i.d. (mm)	Radial Gap (mm)
8	7.2	0.11
9	8.2	0.11
10	9.2	0.11

These values were determined using Ref. 6-13. For each different dimension, the cladding i.d. temperature was assumed to be 750°, 800°, and 850°C so that nine cases were investigated. The fuel-to-cladding gap was assumed to be helium-bonded, and the linear power rating was 820 W/cm.

6.3.1.2. Method of Analysis. Given a cladding temperature, the fuel centerline temperature can be found by determining the temperature increments across the cladding-to-fuel gap and the fuel radial distance. The heat transfer models and associated material thermal properties are described below.

6.3.1.3. Cladding-to-Fuel Gap Temperature Increment. Determination of the temperature increase across the cladding-to-fuel gap can be facilitated by defining the gap conductance h_g as

$$\Delta T_{gap} = \frac{Q''}{h_g} \quad , \qquad (6-25)$$

where Q'' is the surface heat flux related to linear power rating P and rod inner radius R by

$$Q'' = \frac{P}{2\pi R} \quad . \tag{6-26}$$

Neglecting the effect of radiant heat transfer, gap conductance can be written as (Ref. 6-14)

$$h_g = \frac{K_{He}}{t_{gap} + g_f + g_c} \quad , \tag{6-27}$$

where K_{He} = thermal conductivity of helium

$= 2.774 \times 10^{-5}\ T^{0.701}$ W/cm-K (Ref. 6-15), (6-28)

t_{gap} = gap size (cm),

T = temperature (K).

The temperature jump distances g_c and g_f represent the temperature discontinuity between a solid surface (cladding or fuel) and a gas, in which there is a temperature gradient, as a result of incomplete energy exchange between the surface and the gas. For helium gas, the temperature jump distance is given as (Ref. 6-16)

$$g = 687\ K_{He} T^{1/2} \frac{M^{1/2}}{ap} \text{ cm} \quad , \tag{6-29}$$

where M = molecular weight of helium,

p = gas pressure (dyne/cm^2),

a = accommodation coefficient of helium.

To avoid the tedium of numerical iteration, the helium thermal conductivity and temperature jump distance at the cladding and fuel surfaces were evaluated at the cladding i.d. temperature. The change of gap size due to thermal expansion was ignored, and the initial cold gap was used. By obtaining ΔT_{gap}, the fuel surface temperature T_s can be found:

$$T_s = T_{clad\ i.d.} + \Delta T_{gap} \quad . \qquad (6\text{-}30)$$

6.3.1.4. Fuel Centerline Temperature. The fuel centerline temperature T_c is related to fuel surface temperature T_s and linear power by the K-integral:

$$\int_{T_s}^{T_c} KdT = dr = \frac{P}{4\pi} \quad . \qquad (6\text{-}31)$$

The thermal conductivity of $(U_{0.8},Pu_{0.2})C$ is given by the following expression (Ref. 6-17):

$$K = \frac{1 - f}{1 + f} (0.105 + 4.1 \times 10^{-5} T) \quad W/cm\text{-}^\circ C \quad , \qquad (6\text{-}32)$$

where f is fractional porosity, and T is temperature (°C). The fuel centerline temperature can thus be determined by substituting Eq. 6-32 into Eq. 6-31.

6.3.1.5. Results. Based on the foregoing analysis, centerline temperatures were obtained for various fuel rod dimensions and cladding i.d. temperatures. Figure 6-3 gives the fuel centerline temperature results versus rod o.d. The maximum centerline temperature is 2430°C [which is close to the melting temperature (2470°C) of $(U_{0.8},Pu_{0.2})C$] (Ref. 6-13) for a rod o.d. of 8 mm and $T_{clad\ i.d.}$ of 850°C. The fuel centerline temperature decreases with an increase of rod o.d. This tendency is not obvious and disagrees with the idea that the centerline temperature for a given linear power rating is independent of rod diameter (Refs. 6-14, 6-18). This can be concluded from Eq. 6-31, which does not explicitly contain rod dimensions. It is well known that the centerline temperature T_c which appears as the upper limit of the conductivity integral is important. The fuel surface temperature, which is equal to the lower limit of the integral, is also important

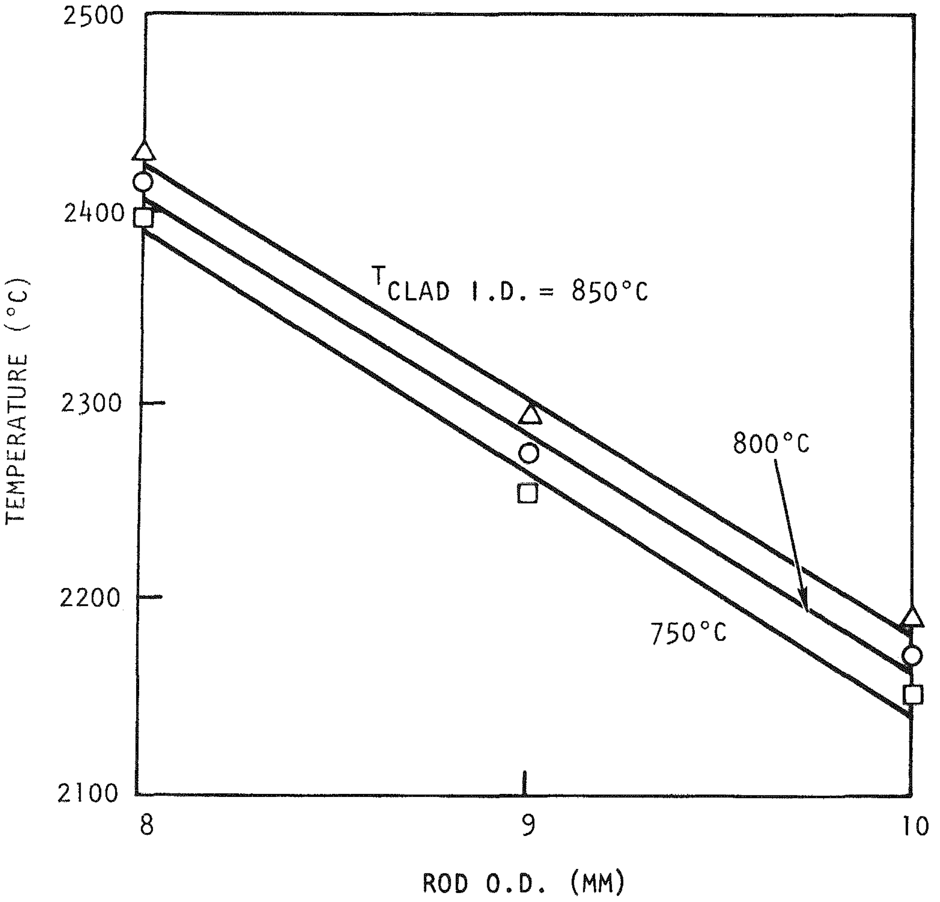

Fig. 6-3. Fuel centerline temperature at a linear power of 820 W/cm and a fuel-cladding gap of 0.11 mm

and depends on the amount of heat flux (cf. Eqs. 6-25, 6-26, and 6-30) which, for a given linear power, is inversely proportional to the rod radius. Therefore, independence of fuel centerline temperature and the rod diameter is only true when linear power and fuel surface temperature are kept constant.

The fuel centerline temperature calculations were based on the cold fuel-to-cladding gap and the thermal conductivity and temperature jump distances evaluated at the cladding i.d. temperature. The temperatures were conservative because thermal expansion and helium thermal conductivity were evaluated at a high temperature, which overshadows the negative effect of the temperature jump distance evaluated at the fuel surface temperature.

6.3.2. Dependence of Rod Diameter on Fuel Temperature and Linear Power for Metallic Thorium and Uranium Fuels

Analyses were performed to assess the dependence of rod diameter on maximum fuel temperature and linear power for metallic thorium and uranium fuels. The maximum fuel temperature was allowed to vary from 850° to 950°C, so that it was maintained below 1000°C, which is a possible beginning swelling temperature. The pellet was assumed to be annular to accommodate swelling, if any. The rod cladding inner radius varied from 0.25 to 0.84 cm, depending on maximum fuel temperature, for linear powers of 328 to 492 W/cm.

6.3.2.1. Fuel Rod Parameters. The following rod geometry, temperatures, linear powers, and fuel thermal conductivity were used for the analysis (Ref. 6-19):

Cladding i.d. temperature = 700°C,
Cladding-to-fuel gap = 0, i.e., closed,
Volume of central hole = 12.5% of pellet volume,
Maximum fuel temperature = 850°, 900°, 950°C,
Linear power = 328, 410, 492 W/cm,
Fuel thermal conductivity = 0.5 W/cm-°C.

6.3.2.2. Method of Analysis. When the cladding-to-fuel gap is closed, solid-solid contact occurs at the roughening on the fuel and cladding surfaces. There are gas pockets between the contact points, and heat is transported by parallel conduction through the contact areas and the gas pockets (heat conduction through the gas film is discussed in Ref. 6-20). The solid-solid contact conductance, derived in Ref. 6-21, is a function of (1) thermal conductivities and roughness heights of the fuel and cladding, (2) contact pressure, and (3) material hardness of the cladding of interest. If the values of these parameters are known, the thermal conductance of a closed gap can be evaluated. However, in view of the large uncertainty associated with the parameters, a constant value is sometimes assigned to the total gap conductance h_{gap} for computational purposes. The estimate $h_{gap} = 1\ W/cm^2\text{-}°C$ is often employed (Refs. 6-22, 6-23) and is used in these calculations.

The maximum fuel temperature T_c is related to the linear power P in the thermal conductivity integral for annular pellets in the form

$$\int_{T_s}^{T_c} K dT = \frac{P}{4\pi}\left[1 - \ln\left(\frac{1+f}{f}\right)^f\right] \quad , \tag{6-33}$$

where T_s = fuel surface temperature,
f = fractional volume of central hole,
K = fuel thermal conductivity.

Substituting $K = 0.5\ W/cm^2\text{-}°C$ and $f = 0.125$ into the above integral yields

$$T_s = T_c - 0.115P \quad . \tag{6-34}$$

The rod cladding inner radius R is obtained by the equation

$$\Delta T_{gap} = T_s - T_{clad\ i.d.} = \frac{Q''_R}{h_{gap}} \quad , \tag{6-35}$$

where

$$Q_R'' = \text{heat flux} = \frac{P}{2\pi R} \qquad (6\text{-}36)$$

6.3.2.3. Results. Based on the preceding heat transfer model and the input values of the parameters, the cladding inner radius (or pellet outer radius) was obtained for various maximum fuel temperatures and linear powers. The results are plotted in Fig. 6-4 for cladding inner radius versus rod linear power and are parameterized with maximum fuel temperature. The cladding inner radius varied from 0.25 to 0.84 cm, depending on the maximum fuel temperature and linear power. For a constant linear power, the cladding inner radius increases with a decrease of maximum fuel temperature. This tendency can easily be seen by combining Eqs. 6-34 through 6-36:

$$R = \frac{P}{2\pi h_{gap}\left(T_c - 0.115P - T_{clad\ i.d.}\right)} \qquad (6\text{-}37)$$

Equation 6-37 explains the increase of cladding inner radius with an increase of linear power.

6.3.3. Fuel-to-Cladding Gap Size Between Vented and Sealed Rods

Fuel-to-cladding gap size as a function of irradiation history was studied by comparing the reference GCFR vented fuel rod and a sealed rod simulating the Clinch River Breeder Reactor (CRBR) fuel rod plenum pressure condition. The purpose of the investigation was to evaluate the possible differences in the dependence of gap size on burnup for vented and sealed rods.

6.3.3.1. Method of Analysis. The analysis was performed using the LIFE-IIIA code (Ref. 6-1). The rod fuel region was divided into four equal axial sections so that one was a smooth section and the other three were surface-roughened. An additional plenum section was connected to the vented rod to represent all the voids inside the rod available for the fission gases. A plenum was also added to the sealed rod to simulate the CRBR plenum pressure condition. Figure 6-5 (from Ref. 6-24) shows a typical CRBR fuel

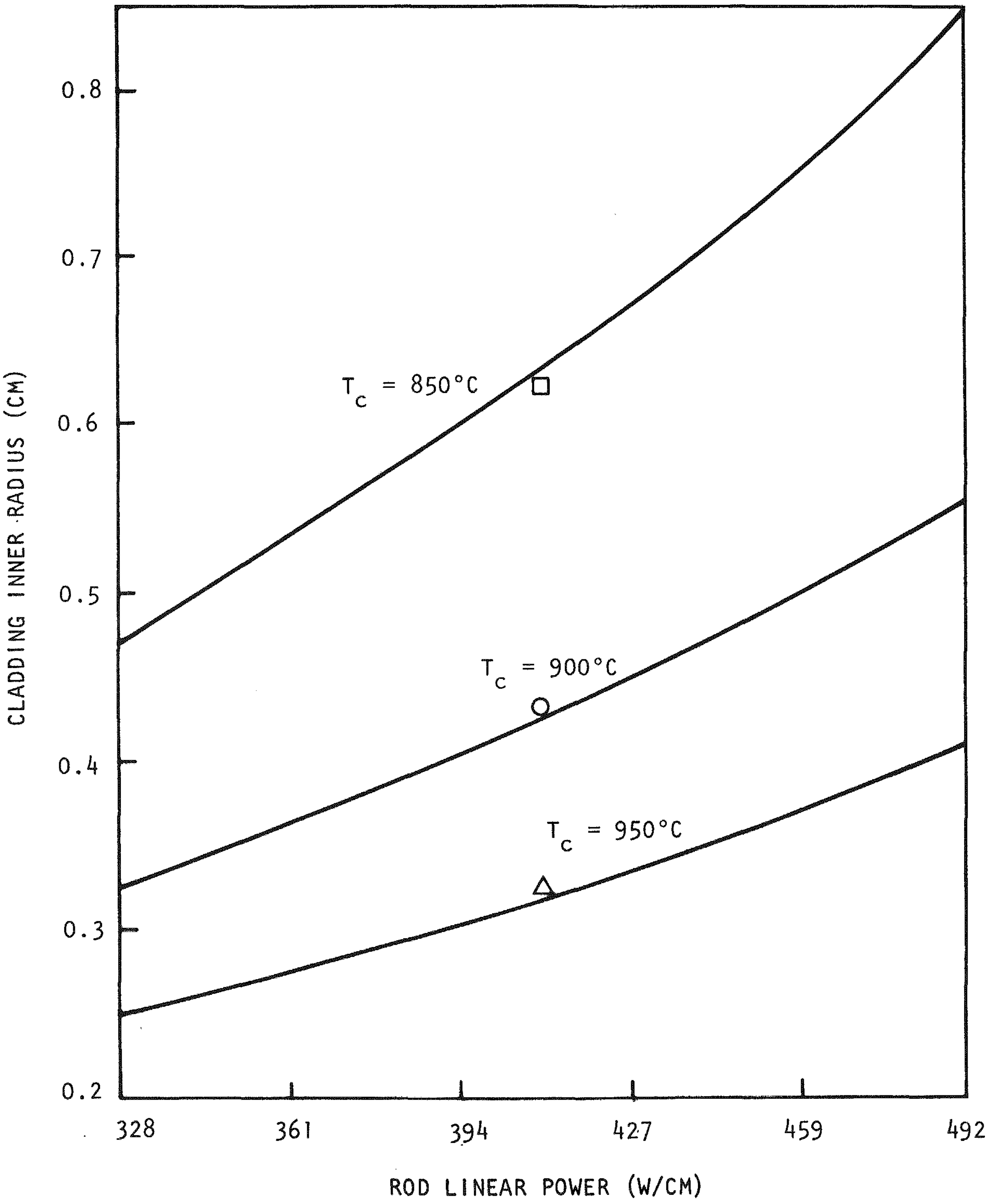

Fig. 6-4. Cladding inner radius for metallic thorium and uranium fuels

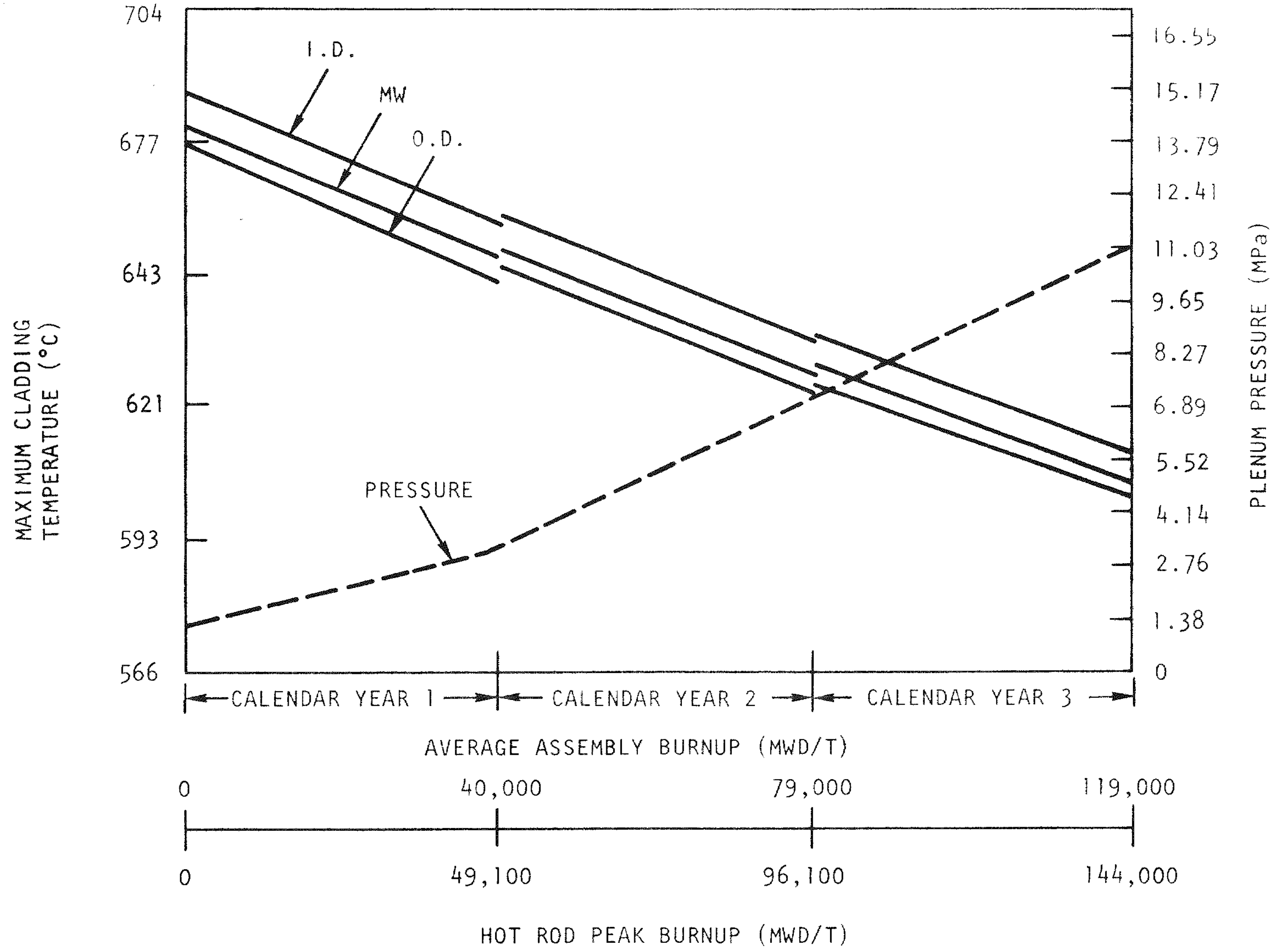

Fig. 6-5. Lifetime cladding temperature/pressure history for hot rod in fuel assembly No. 8 at equilibrium and plant expected operating conditions (0σ level of confidence) (from Ref. 6-25)

rod plenum pressure history; Fig. 6-6 shows the plenum pressure history obtained from the sealed rod analysis. The fuel rod geometry input was obtained from Ref. 6-25; the operating conditions are summarized in Table 6-1. The axial profiles for fast flux (E > 0.1 MeV) and linear power are shown in Figs. 6-7 and 6-8, respectively (Ref. 6-26).

6.3.3.2. Results. The variation of the fuel-to-cladding radial gap size is plotted in Fig. 6-9 for the vented and sealed cases at a position X/L = 0.375 (axial section = 2), where the minimum gap occurred. For the vented rod, the initial hot radial gap was 0.0450 mm, which is smaller than the initial cold radial gap (0.0711 mm) because of thermal expansion. The gap size decreased with an increase in burnup to a minimum value of 0.0087 mm at 3.433 at. % burnup until cladding swelling was initiated. After that, gap size increased with an increase in burnup to 0.0762 mm at EOL. The gap size of the sealed rod varied in the same manner as that of the vented rod; however, the gap closed at 0.6 at. % burnup and remained closed until 2.833 at. % burnup. Thereafter, cladding swelling and irradiation-induced creep caused the gap size to increase to 0.163 mm at EOL.

The larger gap closure early in life and greater gap opening late in life for the sealed rod is the result of internal gas pressure. Early in life, the primary cause of gap closure is fuel swelling, which is lower for the vented rod because of the presence of high system pressure which suppresses fission gas bubble swelling. As irradiation continues, the sealed rod collects enough fisison gases to cause the fuel rod internal pressure to be higher than the system pressure (0.958 MPa for the CRBR design). For both rods, irradiation-induced cladding swelling increases the cladding diameter. In addition, for the sealed rod, irradiation-induced creep increases cladding diameter. For the vented rod, the pressure differential across the cladding remains constant (0.207 MPa) throughout life.

Current analysis indicates that the greatest potential for pellet-cladding mechanical interaction during steady-state operation occurs early in life before burnup reaches 3.5 at. %. Because of the higher hydrostatic

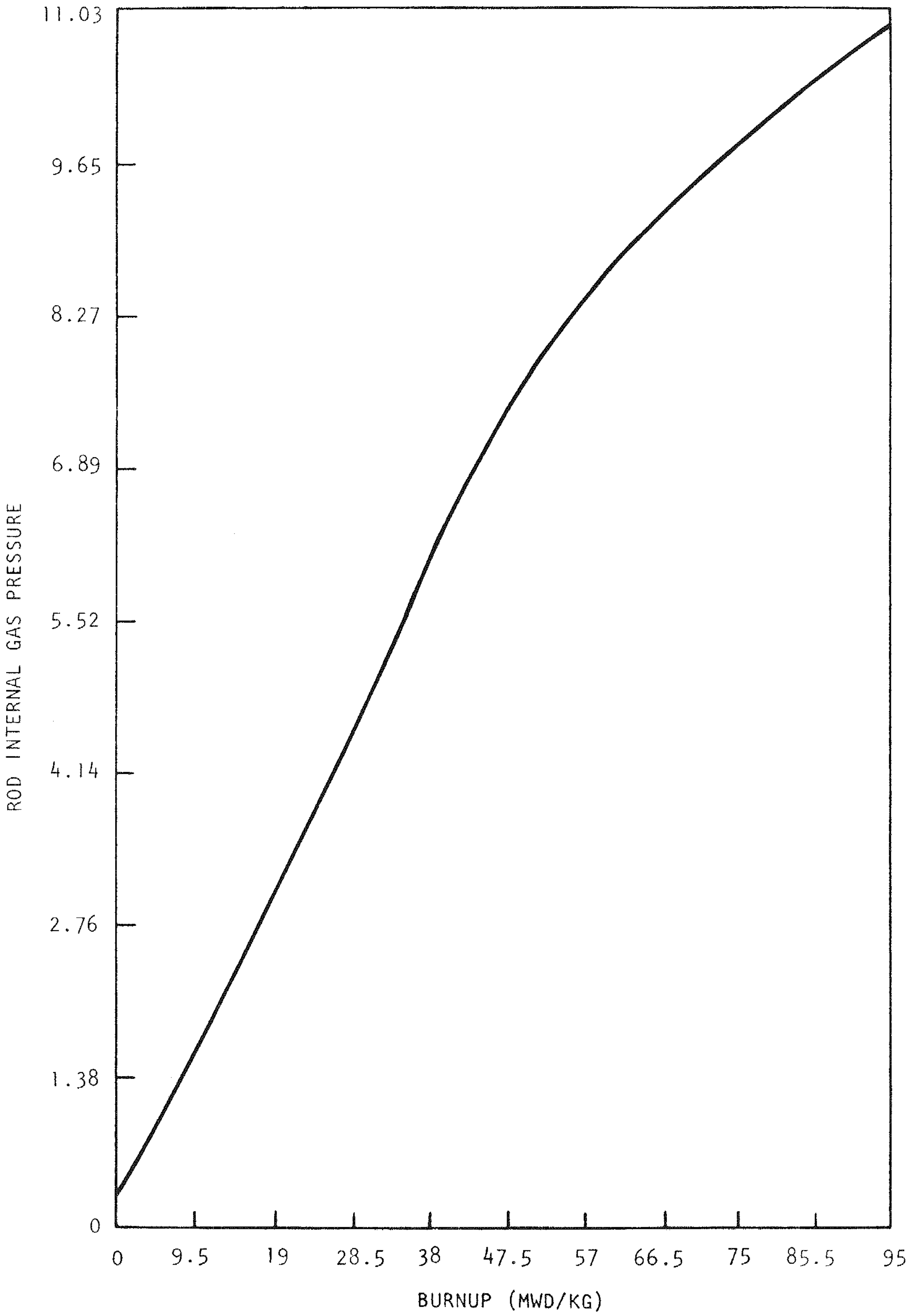

Fig. 6-6. Plenum pressure of sealed rod

TABLE 6-1
OPERATING CONDITIONS

Peak power	360 W/cm
Peak fast flux	3.0×10^{15} n/cm^2-s
Inlet coolant temperature	353°C
Outlet coolant temperature	538°C
System pressure	8.824 MPa (vented)
	0.958 MPa (sealed)
Irradiation time	750 full-power days

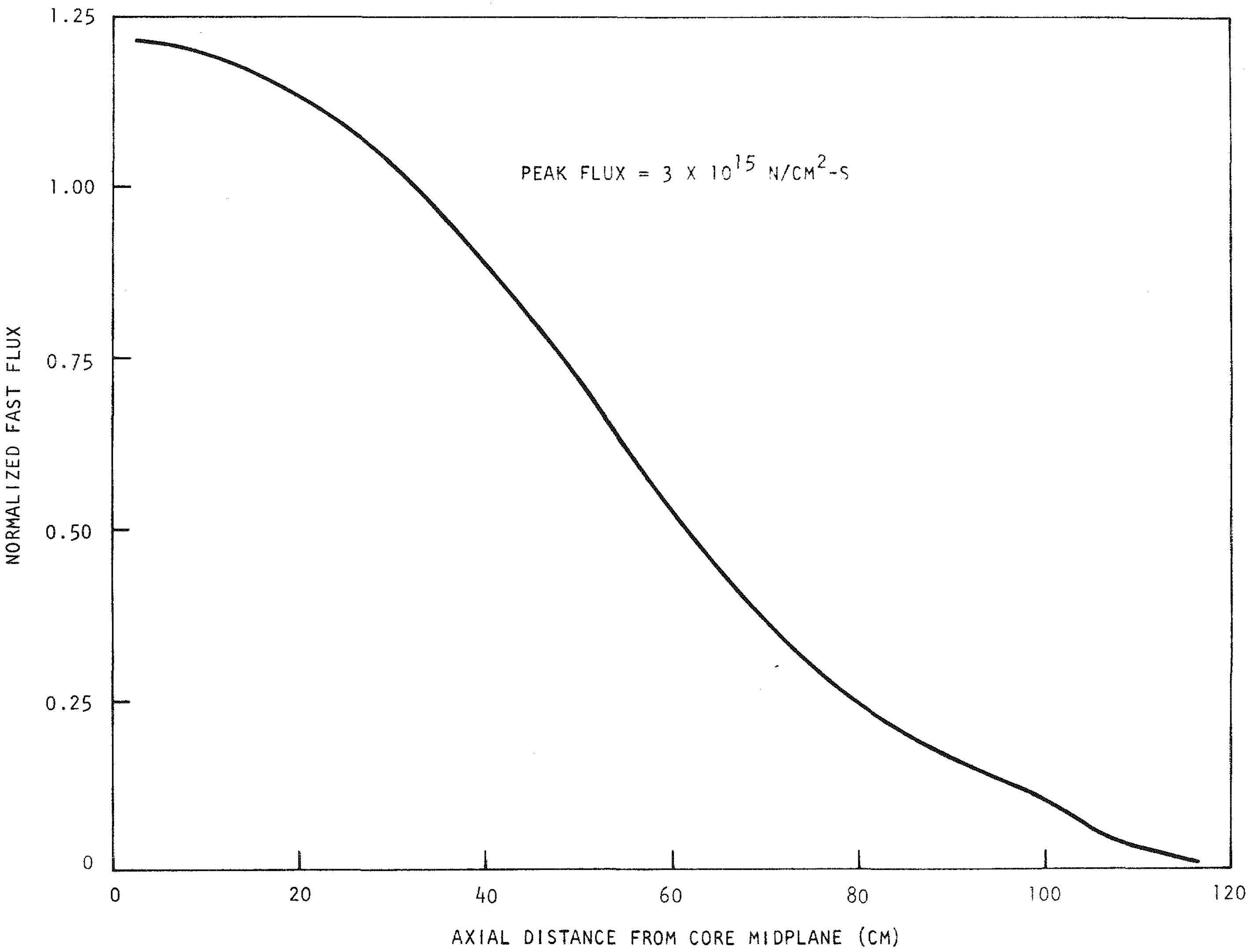

Fig. 6-7. Fast flux profile at core centerline

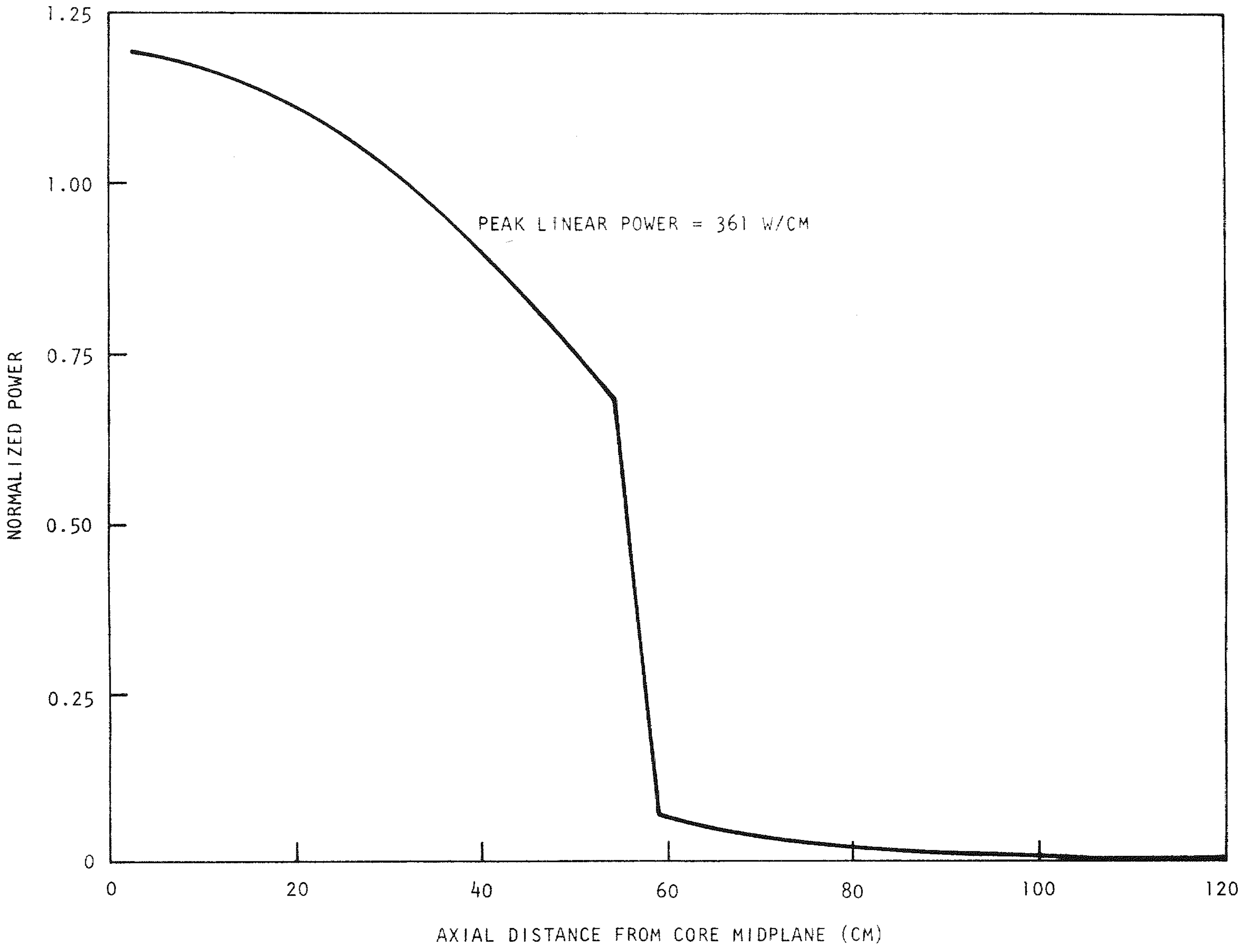

Fig. 6-8. Power profile at core centerline

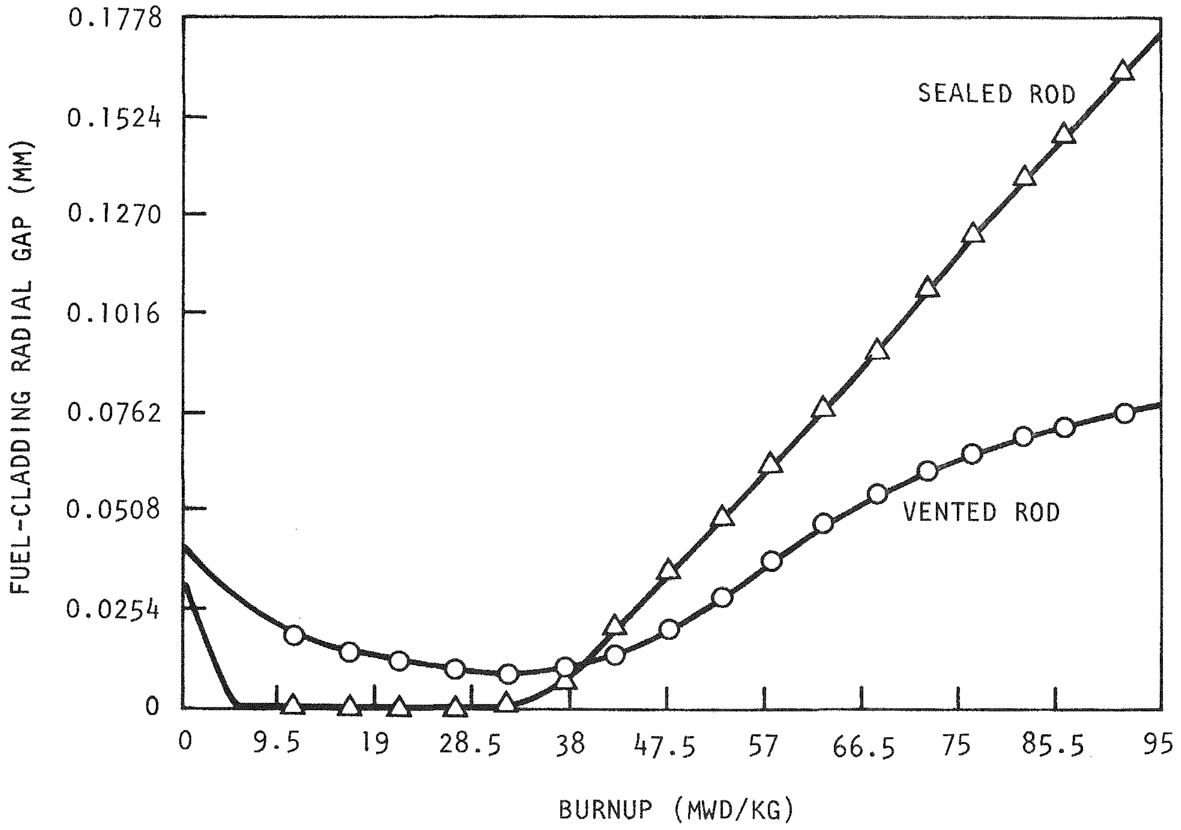

Fig. 6-9. Steady-state fuel-cladding radial gap at X/L = 0.375

pressure in the vented rod, the vented rod has less potential for pellet-cladding mechanical interaction than the sealed rod. This is contrary to the common expectation that the vented rod has a greater potential for pellet-cladding interaction than the sealed rod owing to the lack of internal pressure buildup. As seen in Fig. 6-9, the effect of internal pressure buildup does have a significant effect upon opening of the pellet-cladding gap. However, irradiation-induced swelling by itself causes the gap to increase after approximately 3.5 at. % burnup. Consequently, there does not appear to be any beneficial effect from internal pressure buildup.

6.4. ROD MECHANICAL TESTING

A test plan for the fuel rod mechanical testing program was prepared and is in review, and mechanical tests were initiated. Three ribbed and three smooth rods were subjected to room temperature tensile tests in accordance with the ASTM-A-370 test procedure. The results of these tests are shown in Table 6-2. For the sake of consistency with high-temperature tests to be performed later, the strain rates were specified as follows: for the smooth tubes, these strain rates were 0.006/min up to the yield point and 0.06/min beyond the yield point; the same strain rates were used for the ribbed tubes. Because only about one-third of the actual length of the cladding (i.e., the root diameter section) had the minimum cross section (which would predominantly strain), the cross head speed was maintained at one-third the value used in the smooth tube tests to obtain the proper strain rate.

The cladding used in the tests shown in Table 6-2 was produced by Carpenter Technology Corporation and had a nominal 7.4-mm o.d. and 6.2-mm i.d. The ribbed cladding was fabricated by mechanical grinding by WMC Corporation and the root diameter was 7.2 mm, corresponding to a rib height of 0.1 mm. For purposes of comparison, the smooth cladding o.d. was made equal to the root diameter of the ribbed cladding by mechanical grinding.

The ribbed cladding test data reduction is complicated because the minimum cross section area cannot be accurately computed because of the presence of the helical ribs. The data reduction was performed using the

TABLE 6-2
ROOM-TEMPERATURE TENSILE TEST RESULTS(a)

Specimen	Outside Diameter (mm)	Root Diameter (mm)	Inside Diameter, Nominal (mm)	0.2% Offset Yield Strength [N (MPa)]	Ultimate Tensile Strength [N (MPa)]	Total Elongation (%) (25.4-mm gauge)
R-1	7.402	7.219	6.2	7340 (684)	9274 (864)	26.5
R-2	7.397	7.219	6.2	7250 (674)	9163 (854)	--(b)
R-3	7.397	7.214	6.2	7428 (696)	9208 (863)	20
S-1	7.209	--	6.2	7160 (674)	8763 (816)	29
S-2(c)	7.209	--	6.2	--(c)	8763 (816)	26.5
S-3	7.219	--	6.2	7117 (663)	8718 (807)	26.5

(a) CARTECH values: yield strength = 662 MPa; ultimate tensile strength = 793 MPa; total elongation = 27%.

(b) Ruptured outside gauge length.

(c) Instrumentation failure.

measured root diameter and the nominal inside diameter to obtain the minimum cross section. However, the actual minimum cross section is somewhat greater, which explains the higher values of yield strength and ultimate tensile strength obtained from the ribbed cladding test results. Since yield strength and ultimate tensile strength are material properties, their increased values are related to the strengthening effect of the ribs. Failure begins at the root diameter (i.e., follows the helix) until it has encompassed the entire circumference. At this point the failure goes through the rib in an axial direction with respect to the cladding.

Total elongation has been measured for two of the ribbed specimens. The scatter of the data is greater than that obtained for smooth specimens, and additional testing will be required to define the effect of the ribs on the elongation. The ribs are expected to localize the strain to the area between the ribs; i.e., the strain on the ribs should be lower than the strain in the root section, and the overall effect should reduce the total elongation measured on a given gauge length. To detemine whether this occurs, the pitch and the width of the rib were measured after testing and the measurements compared to measured values of pitch and rib width in a region where no significant strain was expected, i.e., where the grips were used. The elongation based on the pitch measurements was about 30%, and the elongation on the top of the rib was in the range of 11% to 15%. Because of the difficulty of the measurements, the error bars can be as high as ±5%. Additional tests will be conducted to include pre-test and post-test measurements of pitch and rib width, which will provide more data on the effect of the ribs on cladding strength.

Design of the test fixture for conducting compression and flexure tests on fuel rod cladding has been initiated. These tests are designed to simulate the type of loading resulting from rod-spacer interactions during reactor operation.

REFERENCES

6-1. Billone, M. C., et al., "The LIFE-III Fuel-Element Performance Code User's Manual," Argonne National Laboratory Revised Draft, September 1976.

6-2. Booth, A. H., "Determination of the Diffusion Constant of Fission Xenon in UO_2 Crystals and Sintered Compacts," Atomic Energy of Canada Limited Report AECL-692, August 1958.

6-3. Booth, A. H., "A Suggested Method for Calculating the Diffusion of Radioactive Rare Gas Fission Products from UO_2 Fuel Elements and a Discussion of Proposed In-Reactor Experiments That May Be Used to Test Its Validity," Atomic Energy of Canada Limited Report AECL-700, October 1958.

6-4. Belle, J., Uranium Dioxide: Properties and Nuclear Applications, USAEC Division of Reactor Development, 1961.

6-5. Eichenberg, J. D., et al., "Effects of Irradiation on Bulk Uranium Oxide," in Fuel Elements Conference, Paris, November 18-23, 1957, pp. 616-716 (TID-7546).

6-6. Findlay, J. R., et al., "The Emission of Fission Products from Uranium-Plutonium Dioxide During Irradiation to High Burnup," J. Nucl. Mater. 35, 24-34 (1970).

6-7. Rest, J., "A LIFE-III Isotopic Gas-Release Model," Argonne National Laboratory Report ANL/MSD-08, July 1974.

6-8. Bennett, F. O., "Gas-Cooling Modifications to the LIFE-III Code," General Atomic, unpublished data.

6-9. Bennett, F. O., "Revised Nusselt Number Correlation for the LIFE-III Code," General Atomic, unpublished data.

6-10. Noyes, R. C., et al., "Development and Evaluation of the Combustion Engineering Advanced 1000-MW(e) LMFBR Design," in Proceedings of the International Conference of Sodium Technology and Large Fast Reactor Design, Argonne, Illinois, November 1968, part II, pp. 291-330 (ANL-7520).

6-11. Sofer, G. A., et al., "Selected Optimization Studies in the Use of Carbide Fuel in Large Fast Breeder Reactors," in Proceedings of the Conference on Safety, Fuels, and Core Design in Large Fast Power Reactors, Argonne, Illinois, October 1965, pp. 104-122 (ANL-7120).

6-12. Simnad, M. T., "Development of Carbide and Nitride Fuels for Fast Breeder Reactors," General Atomic, unpublished data.

6-13. Nickerson, G. M., et al., "Preliminary Assessments of Carbide Fuel Pins During Mild Overpower Transients in LMFBRs," Nucl. Eng. Design 36, 209-233 (1976).

6-14. Olander, D. R., "Fundamental Aspects of Nuclear Reactor Fuel Elements," ERDA Report TID-26711-P1, 1976.

6-15. Goodman, J., et al., "The Thermodynamic and Transport Properties of Helium," General Atomic Report GA-A13400, October 1975.

6-16. Lloyd, W. R., et al., "Heat Transfer in Multicomponent Monatomic Gases in the Low, Intermediate, and High Pressure Regime," in IEEE Conference Record of 1968 Thermionic Conversion Specialist Conference, October 1968.

6-17. Washington, A. B. G., "Preferred Values for the Thermal Conductivity of Sintered Ceramic Fuel for Fast Reactor Use," TRG Report 2236, September 1973.

6-18. Simnad, M. T., and J. P. Howe, "Materials for Nuclear Fission Power Reactor Technology," General Atomic Report GA-A14012, December 1, 1976.

6-19. Simnad, M. T., General Atomic, private communication.

6-20. Chang, K. H., "A Parametric Study of Mixed Carbide Fuel Centerline Temperature," General Atomic, unpublished data.

6-21. Ross, A. M., and R. L. Stoute, "Heat Transfer Coefficient Between UO_2 and Zircaloy 2," Atomic Energy of Canada Limited Report AECL-1552, June 1962.

6-22. Jankus, V. Z., and R. W. Weeks, "LIFE-II - A Computer Analysis of Fast-Reactor Fuel-Element Behavior as a Reactor Operating History," Nucl. Eng. Design 18, 83-96 (1972).

6-23. Cox, C. M., and F. J. Homan, Nucl. Appl. Technol. 9, 317 (1970).

6-24. "Clinch River Breeder Reactor Project Preliminary Safety Analysis Report," Project Management Corporation (NRC Docket 50-537).

6-25. Veca, A. R., "Core Assemblies Design for a 42 psi ΔP Core (127 Core Assembly Design)," General Atomic, unpublished data.

6-26. Rucker, R., General Atomic, private communication.

7. NUCLEAR ANALYSIS AND REACTOR PHYSICS (189a No. 00584)

The scope of activities planned under this subtask encompasses the validation and verification of the nuclear design methods which will be applied to the GCFR core design. This will primarily be done by evaluating the methods using a critical assembly experimental program specifically directed toward GCFR development. Program planning and coordination activities, critical assembly design and analysis, and the necessary methods development will be carried out.

The major effort during the previous quarter was directed toward calculation of the experimental U-238 Doppler worth in the GCFR phase II assembly. Analysis of the "dry" Doppler coefficient was done in 10 and 28 groups (without simulated steam entry) using an improved methodology for shielding resonance cross sections. A study of the adequacy of various heterogeneity corrections for the plate format of the ZPR cells was made, and conclusions were reached on spatial and quadrature mesh applicability.

During this quarter, the Doppler worth calculation was extended to include the "wet" Doppler coefficient (with simulated steam entry). Control rod worths in the dry and wet cores were evaluated, and the worth of whole-core steam entry was reanalyzed with an improved methodology. The ability to calculate steam entry worths in clean and rodded cores was demonstrated.

7.1. PHASE II GCFR CRITICAL ASSEMBLY ANALYSIS

7.1.1. Analysis of U-238 Doppler Coefficient in a Steam-Flooded Environment

7.1.1.1. Experimental Configuration. ANL measured the U-238 Doppler coefficient in the GCFR phase II reflected configuration using the N-1 natural uranium oxide Doppler capsule at the core center. The sample geometry is described in Ref. 7-1. The experiment was carried out in a manner similar to that of Ref. 7-1. Reference 7-2 gives the details of the experiment and reports an experimental value of -1.197 ± 0.010 Ih/kg for a steam density in the critical assembly void channels of 17.5 g/liter, which is approximately twice the value of the experimental Doppler coefficient for the dry case.

7.1.1.2. Calculational Results. New 28-group bucklings were calculated with 2DB (Ref. 7-3) for the central seven drawers in the wet phase II reflected core. These bucklings were then used in the two spectrum calculations for the 300 and 1100 K Doppler sample temperatures. Region 1 of the spectrum code modeled the sample, and region 2, the remainder of the central seven drawers. Spatial self-shielding in the fuel plates and U_3O_8 plates was modeled using an average chord length and average atom densities. Subsequently, 10- and 28-group flux calculations for the phase II assembly with the Doppler sample were done in R-Z geometry using 2DB. A real flux calculation was done for the hot sample (1100 K), and an adjoint flux calculation was done for the cold sample (300 K), so that the Doppler worth could be calculated by exact perturbation theory using the associated perturbation code PERT (Ref. 7-4). Radial and axial directional diffusion modifiers, obtained using the Benoist method (Ref. 7-5), were used in 2DB and PERT to account for neutron streaming in the void channels.

Table 7-1 compares the 28-group wet calculation with the 10- and 28-group dry calculations. The presence of steam produces a softer spectrum and consequently a larger Doppler signal. There are only small changes in the contributions from the sample capsule and sample core resonance interactions. Approximately 77% of the calculated Doppler effect was due to resonance broadening in the resolved energy range, with the remainder in the unresolved range.

In summary, careful attention to resonance interaction, shielding, and leakage effects provided accurate calculations of the Doppler effect of a central UO_2 sample in dry and steam-filled GCFR simulations. Use of comparable methods in the design of the GCFR should allow reliable

TABLE 7-1
MEASURED DOPPLER WORTHS IN THE PHASE II GCFR CRITICAL ASSEMBLY COMPARED WITH GA CALCULATIONS

	10-Group Calculation for Dry Phase II	28-Group Calculation for Dry Phase II	28-Group Calculation For Wet Phase II
Contributions to Calculated Doppler Worth (Ih/kg U-238)			
UO_2 sample	-0.545	-0.571	-1.197
Sample/capsule resonance interaction	-0.0014	-0.0010	-0.0017
Sample/core resonance interaction	-0.0446	-0.0272	-0.0329
Total calculated Doppler worth (Ih/kg)	-0.591	-0.599	-1.232
Experimental Doppler worth (Ih/kg)	-0.623	-0.623	-1.197
C/E	0.949	0.962	1.029

predictions of Doppler effects in a normal operating GCFR and the influence of Doppler effects on the consequences of accidental steam ingress.

7.1.2. Studies of Heterogeneity Corrections

Cell heterogeneity corrections were analyzed for the unrodded configurations, and a new three-drawer phase II core cell model has been adopted for DTFX (Ref. 7-6) calculations. In this model, the fuel plate density is diluted by a factor of 0.9482 to provide the same effective mass-to-surface ratio as provided by the plate loadings in the matrix, explicitly accounting for the matrix steel interruptions of the vertical stack. To achieve the proper cell-average composition, the width in the three-drawer model was slightly expanded by widening the cladding of the fuel and void regions. Table 7-2 compares the results of this new model, designated the equivalent chord model, with previous data provided by an exact TWOTRAN run (Ref. 7-7) and the older Wade-Gelbard DTFX Model (Ref. 7-8). The rigorous TWOTRAN calculations validate the use of the more approximate DTFX calculations and one-dimensional models. For the 2DB eigenvalue results, the 0.15% decrease in eigenvalues using the TWOTRAN and new DTFX shielding factors is believed to be due to lower scattering cross sections for U-238 in groups 8, 9, and 10. The lower scattering cross sections were provided by an evaluation of exact in-plate values from the GGC-5 (Ref. 7-9) edit.

Following this analysis, the equivalent chord model was used in one-dimensional DTFX calculations for 28-group plate flux advantage factors for four configurations of the phase II three-drawer core cell: (1) standard dry cell loading; (2) a cell with 17.5-g/liter CH_2 in the void channels; (3) a dry cell with a central B_4C column; and (4) a 17.5-g/liter CH_2-flooded cell with a B_4C column. The procedures for the 28-group cross section preparations were similar to those for the 10-group cases in that in-plate cross sections for the plutonium and uranium isotopes were derived from the GGC-5 edits for the resolved resonance range (groups 16 through 28) and used in the fuel regions of the DTFX cell. For the B_4C plate, the GGC-5 output cross sections were adjusted to correct for the self-shielding already provided by the two-region spectrum calculation.

TABLE 7-2
HETEROGENEITY EFFECTS DETERMINED BY DIFFERENT CELL MODELS AND CODES

	DTFX	DTFX	TWOTRAN
Cell model	Wade-Gelbard	Equivalent chord	Exact two-dimension
Order/quadrature	P_3-S_{16} (a)	P_1-S_{16} (a)	P_1-S_8 (b)
Fuel plate mesh (cm)	0.085	0.1275	0.1700
Fuel flux factor results			
Group 1	1.1603	1.1627	1.1731
Group 2	1.0837	1.0849	1.0829
Group 3	1.0268	1.0273	1.0283
Group 4	1.0100	1.0103	1.0106
Group 5	0.9972	0.9972	0.9970
Group 6	0.9932	0.9927	0.9936
Group 7	0.9844	0.9840	0.9841
Group 8	0.9882 (c)	0.9710	0.9736
Group 9	0.9653 (c)	0.9482	0.9494
Group 10	0.8921 (c)	0.8777	0.8838
Cell calculation of k	1.0030	0.9926	0.9928
k calculated by 2DB for loading 136 using fuel flux factors	0.9884	0.9868	0.9870

(a) Double-P_n.

(b) Double-P_n in axial direction; Chebyshev expansion in XY coordinates.

(c) Factors used in 2DB calculations and derived from GGC-5 two-region cell approximation.

Table 7-3 lists the 28-group DTFX flux advantage factors for the fuel plate in configurations 1 and 2 and the boron carbide plate in configurations 3 and 4. These DTFX calculations were done with P_1 anisotropic scattering and an S_{12} double-P_n quadrature set (internally provided by the code). For the rodded cases, the edits indicated extensive use of negative-flux fix-ups in the B_4C region (with 6 intervals for the 1.2-cm width) in groups 25 to 28, where the B-10 cross section goes to hundreds of barns.

7.1.3. Evaluation of Steam Worth With Improved Methodology

7.1.3.1. Effect of Weighting Function. As reported in Ref. 7-10, the weighting spectrum for the fine-group-average cross sections in the GAM format has been modified to include the effects of actual dilution of the isotopes oxygen, U-238, iron, chromium, and nickel. Calculations on the reflected phase II core with steam simulated at 17.5 g/liter were carried out with the diffusion code 2DB. The effect of different weighting methods and differently derived cell heterogeneity factors is shown in Table 7-4. The last column indicates good agreement with experimental values.

7.1.3.2. Effect of Group Structure. Reanalysis of the phase II steam entry worth with the new cross section weighting functions was carried out in the standard 10- and the 28-group analyses. Tables 7-5 and 7-6 illustrate the 2DB calculations utilizing DTFX-derived cell heterogeneity factors. Results for all higher-density (17.5 g/liter) steam worths in the 10- and 28-group calculations were comparable, with the 10-group results giving consistently higher calculated/experimental (C/E) ratios. The 28-group analytical values are in satisfactory agreement with the experimental values. At the lower steam density (8.8 g/liter), the calculational discrepancies were greater. This might be due to the approximation made in cell calculations for smearing the CH_2 into all void channels at the 8.8 g/liter average channel density, whereas the true loading consisted of 17.5-g/liter foam in the void channels of alternate drawers. Figure 7-1 illustrates the variation of reactivity worth with steam density for varying densities of CH_2 foam measured in the unrodded core.

TABLE 7-3
SELECTED RESULTS OF 28-GROUP DTFX RUNS FOR HETEROGENEITY FACTORS FOR PHASE II CORE

Energy Group Number	Standard Cell Factors for Pu-U-Mo Plate		Rodded Cell Factors for B_4C Plate	
	Dry	17.5-g/liter CH_2	Dry	17.5-g/liter CH_2
1	1.188	1.191	0.916	0.913
2	1.173	1.177	0.927	0.926
3	1.162	1.166	0.942	0.941
4	1.099	1.104	0.940	0.939
5	1.077	1.081	0.950	0.951
6	1.052	1.057	0.948	0.951
7	1.015	1.021	0.911	0.918
8	1.017	1.023	0.956	0.963
9	1.004	1.011	0.952	0.963
10	0.997	1.002	0.944	0.957
11	0.996	0.999	0.956	0.968
12	0.994	0.995	0.987	0.992
13	0.990	0.986	1.036	1.018
14	0.986	0.986	0.909	0.901
15	0.980	0.976	0.945	0.916
16	0.974	0.960	0.981	0.897
17	0.968	0.960	0.875	0.801
18	0.956	0.946	0.835	0.753
19	0.957	0.942	0.747	0.667
20	0.929	0.913	0.744	0.622
21	0.923	0.904	0.670	0.534
22	0.906	0.873	0.606	0.436
23	0.858	0.834	0.425	0.311
24	0.791	0.739	0.330	0.193
25	0.854	0.789	0.223	0.126
26	0.744	0.719	0.117	0.071
27	0.896	0.854	0.070	0.052
28	0.854	0.575	0.032	0.015

TABLE 7-4
COMPARISON OF STEAM WORTH ANALYSES USING VARIOUS METHODS FOR RESONANCE SHIELDING AND CELL-HETEROGENEITY ADJUSTMENTS

	Number of Groups				
	10	10	10	10	28
Weighting of σ_{scat} in GFE-4	1/E	$1/\Sigma t$	$1/\Sigma t$	$1/\Sigma t$	$1/\Sigma t$
Cell heterogeneity factors					
Fast range	DTFX	DTFX	TWOTRAN	DTFX	DTFX
Resolved resonance range	GAROL(a)	GAROL	TWOTRAN	DTFX	DTFX
B_4C self-shielding	None	None	TWOTRAN	DTFX	DTFX
C/E for 17.5-g/liter CH_2 flooding in 1210-liter core					
With no B_4C rods	2.08	1.30	1.19	1.23	1.00
With center rod	1.10	0.81	1.24	1.32	1.06
With 8 rods	1.21	0.07	1.01	1.22	0.97

(a) See Ref. 7-11.

TABLE 7-5
10-GROUP ANALYSIS OF PHASE II STEAM WORTHS USING DTFX HETEROGENEITY FACTORS

Core Radius (cm)	B_4C Rods Installed	8.8-g/liter CH_2		17.5-g/liter CH_2	
		Calculated Worth (Ih)	C/E	Calculated Worth (Ih)	C/E
54.79	None	309	1.47	672	1.25
56.23	None	268	1.53	597	1.23
56.23	Center	245	1.51	557	1.32
56.23	Center + ring	--	--	434	1.22
59.38	Center + ring	103	3.55	298	1.47

TABLE 7-6
28-GROUP ANALYSIS OF PHASE II STEAM WORTHS USING DTFX HETEROGENEITY FACTORS

Core Radius (cm)	B_4C Rods Installed	8.8-g/liter CH_2		17.5-g/liter CH_2	
		Calculated Worth (Ih)	C/E	Calculated Worth (Ih)	C/E
54.79	None	186	0.88	555	1.03
56.23	None	148	0.84	484	1.00
56.23	Center	126	0.78	449	1.06
56.23	Center + ring	--	--	346	0.97
59.38	Center + ring	-8.3	-0.29	209	1.04

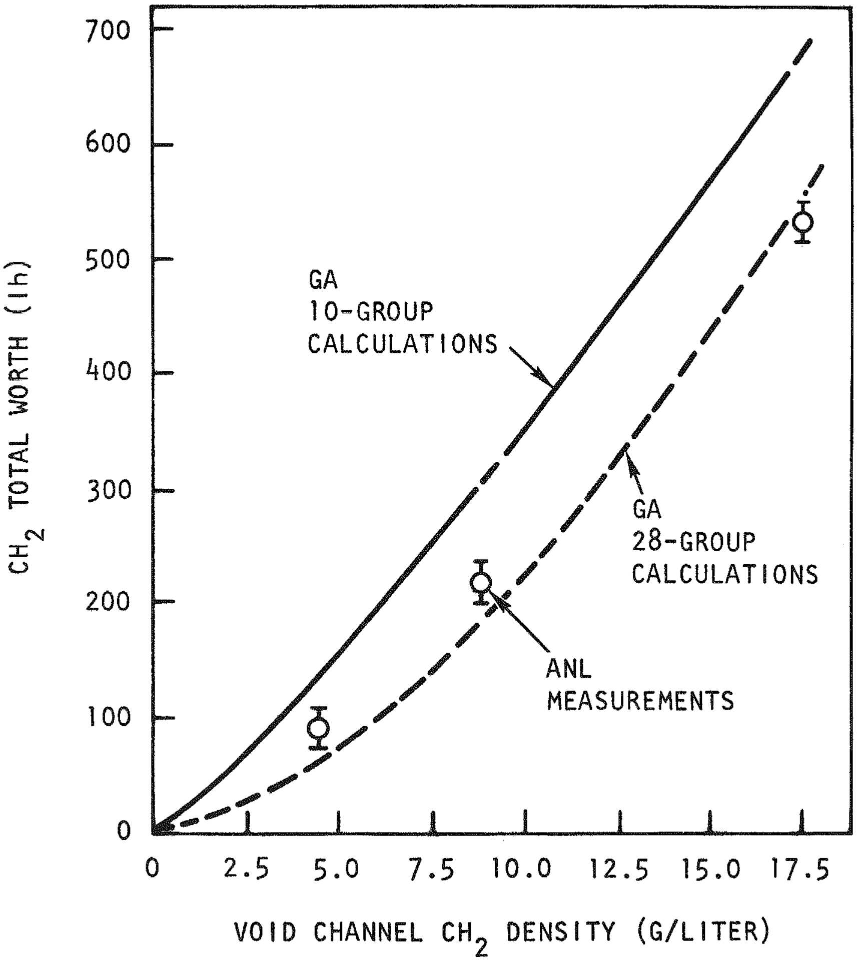

Fig. 7-1. Steam flooding worth in unrodded phase II GCFR assembly (54.8-cm core)

7.1.3.3. Steam Worth in Rodded Configurations. Tables 7-5 and 7-6 show the effect of B_4C rods on steam ingress worth. The heterogeneity factors were obtained with the equivalent chord model. For the rodded-cell DTFX, the B_4C plate density was reduced by a chord factor of 0.805 to achieve the same mass-to-surface ratio in the one-dimensional slab as in the two-dimensional column.

Figure 7-2 shows the variation of steam worth with steam density in the phase II core having eight inserted B_4C rods. It is concluded that rodded core steam worths can be predicted with the same precision as steam worth in a clean core. However, this requires that a reasonable effort be expended to re-evaluate the self-shielding effects for the control rods in different steam environments.

7.1.4. Evaluation of B_4C Rod Worths in Dry and Wet Cores

Table 7-7 shows the effects on the rod worth calculations of various methods for determining rod self-shielding factors. The spectrum-average shield factor for a dry core is about 0.91 to 0.93, which means up to a +10% error if shielding is ignored. However, for the flooded environments, the shielding factors change dramatically, producing errors of up to 55% for rod worths calculated without evaluating internal shielding. The differences between one- and two-dimensional treatments of cell heterogeneity and rod modeling are also shown in Table 7-7.

Without steam, the rod worths produced using the TWOTRAN and DTFX factors agree to within 1/2%. With 17.5 g/liter CH_2 in the voids, the rod worths calculated using the TWOTRAN factors are 2% to 3% greater than those obtained with DTFX shielding; this is a semmingly small effect. For the 8-rod insertion worth, however, a 3% uncertainty translates to ±60 Ih, which is a 17% uncertainty for the rodded steam worth. There was excellent agreement between 10- and 28-group rod worth calculations for dry and steam-flooded conditions when the same cell models were used in DTFX; the differences are within 1%.

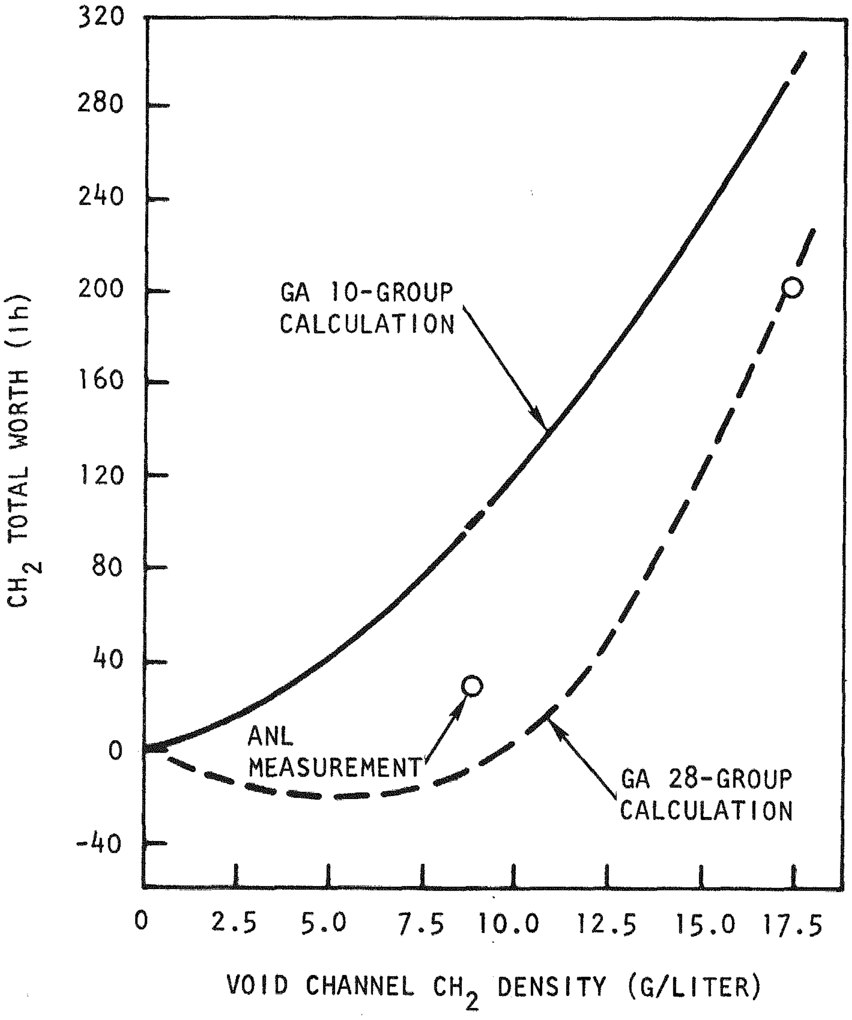

Fig. 7-2. Steam flooding worth in phase II GCFR assembly with eight B_4C rods in a 59.4-cm-radius core

TABLE 7-7
COMPARISON OF MEASURED AND CALCULATED WORTHS OF B_4C RODS IN PHASE II CORE FOR DRY AND FLOODED ENVIRONMENTS

Steam Flooding (g/liter CH_2 in voids)	Number of B_4C Rods Inserted	Measured Total Worth of Installed Rods (Ih)	C/E			
			10-Group Analyses			28-Group Analysis DTFX Factors
			No B_4C Shielding	TWOTRAN Shield Factors	DTFX Shield Factors	
Dry	1	-484 ± 5	1.051	0.982	0.979	0.981
8.8	1	-491 ± 4	1.187	--	0.998	0.995
17.5	1	-545 ± 4	1.464	0.966	0.944	0.936
Dry	8	-1934 ± 34	1.081	0.994	0.989	0.999
17.5	8	-2061 ± 33	1.309	1.037	1.007	1.005

The worth of the central mock-up rod is enhanced by about 13% owing to steam ingress at 17.5 g/liter CH_2 in the voids. However, the small sample worth of B-10 measured at the center of the wet core is 50% greater than that in the dry core. The fact that the wet/dry worth ratio for the mock-up rod is much less than the wet/dry worth ratio for the central sample is a consequence of the extensive self-shielding in the 1.27-cm-thick plate of B_4C. This implies that enhancement of control rod worths in a GCFR due to steam ingress could be increased by using more rods of smaller diameter.

REFERENCES

7-1. Pond, R. B., "^{238}U Doppler Effect Measurement in GCFR-II," Argonne National Laboratory, private communication.

7-2. Bhattacharyya, S. K., "Measurement of the ^{238}U Doppler Effect in the Steam-Filled GCFR Phase II Assembly," Argonne National Laboratory, private communication.

7-3. Little, W. W., Jr., and R. W. Hardie, "2DB, A Two-Dimensional Diffusion-Burnup Code for Fast Reactor Analysis," USAEC Report BNWL-640, Battelle Northwest Laboratory, January 1968.

7-4. Hardie, R. W., and W. W. Little, Jr., "PERT-IV, A Two-Dimensional Perturbation Code in Fortran-IV," USAEC Report BNWL-409, Battelle Northwest Laboratory, 1967.

7-5. Benoist, P., "Streaming Effects and Collision Probabilities in Lattices," Nucl. Sci. Eng. 34, 285 (1968).

7-6. Mathews, D. R., General Atomic, private communication.

7-7. Lathrop, K. D., and F. W. Brinkley, "Theory and Use of the General-Geometry TWOTRAN Program," USAEC Report LA-4432, Los Alamos Scientific Laboratory, May 1970.

7-8. Wade, D. C., and E. M. Gelbard, "Neutron Streaming in Plate Criticals," in Advanced Reactors: Physics, Design and Economics, Pergamon Press, Oxford, 1975, pp. 379-391.

7-9. Mathews, D. R., et al., "GGC-5, A Computer Program for Calculating Neutron Spectra and Group Constants," Gulf General Atomic Report GA-8871, September 27, 1971.

7-10. Hess, A. L., and R. A. Rucker, "Evaluation of Full-Core Steam Flooding Worth in Simulated GCFR Configurations," Trans. Am. Nucl. Soc. 26, 532 (1977).

7-11. Stevens, C. A., and C. V. Smith, "GAROL, A Computer Program for Evaluating Resonance Absorption Including Resonance Overlap," General Dynamics, General Atomic Division Report GA-6637, August 24, 1965.

8. SHIELDING REQUIREMENTS (189a No. 00584)

The purposes of the shielding task are to verify the adequacy of the methods and data (physics and engineering) for the design of GCFR shields and to evaluate the effectiveness of various shield configurations. This task also coordinates and provides liaison with the analytical and experimental GCFR shielding activities at ORNL.

During the last quarter, studies of the revised upper axial shield assembly were continued, and the DOT II (Ref. 8-1) two-dimensional neutron transport calculations were completed. The candidate grid plate shielding materials were compared, and a report summarizing the grid plate design confirmation experiment requirements was written (Ref. 8-2). A method for evaluating irradiation exposure for damage to graphite was adopted, and an auxiliary computer program was written for performing sensitivity analyses of ex-core or in-core damage or detector response to the core and blanket source distribution. During this quarter, a revision of the upper axial shield assembly was completed, the shielding effectiveness of two proposed core catchers was examined, a proposed shielding material was analyzed, and several improvements were made to the DOT II code.

8.1. REVISED UPPER AXIAL SHIELD

The initial analysis of the revised upper axial shield is presented in Ref. 8-3. During the last quarter, neutron damage and gamma ray heating studies were initiated (Ref. 8-4), and it was concluded that near the coolant inlet ducts, the ratio of fluence damage limit to calculated fluence at the liner was marginal with respect to the 47°C nil ductility temperature shift (NDTS). The two major changes made during this quarter were as follows: a 4-cm-thick stainless steel liner was determined to be the best choice for the 300-MW(e) GCFR shielding, and the upper axial shield above the grid plate in the radial direction was reduced in thickness to allow space for the fuel locking mechanism. The thickness of the shield above the grid plate was reduced to 15.24 cm to a height above the grid plate of 167.64 cm. The inside surface above 167.64 cm makes an angle of 30 deg with the vertical direction. The container walls for the graphite were reduced to a thickness of 1.27 cm to reduce the weight of the shield.

The results of these changes are shown in Fig. 8-1. The stainless steel liner shield is shown at the inlet duct, where the liner is recessed to keep the liner shield in line with the cover of the insulation. The distance that the shield must be put into the inlet duct to protect the liner cannot be determined by the present two-dimensional R-Z calculations; a separate two-dimensional study is necessary. This liner shield is also required between the ducts on the circumference of the reactor cavity.

One-dimensional 1DFX (Ref. 8-5) transport calculations were done to approximate the liner shield at the top of the outer radial shield and indicated that the configuration shown in Fig. 8-1 was adequate. This configuration will be recalculated with a two-dimensional transport code to confirm the results.

8.2. LOWER SHIELD

During this quarter, preliminary analysis was performed to investigate the shielding effectiveness of two proposed core catcher models (Section 12.4). One-dimensional slab neutron transport calculations were performed with the 1DFX code to approximate the shielding effectiveness through a vertical section in the lower axial horizontal region of the core catcher. (See Ref. 8-6 for a description of the calculation method.) The 47°C NDTS margin at the liner was calculated to indicate its effectiveness as a shield during normal operation.

Core catcher model No. 1 was analyzed in two configurations and is mainly composed of boron nitride and graphite (Fig. 8-2). For model 1, the actual fluence limit necessary to produce the 47°C NDTS is much greater than

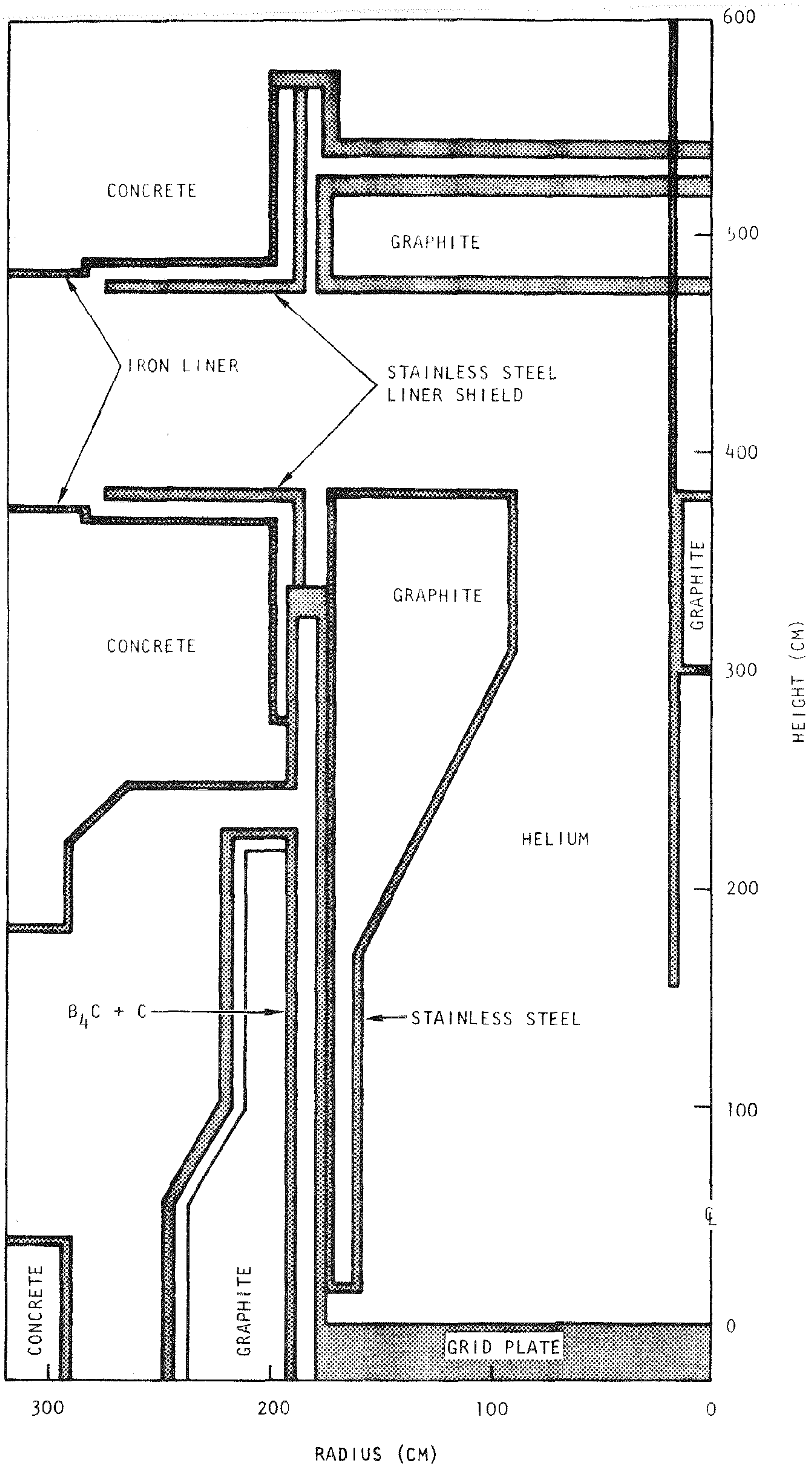

Fig. 8-1. Revised upper axial shield configuration

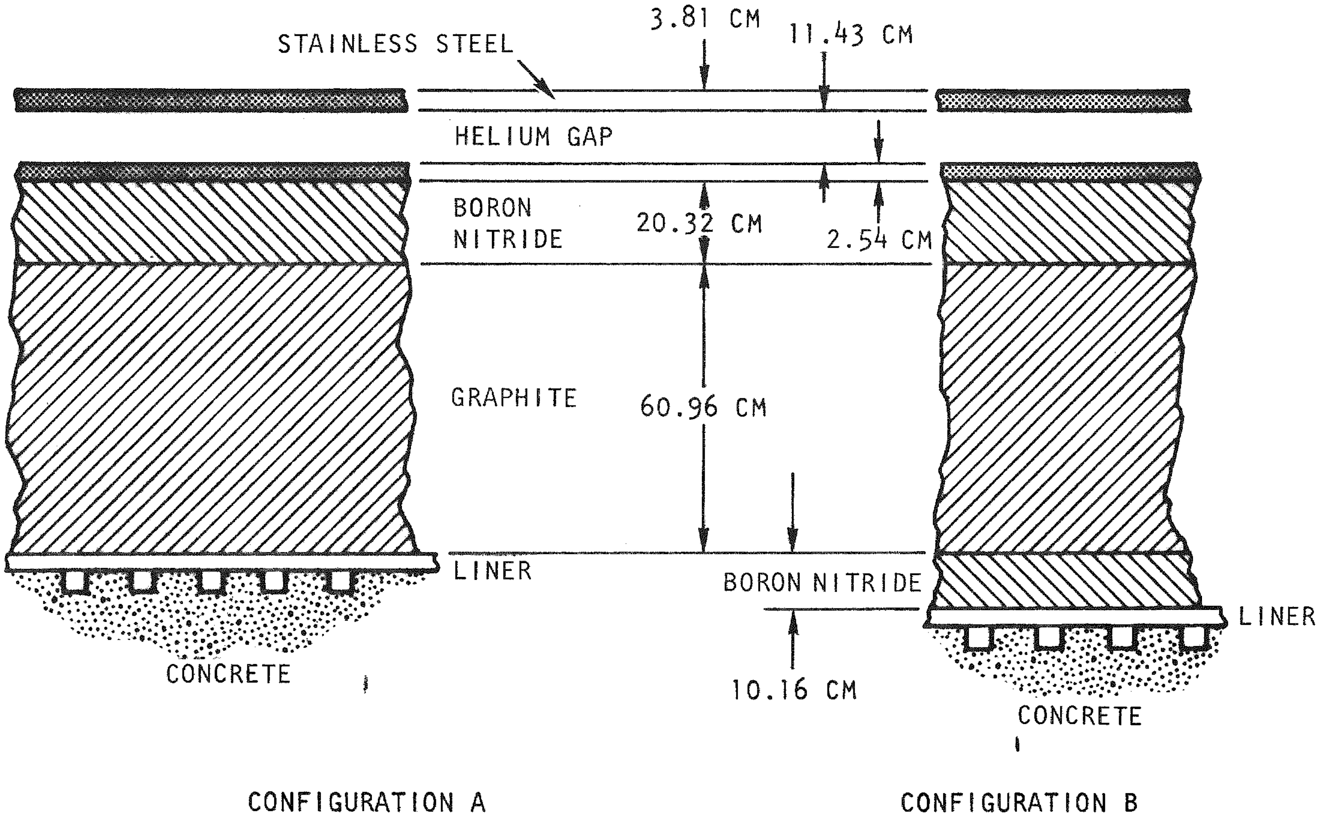

Fig. 8-2. Nuclear shielding model of proposed core catcher model No. 1

the calculated fluence. Configuration A is conservative by a margin of $\sim$3000, and configuration B, by a margin of $\sim 10^5$. Consequently, shielding of the liner below the core catcher during normal operation would not pose a problem.

The proposed core catcher model No. 2 was analyzed in four configurations and is shown in Fig. 8-3. The materials and components used in all configurations are (1) 2.54-cm stainless steel preshield (a proposed stainless steel honeycomb was not included in this analysis); (2) 15.24-cm MgO; (3) 2.54-cm or 0.635-cm tungsten or U-238; (4) 38.1-cm graphite or 33.0-cm graphite and 5.08-cm B_4C + C; and (5) 5.08-cm SiO_2. The one-dimensional slab calculations were performed in the same manner as those in Ref. 8-6 and resulted in the following margins of conservatism relative to the liner 47°C NDTS fluence limit:

Configuration	Margin
2A	10.9
2B	7.1
2C	5.6
2D	219

It is concluded that if the thicknesses of the preshield stainless steel, MgO, graphite, and SiO_2 are fixed because of other core catcher considerations, then any tungsten or U-238 thickness would be satisfactory from a shielding point of view. Furthermore, if B_4C is needed to reduce the gamma ray heating of the concrete (configuration 2D), any appropriate core catcher material can be used in place of tungsten or U-238.

8.3. METHODS DEVELOPMENT

The following improvements were made to the DOT-II code (Ref. 8-1):

1. Additional FIDO (Ref. 8-7) format input options were incorporated.

2. The code was overlayed to enable relative addressing.

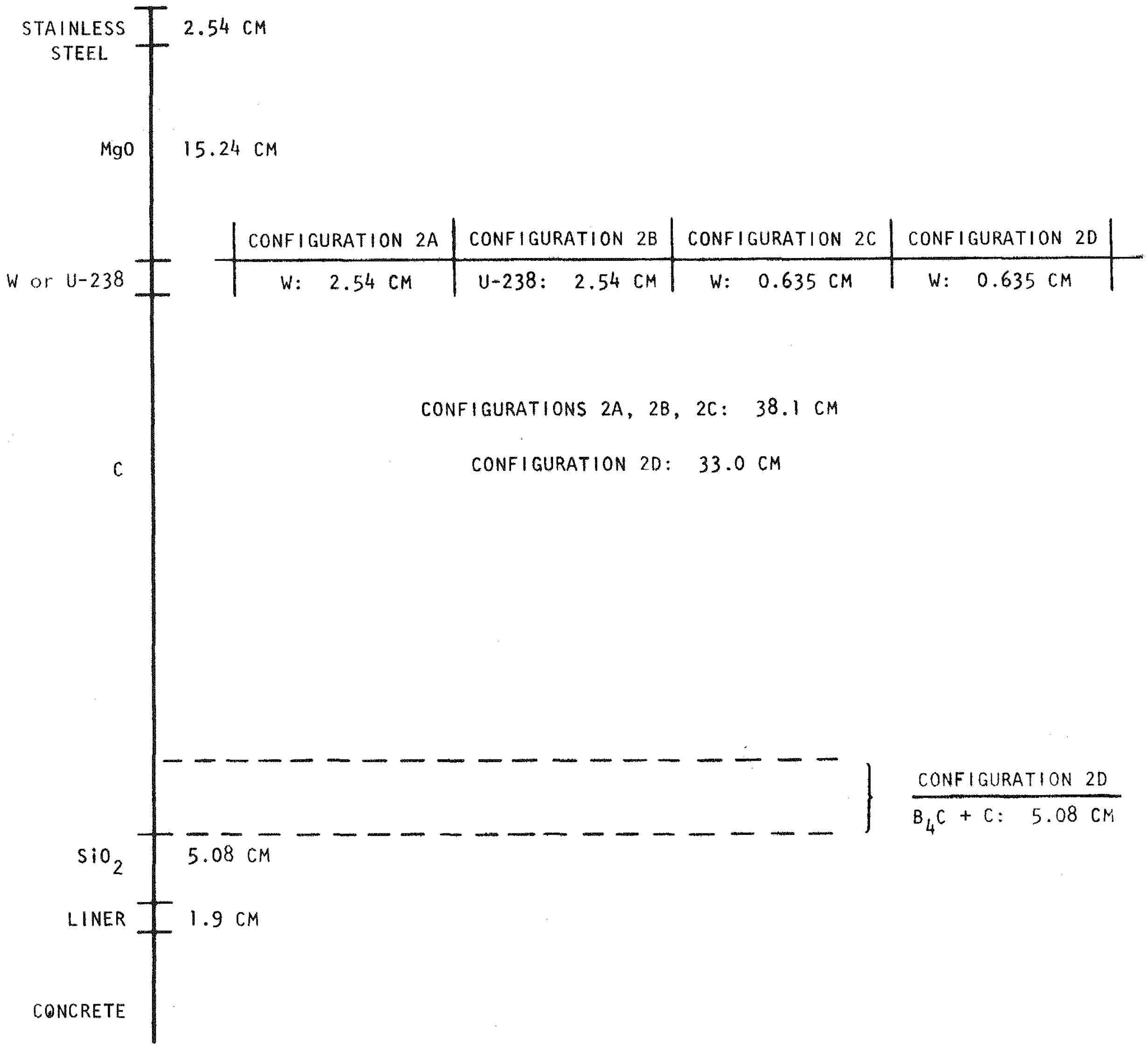

Fig. 8-3. Nuclear shielding model of proposed core catcher model No. 2

3. Variable dimensioning was incorporated so that memory can be dynamically allocated; the maximum problem size is 260,000 words.

The following radiation shielding information center code packages were obtained for possible implementation on the UNIVAC computer:

1. SWANLAKE (Ref. 8-8).
2. DOMINO (Ref. 8-9).
3. DOT 3.5 (Ref. 8-10).

REFERENCES

8-1. Mynatt, F. R., "DOT Two-Dimensional Discrete Ordinates Transport Code," Oak Ridge National Laboratory Report ORNL-CCC-89, K1694, October 1969.

8-2. Broido, J. H., "Grid Plate Shielding Design Configuration Experiment," General Atomic, unpublished data.

8-3. "Gas-Cooled Fast Breeder Reactor Quarterly Progress Report for the Period May 1, 1976 Through July 31, 1976," ERDA Report GA-A13975, General Atomic, August 31, 1976.

8-4. "Gas-Cooled Fast Breeder Reactor Quarterly Progress Report for the Period February 1, 1977 Through April 30, 1977," ERDA Report GA-A14358, General Atomic, May 1977.

8-5. Archibald, R., K. D. Lathrop, and D. Mathews," 1DFX - A Revised Version of the 1DF (DTF-IV) SN Transport Theory Code," Gulf General Atomic Report Gulf-GA-B10810, September 27, 1971.

8-6. "Gas-Cooled Fast Breeder Reactor Quarterly Progress Report for the Period February 1, 1976 Through April 30, 1976," ERDA Report GA-A13975, General Atomic, May 1976, p. 8-4.

8-7. "ANISN-W: A One-Dimensional Discrete Ordinates Transport Code," RSIC Computer Code Collection CC-82, Oak Ridge National Laboratory.

8-8. Bartine, D. E., F. R. Mynatt, and E. M. Oblow, "SWANLAKE - A Computer Code Utilizing ANISN Transport Calculations for Cross Section Sensitivity Analysis," Oak Ridge National Laboratory Report ORNL-TM-3809, May 1973.

8-9. Emmett, M. B., C. E. Burgait, and T. J. Hoffman, "DOMINO - A General Purpose Code for Coupling Discrete Ordinates and Monte Carlo Radiation Transport Calculations, Oak Ridge National Laboratory Report ORNL-4853, July 1973.

8-10. "DOT 3.5: A Two Dimensional Discrete Ordinates Transport Code," RSIC Computer Code Collection ORNL-CCC-276, Oak Ridge National Laboratory.

9. SYSTEMS ENGINEERING (189a No. 00585)

9.1. CORE THERMAL-HYDRAULIC PERFORMANCE

GACOOL (Ref. 9-1) was used to study preliminary thermal-hydraulic performance and orificing requirements for the GCFR core during the first 3-yr fuel cycle. The primary objective of this work was to test the capability of GACOOL to (1) perform overall core studies, (2) develop interfacing computer programs, and (3) establish procedures for using the core nuclear data bank for sizing core and blanket orifices and performing thermal management studies. The initial part of this work focused on establishment of three-dimensional, time-dependent power distribution information for the core, axial blanket, and radial blanket regions.* There are currently no comprehensive power distribution information data available for the core and radial blanket assemblies which are suitable for GACOOL input. However, there are several reports (Refs. 9-3 through 9-8) which provide information. Among the above, the core data given by Ref. 9-7 and radial blanket data given by Ref. 9-8 are the most comprehensive, and these data together with the power fraction data and standard axial power profiles provided the three-dimensional, time-dependent power distribution data for the core, axial blanket, and radial blanket regions.

There are some differences between the data of Refs. 9-7 and 9-8 and the present core and blanket design. In addition, the radial blanket data (Ref. 9-8) are for a ThO_2 radial blanket, and the core and radial blanket power distribution data are based on a management scheme which is different from the currently favored one. In spite of these differences, the results are useful for indicating some trends and are important for establishing the capability of GACOOL to perform a sensitivity analysis of core orifice systems and to carry out thermal management studies.

---

*The nuclear data bank (Ref. 9-2) will be the source of power distribution information for GACOOL.

The assembly identification numbers and the arrangement of the core and radial blanket assemblies are shown in Fig. 9-1. The core and radial blanket power distribution at the beginning and end of each of the three cycles is shown in Figs. 9-2 through 9-4. The vertical bars in these figures indicate the power densities of the core and radial blanket assemblies, with the core showing decreasing and the blanket increasing values.

The ideal orifice sizes required to maintain the specified maximum cladding temperature of 700°C are shown in Figs. 9-5 through 9-7 for each of the three fuel cycles. Each orifice is sized to accommodate the larger of the two coolant flow rates calculated for the beginning-of-cycle and end-of-cycle power distributions. For the case of ideal orificing, the orifice diameters range from 8.3 to 16.3 cm for the fuel and control assemblies. The maximum fuel assembly is assumed to have no orifice. In the radial blanket assemblies, the orifice diameters range from 1.0 to 3.0 cm for the first row and from 0.2 to 1.1 cm for the second row. The very small orifice size required for the second row blanket is due to the very low power densities of the ThO_2 blanket during the first fuel cycle (see Fig. 9-2).

The results of the orificing study were used to determine the mixed-mean outlet temperatures of the individual core assemblies during the first 3 yr. Three orificing schemes (A, B, and C) were assumed. In scheme A, all core and radial blanket assembly orifices are replaced during refueling. Figure 9-8 shows the results for this scheme for the beginning of the first fuel cycle, assuming a maximum cladding temperature of 700°C. This scheme achieves the highest mixed-mean reactor outlet temperature with most of the core assemblies performing close to their maximum cladding temperature limit. The maximum cladding temperatures of the radial blanket assemblies at the beginning of the cycle are considerably below 700°C; however, the cladding temperatures increase during the cycle and reach a maximum of 700°C at the end. The helium pressure drops and reactor outlet temperatures for all three schemes are shown in Fig. 9-9 for the three cycles; a linear variation in core assembly power density during each cycle was assumed. For a given reactor thermal power and maximum cladding temperature, the core outlet temperature increases during each given cycle, and the

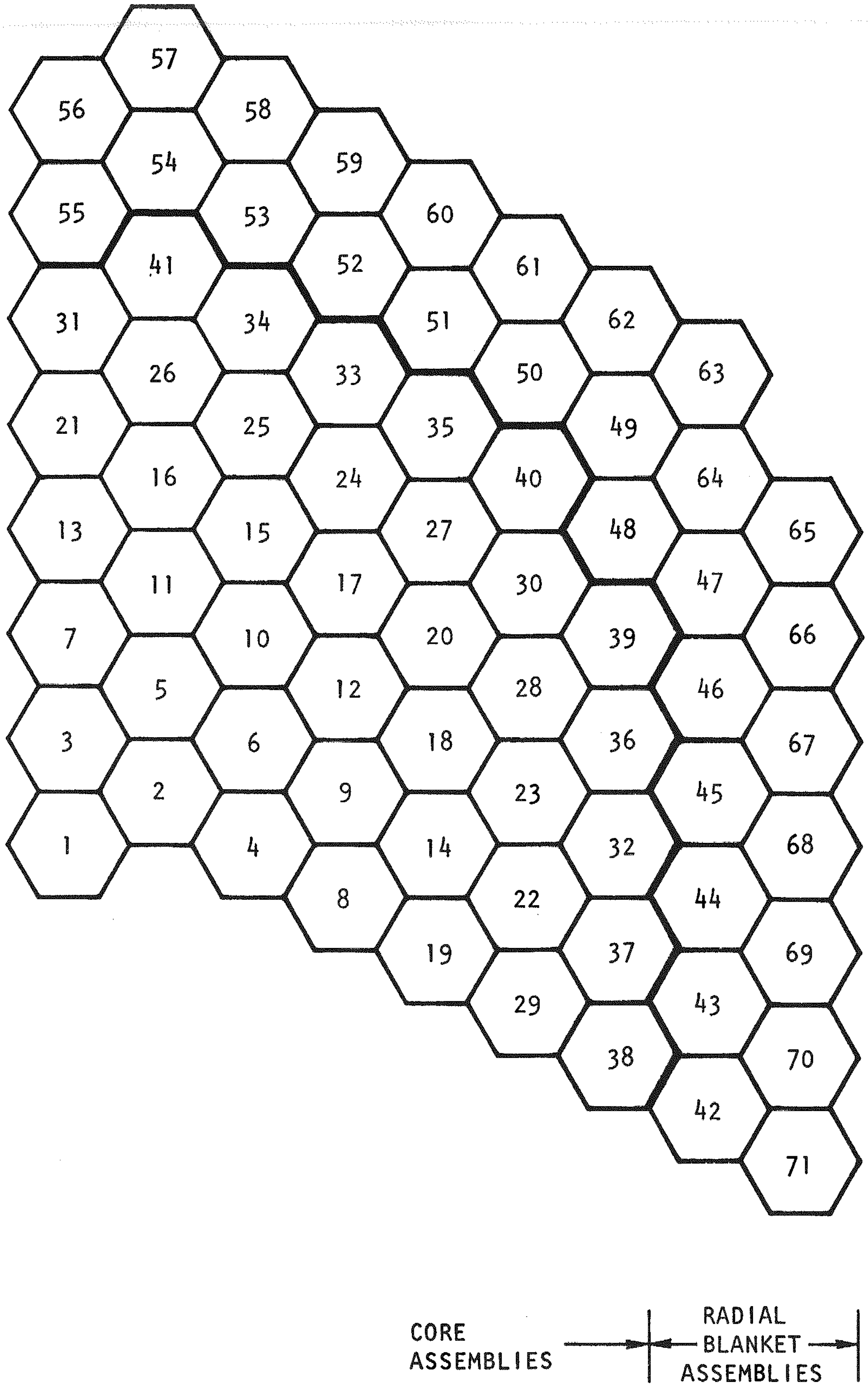

Fig. 9-1. 300-MW(e) GCFR core assembly (120-deg symmetry) with assembly identification numbers

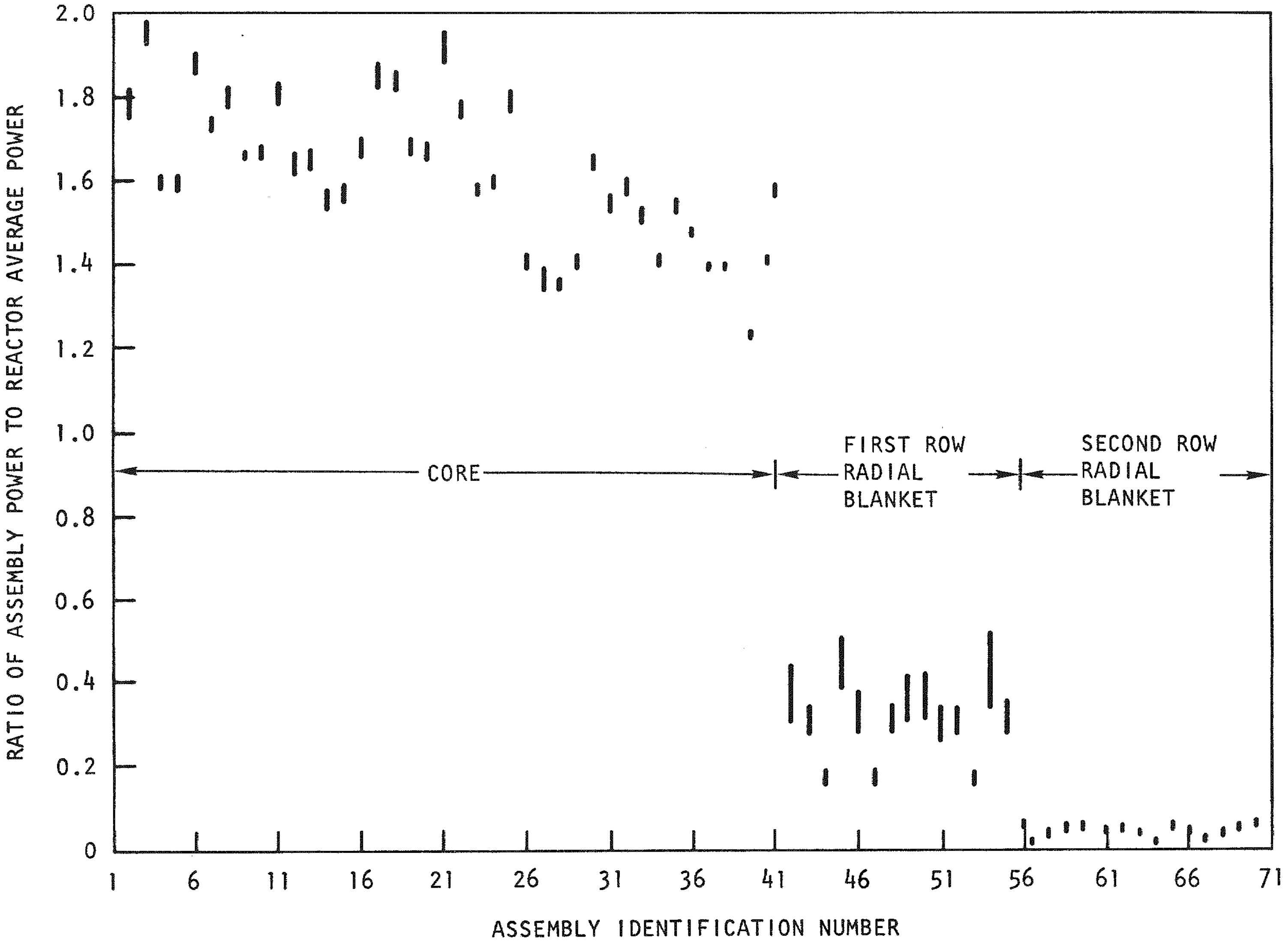

Fig. 9-2. Core and radial blanket power distribution at beginning and end of first cycle (0 to 250 days)

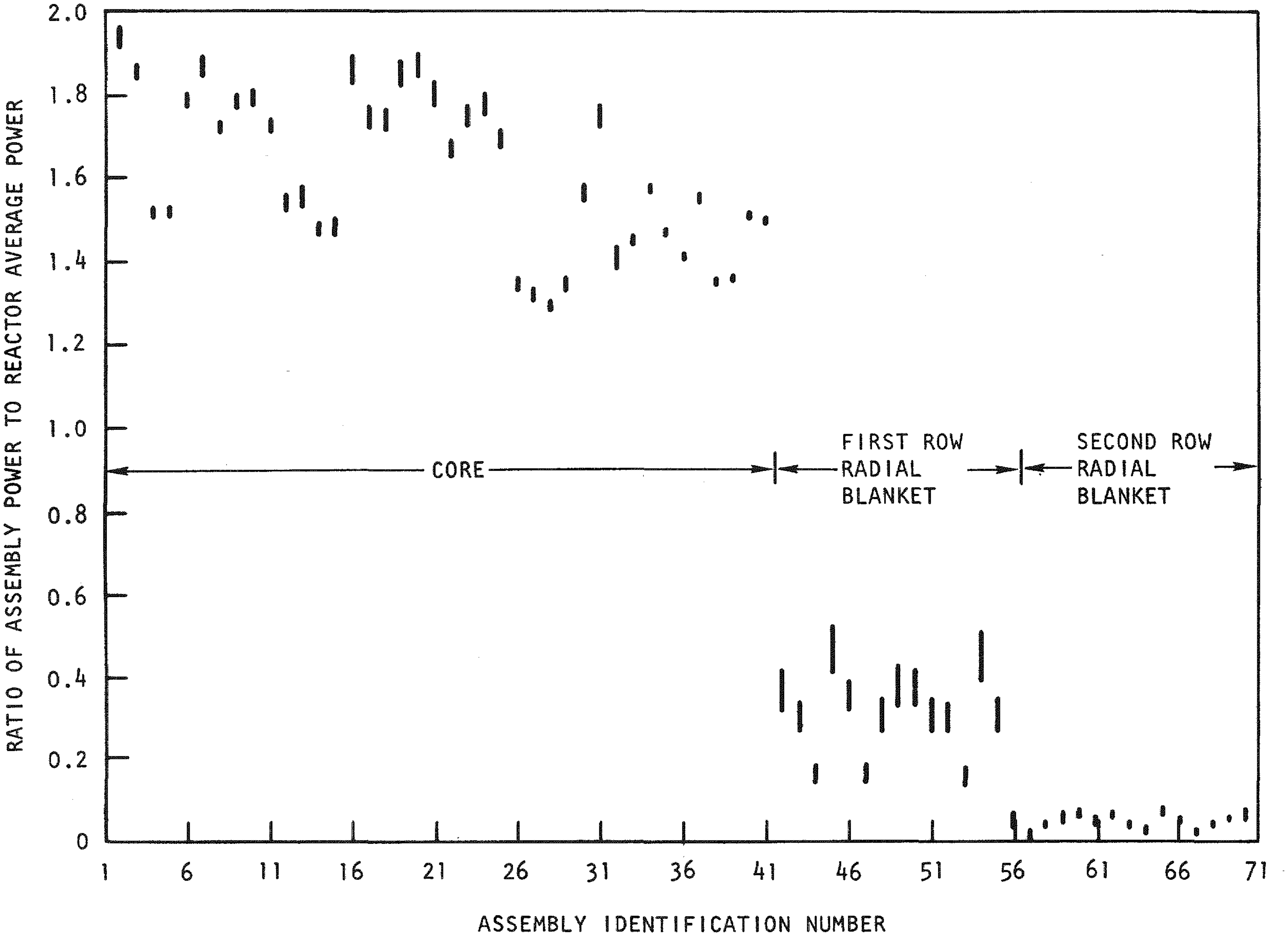

Fig. 9-3. Core and radial blanket power distribution at beginning and end of second cycle (250 to 500 days)

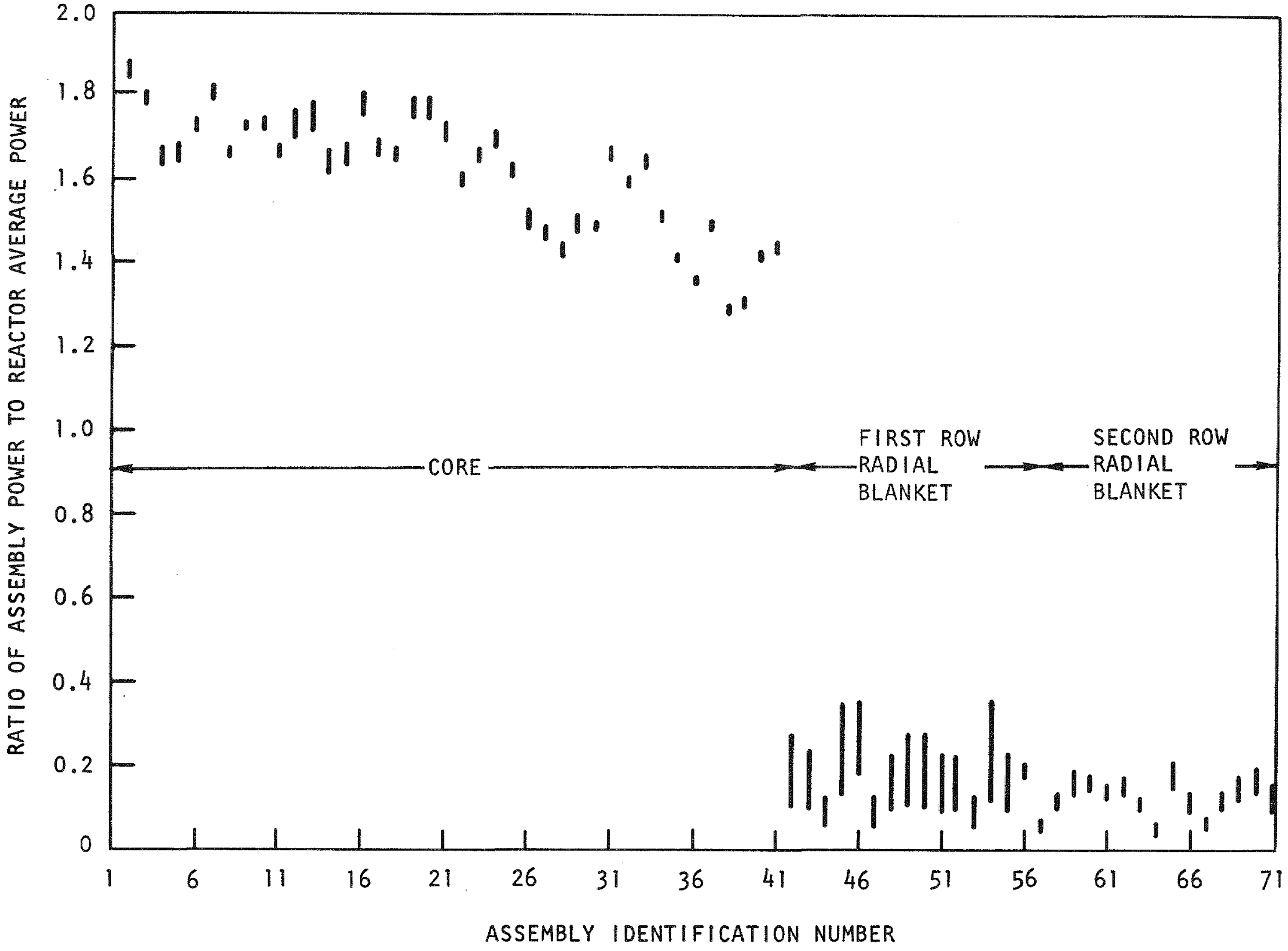

Fig. 9-4. Core and radial blanket power distribution at beginning and end of third cycle (500 to 750 days)

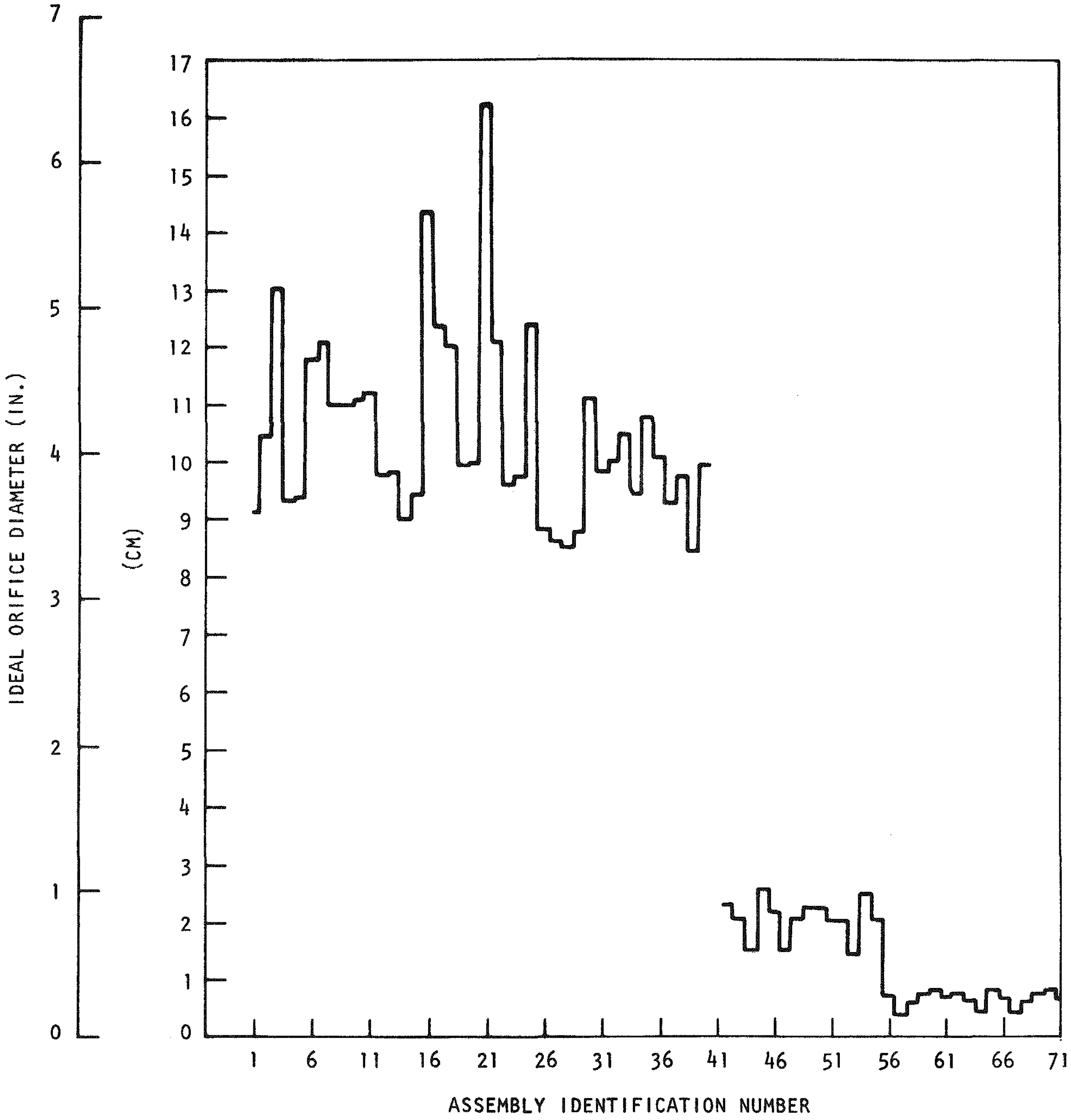

Fig. 9-5. Ideal diameter sizes for core and radial blanket assemblies during first cycle (0 to 250 days)

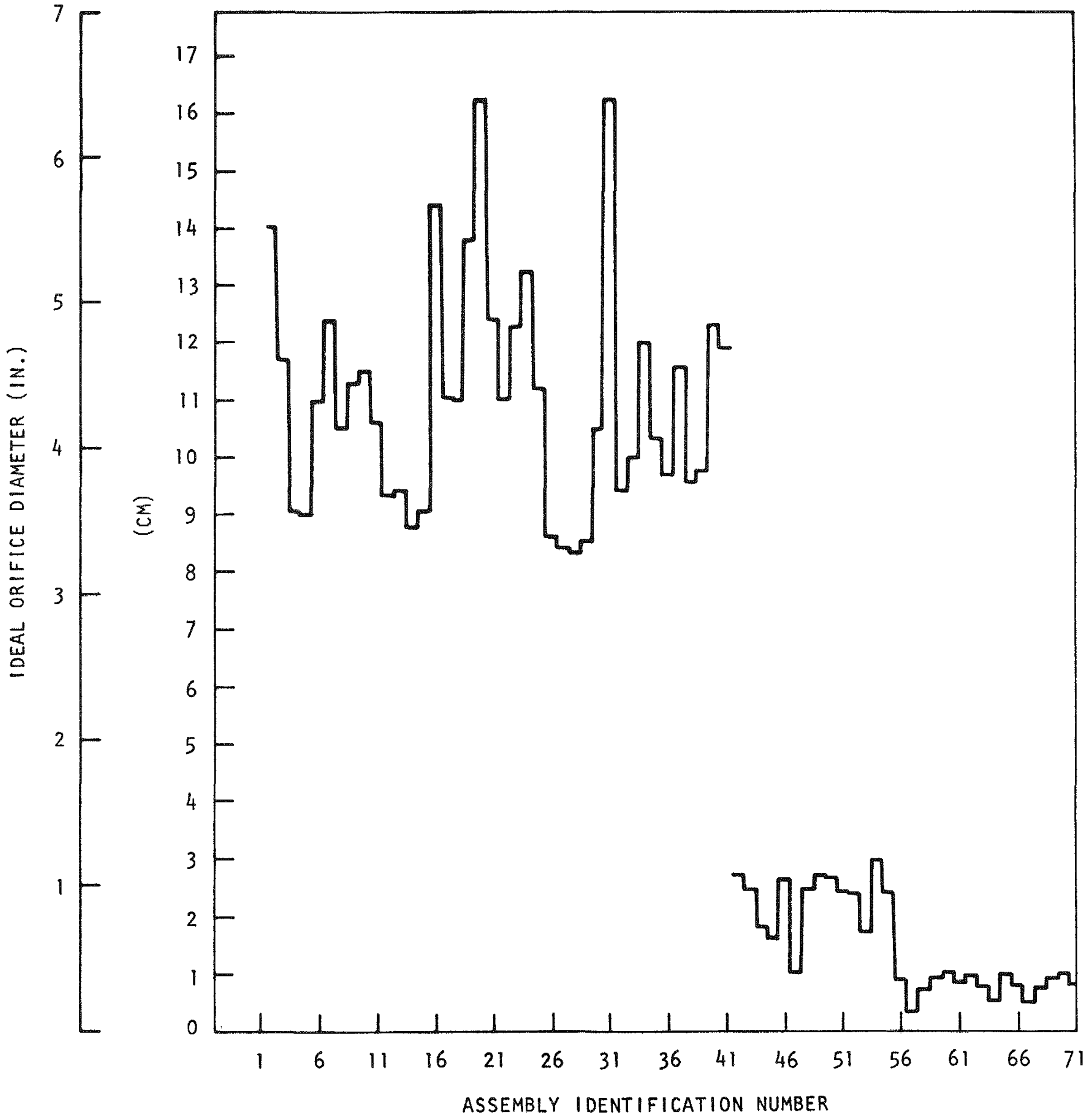

Fig. 9-6. Ideal diameter sizes for core and radial blanket assemblies during second cycle (250 to 500 days)

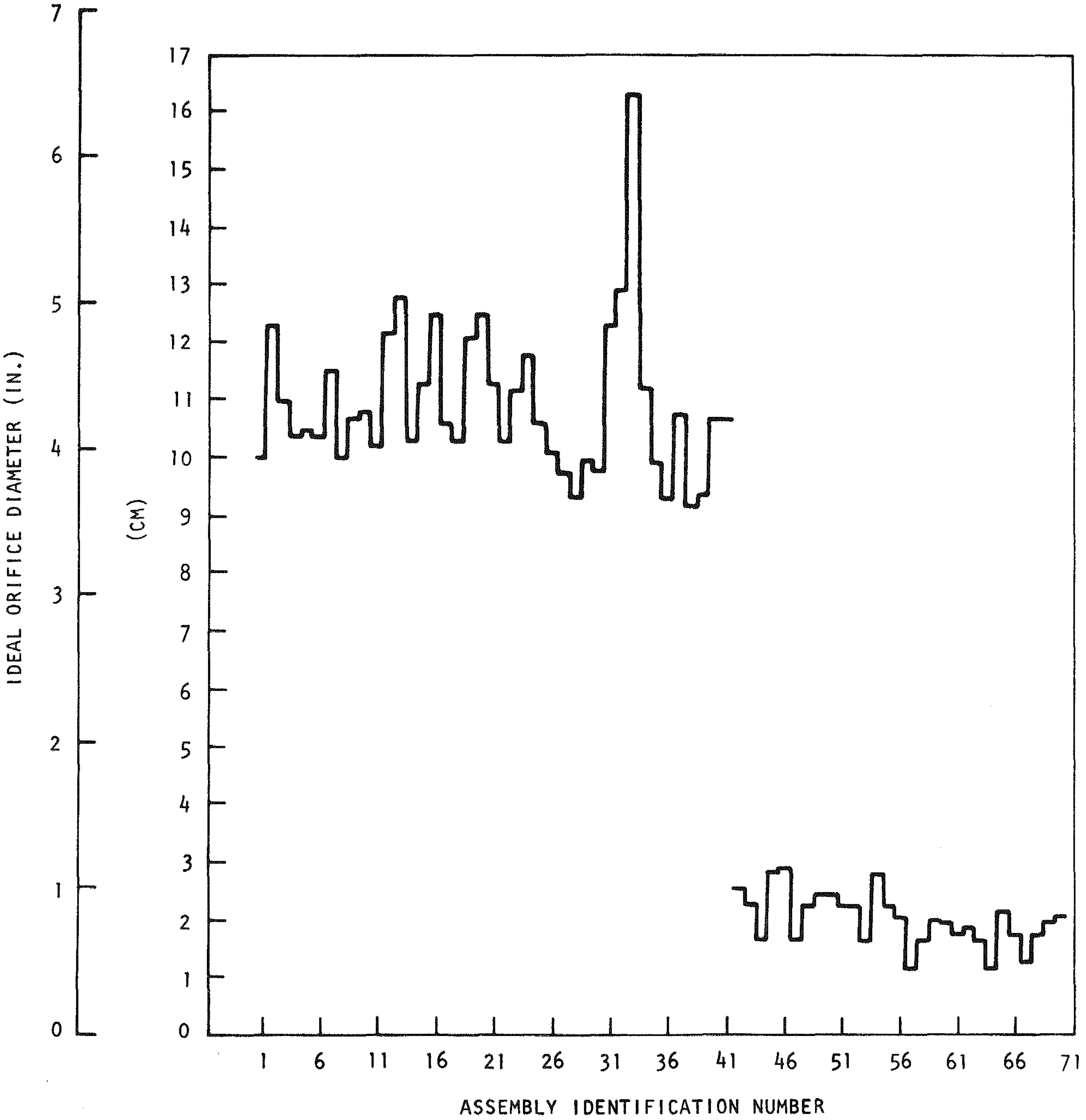

Fig. 9-7. Ideal diameter sizes for core and radial blanket assemblies during third cycle (500 to 750 days)

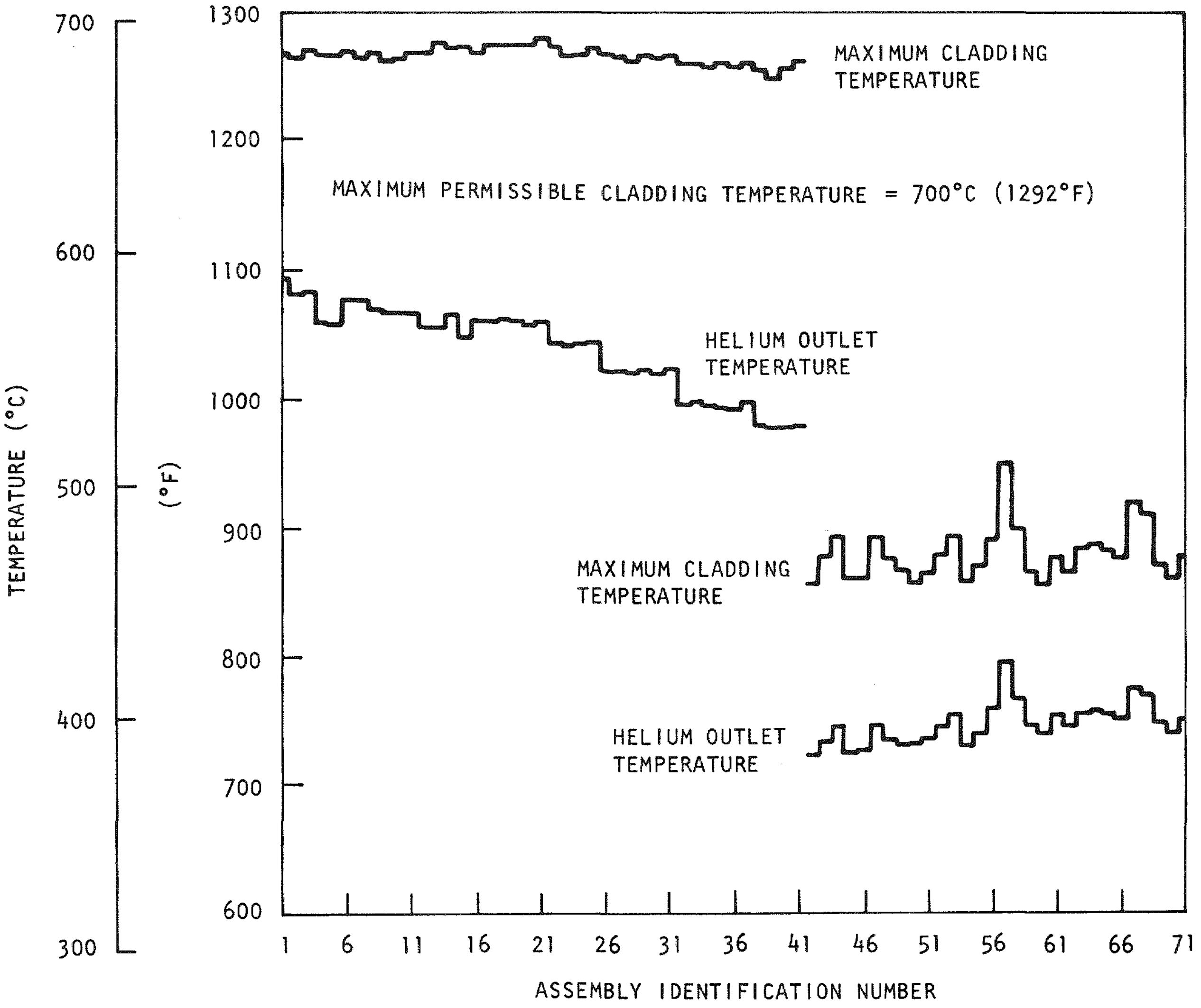

Fig. 9-8. Maximum cladding temperature and helium outlet temperature at beginning of first cycle (time = zero) for scheme A

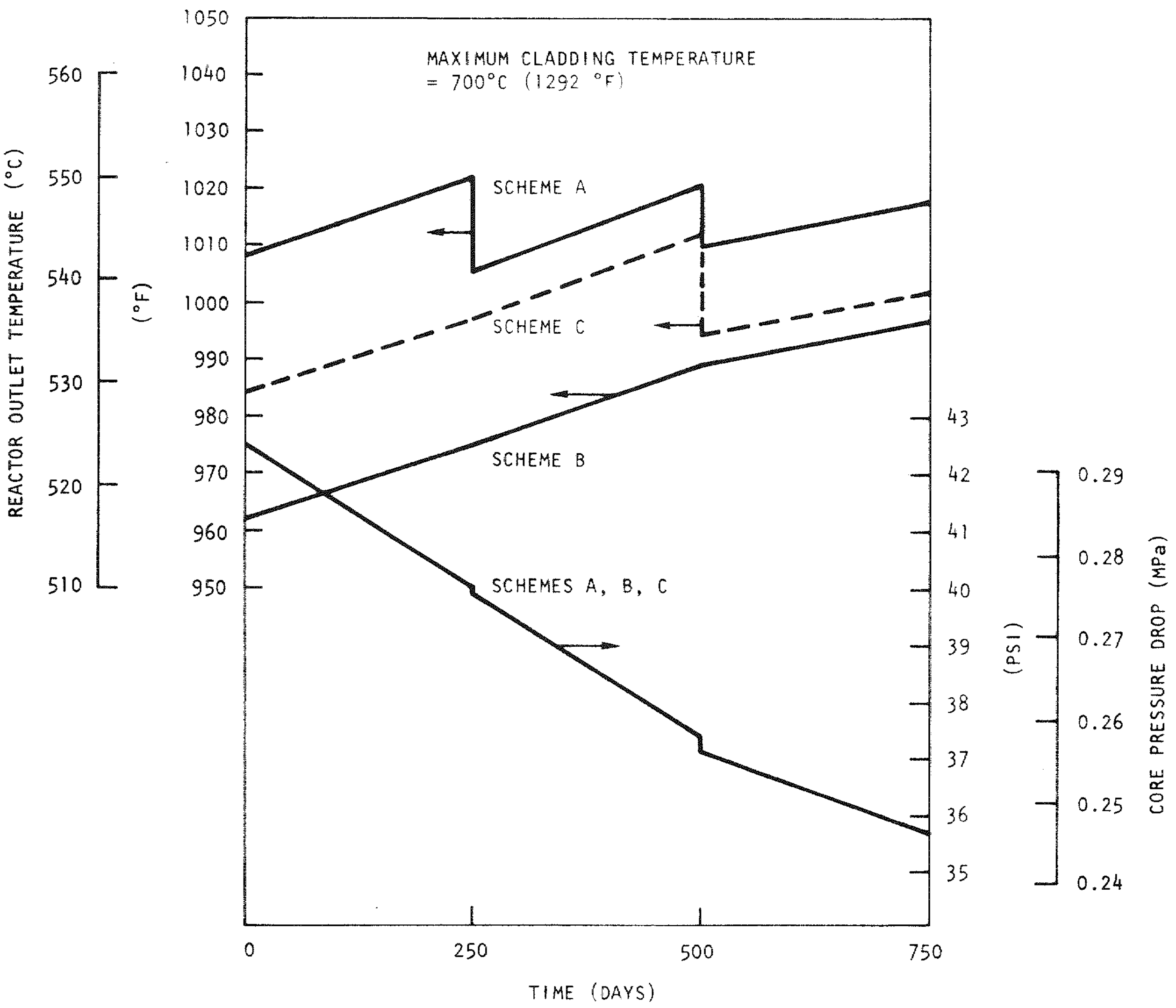

Fig. 9-9. Reactor mixed-mean outlet temperature and pressure drop as a function of time between refueling

core pressure drop decreases. As reported by Ref. 9-9, this behavior is also observed in the case of LMFBRs and requires further investigation (the core pressure drop for schemes A, B, and C are identical, as shown in Fig. 9-9).

In scheme B, the orifices are not replaced during the life of a given assembly, and the orifice sizes for the core and radial blanket assemblies are assumed to be large enough to limit the maximum cladding temperature to 700°C during the life of the assembly. The orifice size for each assembly is the largest of the values shown in Figs. 9-5 through 9-7. As a result, the reactor outlet temperature in scheme B is considerably lower than that in scheme A, (Fig. 9-9); the core pressure drop is the same as that in scheme A. The variations in maximum cladding temperature and reactor outlet temperature for scheme B are shown in Fig. 9-10 for the beginning of the first cycle. In scheme C, the orifices are replaced every 2 yr after new core assemblies have replaced the original cores. The maximum cladding temperature and helium outlet temperature at the beginning of the first cycle for scheme C are shown in Fig. 9-11. This scheme results in higher maximum cladding and core outlet temperatures than scheme B; however, they are lower than the corresponding temperatures in scheme A (Fig. 9-9).

The results of this preliminary analysis emphasize the importance of core orificing, and the study can be extended to include various fuel management concepts and enrichment zoning. The capability of GACOOL to accept generalized three-dimensional power distribution is important for realistic prediction of core performance during off-design conditions.

9.2. SYSTEM INTEGRATION

A preliminary draft of the GCFR System Integration Plan has been informally submitted to ERDA for comment. It is expected that written comments will be received from ERDA in time to be incorporated into the formal draft, which is scheduled to be submitted on September 30, 1977. A

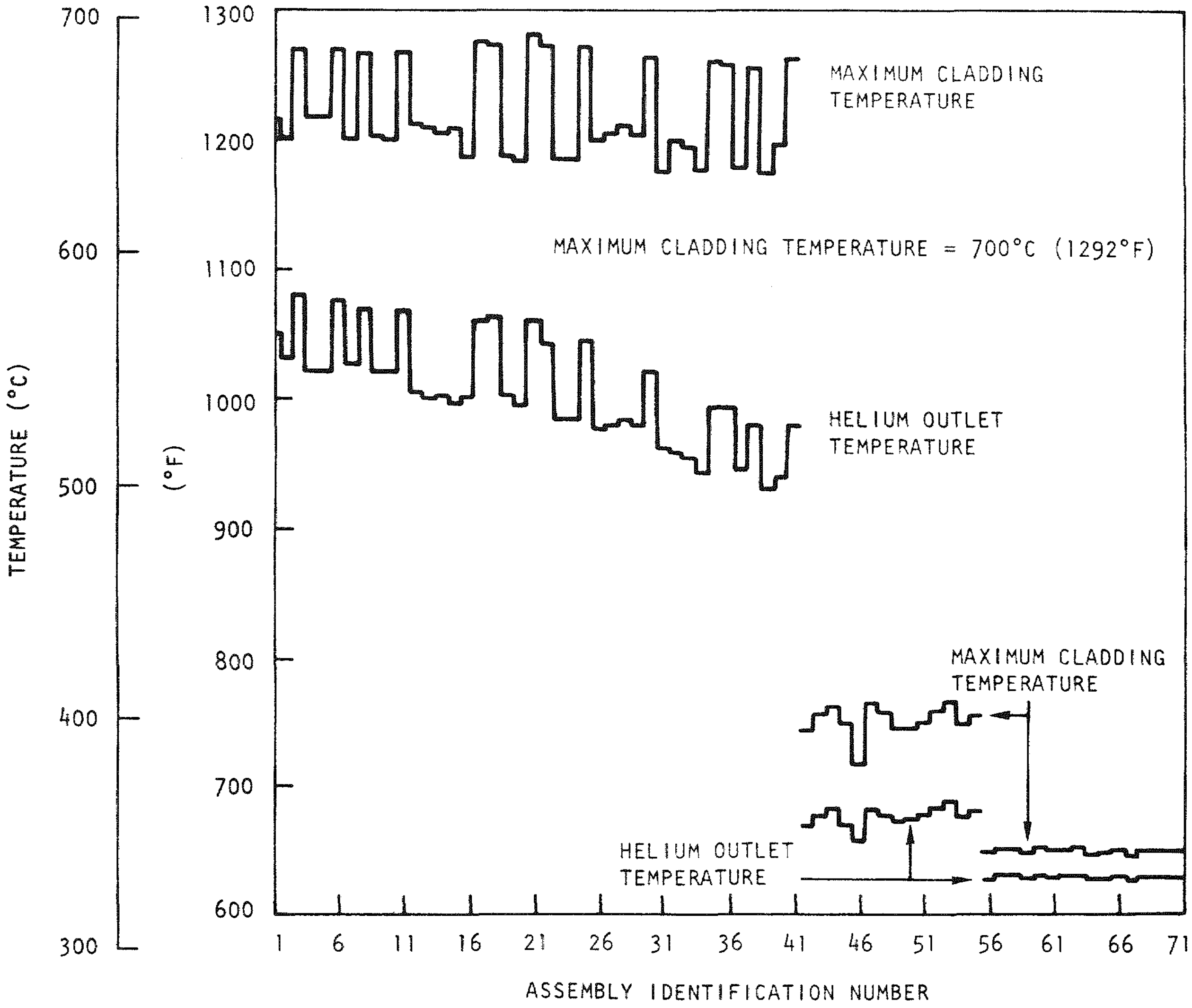

Fig. 9-10. Maximum cladding temperature and helium outlet temperature at beginning of first cycle (time = zero) for scheme B

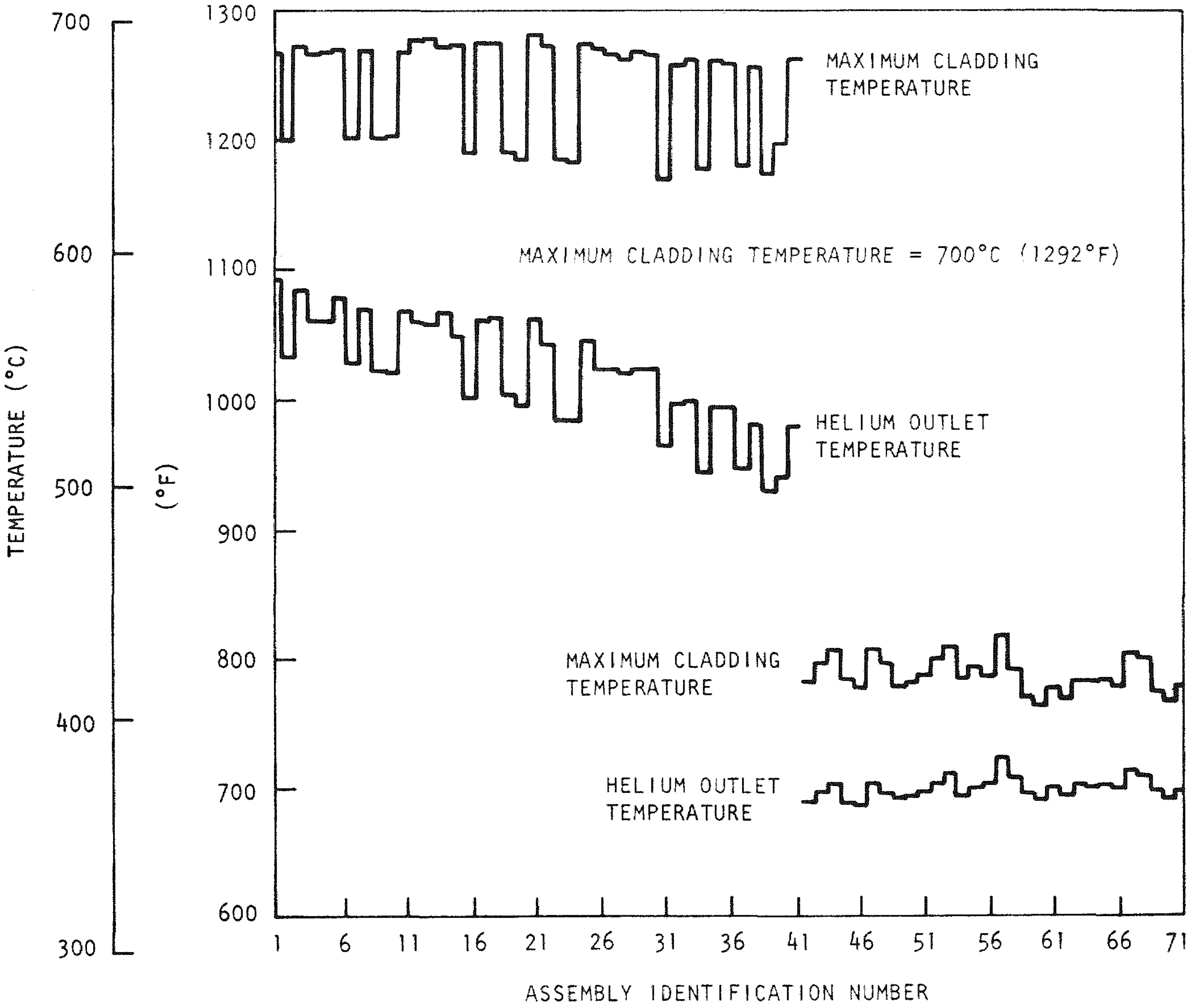

Fig. 9-11. Maximum cladding temperature and helium outlet temperature at beginning of first cycle (time = zero) for scheme C

substantial portion of this quarter's effort was spent on detailed work planning, coordination, and reorganization to strengthen overall system integration capabilities.

9.3. DOCUMENTATION MANAGEMENT

The purpose of this subtask is to develop and implement effective documentation management. General design descriptions of NSS systems and the overall demonstration plant will be prepared and collected in a design (baseline data) book.

During this quarter, preliminary work on the design (baseline data) book was completed. A table of contents and sample formats were prepared, and representative data were reviewed. In addition, a summary description of the design and document control system for the GCFR demonstration plant was submitted to ERDA.

REFERENCES

9-1. Medwid, W. A., "GACOOL - A Computer Program for Gas-Cooled Fast Breeder Reactor Core Thermal-Hydraulic Performance Analysis," General Atomic, unpublished data.

9-2. "Gas-Cooled Fast Breeder Reactor Quarterly Progress Report for the Period February 1, 1977 Through April 30, 1977, ERDA Report GA-A14358, May 1977.

9-3. Ojima, M., "Radial Blanket Power Distribution for the 300 MW(e) GCFR-Demo," General Atomic, unpublished data.

9-4. Perkins, R. J., "Power Density in the Radial Blanket Near the Core-Blanket Interface," General Atomic, unpublished data.

9-5. Rodrigues, V., "Radial Blanket Power Distribution - 300 MW(e) Demo - Low ΔP 4 Yrs. Residence Time," General Atomic, unpublished data.

9-6. Rodrigues, V., and C. J. Hamilton, "1-D Study of the Axial Power Distribution in the GCFR Demo Plant," General Atomic, unpublished data.

9-7. "300-MW(e) Gas-Cooled Fast Breeder Reactor Demonstration Plant," General Atomic Report GA-A13045, July 15, 1974.

9-8. Ojima, M., "Radial Blanket Power Distribution," General Atomic, unpublished data.

9-9. Carelli, M. D., and R. A. Markley, "Preliminary Thermal-Hydraulic Design and Predicted Performance of the Clinch River Breeder Reactor Core," ASME Paper No. 75-HT-71.

10. COMPONENT DEVELOPMENT (189a No. 00586)

10.1. REACTOR VESSEL

The scope of this subtask is to ensure that the design of the PCRV and related components which contribute to the integrity of the pressure boundary is satisfactory and to test critical component configurations to make certain that they attain the design objectives. This subtask will demonstrate by analyses and tests that the PCRV and its penetrations and closures meet the design criteria, and it will also ensure that (1) the design of the thermal barrier satisfactorily protects the liner and PCRV from the effects of high temperatures, and (2) the flow restrictors for the large penetrations can be developed to limit the flow of helium from the primary coolant systems to acceptable levels in the event of structural failure of a penetration or closure component.

During the last quarter, a cost comparison study of two PCRV configurations with resuperheat steam generators and nonresuperheat steam generators was conducted. Each PCRV configuration has a reverse flow helium circulator with a bypass duct leading the coolant from the steam generator to the inlet of the helium circulator plenum. Configuration C-2 (Fig. 10-1) does not have a resuperheater, and configuration C-3 (Fig. 10-2) has a resuperheater. The costs of the two PCRV configurations will be integrated with the plant costs.

A 1/15-scale model of the steam generator cavity closure was pressure tested at ORNL. The tests were performed for the elastic and inelastic stress ranges and for overpressurization to produce structural failure. At a pressure of 75.8 MPa (11,000 psig) (∿7 maximum cavity pressure), testing was suspended; no structural distress had been shown by the model.

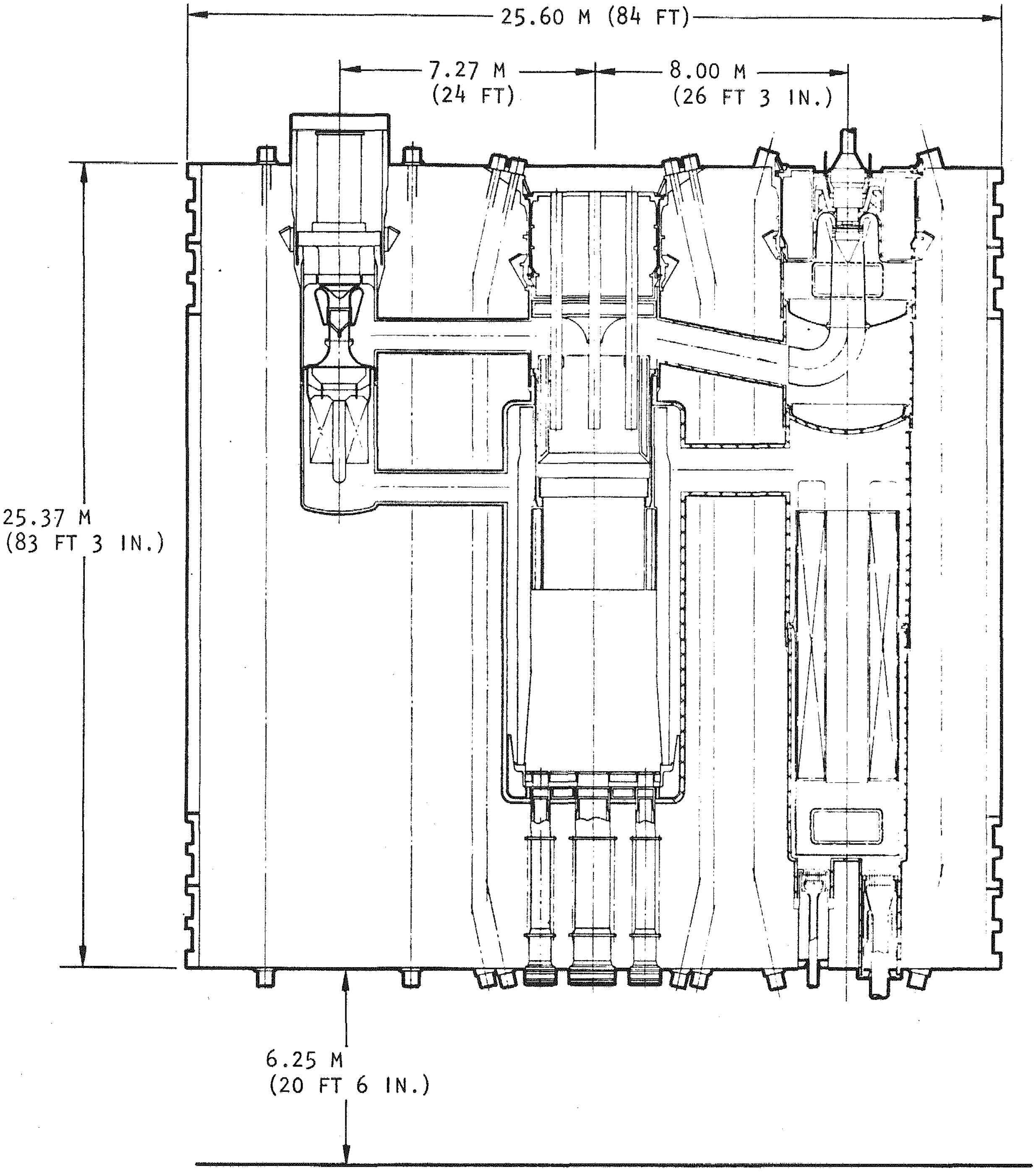

Fig. 10-1. PCRV configuration C-2 (with nonresuperheat steam generator)

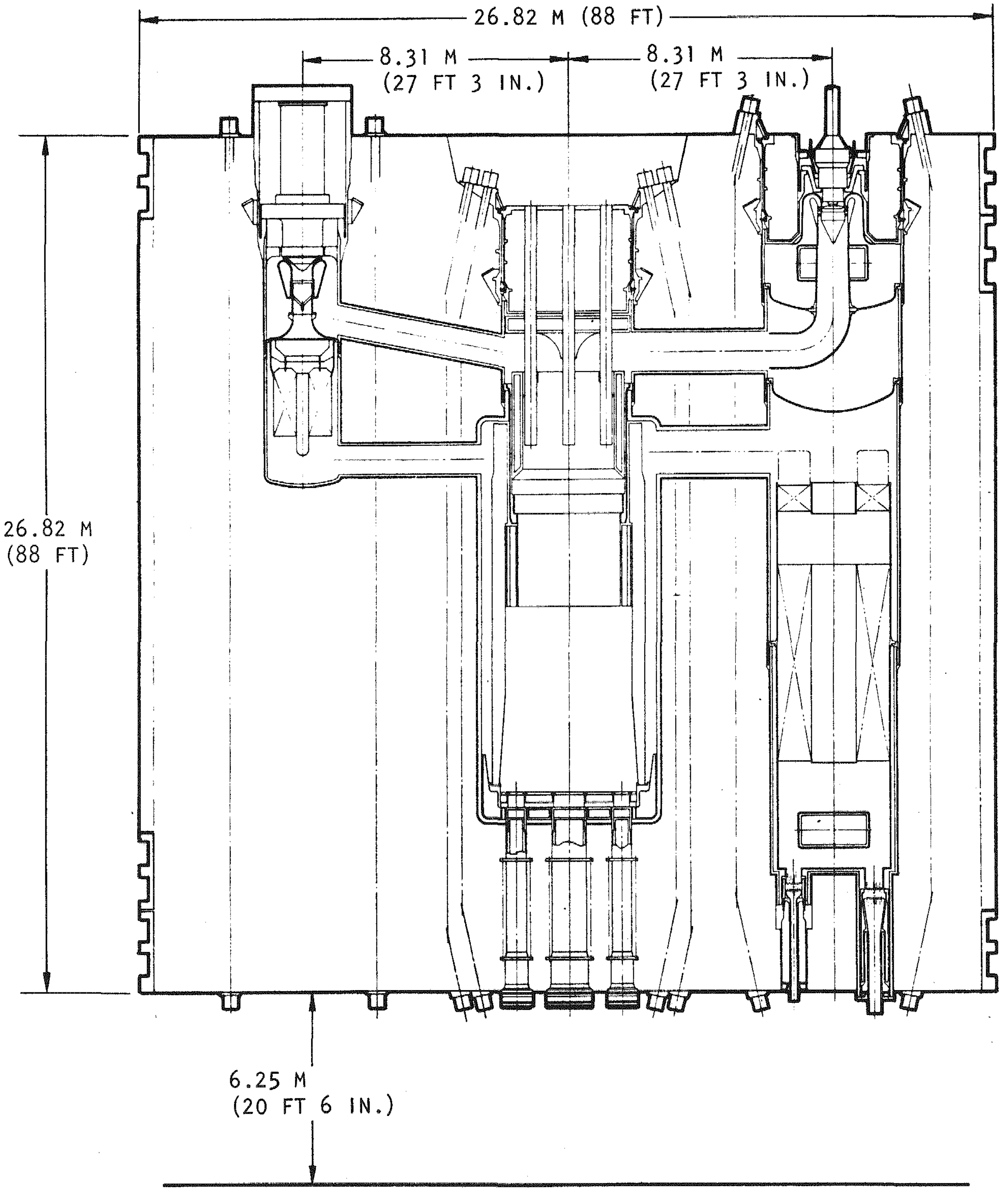

Fig. 10-2. PCRV configuration C-3 (with resuperheat steam generator)

During this quarter, layout studies were undertaken for PCRVs with helium circulators using extreme drives mounted in the bottom head. These studies were conducted to ensure that (1) the demonstration plant has the same basic arrangement as the commercial size plant and (2) the helium circulator is designed to be tested at full power in the primary loops after installation. Since the power for helium circulators increases with an increase in reactor power, the power required for the helium circulators of the commercial size GCFR plants necessitates very large drive motors. Placing the drive of the helium circulator external to the pressure boundary eliminates the space restrictions for the circulator in the cavity closure. In addition, testing of the primary coolant loops at full power suggests that the circulators should have external drives, and it was proposed that these circulators be placed in the bottom head of the PCRV.

The PCRV configuration shown in Fig. 10-3 was prepared with a horizontal circulator cavity in the bottom head. The external drive is an electric motor, although a steam-driven turbine can be used. Since the circulator cavities interrupt the wire-winding channels of the circumferential prestressing system, a system of horizontal tendons was used to produce prestressing to the concrete (Fig. 10-4). There were severe problems in routing and placing the tendons, and although a layout study indicated that a system of horizontal tendons might be feasible, a three-dimensional stress analysis would be required to conclude whether it were possible. Routing of the ducting for the primary coolant loops is unique for the new PCRV configuration (Figs. 10-4 and 10-5) and results in a large number of vertical tendons with congestion on the upper head.

A second PCRV configuration, D-2, which has a vertically mounted helium circulator mounted in the bottom head at the lower surface of the PCRV was examined. Figure 10-6 shows a vertical cross section of the PCRV with routing of the coolant ducts; the helium circulator has the external drive mounted in the same cavity as the auxiliary helium circulator. Figure 10-7 shows the plan view of this PCRV design, the routing of the ducts, and the placement of the tendons. An advantage of this configuration over that

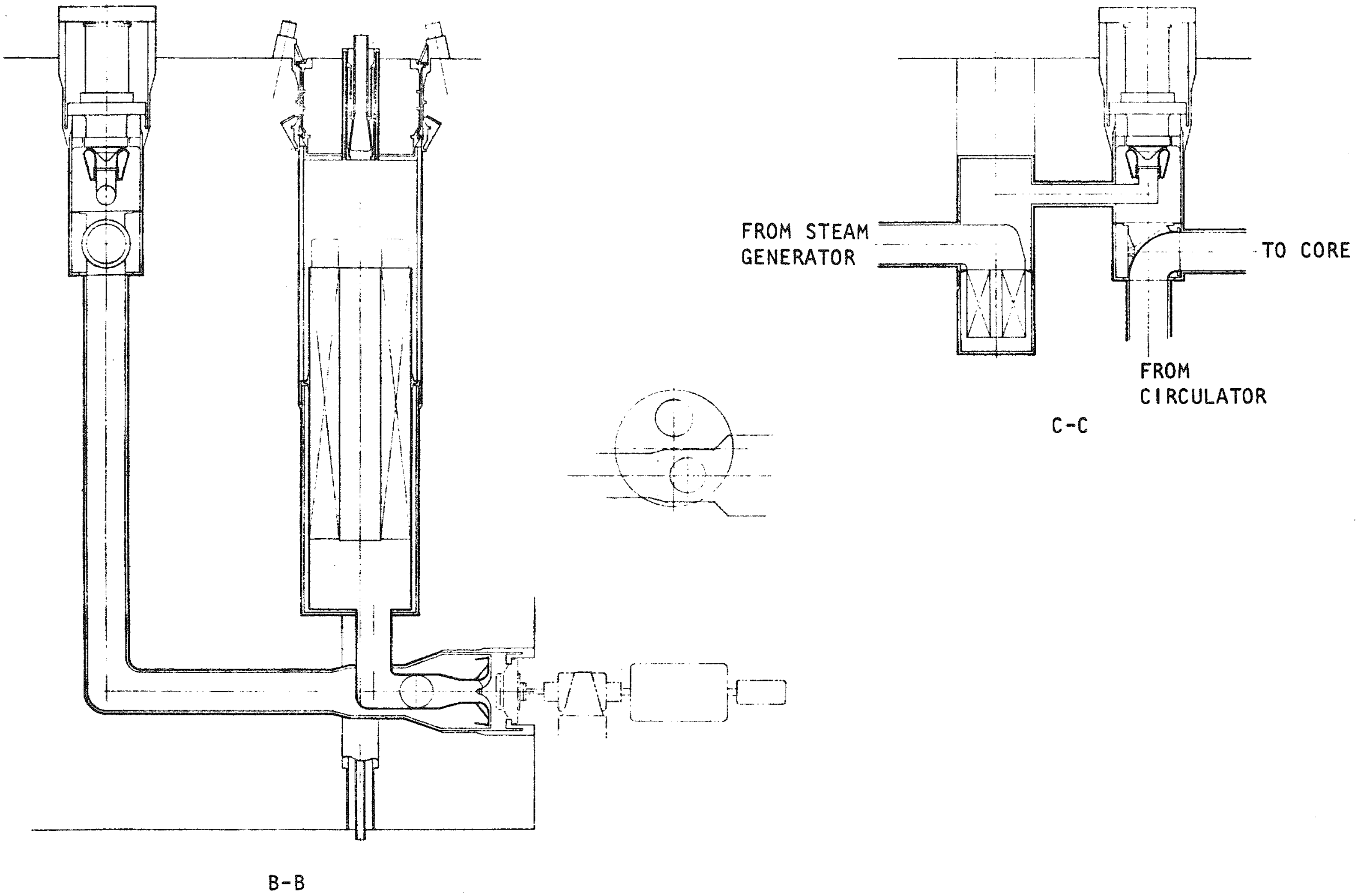

Fig. 10-3. PCRV configuration D-1 (with external drive and horizontal helium circulator mounted in bottom head)

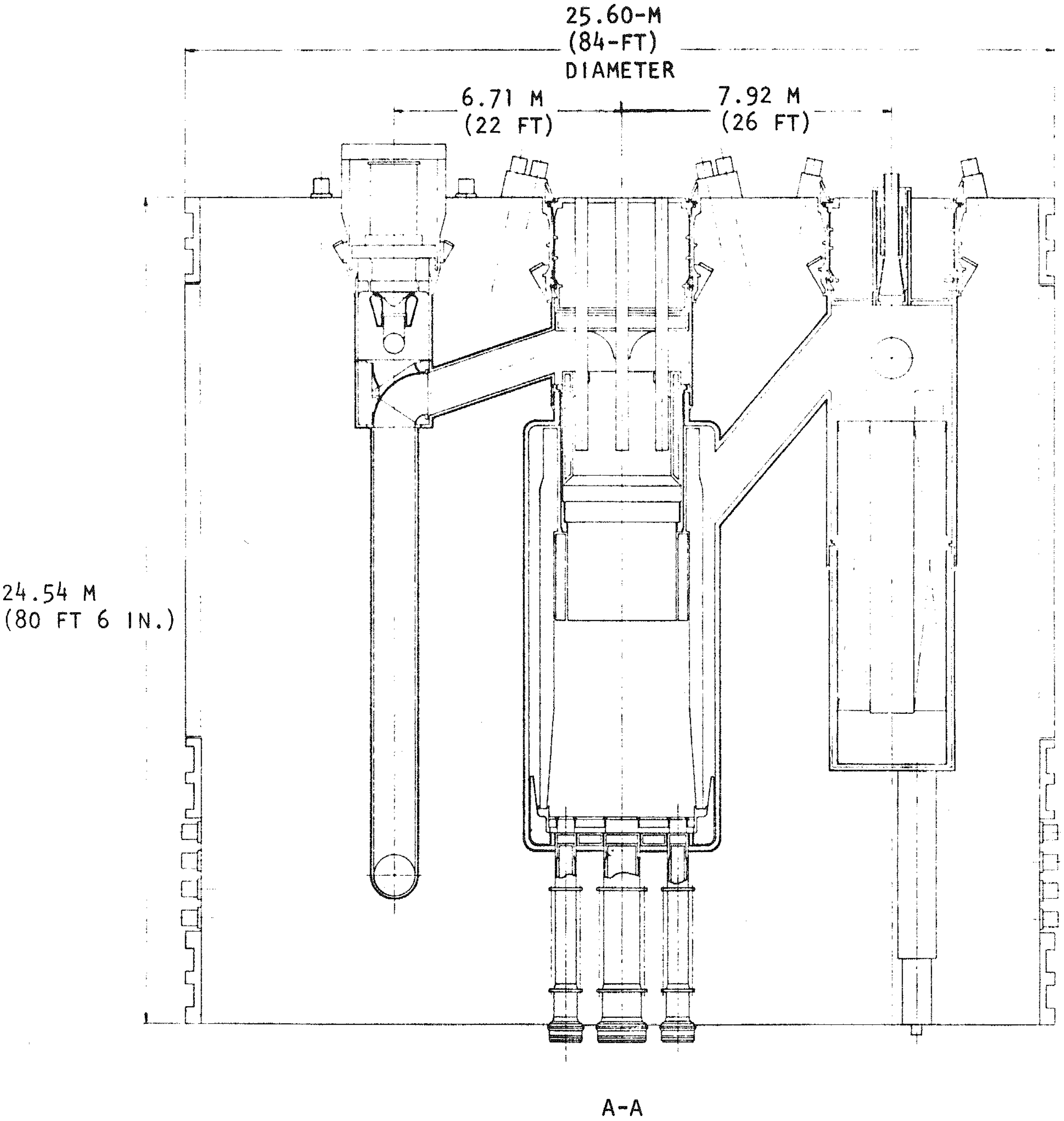

Fig. 10-4. Routing of primary coolant ducts for configuration D-1

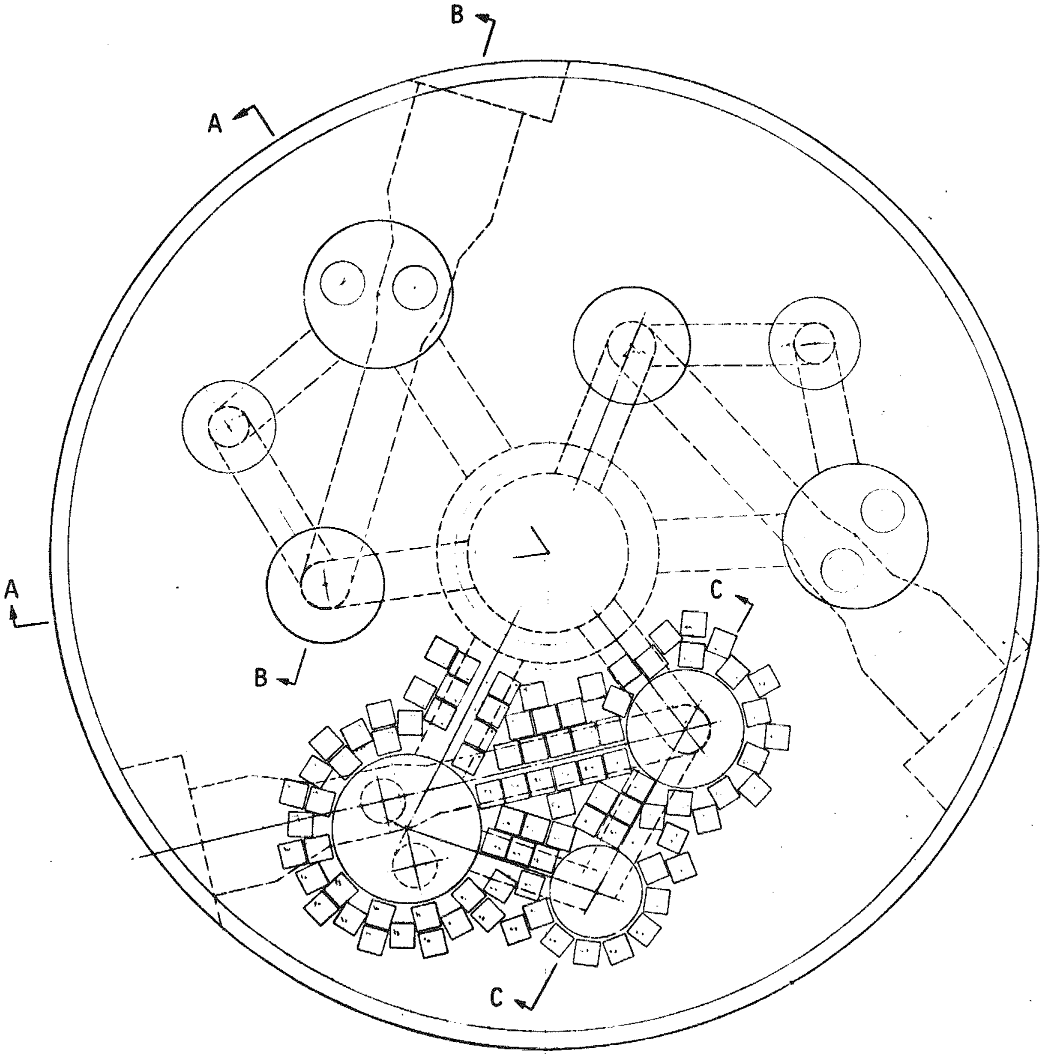

Fig. 10-5. Plan view of configuration D-1

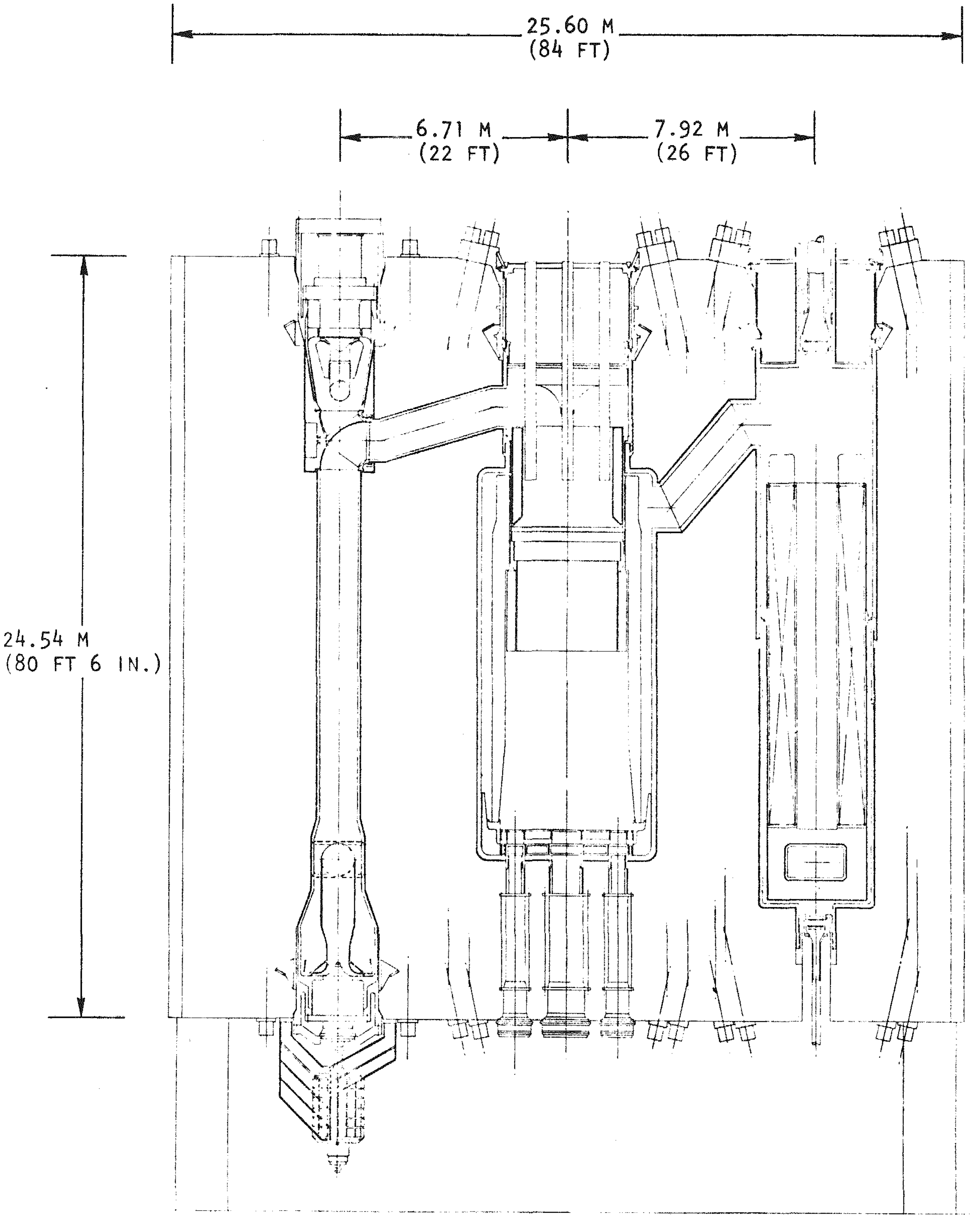

Fig. 10-6. PCRV configuration D-2 (with external drive and vertical helium circulator mounted in bottom head)

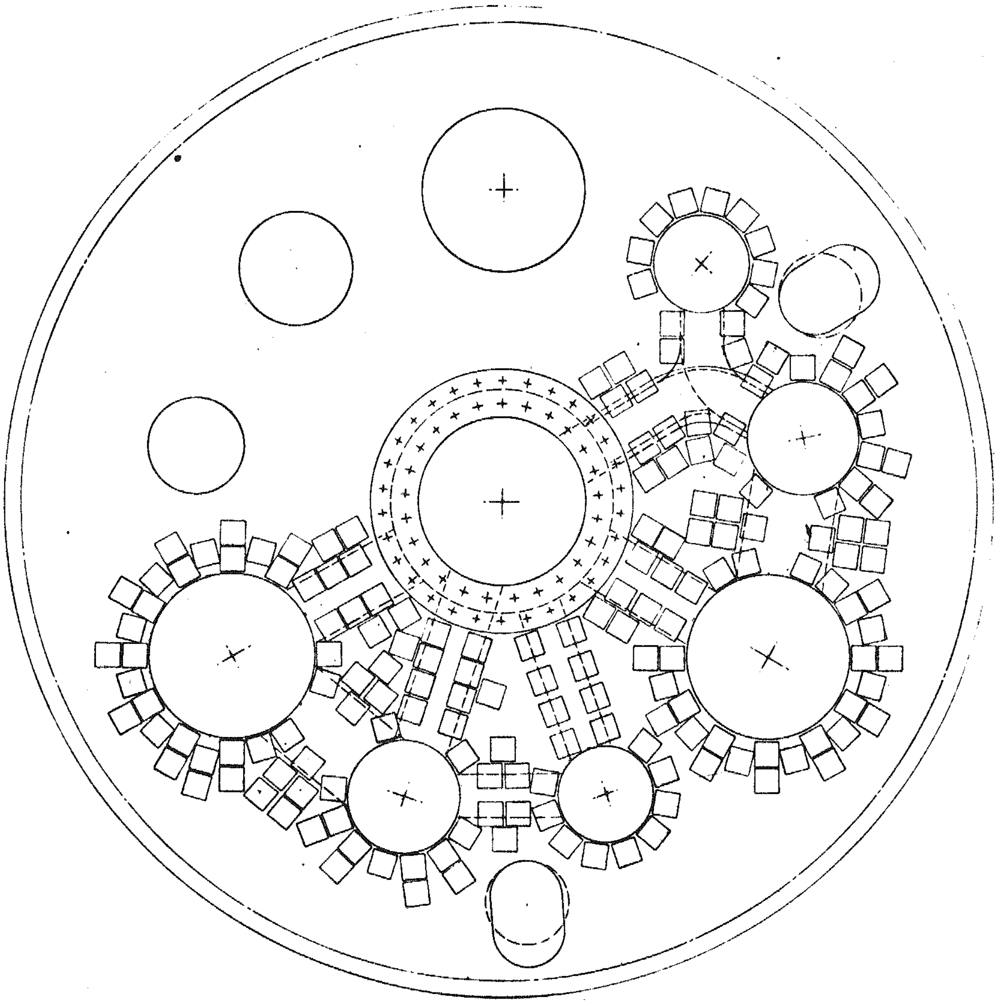

Fig. 10-7. Plan view of configuration D-2

with the horizontally mounted circulator in the side of the PCRV is that the circumferential prestressing system is not interrupted and does not involve using a horizontal system of tendons in the lower head. These configurations are being evaluated in conjunction with a study to select a design for helium circulators and drives.

The first test of the 1/15-scale model of the steam generator cavity closure showed that the closure model could sustain seven times the maximum cavity pressure of 10.1 MPa (1460 psi) without any failure. To establish a better safety factor and failure mode, GA has requested that ORNL proceed with fabrication, pretest analysis, and testing of a reduced-depth version of the 1/15-scale model. This model is identical to the previously tested model except that the depth is halved and the shear console inside the model is removed. It is hoped that this model will reach its ultimate strength in the test.

A conceptual design study for a molten core retention and cooling system was initiated. The objective of this study is to identify and develop a viable safety backup system which, if required, would protect the public from the consequences of a postulated core meltdown accident. Approaches ranging from simple retention systems which rely mainly on the inherent retention capability of the PCRV, containment, and surrounding soil to engineered core debris retention devices with active heat removal systems was considered. Since the design of such systems is dependent on the scenario after a core meltdown, a conservative approach was adopted to cover the expected range of uncertainties. The approach initially adopted for the GCFR is to retain the debris within the vessel using a crucible and forced cooling system.

Several core retention concepts have been designed and are currently being analyzed for their thermal behavior, secondary criticality margin, and shielding effectiveness. The concepts under investigation include a ceramic crucible, a sacrificial (melting) bed, and a metal bath. All configurations are designed to interface with and protect a single central refueling penetration.

The design criteria document for the PCRV cooling system (Ref. 10-1) was reviewed and issued.

10.2. CONTROL AND LOCKING MECHANISMS

Components for the conceptual design of the alternate core assembly locking mechanism described in Ref. 10-2 were sized to meet applied loading conditions. Because the core assembly must be secured to the grid plate to resist the separating action from gravity and pressure, a very large preloading force must be provided. Therefore the feasibility of having this requirement satisfied by the lock actuating machine is being explored.

Two locking machine grapple mechanism configurations were explored. One concept employed pneumatic power for the actuating motions, and the other was based on electric-motor-powered mechanisms. Both concepts are potentially feasible but are extremely complex owing to the numerous precisely controlled independent motions required in the lock actuation process. There are some questions on the degree of reliability which can be achieved with electrical position controllers and mechanical force producers because of the environment in which this mechanism must operate. Pneumatic-powered force producers are essentially insensitive to the environment but still require electrical position feedback and controlling devices. Remote location of the controllers introduces response and accuracy problems. A low-stiffness force-transmitting medium, such as a gas over long transmission lines or exposure of the lines to a large, sharp temperature gradient may cause such problems. Therefore, a different approach for securing the core assembly to the grid plate is being explored to alleviate the complexity of the lock actuating mechanism. Instead of resisting the gravitational and pressure forces using a highly loaded retaining device, a method of utilizing these separating forces to retain and securely clamp the core assembly to the grid plate is being investigated. Simplified low-force motions which require engagement of the primary retention mechanism could then be used in the remote lock actuation functions. Preliminary design layouts of this locking scheme indicate some encouraging possibilities. For example, it may be possible to

1. Eliminate the need for a lock actuation machine by utilizing the control rod drive installations as a mechanism path for operating surrounding and adjacent core assembly locks.

2. Eliminate the separate instrument tree concept by utilizing the control rod drive installations to support conduit paths for leading thermocouples into surrounding and adjacent core assemblies.

3. Accommodate the PES interconnections and monitoring lines in a separate, predrilled manifold plate located on top of the grid plate.

These possibilities are being investigated.

10.3. FUEL HANDLING DEVELOPMENT

Preparation of conceptual designs, descriptions, and analyses for the GCFR fuel transfer cask, lifting transfer cask, and transfer cask car(s) was initiated by Aerojet Manufacturing Company, and studies on the effects of core assembly handling methods and equipment were performed using initial data on assembly bowing. The interacting forces between core assemblies were determined, and a conceptual design of a spreading device was prepared. A design study was initiated on a scheme for refueling through a single PCRV bottom heat penetration.

10.4. CORE SUPPORT STRUCTURE

The purposes of this subtask are to assure the availability of structural analysis methods and to determine the materials mechanical behavior required for assessing the structural integrity of the GCFR core support structure under all anticipated operational and safety-related loading conditions in the GCFR environment.

During this quarter, a perforated circular plate with hexagonal penetrations was investigated. The concept of an equivalent solid plate with effective elastic constants was used, and the axial deflection at the center of the grid plate versus the width of ligament, including the ligament efficiency, was plotted.

10.4.1. Seismic Structural Analysis of GCFR Core Support Structure With Effects of Core Assemblies

A special task force has been organized to solve the core support structure seismic problem. For the theoretical approach, techniques to synthesize substructures to form a composite system will be used. Each substructure will be treated as a continuous structure, and the vibration modes or displacement functions of each substructure will be combined using generalized coordinates. The boundary compatibility will be handled using the displacements of the substructure relative to the interface coordinates, thereby avoiding a large number of LaGrangian multipliers. A dynamic model of the GCFR core support grid plate which uses solids of revolution as finite elements was developed for the finite element analyses, and the fuel and blanket assemblies are being modeled for the proposed configuration.

10.4.2. Grid Plate Thermal Analysis

A thermal analysis of the grid plate has been performed to predict radial and axial temperature distributions in the grid plate under steady-state, normal operating conditions at 100% power. Detailed gamma heating distributions from ORNL were used (Ref. 10-3).

10.4.3. Thermal Stress Analysis of the Grid Plate

Thermal stress analysis of the grid plate based on the temperature distribution discussed in Section 10.4.2 has been initiated. A finite element model with a two-dimensional axisymmetric solid element symmetric to the vertical axis is being used.

10.5. REACTOR SHIELDING ASSEMBLIES

The purpose of this task is to design and develop analytical methods and experimental programs to evaluate the reference design of the reactor shields. This evaluation is expected to cover nonuniform temperature distribution, material behavior, seismic effects, hydrodynamic tests, and structural analysis. Alternate shield configurations will also be studied to develop a satisfactory and optimized shield design.

During the previous quarter, preliminary plant layout criteria drawings for the upper, lower, and radial shielding were completed, and weight calculations for the present shield design were performed to provide information for the plant dynamic design. During this quarter, major emphasis was placed on two items: (1) design criteria and (2) inner shield design.

10.5.1. Design Criteria

Design criteria for the shield structure are being reviewed. These criteria are expected to cover but not be limited to

1. Residual ductility requirements.
2. Maximum permissible NDTS.
3. Gamma dose on tendon lubricant.
4. Maximum permissible nuclear heating.

10.5.2. Inner Shield Design

Based on the present structural criteria, the design life of the inner shield is less than the operating life of the GCFR plant. Thus, a provision in the mechanical design of the inner shield is required so that the inner shield could be replaced during the plant life if necessary.

Therefore, the inner shield is currently being designed to be consistent with the design capacity of the fuel handling machine and the size of the bottom head fuel penetration. Based on the present design configuration, the inner shield will be supported by the outer shield which in turn will be supported from either the bottom of the PCRV core liner or the core lateral liner. This configuration is being evaluated in terms of seismic design and ease of removal.

10.6. MAIN HELIUM CIRCULATOR, VALVE AND SERVICE SYSTEM

The purpose of this subtask is to develop the helium circulator, its service system, and the main loop isolation valve to demonstrate performance and reliability by testing under anticipated operating conditions. The overall objective for FY-77 is to initiate predesign and performance analysis of the circulator configuration, service system, and loop isolation valve. Work is continuing on the conceptual designs of an axial flow helium circulator driven by an axial flow steam turbine in series with the plant main turbine. The initial design consisted of a single-stage integral circulator on a common shaft with a single-stage steam turbine drive. However, after reviewing the design parameters, safety requirements, requirements for commonality between demonstration plant and commercial plant, test facility requirements, and preoperational hot flow tests in the reactor, it was decided to evaluate a number of alternate circulators and drive systems. Integral designs with the circulator and drive motor on a common shaft and external drive motors on a separate shaft were investigated.

Conceptual drawings were made of (1) a two-stage axial flow circulator driven by a two stage turbine using the same bearing housing design as that for the single stage circulator (Fig. 10-8); (2) a two-stage circulator driven by a two-stage turbine in a series flow external arrangement (separate shaft and housing) (Fig. 10-9); (3) a centrifugal flow circulator driven by a multistage parallel flow turbine in an external arrangement (Fig. 10-10); and (4) a centrifugal flow circulator driven by an external electric drive motor (Fig. 10-11). Preliminary sizing of the circulators

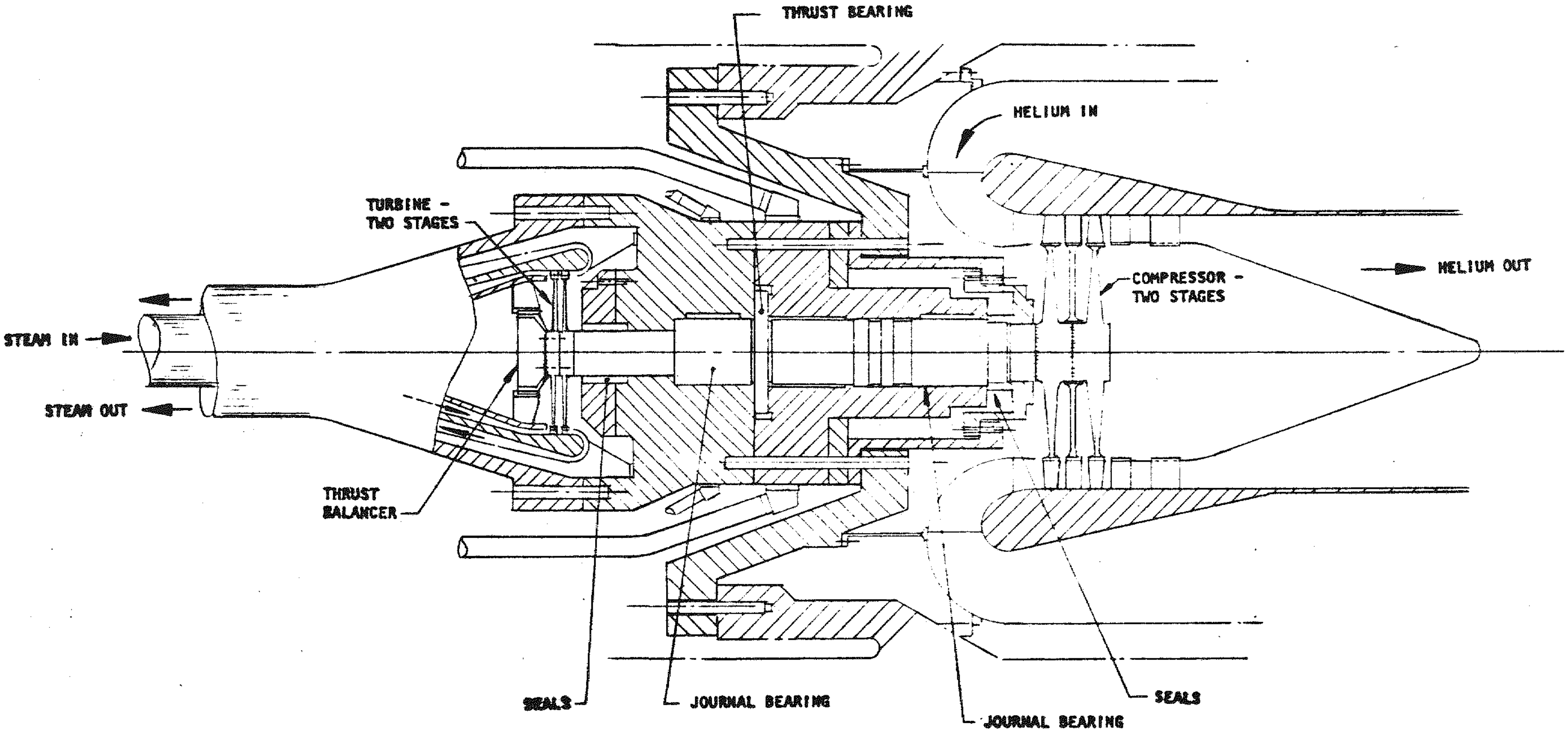

Fig. 10-8. Schematic of integral design series flow circulator

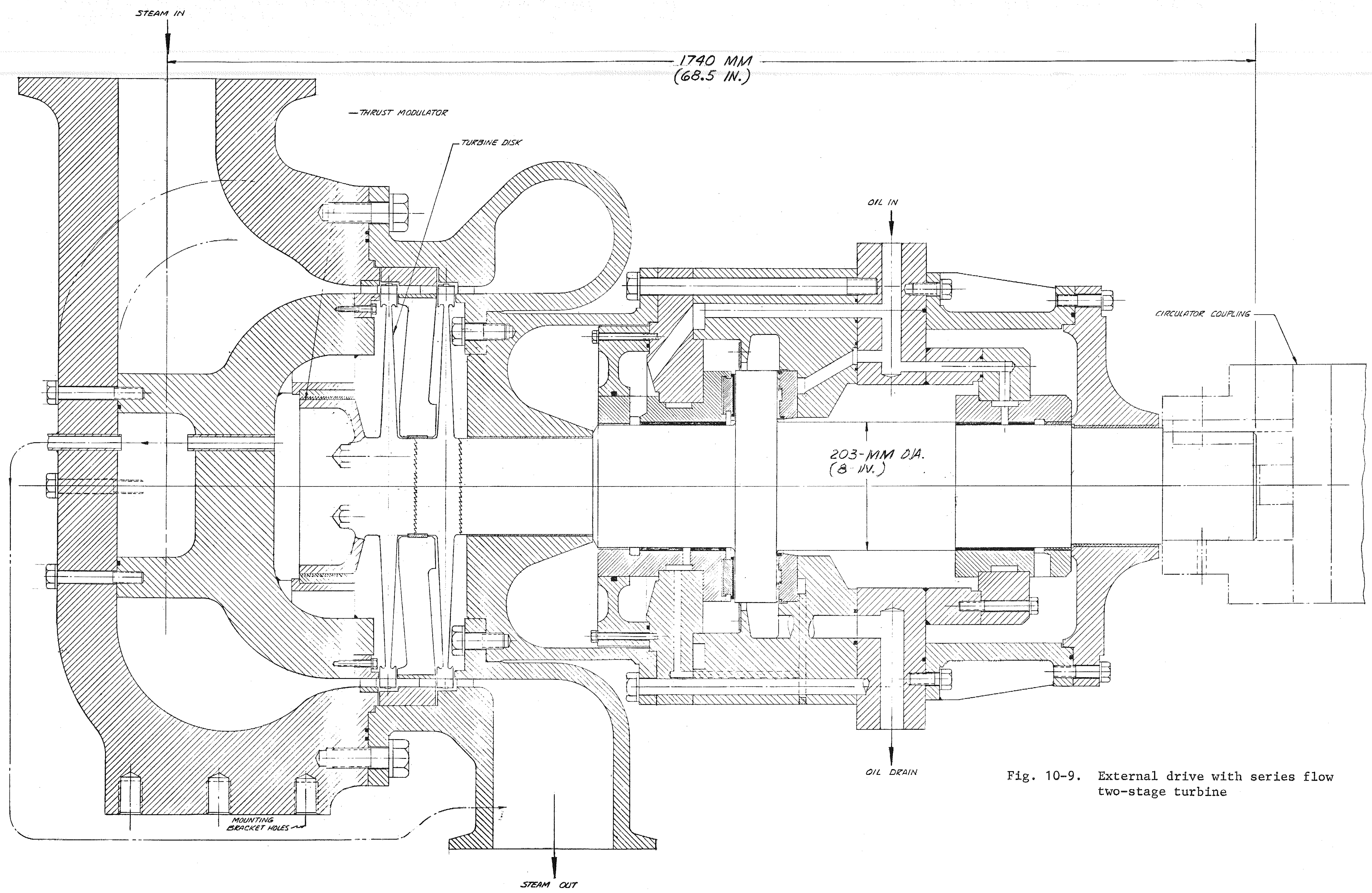

Fig. 10-9. External drive with series flow two-stage turbine

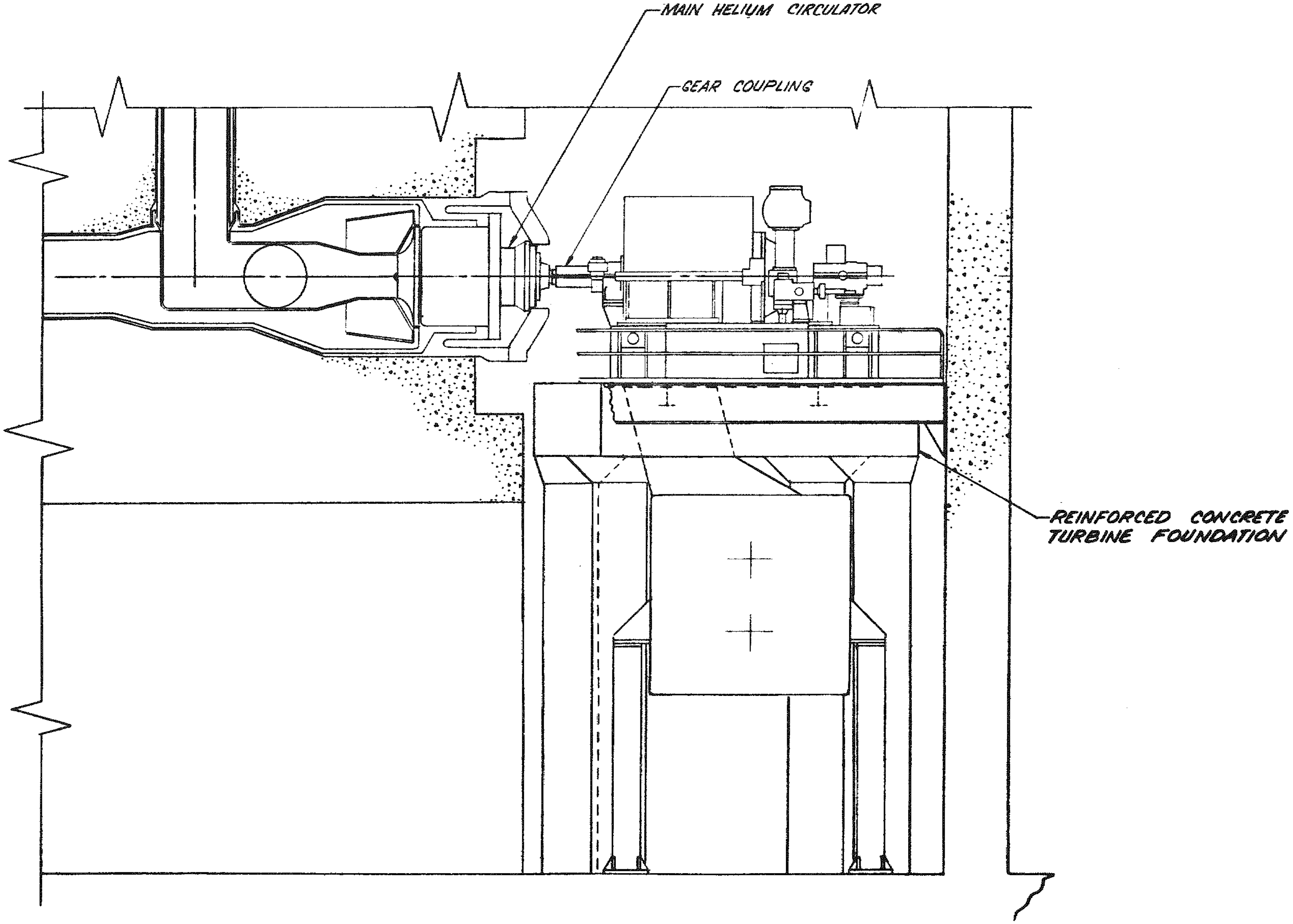

Fig. 10-10. Multistage condensing turbine installation

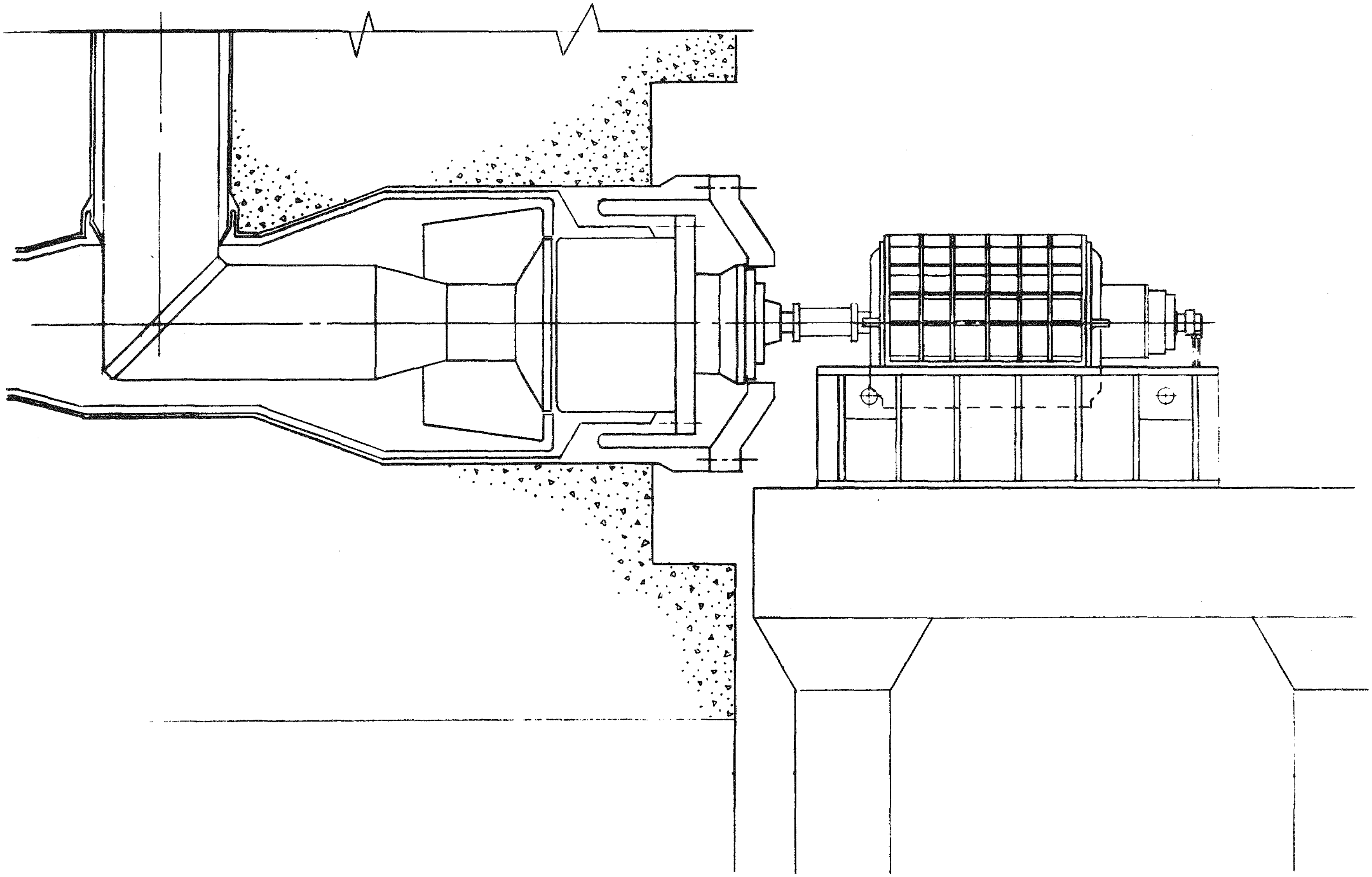

Fig. 10-11. Electric motor drive (horizontal installation)

for all four configurations was made based on a new set of design conditions with a circulator pressure rise of 0.415 MPa (60 psi). This pressure rise is based on a system design study to obtain similar conditions for the 300-MW(e) demonstration plant and a larger commercial plant.

The two-stage circulator and two-stage turbine drive have much lower stress levels than the single-stage designs, and most of the critical design parameters on the blades have been changed to more conservative levels in the two-stage design. The bearings, shaft, and bearing housing are basically the same for the single- and two-stage machines, but the rotating speed is reduced from 8400 rpm for the single-stage design to 6000 rpm for the two-stage design. The design of each stage of the two-stage circulator is similar to that for high-temperature gas-cooled reactor (HTGR) circulators and conventional multistage turbine designs. Optimization studies for this design are continuing.

A multistage steam turbine similar to the types used to drive boiler feed pumps might be used. This type of turbine can operate in series using steam from the steam generator or in parallel with extraction steam from the main turbine generator.

The electric drive motor arrangement consists of a single-stage radial flow compressor which is within the state-of-the-art. However, to obtain a desirable overall diffuser diameter, it is necessary to use three rows of cascades and a 90-deg turn into the final diffuser section; an external drive train is required to obtain variable speed. One drive train option consists of a constant speed (3600 rpm) electric motor connected via a fluid coupling to the circulator. An alternate drive train would use a constant speed motor to drive an alternator through a fluid coupling. The power generated by the alternator would then be supplied to an electric motor drive connected directly to the circulator. Variable circulator speed would be obtained by variable alternator speed and thus, the frequency delivered to the drive motor.

Since the circulator drive unit is likely to be external to the PCRV, studies were initiated to evaluate both oil and water bearings for the alternate circulator concepts. Layout drawings of the PCRV illustrating horizontal and vertically oriented circulators were evaluated, and it seems possible to install a centrifugal circulator in a horizontal installation. However, it is a more complicated design, which may result in a more expensive vessel than that of the vertical arrangements because of the difficult design and installation of tendons.

10.6.1. Series Flow Turbine Drive

A two-stage circulator driven by an external two-stage turbine in series with a main plant turbine has a number of advantages. Any future variations of performance requirements will have a minimal effect on the overall concept, and the design satisfies demonstration plant and commercial plant requirements. The compressor and turbine are well within the state-of-the-art of conventional technology, and the performance predictions are conservative. The external drive arrangement is very compact compared with electric drive and multistage parallel flow turbines and fits in a vertical and a horizontal installation. Only the compressor needs to be tested in a test facility because the turbine can be separately tested by a turbine manufacturer. The test facility can therefore be simplified by using a direct electric motor drive or gas turbine drive. Hot flow tests in the reactor can be accomplished in the same fashion. High plant cycle efficiency, compactness, and the safety of using residual heat for steam generation during emergency shutdown can be maintained without outside power and without interfering with main plant turbine operations. The main disadvantage of the external drive is that it is more complicated than the integral design.

A high-pressure, barrel-type turbine drive design was formulated from a large KWU main turbine generator set. This multistage drive turbine is connected in series with the main steam but mounted outside the PCRV on a foundation adjacent to the circulator penetration in the side of the PCRV (Fig. 10-12).

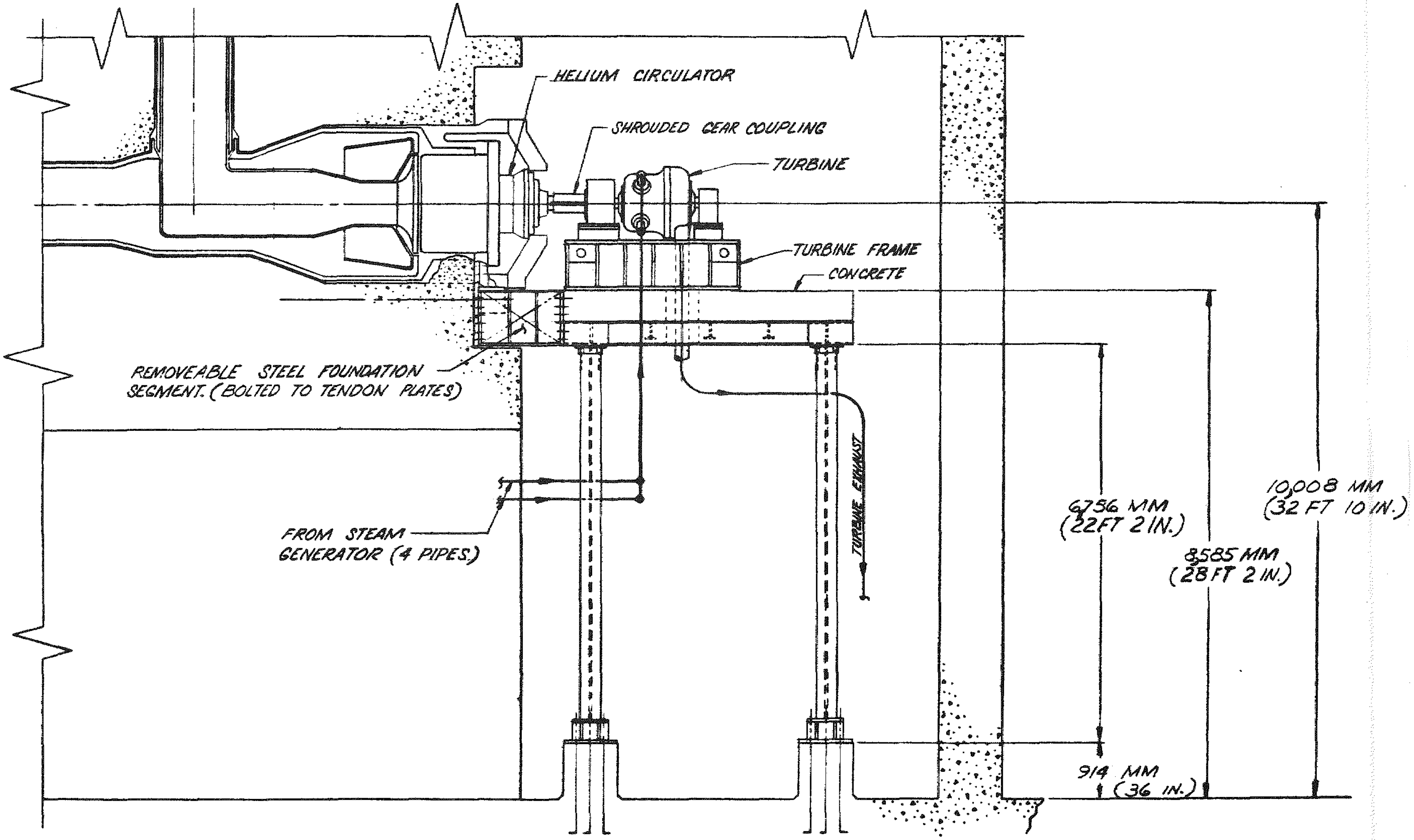

Fig. 10-12. High-pressure barrel type turbine installation

Vibrations in the turbine and compressor blades from aerodynamic and mechanical loads in the circulator are being evaluated. Two- and three-dimensional analyses will be made of all possible natural frequencies which may occur in various partial sections of the blades. Such analyses are desirable for a machine which is to be operated continuously for many years without being disassembled for inspection or repair. These analyses will enable improvement of the blade characteristics.

10.6.2. Conventional Steam Turbine Drives for the Main Helium Circulator

Conventional steam turbine mechanical drives similar to those used to drive boiler feed pumps in fossil-fired power plants are being considered as the main helium circulator drive for horizontal installations. This type of turbine can operate on low-pressure steam from the main turbine generator or high-pressure steam from the superheater. It has multiple stages, exhausts to a condenser, and is capable of variable-speed operations.

A vertical shaft machine manufacturer has not been identified, and only a turbine with a throttle pressure up to 10.3 MPa (1500 psia) for full nozzle arc admission has been located. Consequently, information on conventional horizontally mounted boiler feed pump drive turbines was obtained and used to prepare equipment outline drawings. These drawings were used to formulate conceptual equipment layouts of the multistage turbine, condenser, and foundations required for a series or a parallel circulator drive. Flow diagrams have also been prepared.

A list of the possible multistage steam turbine drive concepts for the main circulator has been formulated. There are nineteen parallel and one series concepts, all of which appear to be workable. A tentative ranking method is being developed to reduce the number of possibilities to a practical quantity.

10.6.3. Electric Motor Drive

An electric-motor-driven circulator with a single-stage radial flow compressor could be used as the main circulator drive on the GCFR. The GCFR helium flow/pressure rise requirements are satisfied by a 3600-rpm electric motor driving a 1.53 m (5-ft) diameter radial flow impeller. Oil-lubricated bearings would be used.

Several electric drive circulator arrangements and speed control systems have been investigated:

1. Electric motors either submerged in high-pressure helium at PCRV pressure (Fig. 10-13) or located external to the PCRV (Fig. 10-11) and driving the compressor through high-pressure rotating shaft seals.
2. Circulator speed control including fluid couplings, variable compressor guide vanes, and variable frequency power supplies (solid state systems and motor generator sets).
3. Backup drives such as pony motors, alternate power sources, etc., for use in case of failure of the main drive system.

Various options for start-up, speed control, and frequency conversion were also investigated.

The major problem areas which still need to be fully addressed are as follows:

1. Electric motor development. Some motor designs have been made. The mechanical requirements of high overspeed capability and operation below the first critical speed necessitate the use of turbogenerator technology. Exploratory designs of squirrel cage induction motors show the feasibility of meeting the required power output when forged motors and water-cooled windings are

NOTE ALL DIMENSIONS ARE IN MILLIMETRES UNLESS OTHERWISE SPECIFIED.

CONVERSION TABLE			
MM	FT.-IN.	MM	FT. IN
5500	18'-0½"	300	11.8"
4152	13'-7½"	228	8.97"
3100	10'-2"	65	2.56"
2620	8'-7⅛"		
2220	7-3⅜"		
1930	6'-4"		
1676	5'-6"		
1600	5'-3"		
900	35.4"		
720	28.34"		

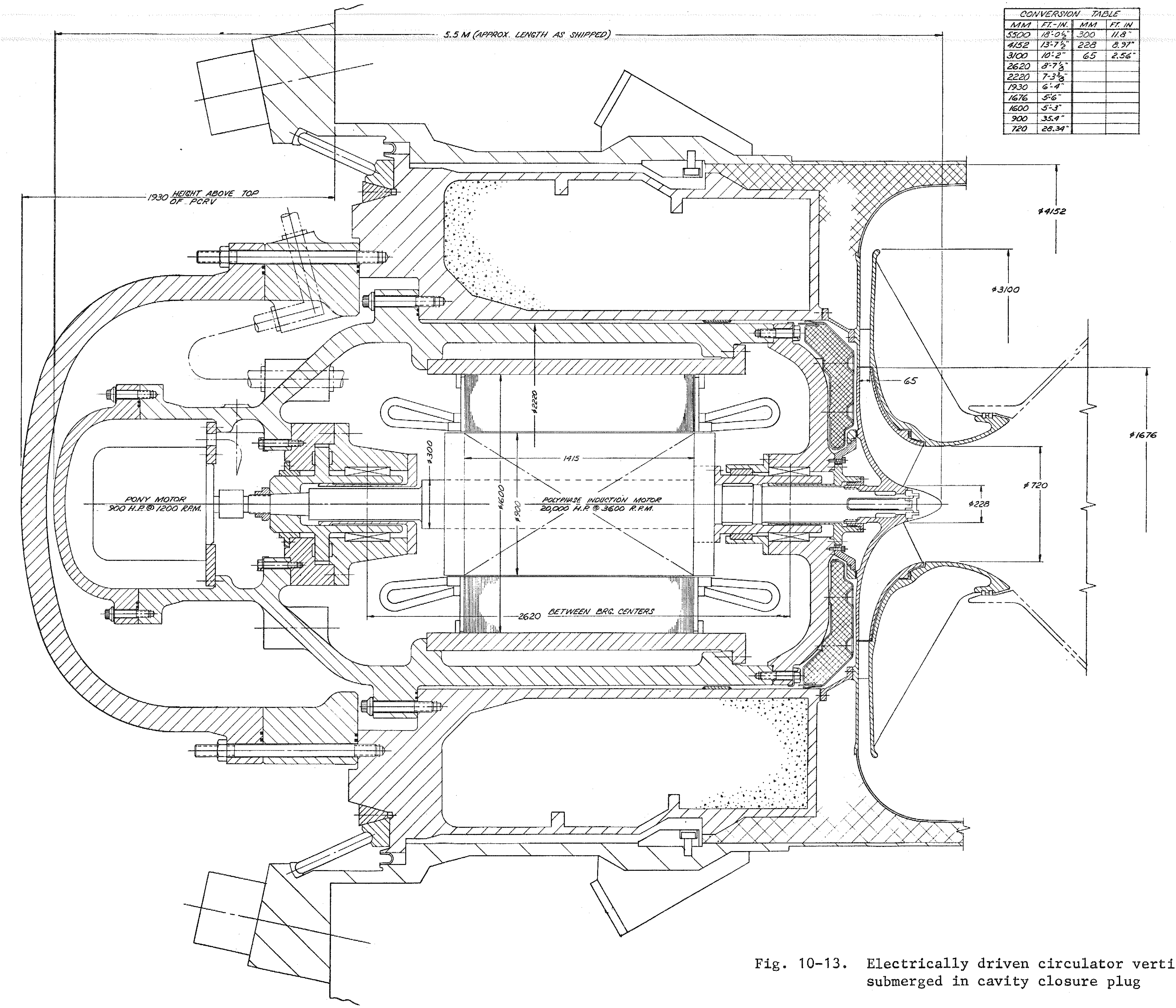

Fig. 10-13. Electrically driven circulator vertically submerged in cavity closure plug

used. Outlines have been made of 18-MW electric motors operating at 3600 and 6000 rpm, and the electrical design has been evaluated to confirm that the machine rating is practical. The number of possible suppliers is somewhat limited, and further investigation is needed to determine a supplier willing to develop such a motor and qualify it for safety-related use in a GCFR.

2. Main/auxiliary circulator diversity. The present auxiliary circulator is a radial flow compressor driven by an electric motor. If this arrangement is chosen for the main circulator, licensing requirements for safety system diversity may require that the auxiliary circulator configuration be changed to avoid common mode failures.

The submerged 3600-rpm motor (mounted vertically in the top of the PCRV in the steam generator closure plug) appears to have several advantages over the horizontally mounted electric motor drive:

1. No rotating external shaft seal required.
2. Low impact on PCRV structure.
3. Adequate space for efficient diffuser.
4. Greatly reduced static thrust loads.
5. Water-cooled rotor may not be necessary.

The drawbacks of this configuration are

1. Higher motor windage losses.
2. Less accessibility for inspection and maintenance.

3. Possible electrical insulation problems in high-pressure helium.

4. Uncertainty of commercial size availability.

10.6.4. Circulator Accident Conditions

A downstream steam pipe rupture accident for the series flow turbine drive was investigated to determine its momentary effect on steam flow, circulator speed, and thrust loads. It was concluded that under the worst circumstances, the exit pressure acting across the turbine disk is about 2.8 MPa (400 psia), resulting in overall thrust loads which would be unacceptable at the thrust bearing. The momentary overspeed during such an accident would be 133% of normal operating speed. The effects of a single circulator steam pipe failure and a common main steam pipe rupture on the remaining operating circulators were investigated. It was concluded that by using a thrust modulator to counteract the effects of even a total loss of steam back pressure to one circulator it is possible to maintain reasonable thrust loads during all steam pipe rupture accidents. The thrust modulator works similar to a conventional steam turbine balancing piston.

10.6.5. Circulator Shaft, Bearings, and Seals

The objective of this subtask is to determine the feasibility of using oil bearings and seals in selected circulator alternate drive systems. The advantages and disadvantages of using water and oil are summarized in Table 10-1. Preliminary calculations on the oil bearings indicate that they are feasible. These calculations have primarily been carried out for the horizontally mounted circulator, which can be used with either an electric motor drive or a steam turbine drive through a flexible coupling which uncouples the rotor vibrations of the drive from those of the circulator. The horizontally mounted circulator shown in Fig. 10-14 is similar to the Peach Bottom circulator in that the overhang of the circulator rotor

TABLE 10-1
INFLUENCE OF BEARING LUBRICANTS

	Oil	Water
Safety	No oil can enter main helium system [oil decomposes at 371°C (700°F)]	Some water can be tolerated
Radiation	Tolerant	Insensitive
Complexity	Complex	Complex
Experience	Wide experience	Limited
Boundary lubrication	Very good	Insignificant
Buffer helium cleanup	Small adsorber	Large adsorber (can be recycled)
Losses and flows	Medium	Large
Hydrostatic jacking for low speed and start-up	Not required (thrust limited)	Necessary
Fire resistance	None	High
Cleanup of containment	Time consuming	Easy
Power loss	Low (100 to 200 hp)	High (600 hp)
Compatibility with steam	No	Yes
Compatibility with electric drive	Yes	Yes
Total loss of pressure	Limited lubrication	Loss of lubrication

precludes ready access to the inboard bearing and seal in a radial direction. To enable the seal to be removable from the coupling end, it is necessary that the seal diameter be the largest diameter along the shaft. The design also requires a method of shaft support during maintenance which allows assembly and disassembly without the bearing support because it is impossible to remove the seal with the inner bearing in place.

Critical speed and seal accessibility requirements place conflicting demands on shaft diameter and overhang. A stiff shaft (operating speed below first critical) limits the overhang with a given shaft diameter. However, the low leakage requirement necessitates a long overhang and a small shaft diameter so that many labyrinths and a small leakage area are possible. The accessibility feature requires the seal diameter to be the largest on the shaft. Figure 10-14 shows a configuration with a nonrenewable and heavier shaft section between inboard and outboard bearings. Figure 10-15 shows a scheme in which the seal on the inboard bearing is located on a larger shaft and can be removed for inspection. The development of a rotating shaft seal which operates at a differential pressure of 10 MPa (1450 psi) and a rubbing velocity of 40 m/s (131 ft/s) and is small enough to be used in the circulator has design risk associated with it.

Table 10-2 presents some of the major assumptions made in the circulator bearing design; the bearing design data are listed in Table 10-3. Most of the parameters are within conventional ranges. The temperature rise on the larger inboard bearing is of concern, although a more detailed optimization would lower this number to an acceptable value. The calculations were carried out for a plain journal bearing, but the steady-state load-carrying capabilities of a tilting pad journal are not very different. The stiffness and damping coefficients are for a tilting pad journal pivoted at the center with no preload. The vertical stiffnesses are adequate, but the bearing is assymetric with unequal stiffnesses in the horizontal and vertical directions. The horizontal stiffness is marginal, but can be increased by optimizing the design. In Fig. 10-4 both bearings are identical to the outboard bearing design listed in Tables 10-2 and 10-3.

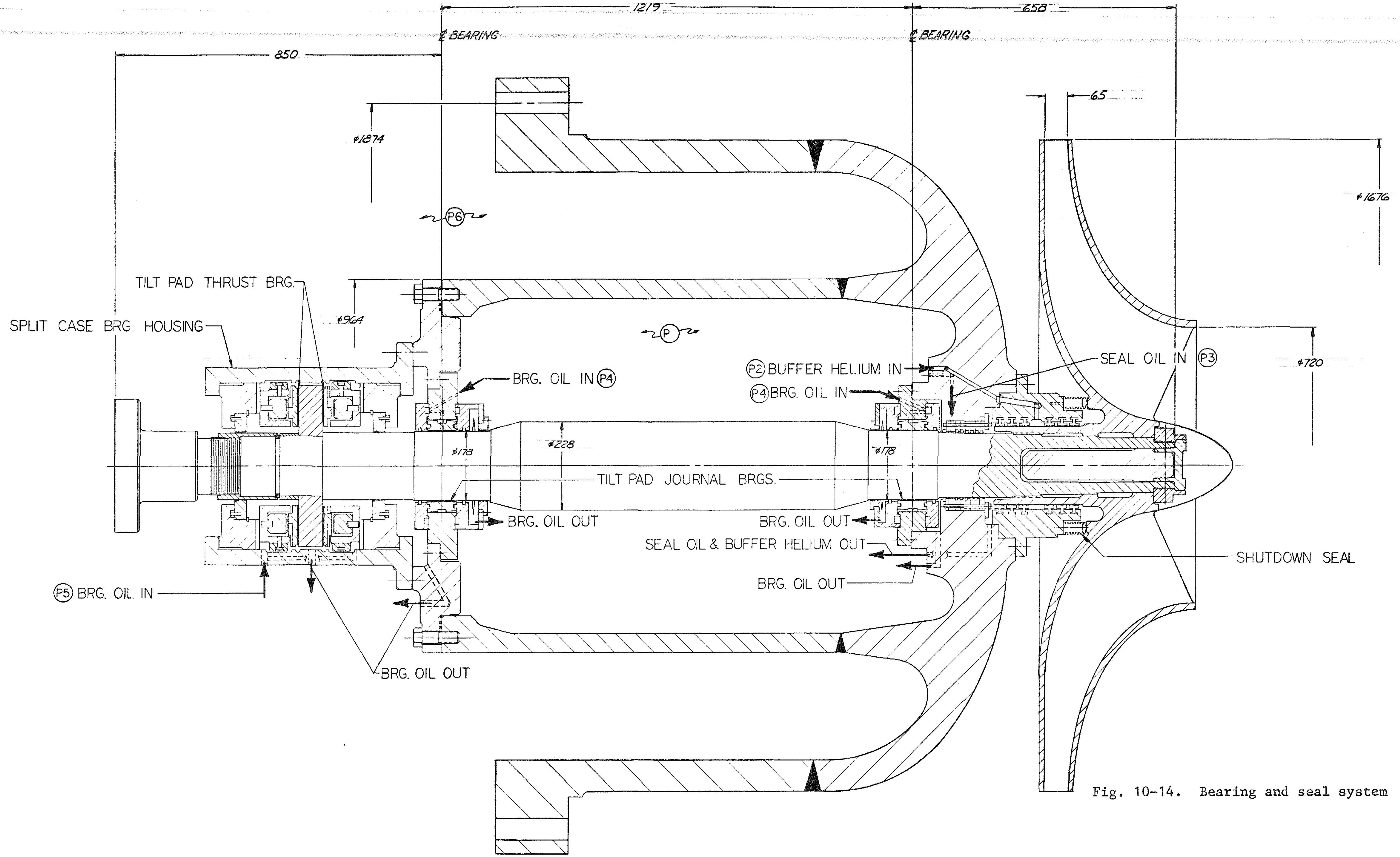

Fig. 10-14. Bearing and seal system

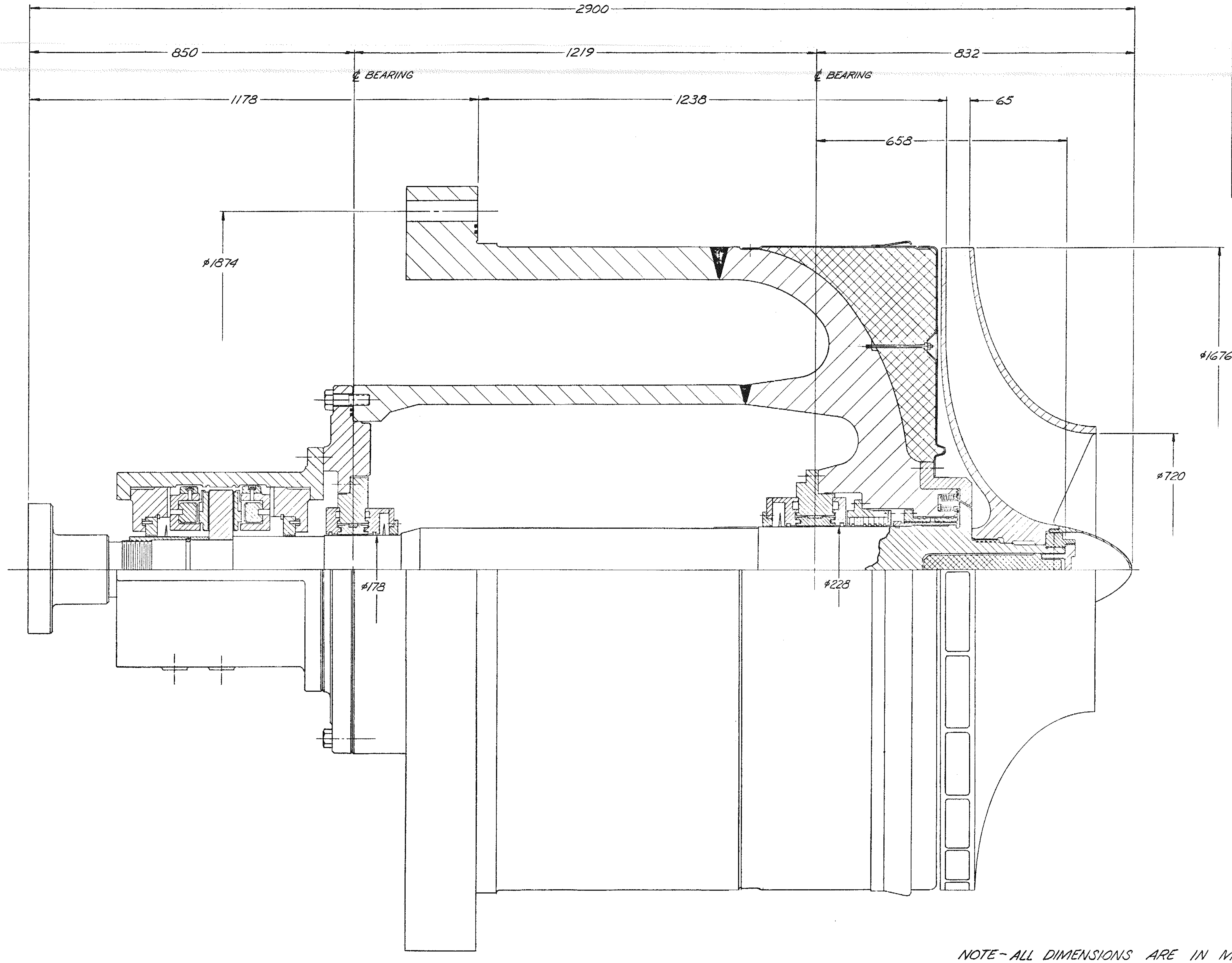

CONVERSION TABLE			
MM	FT.-IN.	MM	FT.-IN.
2900	9'-6 3/16"	178	7"
1874	6'-1 3/4"	65	2.54"
1676	66"		
1238	48.75"		
1219	48"		
1178	46.375"		
850	33.5"		
832	32.75"		
720	28.34		
658	25.875"		
228	9"		

NOTE - ALL DIMENSIONS ARE IN MILLIMETRES UNLESS OTHERWISE SPECIFIED.

Fig. 10-15. Bearing and seal assembly

TABLE 10-2
JOURNAL BEARING DATA

Item	Outboard	Inboard
Speed (rpm)	3,600	3,600
Length/diameter	0.5	0.5
Clearance/radius	0.002	0.002
Diameter [mm (in.)]	150 (5.91)	230 (9.06)
Viscosity of oil [Pa·s (lbf·s/ft^2)]	0.05 (1.04 x 10^{-3})	0.05 (1.04 x 10^{-3})
Load [N (lb)]	12,610 (2,835)	12,610 (2,835)
Load/clearance [MN/m (lbf/in.)]	84 (0.48 x 10^6)	54.8 (0.312 x 10^6)
Specific heat of oil [J/kg·K (Btu/lbm-°F)]	1,674.7 (0.4)	1,674.7 (0.4)
Specific gravity of oil [kg/m^3 (lbm/in.^{3})]	830 (51.79)	830 (51.79)
Number of pads	5	5

TABLE 10-3
JOURNAL BEARING DESIGN

Item	Outboard	Inboard
Sommerfeld number	0.669	1.573
Eccentricity ratio	0.36	0.23
Minimum film thickness [mm (mils)]	0.096 (3.8)	0.177 (7)
Unit load [kPa (psi)]	1121 (162.5)	477 (70)
Temperature rise [°C (°F)]	50 (90)	60 (108)
HP_{loss}/bearing [kW (hp)]	10.1 (13.5)	35 (46.8)
Flow [m^3/s (gpm)]	1.145×10^{-4} (1.815)	2.264×10^{-4} (4.18)
Stiffness coefficients		
Horizontal [MN/m (lbf/in.)]	33.6 (0.2×10^6)	32.9 (0.19×10^6)
Vertical [MN/m (lbf/in.)]	336 (1.92×10^6)	137 (0.78×10^6)
Damping coefficients		
Horizontal [MN·s/m (lbf·s/in.)]	0.45 (2500)	0.58 (3230)
Vertical [MN·s/m (lbf·s/in.)]	1.14 (6400)	0.67 (4900)

10.6.6. Main Loop Isolation Valve

A preliminary investigation has been made on main loop isolation valves for the radial flow main circulator. Three possibilities were considered:

1. A butterfly valve in the compressor inlet ducting.
2. A ring valve in the diffuser discharge.
3. Other types of valves located in the main loop ducting away from the circulator.

The butterfly valve in the compressor inlet ducting seems to be the most promising. The ring valve requires a considerable increase in penetration diameter and is not self-actuating. It may be possible to locate a valve in the ducting away from the circulator, but limited access for actuator installation, valve replacement, and in-service inspection make this arrangement difficult. Valve concepts for an axial flow circulator design are evaluated in Ref. 10-4.

10.7. STEAM GENERATOR

The purpose of this subtask is to design and develop a steam generator which meets the operational, performance, and safety requirements of the GCFR. Work will be performed on the following: (1) optimization of tube geometry for performance, cost, and boiling stability; (2) structural and stress analysis of tubing, tube sheets, and tube supports; (3) thermal growth studies; and (4) preliminary vibration analysis for the chosen tube geometry and support system.

A steam generator using a 17.2-MPa (2500-psi) steam cycle for the 300-MW(e) GCFR system was sized and the information used in safety studies of the nonresuperheat steam generator. As part of the updated steam generator development plan, the tasks associated with the low-flow boiling stability test have been defined. The required tasks are divided into two phases: model and full-size tests. The model test uses an approximately 1/4-scale model of a steam generator coil and covers the range of 100% power/flow to 2% flow; and follows the sequence for a reactor shutdown. A helium-water/steam combination or an air-freon combination could be used to closely simulate the thermal hydraulic and boiling characteristics of the design steam generator coil. This test would provide meaningful boiling data much earlier than the full-scale test and could result in an improved full-scale test plan.

The test program for the full-size tests consists of three parts:

1. Low-flow boiling stability test to be performed at low flow (2%) under steady-state conditions in a full-length test section.

2. Transient boiling behavior test to be performed over the range of 100% to 2% flow following the sequence for a reactor shutdown. A zero water flow period of about 1 min is included in this test, which requires a full-length test section.

3. 100% power/flow boiling behavior test to determine critical heat flux distribution, temperature fluctuations, and associated thermal stresses in the evaporator. This test requires only the evaporator section but may utilize the same test section as tests one and two.

Tests one and two have the highest priority because they will determine if the steam generator performance required after a reactor shutdown can be obtained. Test three will follow the successful completion of the previous tests. If necessary, after LMFBR steam generator corrosion data are examined, corrosion data will be gathered for a helical coil evaporator tube in which critical heat flux occurs in different tube quadrants along much of the evaporator length. Recent information indicates that contrary to earlier work which demonstrated high corrosion rates, the water-side corrosion rate for 2-1/4 Cr - 1 Mo steel is moderate under heat transfer conditions and at the location of critical heat flux. Hence, the corrosion allowance 0.762 mm (0.030 in.) used in the GCFR steam generator design is adequate. A schedule for the low-flow boiling stability tests has been determined, and a report on steam generator designs issued (Ref. 10-5).

10.8. AUXILIARY CIRCULATOR, VALVE AND SERVICE SYSTEM

The general objectives of this task are (1) to prepare and issue a core auxiliary cooling system (CACS) component development plan document; (2) to develop components for the CACS which meet reliability and safety criteria; and (3) to demonstrate the performance and reliability of critical components by testing under anticipated operating conditions.

10.8.1. Core Auxiliary Heat Exchanger Conceptual Design

Work started on a bottom-fed core auxiliary heat exchanger (CAHE) with a bayonet straight-tube design versus a helical tube bundle is continuing. Provisions for in-service inspection were investigated, and it was concluded that with the present technology, it is feasible to conduct an in-service in the straight tube. However, for the helical tubing and with the present design configurations, the only inspectable parts may be limited to the lead-in and lead-out tubes. Therefore, it may be necessary to develop a special probe device and technique (eddy current or ultrasonic) to have a 100% in-service inspection capability for the current helical coil design. The advantage of 100% internal inspection with the bayonet straight-tube CAHE design will be weighed against the possible design impacts on the PCRV after the CAHE design configurations are more clearly defined.

10.8.2. Alternative Auxiliary Circulator Drive System and Components

It was recommended that a contract for a GCFR auxiliary circulator drive and control system design evaluation be awarded to Aerojet Manufacturing Company.

10.8.3. Core Auxiliary Cooling System Simulation Project

A dynamic simulation for the GCFR CACS has been initiated. The mathematical model for the system has been completed, including some of the digital codes.

10.9. HELIUM PROCESSING COMPONENTS

There was no activity on this subtask during this quarter and it has been rescheduled for FY-78.

REFERENCES

10-1. "PCRV Cooling System," General Atomic, unpublished data.

10-2. "Gas-Cooled Fast Breeder Reactor Quarterly Progress Report for the Period February 1, 1977 Through April 30, 1977," ERDA Report GA-A14358, General Atomic, May 1977.

10-3. Jovanovic, V., "Preliminary Thermal Analysis of the 300-MW(e) Gas-Cooled Fast Breeder Reactor Grid Plate," ERDA Report GA-A14457, General Atomic, June 1977.

10-4. Johnson, E. R., "Main Loop Isolation Valve," ERDA Report GA-A14149, General Atomic, May 1977.

10-5. Baroczy, C. J., "Evaluation of Steam Generator Designs for Application to the 300-MW(e) Gas-Cooled Fast Breeder Reactor," ERDA Report GA-A14123, General Atomic, May 1977.

11. PLANT DYNAMICS (189a No. 00638)

11.1. CONTROL SYSTEMS

The coding for the simplified plant dynamic simulation has been completed. This time-varying nonlinear simulation based on the analytical models developed earlier is being checked out by matching steady-state conditions with independently calculated total plant heat balances and comparing the transient results with those obtained from a transient code used for safety analyses.

11.2. SEISMIC ENGINEERING

Since the GCFR reference design has been changed during the last year, the general seismic model is being updated. Preliminary seismological and soil data from Amarillo (Ref. 11-1) have been used to determine the seismic loads, accelerations, and maximum amplitudes for safe shutdown earthquake (SSE) and operating basis earthquake (OBE) conditions, and forces and moments applied to a final stress analysis of GCFR components. Seismic excitation of NSS systems has been specified to analyze, design, and verify their adequacy when subject to earthquake loading for an OBE and an SSE. The input motion to the overall plant was specified by horizontal and vertical ground response spectra (Ref. 11-2). The designated shape of the spectra and the horizontal acceleration determine the input motion.

The overall seismic model of the GCFR is a linear spring mass model with mass points and interconnecting, linearly elastic springs (Fig. 11-1). It has 52 node points with the representative spring mass system. The SAP-IV computer program (Ref. 11-3) was used to model the general seismic analysis of the GCFR. This program can carry out a response spectrum or time-history analysis using mode superposition or direct integration; localized nonlinearities can also be determined.

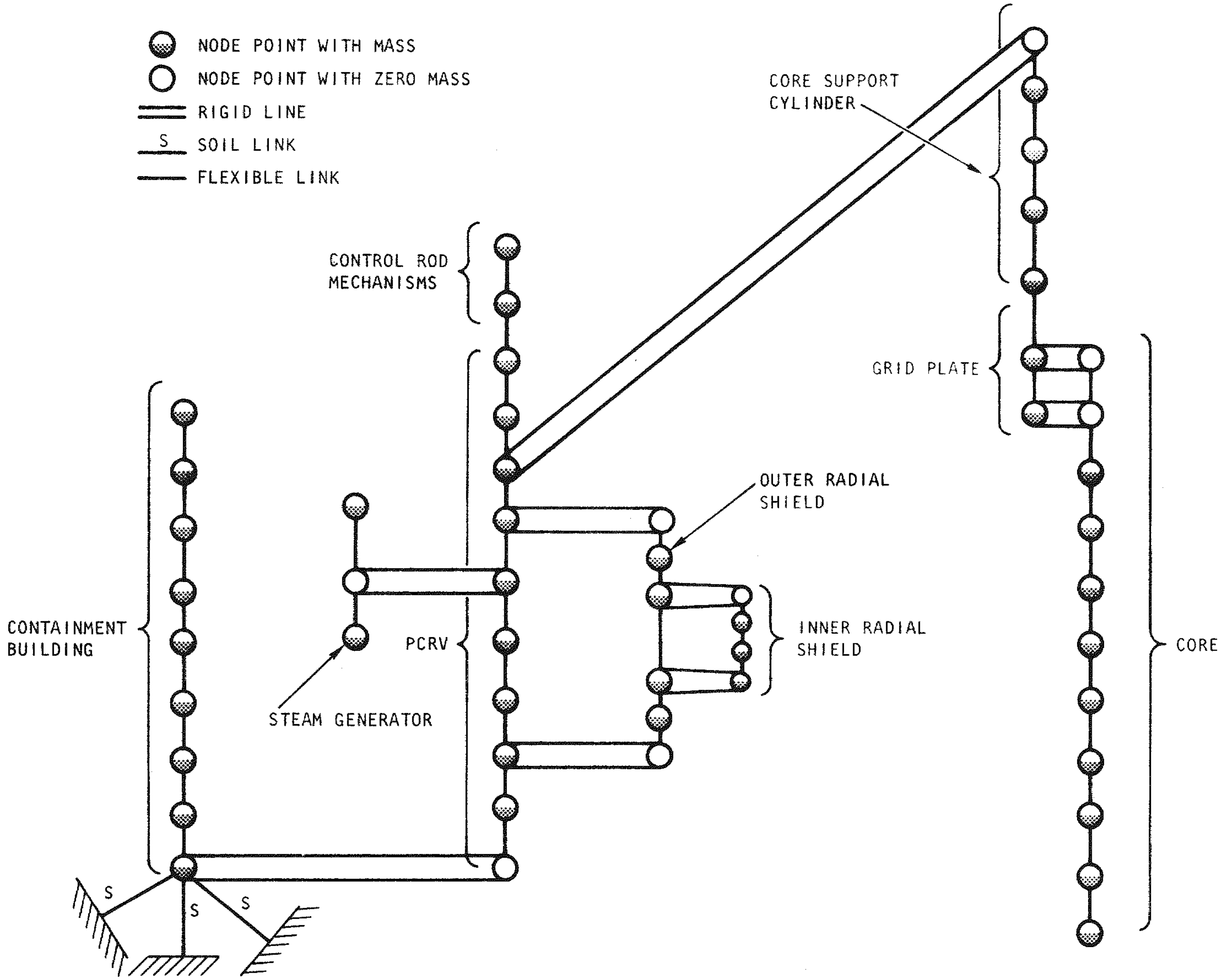

Fig. 11-1. Seismic model of GCFR

The reactor containment building and PCRV are supported on a common base mat. The mathematical model for the containment building was formulated to be an assemblage of nine lumped mass points interconnected by eight flexible beams. At present, soil-structure interaction is modeled by linearly elastic springs. A parameter study will be conducted to determine the effect of soft soil or hard rock foundations; nonlinear soil properties will also be considered.

The seismic model of the PCRV is formulated as an assemblage of ten lumped mass points interconnected by nine flexible beams. Considering the extreme rigidity and huge mass of this structure, the spring-mass representation of this model is adequate. The steam generator, which is an integral part of the PCRV, is represented by three mass points with two linearly elastic beams.

The seismic model of the inner and outer radial shields is represented by ten mass points and eight linearly elastic beams. This model is attached at two points by rigid links to the PCRV model.

The core and core support structure contain the core support cylinder, grid plate, and core. In the general seismic model, the core support cylinder is represented by five mass points and four linearly elastic beams. The grid plate is modeled by two mass points with one elastic beam and one spring, representing the lowest asymmetric (shear) and axisymmetric (drum) modes and frequencies. The core is represented as a single beam by eleven mass points and ten beam elements (Fig. 11-1). The absolute and relative amplitudes of the core assemblies, forces, and stresses will be determined by a three-dimensional model for the core, grid plate, and core support cylinder. The control rod mechanism is modeled at the top of the PCRV by two elastic beams and mass points.

The results obtained from the core seismic model may be used to define the gross motion of the combined core assemblies without determining the relative motion or possible impacts between core assemblies. The general seismic model will also provide the required time history or frequency spectrum at the upper flange of the core support cylinder. This information will be used as input for a detailed finite element analysis of the combined core, grid plate, and core support cylinder. The loads determined for the major GCFR components will be used in stress analyses.

11.3. FLOW AND ACOUSTIC VIBRATIONS

A scoping study was carried out to determine the acoustically induced dynamic loads on the primary coolant boundary components during normal operation of the 300-MW(e) GCFR demonstration plant. This work is based on the reference design documented in Ref. 11-4. The 300-MW(e) GCFR demonstration plant and the 1284-MW(e) steam cycle HTGR, for which detailed acoustic analyses have been performed and design requirements formulated, were compared. A modal analysis of the primary coolant system excluding the reactor core volume was made. This analysis showed that the modal density

$$n_1 = \frac{\omega^2 V_1}{2\pi^2 c^3} + \frac{\omega A_1}{8\pi c^2} \text{ [modes/(rad/s)]} \quad ,$$

where V_1 = primary coolant volume excluding the reactor core (m^3),
A_1 = primary coolant boundary surface area excluding the reactor core (m^2),
c = velocity of sound (m/s),
ω = angular frequency (rad/s),

is equal to

$$n_1 = 1.037 \times 10^{-8}\omega^2 + 3.130 \times 10^{-5}\omega \text{ [modes/(rad/s)]} \quad .$$

The first term is a linear function of V_1 and the second, a linear function of A_1. Hence, a reduction of primary coolant volume implies a decrease of modal density. The model density for the 1284-MW(e) steam cycle HTGR is approximately a factor of 3 higher than that for the breeder demonstration plant.

Only high frequency viscous damping and separation damping were considered when determining modal damping; all other mechanisms were negligible. It was found that the frequency dependence of the modal damping could be expressed as

$$\eta = 0.13\omega^{-1/2} + 18.92\omega^{-1} \quad .$$

The reverberant limit marked by the blend frequency determined by

$$n(\omega)\omega\eta(\omega) = 1$$

is equal to 590 rad/s. The blend wavelength is therefore equal to approximately 16 m, which is much larger than the PCRV cavity dimensions, indicating that the acoustic fields are neither homogeneous nor isotropic and a detailed modal analysis is required.

Since 78% of the total pressure drop of the system occurs in the reactor core, and approximately 10% in the steam generators, it was expected that significant acoustic energy dissipation would also take place in these regions. The frequency dependence of the damping loss coefficient for the steam generator can be expressed as

$$\eta_{sg} = 0.160\omega^{-1/2} + 26.27\omega^{-1} \quad .$$

Therefore, the linear attenuation coefficient α_{sg} is given by

$$\alpha_{sg} = 5.35 \times 10^{-5}\omega^{1/2} + 8.76 \times 10^{-3} \ (m^{-1}) \quad .$$

Assuming that the effective length L_{sg} of the steam generator is equal to ∿14 m, it can easily be shown that

$$\frac{p_{in}}{p_{out}} = e^{7.57x10^{-4}\omega^{1/2}+0.12} \quad ,$$

where p_{in} = sound pressure with an angular frequency ω entering the steam generator,

p_{out} = sound pressure with an angular frequency ω leaving the steam generator.

The attenuation ranges from 1.1 dB for low angular frequencies to 2.5 dB for ω = 50,000 rad/s. Therefore, it can be concluded that sound can traverse the steam generator without much attenuation. Because total attenuation is a linear function of effective length, it is clear that less attenuation occurs in the shorter steam generators of the 300-MW(e) demonstration plant than in those of the 1284-MW(e) steam cycle HTGR. Less attenuation also occurs in the shorter GCFR core than in the steam cycle HTGR core. It was found that

$$\alpha_c = 5.03 \times 10^{-4}\omega^{1/2} + 7.95 \times 10^{-3} \ (m^{-1}) \quad .$$

Because the length of the reactor core L_c is only 2.62 m, the attenuation is only 0.23 dB at 50 rad/s, increasing to 2.36 dB at 50,000 rad/s. For ω < 700 rad/s, $\alpha_c L_c < \alpha_{sg} L_{sg}$,

but for ω > 700 rad/s,

$$\alpha_c L_c > \alpha_{sg} L_{sg} \quad .$$

The acoustic strengths of the most important acoustic sources have been determined. The main helium circulators proved to be the most important sources, emitting 428 W (146 dB linear re 10^{-12} W) each and causing high dynamic loads in the cold gas return duct, the circulator exit plenum, and the steam generator exit annulus. The source strength of one main helium circulator for the 1284-MW(e) steam cycle HTGR is 217 W. The space-time averaged acoustic design loads for the main circulator exit plenum for the angular frequency range 20,000 to 160,000 rad/s (3,200 to 25,600 Hz) were $\sim$15 times higher than those specified for the steam cycle HTGR.

The core exit orifices were also of significant importance. The overall acoustic source strength per jet was equal to 0.19 W (113 dB linear re 10^{-12} W). A conservative upper limit for the total source strength of the reactor can be obtained by assuming that all jet exit velocities are equal to 180 m/s and all orifice diameters are 7.5×10^{-2} m. This results in an overall value of 50.9 W. Because the acoustic emission of the jets is generally highly dependent on the geometry of the cavities, a detailed modal analysis was performed and indicated that the maximum modal power input occurs at 2,400 rad/s. Since the modal power $\Pi_r \propto V^{-1}$ and assuming that all other parameters are constant, smaller cavities imply higher modal powers.

The results of the scoping study are as follows. The total acoustic energy input in the 300-MW(e) GCFR demonstration plant is somewhat higher than that of the 1284-MW(e) steam cycle HTGR, but the modal density and modal damping are lower, and the damping in the steam generators and the reactor core is small. This leads to higher modal energies for the GCFR system. Because the net power flow between two coupled systems is proportional to the difference in the modal energies of the two systems, the net power flow from the fluid to the structure is higher. Consequently, the time-space averaged dynamic loads are expected to be significantly higher for the GCFR system than for the present generation of steam cycle HTGRs.

REFERENCES

11-1. Johnson, S. E., "Design Criteria: Plant Site (300-MWe GCFR)," General Atomic, unpublished data.

11-2. USAEC Regulatory Guide 1.60 Rev. 1, December 1973.

11-3. Bathe, K. J., E. L. Wilson, and F. E. Peterson, "SAP-IV - A Structural Analysis Program for Static and Dynamic Response of Linear Systems," University of California, Berkeley, College of Engineering, EERC Report 73-11, June 1973 (Rev. April 1974).

11-4. "300-MW(e) Gas-Cooled Fast Breeder Reactor Demonstration Plant," General Atomic Report GA-A13045, July 15, 1974.

12. REACTOR SAFETY, ENVIRONMENT, AND RISK ANALYSIS
(189a No. 00589)

The purpose of this task is to investigate the safety characteristics of the GCFR. A liaison and coordination subtask integrates the ERDA-sponsored GCFR safety work at GA and the national laboratories into a national GCFR safety program which is responsive to the need for GCFR safety research. A GCFR Safety Program Plan is being developed to define the safety research needed for the demonstration plant and the longer-term GCFR commercialization program. Safety research at GA includes probabilistic accident analysis, accident consequence analysis, radiological and environmental analyses, and PAFC analyses.

Logical probabilistic methods are employed to determine the probabilities associated with various accident initiation and progression sequences and to identify potential design modifications which would help reduce risks. The thermal behavior of the fuel assembly under conditions of loss of shutdown heat removal is being analyzed to determine the heat-up and melting sequence of the cladding, duct walls, and fuel, because duct wall melting has been identified as an important phenomenon influencing the accident sequence. PAFC analyses are being performed to assess the capability of the current design and to identify potential modifications which could improve the molten fuel containment capability. The behavior of fuel aerosols in the PCRV and the containment is being investigated, with the initial objective of defining the level of detail which is required or desirable for analysis of areosol behavior following low-probability accidents leading to core damage. A methodology for integrating reliability considerations into the GCFR engineering effort at the system, subsystem, and component levels is being developed for trial use on a selected system, with the objective of determining the optimal use of reliability engineering methods in the GCFR.

12.1. REACTOR SAFETY PROGRAM COORDINATION

A midyear review of the GCFR safety program was performed, and the following was concluded:

1. GA will review the capability of Los Alamos Scientific Laboratory (LASL) to perform depressurized accident condition testing (DACT) and make a joint GA/LASL recommendation to ERDA. This is being done.

2. GA and LASL will develop a joint recommendation for the work to be accomplished during FY-78 under the duct melting and fallaway test (DMFT) program at LASL. This has been accomplished.

3. GA will identify alternate GCFR fuel cycles and assess their impact on GCFR safety analyses on a best effort basis. This effort will be completed by the end of FY-77.

4. ANL will examine the effect of high-burnup fuel and control rods on the behavior of the GCFR under accident conditions. This assessment will be included in ANL's year-end report.

The GCFR prelicensing review has been reinitiated, and GA has concluded that the programs to investigate accidents leading to loss of coolable core geometry generally correspond to the concerns of the Advisory Committee on Reactor Safety.

12.2. PROBABILISTIC ACCIDENT AND RISK ANALYSIS

12.2.1. Introduction

Accident initiation and progression analysis (AIPA) techniques developed in FY-74, -75, and -76 (Refs. 12-1 and 12-2) are being applied to the probabilistic analysis of potential accident sequences leading to low-probability, high-consequence outcomes. The consequences of these sequences are also under study at ANL and at GA under other subtasks. The objective of this work is to assess the risks of these accident chains in the GCFR.

During FY-77, the analysis effort has been focused on two areas which have been shown to significantly affect GCFR risks. The first area involves the development of a more detailed probabilistic analysis of GCFR residual heat removal (RHR) systems; the second area involves the development and assessment of containment event trees for the GCFR.

12.2.2. Residual Heat Removal Reliability Analysis

A more detailed probabilistic analysis of GCFR RHR systems is being performed to further identify the level of achievement of the current design and to consider potential design improvements. Forced-convection shutdown cooling is achieved in the GCFR by using two separate RHR systems, each of which has multiple loops for redundancy. The normal operational RHR system utilizes steam-driven main circulators, main cooling loops, and portions of the normal steam power conversion system components. A diverse backup safety RHR system is provided by the CACS, which utilizes electric-motor-driven circulators and pressurized water loops which exhaust heat to the atmosphere. Various peripheral systems support the RHR system functions; these systems include normal power conversion system components, control air system, component cooling water systems, and electrical power systems. Reliability models are being developed to qualitatively represent and quantify GCFR main loop, CACS, and support system operation as necessary to provide RHR.

During this quarter, an analytical study on the GCFR RHR systems was completed. The purpose of this study was to use qualitative and quantitative reliability analysis techniques to critique the conceptual designs of the GCFR core cooling systems using various operating assumptions to indicate the areas in which the reliability may be improved or closer analysis may be desired. The basic approach of this study was as follows:

1. The two RHR systems and support system designs were analyzed for single failure points and significant intersystem dependencies. Failure modes and effects analyses (FMEAs) and detailed reliability block diagram models were developed to accomplish the analyses.

2. The RHR system models were quantified using the generic data base generated under the GCR data bank task (see Section 15). Because of the significant uncertainties involved in applying the generic failure rate data to specific GCFR components, the use of sophisticated computational methods was considered to be unwarranted. Approximate solutions were therefore considered to be adequate for the purposes of this study.

3. A quantitative framework for assessing the adequacy of the current GCFR design was provided by selecting a target probability for a failure of the RHR function of less than 10^{-6} per year. Probabilities of 10^{-3} per demand and 10^{-4} per demand were allocated to the main loop cooling system and CACS, respectively.

4. Analytical results were compared with allocated results, and the potential for intrasystem common mode failures in preventing goal achievement was considered. Potential design improvements were recommended where necessary.

5. The two RHR systems were reviewed with respect to diversity of component type, specification, and location. A review was also made of potential system degradations due to initiating failures to ensure that the assumptions of system dependence were reasonable.

A major conclusion of this study is that a number of support systems in the current conceptual design of the GCFR are common to both RHR systems, and this common link is unacceptable if the allocated reliabilities are to be met. Several reliability improvements have also been identified for the main loop cooling system.

12.2.3. Containment Event Analysis

Work has been completed which identifies the key physical phenomena threatening containment integrity in a core meltdown accident and compares the effectiveness of various PAFC schemes for reducing public risk. The accident considered involves a full core meltdown with loss of all upward and downward cooling capability. The potential for failure by static overpressurization, dynamic overpressurization, missile impact, and melt-through was examined, and overpressurization effects were analyzed with the aid of the CONTEMPT-G (Ref. 12-3) computer code. The effects of the following events were included: primary coolant blowdown; generation of carbon monoxide from fuel-graphite reactions; decomposition of concrete, releasing carbon dioxide and water; reaction of water and molten steel, generating hydrogen; and recombination of hydrogen in the containment atmosphere. The consequences were estimated for each of the failure modes at various times using the TDAC (Ref. 12-4) computer code, and the relative risks were assessed by comparing the likelihood of failure with the resultant consequences. Ex-vessel and in-vessel fuel containment schemes were evaluated on the basis of their effectiveness for reducing overall risk. The results indicate the following:

1. The greatest public risk is attributable to accidents involving loss of upward containment integrity, particularly that induced by static overpressurization. This failure is expected to occur more than 24 hr after shutdown and would precede melt-through in all cases. Its primary cause is non-condensable gases generated by concrete decomposition (CO_2) and metal-water reactions (H_2).

2. In-vessel retention of molten debris, i.e., prevention of cavity liner failure, essentially eliminates the risk from core meltdown accidents. Prevention of concrete decomposition removes the

potential for H_2 and CO_2 generation and thus the threat from static or dynamic overpressurization. Without hydrogen as a detonator, it is difficult to identify an energy source for missile launching in the containment, and thus the likelihood of failure by this mode is reduced. Melt-through is prevented by definition.

3. Ex-vessel retention is ineffective in reducing overall risk since decomposition of the concrete in the PCRV bottom head alone is sufficient to induce shell rupture by static overpressurization. In addition, there is still a potential for hydrogen explosions and missile generation.

4. A nonlimestone aggregate concrete such as that used in the Fort St. Vrain reactor reduces the risk from the key failure mode, i.e., static overpressurization. In this case, failure is greatly delayed or avoided. If this type of concrete is used in conjunction with a hydrogen getter or recombiner, the risk of failure can be reduced to melt-through alone.

5. Use of a containment venting system could reduce the overall risk by greatly reducing the likelihood of static or dynamic overpressurization. The consequences would be similar to, but slightly higher than, those for melt-through, but much lower than those for shell rupture.

12.3. ACCIDENT CONSEQUENCE ANALYSIS

12.3.1. Introduction

The consequences of low-probability accident sequences leading to core damage are investigated under this subtask to determine the expected behavior of the GCFR core and the performance of its activity barriers in mitigating the potential release of activity from the containment. Particular emphasis is given to analysis of the loss of decay heat removal accident, which has been shown to be the dominant contributor to the probability of a loss of coolable core geometry. Analyses of unprotected accidents are mainly being performed at ANL.

12.3.2. Analysis of Loss of Decay Heat Removal Accident

12.3.2.1. Fuel Rod Bowing and Stresses. During the previous quarter, the total stresses produced in the fuel rods as a result of adverse nonlinear temperature distributions after cladding melting during a loss of decay heat removal accident were investigated. This was done using strength of materials methods (Refs. 12-5, 12-6). The strength characteristics of bonded fuel pellet stacks at elevated temperatures are not known, although out-of-pile, direct electrical heating experiments at ANL are expected to yield information on their failure strength. This information is vital for determining the validity of the stress analysis. Test requirements and procedures are being developed for experimental verification of the interpellet bonding strength of sintered fuel pellets. This pellet bonding is influenced by temperature distribution in the fuel rods during normal operation and slow fuel heat-up under loss of decay heat removal accident conditions.

12.3.2.2. Molten Steel Buildup in Lower Axial Blanket. The BOXRAD (Ref. 12-7) computer program has been modified to analyze the buildup of a steel pool in the lower portion of the assemblies due to freezing of steel in the lower axial blanket (as indicated by analyses at ANL). If molten cladding freezes in the lower axial blanket, subsequent molten cladding and duct steel dripping down would build up in the channels between the fuel pins and could eventually spill out of the fuel assembly through holes formed in the duct wall as it melted. Because of the steel spilling into the gap, adjacent fuel assemblies may become welded together by the refreezing steel before they fall away after circumferential duct melting. If enough fuel assemblies become welded together, molten fuel collected on top of the refrozen cladding could form a critical configuration.

Because of the difficulty of precisely modeling the behavior of a fuel assembly as it melts, the effects of the various factors influencing the severity of the transient were parametrically studied to determine the most important effects. Figure 12-1 shows the progression of a transient in time. For this particular transient, a steel plug was assumed to form at the location of the first grid spacer in the lower axial blanket. The steel pool buildup includes molten cladding and duct material. Spillover of the molten steel occurs before total circumferential melting of the duct wall. Total circumferential duct wall melting is when the duct corners have melted. Corner melting occurs 65 s after the duct midflat has melted. Spillover is assumed to take place at the point in time and space where the midflat duct melting curve and the molten cladding buildup curve intersect. Figure 12-2 shows the effect of varying plug formation height. This parameter has considerable influence on the time difference between cladding spillover and circumferential duct melting. A steel melt penetration of over 30 cm into the lower axial blanket is required to prevent steel spillover prior to circumferential duct melting. Such deep penetration is not currently anticipated, but will be investigated as part of the DMFT (see Section 13).

12.3.2.3. Natural Convection Effects in a Blocked Fuel Assembly After Loss of Flow in Shutdown Reactor. An analysis has been initiated to investigate radial and axial heat transfer mechanisms due to natural convection in a blocked fuel assembly. The blockage is a result of molten cladding material freezing near the core - lower blanket interface. Radial heat transfer in a blocked fuel assembly is heat transfer from the hot fuel rods to the cool duct wall. Natural convection increases radial heat transfer, causing the duct wall to heat up faster and, consequently, to melt earlier. This would have a desirable effect on the time delay between duct melting and fuel melting. The results of Ref. 12-8 were used for the analysis. Reference 12-8 reports a systematic investigation of heat transfer and convection phenomena in enclosed plane air layers in horizontal, vertical, and oblique positions. The present analysis used a one-dimensional simulation of the rod bundle in a slab geometry. The masses of fuel and cladding were conserved in each row, and the helium gaps were chosen to conserve the helium volume. The temperatures were determined from BOXRAD analyses.

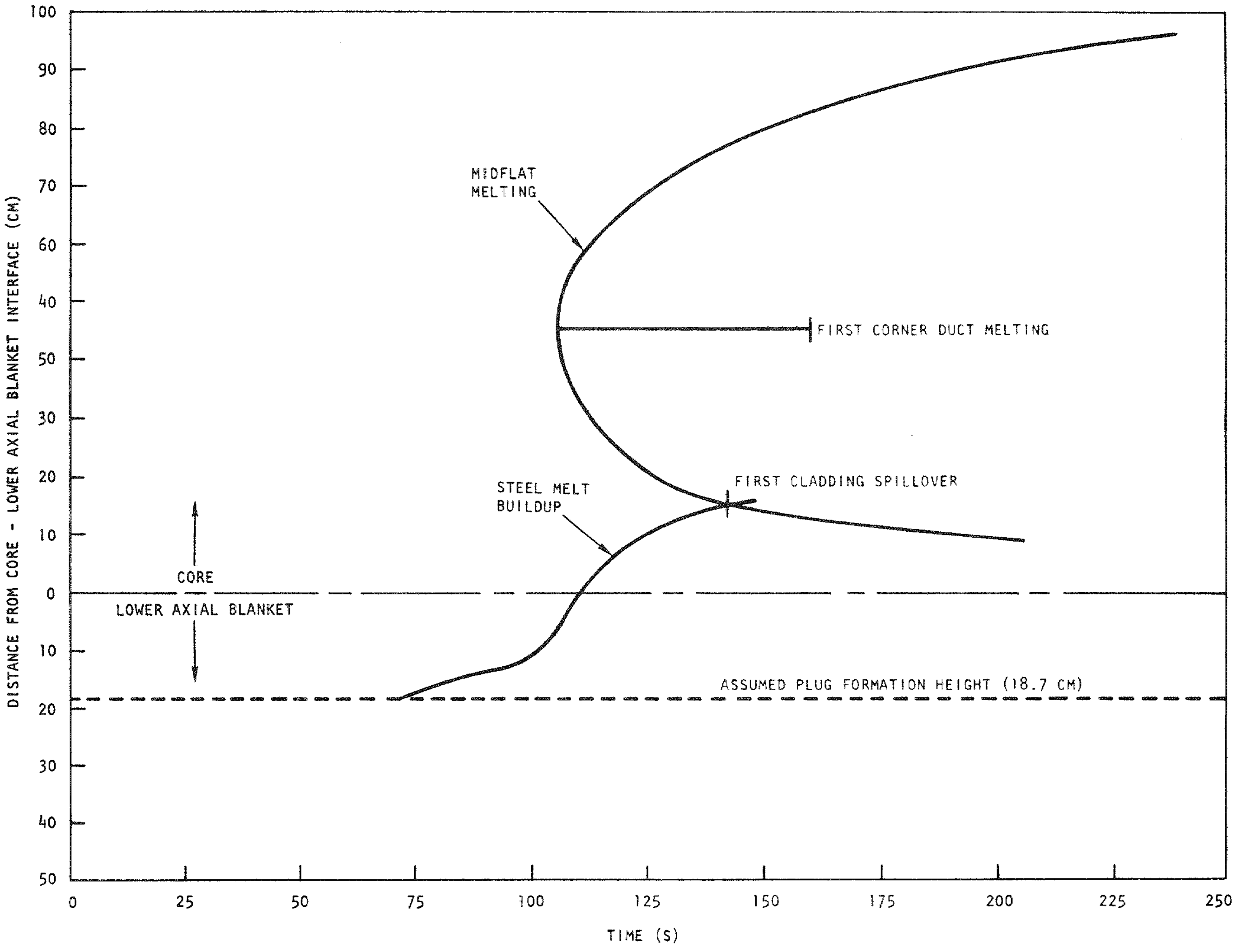

Fig. 12-1. Relative timing of steel melt buildup and axial duct melting during a loss of decay heat removal accident

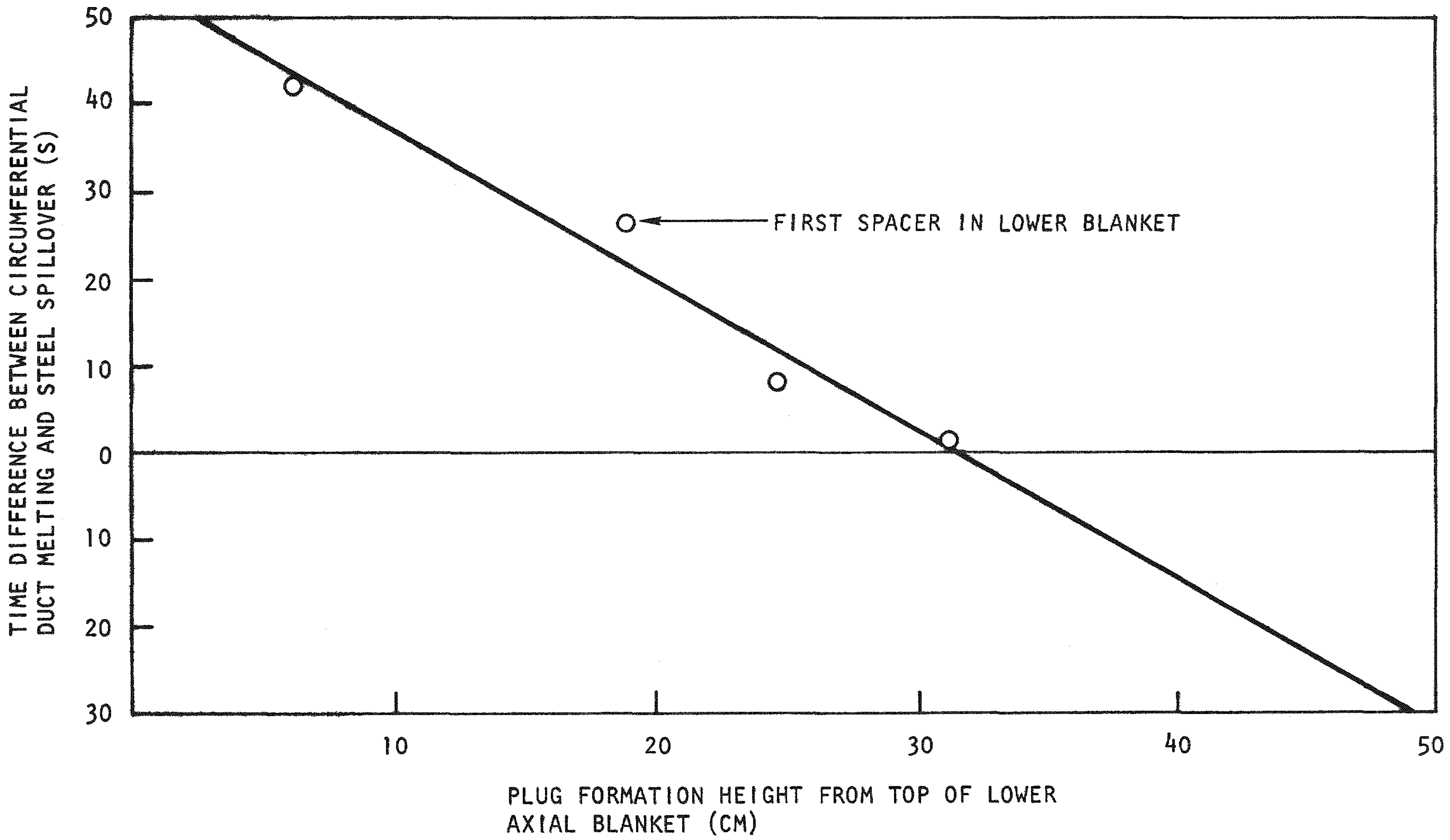

Fig. 12-2. Relative timing of circumferential duct melting and steel spillover as a function of steel freezing location

An undeformed rod bundle geometry was assumed. The results show that natural convection has no influence on the time delay between melting of the duct and the fuel. Axial heat transfer due to natural convection in a blocked fuel assembly expedites heat transfer from the hot core to the cool helium in the PCRV, causing a faster relief valve opening. The complicated geometry of a blocked fuel assembly makes the analysis of axial heat transfer more difficult. Based on Ref. 12-9, it can be proven that natural convection through the inlet nozzle of a fuel assembly is possible.

The next step in the analysis was to evaluate the upper limit of axial heat transfer due to natural convection for a fuel assembly with a very simple geometry. The following assumptions were made:

1. Steady state.
2. Hot up-flow in the fuel assembly center, cold down-flow along the duct wall.
3. Hot mass flow up equals the cold mass flow down.
4. Velocity of cold up-flow equals velocity of the hot down-flow.
5. No mass transfer between cold down-flow and hot up-flow, but lateral heat transfer is permitted.
6. Mixing of cold down-flow and hot up-flow above the grid manifold.
7. Only heat transfer from the hot fuel rods to the helium, but no heat exchange between helium and upper axial blanket.

The analysis of axial heat transfer essentially uses the equilibrium between buoyancy-induced pressure drop and friction pressure drop. It is concluded that natural-convection heat transfer may not be negligible. The next step in the analysis will include the heat-up phase of the upper axial blanket so that a more realistic assessment can be made of the rate of heat transfer from a blocked GCFR assembly to the upper plenum by natural convection.

12.4. POSTACCIDENT FUEL CONTAINMENT

Several core catcher concepts were evaluated during this quarter. Three have been determined to be feasible candidate concepts for the GCFR: the sacrificial bed, the high-temperature crucible, and the heavy metal bath. The sacrificial bed has been studied in detail in Ref. 12-10, so only the second and third concepts are discussed. Decay heat rates and source distributions were calculated.

12.4.1. High-Temperature Crucible

The high-temperature crucible is made of a high-temperature material which can contain molten fuel and stainless steel without chemical interaction. Heat is removed from the pool surface as well as through the crucible floor and side walls to an engineered cooling system. An annular tray geometry for this concept is shown in Fig. 12-3. The upward, downward, and sideward heat fluxes from the proposed core catcher and the fuel pool temperatures have been estimated.

Data from a previous one-dimensional transient analysis (Ref. 12-11) were used to establish a simple two-dimensional steady-state analysis for the molten fuel contained in the proposed annular tray core catcher. The fraction of upward heat flow and the molten fuel temperatures were estimated using Ref. 12-12. Nusselt numbers at the upper boundary of the molten fuel pool were calculated using the Kulacki and Emara correlation (Ref. 12-13), which covers the higher Rayleigh number range of molten fuel conditions. Average Nusselt numbers at the horizontal boundary were calculated using the Baker correlation (Ref. 12-14). The maximum horizontal Nusselt numbers, which occurred at the upper corner of the molten fuel pool, were calculated using the Jahn and Reineke correlation (Ref. 12-15).

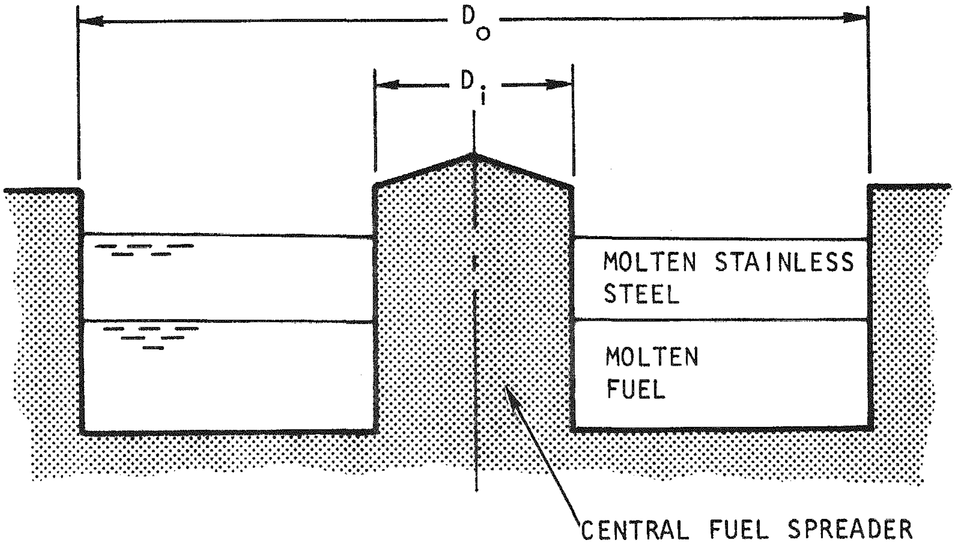

D_i = MOLTEN POOL I.D. = 1.27 M

D_o = MOLTEN POOL O.D. = 4.572 M

Fig. 12-3. Reference core catcher

The results of the quasi-steady-state analysis are given in Table 12-1. Two quasi-steady-state times and two crucible sizes were chosen for the calculation. Table 12-1 indicates that the Nusselt numbers and heat fluxes are not very sensitive to the assumed quasi-steady-state times. The upward and average sideward heat fluxes are about three times as large as the downward heat fluxes. The maximum sideward heat fluxes, which occur at the upper corner of the molten fuel pool, are about 1.5 times larger than the average sideward heat fluxes. The thicker fuel layer (0.424 m) has higher Nusselt numbers and heat fluxes at all surfaces but smaller fractions of upward and downward heat flow and a larger fraction of sideward heat flow. All fuel pool temperatures are below the boiling point.

Sideward heat removal appears to be especially difficult because conduction is the only available mode of heat transfer through the wraparound shield; the upward heat flux can be removed more efficiently by thermal radiation. To remove sideward heat effectively, a highly conductive material can be used to spread the sideward heat evenly over a large cavity liner area so that a uniform cooling load can be achieved. An even better way is to enlarge the lower reactor cavity to permit a wider and thinner molten fuel pool so that sideward heat flux can be reduced.

According to previous analyses (Ref. 12-11), the fuel pool reaches its quasi-steady-state (or maximum pool temperature) early, i.e., 0.5 to 1.0 hr, after an accident. The fuel pool temperatures as a function of the fuel pool thickness using the decay heat rates are shown in Fig. 12-4. The boiling temperatures of fuel at 0.1 and 0.2 MPa are also shown in Fig. 12-4. The maximum nonboiling pool thickness for an equilibrium system pressure at 0.18 MPa is about 0.4 to 0.45 m. Therefore, the 0.424-m pool depth for the reference core catcher is approximately the marginal thickness for a nonboiling pool. However, enlarging the core catcher area by 25% reduces the pool thickness to 0.339 m, avoiding a boiling pool.

Based on the present analysis, the following suggestions are made for improving the proposed core catcher design:

TABLE 12-1
RESULTS OF MOLTEN FUEL HEAT TRANSFER

	Assumed Time to Reach Quasi-Steady State			
	10 hr		20 hr	
	Specified Pool O.D. = 4.572 m	Specified Pool O.D. = 5.072 m	Specified Pool O.D. = 4.572 m	Specified Pool O.D. = 5.072 m
Decay heat in melt (MW)	6.0	6.0	5.0	5.0
Fuel layer thickness (m)	0.424	0.339	0.424	0.339
Liquid fuel thickness (m)	0.351	0.266	0.351	0.266
Nusselt no., upper surface(a)	36	27	35	26
Nusselt no., lower surface(a)	7	6	6	5
Nusselt no., side surface(a)	43	31	41	29
Upward heat flux (kW/m^2)	240	201	198	167
Downward heat flux (kW/m^2)	74	72	63	59
Sideward heat flux (kW/m^2)	245	194	201	161
Maximum sideward heat flux (kW/m^2)	366	312	303	261
Upward heat flux/downward heat flux	3.2	2.8	3.1	2.8
Sideward heat flux/downward heat flux	3.3	2.7	3.2	2.7
Fraction of upward heat flow	0.60	0.63	0.60	0.64
Fraction of downward heat flow	0.18	0.23	0.19	0.22
Fraction of sideward heat flow	0.22	0.14	0.21	0.14
Fuel pool temperature (°C)(b)	3077	3000	3048	2960

(a) Nu = 1.0 is pure conduction.

(b) Melting point of fuel = 2800°C; boiling point of fuel = 3350°C at 0.17 MPa.

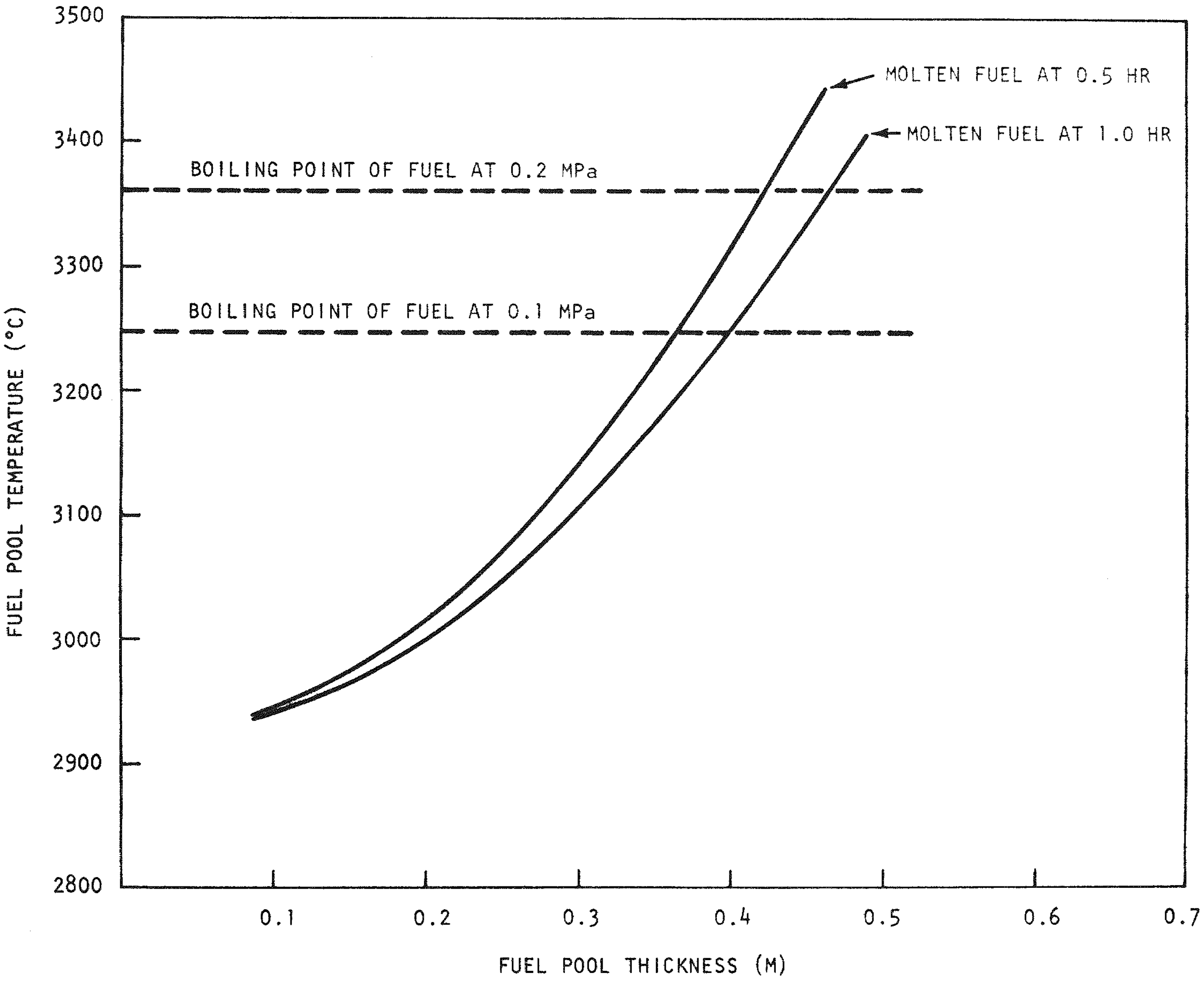

Fig. 12-4. Fuel pool temperature vs thickness

1. A thin pool of molten fuel should be maintained to reduce the high sideward heat flux.

2. The maximum local pool depth should be limited by the boiling pool depth.

3. A highly conductive metal such as tungsten may be used as a crucible material to spread the heat evenly so that a more uniform liner cooling load can be achieved.

4. A sacrificial material such as magnesia may be used as a lining material above the metal crucible.

12.4.2. Heavy Metal Bath

The heavy metal bath core catcher concept has solid fuel chunks suspended in a molten metal pool. Decay heat may be removed to reactor cooling systems by internal convection, conduction, and radiation. Depleted uranium and its alloys are potential candidate materials for the heavy metal bath core catcher. They have higher densities than the oxide fuel, and their melting points vary over a suitable range, i.e., higher than the reactor operating helium temperature and lower than the melting point of steel. For uranium and its alloys, the boiling point is very high (3800°C) and the thermal conductivities are high (300 W/m-°C). They are also chemically compatible with molten oxide fuel and possess good shielding properties for neutron and gamma radiation. The alloys U - 10% Mo, U_3Si, and U-Fe have superior irradiation resistance and are more stable under thermal cycling and thermal gradients than uranium. The material and fabrication costs are relatively low, and the metal and its alloys can be easily fabricated (cast, rolled, extruded, and machined and welded).

The proposed heavy metal core catcher is shown in Fig. 12-5. The lower shield and its wraparound shield are mostly composed of uranium (or its alloys) bricks. A thermal barrier layer (such as SiO_2 or MgO) could be placed between the uranium bricks and the cavity liner and the uranium

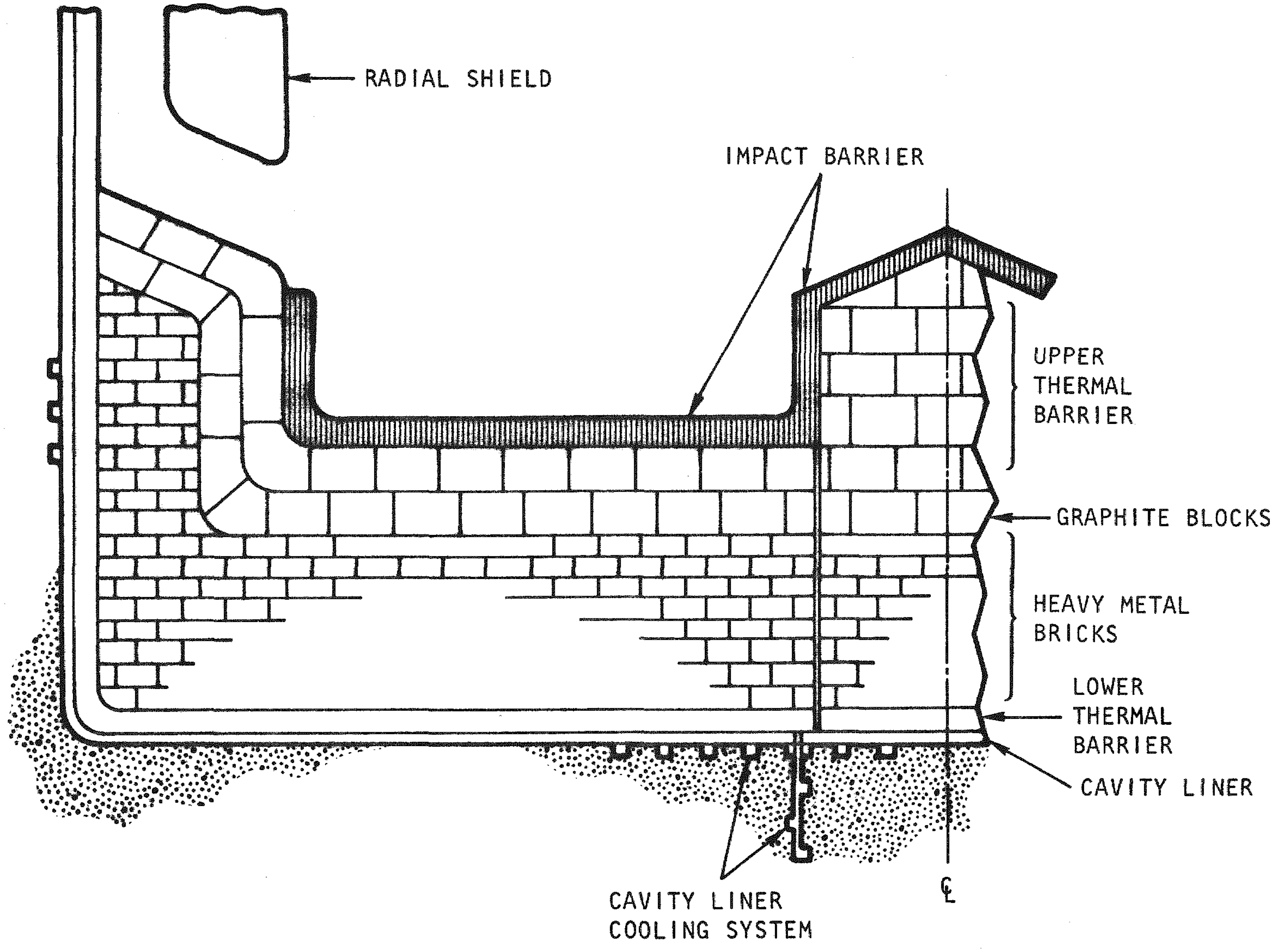

Fig. 12-5. Proposed heavy metal bath core catcher

bricks covered by a layer of graphite with stainless steel casing. Under normal operating conditions, the thermal barrier reduces the heat loss to the liner cooling system, and the graphite with steel casing serves as part of the lower shield and protects the uranium bricks. As required by normal operating conditions, impact barriers such as a honeycomb structure may be placed directly above the graphite layer or on top of a steel preshield. An upper thermal barrier, if required, may also be placed between the impact barrier and the graphite layer.

The thickness of the uranium metal layer depends upon shielding requirements and the heavy metal pool size required to float the core debris materials. A first estimate is that this thickness should be around 0.3 m. The graphite layer above the uranium metal bricks would probably be 0.1 m thick, and the combined thermal barriers (upper and lower) would also be around 0.1 m thick. Magnesia could be the thermal barrier material since it could serve as an insulator and a radiation shield. If the magnesia layer gave sufficient protection to the uranium bricks, the graphite layer could be eliminated to avoid the problems associated with carbide-forming chemical reactions. These decisions should not be made until the results of physics and heat transfer studies are obtained. The impact barrier structure needs another 0.1 m of thickness, and it could be made thicker if it were used as a neutron reflector. A central fuel spreader could also be added to the design, but it is expected to melt during core retention. Sideward penetration of molten materials into the gaps between the uranium bricks can be prevented by radially placing uranium metal plates between each layer of bricks.

The scenarios for molten fuel retention in the heavy metal bath core catcher are as follows:

1. As the core debris mass drops from its original location, it encounters the impact barrier.

2. After melting of the impact barrier and the next layer of the upper thermal barrier, the core debris is in contact with the graphite layer.

3. Chemical reactions forming carbides are expected to occur. However, since the amount of graphite is limited, only some of the metals and oxides are converted to carbides. The amount of CO generation is also limited.

4. As the chemical reactions proceed at the graphite layer, the top layer of the uranium bricks could be molten. Therefore, some of the graphite blocks could float, but they continue to react with the molten stainless steel until all the graphite is used up.

5. Next, an intermediate core retention condition could be reached. A heavy metal bath is formed and contained in a crucible of its own solid material, with a layer of molten stainless steel formed on top of the heavy metal pool. Solid chunks of the oxide or carbide fuel could be sandwiched between the two molten layers.

6. Stainless steel is gradually dissolved into the uranium metal pool. The solid fuel chunks could temporarily be denser than the compound solution of uranium and stainless steel and sink to the bottom of the pool. Then, more solid uranium is molten, and the density of the pool increases. The solid fuel chunks float again, reaching the final configuration shown in Fig. 12-6.

7. The size of the pool may keep increasing until the quasi-steady state is reached; a slow refreezing process follows. If the cooling supply is continuous, an in-vessel PAFC will be successful.

A deep pool condition is expected for molten uranium (with suspended solid fuel chunks). According to Ref. 12-13, the sideward heat flux should be several times as large as the downward heat flux. Therefore, the pool growth should be faster in the sideward direction. A maximum pool size and maximum heat fluxes are reached when a quasi-steady state has been approached. The required cooling load must be designed according to the maximum sideward heat flux at the cavity liner level. All the metallic decay heat sources

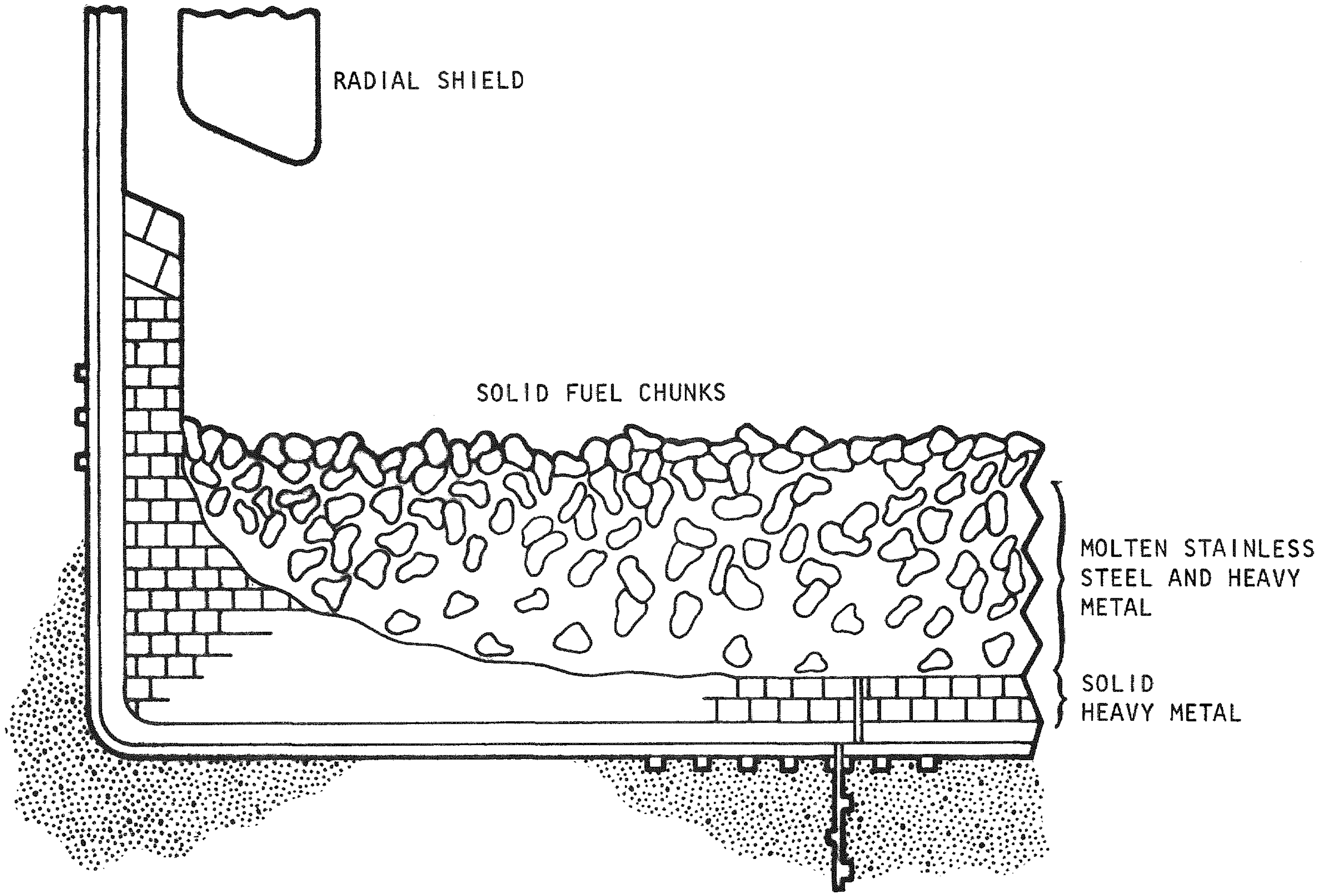

Fig. 12-6. Final core retention configuration

(about 20% of the total) would stay with the liquid uranium. Therefore, the uranium pool should behave as a natural convection pool. However, the heat transfer mechanism is more complicated with the presence of the solid fuel chunks. Because of the density difference, about two-thirds of the solid fuel chunks should be submerged in the uranium pool. Heat removal by natural convection through the uranium pool and by conduction through the high-conduction uranium solids should be excellent. The small portion of solid fuel chunks exposed to helium would be cooled by thermal radiation and helium convection. With natural convection currents in the uranium pool, the solid fuel chunks should roll up and down with the current. Fuel melting could occur inside any large size fuel chunk, but once it broke, it would refreeze in the surrounding liquid uranium.

The actual heat transfer phenomena could be more complicated, and an experimental investigation for proposed core catcher conditions appears necessary to prove the feasibility of the concept. The most serious problems of this core catcher design are the possibilities of molten fuel penetration through gaps and cracks and flotation of lighter materials above the molten fuel pool. These problems can be solved with heavy metal bricks (depleted uranium or its alloys) in the lower shield owing to the higher density and lower melting point of the metal compared with those of oxide fuel. Since this prevents problems of fuel penetration and material flotation, the uranium bricks can be simply shaped to reduce the fabrication cost. The temperature of the heavy metal pool is expected to be quite low (less than the melting point of stainless steel), so that the oxide fuel would always be solid, minimizing fuel evaporation. Compared with other pool-type core catchers, such as the sacrificial bed, the melting process for forming a heavy metal bath seems to be more dependable than the dissolving process for forming a compound solution pool of fuel and sacrificial materials.

Studies should be made on the following items to prove the feasibility of the concepts:

1. Compatibility of oxide fuel (UO_2-PuO_2) and metallic uranium or its alloys.

2. Phenomena of heavy metal pool formation and growth.

3. Heat transfer correlations of the heavy metal pool with solid fuel suspension.

12.4.3. Decay Heat Analysis

Two analyses of nuclear afterheat were completed during this quarter. The first re-evaluated the afterheat, and the second characterized it according to chemical groups.

12.4.3.1. Re-Evaluation of Afterheat. The afterheat used in current GCFR design studies is the light water reactor (LWR) afterheat promulgated in Ref. 12-16. Several alternate decay heat curves were considered: (1) the current fast test reactor (FTR) decay heat curve developed using the RIBD computer code (Ref. 12-17); (2) LWR decay heat (Ref. 12-18) which is about 10% lower than the Ref. 12-17 decay heat for the first several hours following shutdown; (3) a new decay heat curve for the CRBR; and (4) decay heats based on ENDF/B-IV (Ref. 12-20) fission product data files. The current CRBR decay heat calculations are based on approach 4. Since the basic CRBR afterheat data have been developed at HEDL, the computer code and most current data base used by HEDL were obtained. An extended heavy metal fast fission data base has also been obtained from HEDL to enable decay heat evaluation of alternate fuel cycles.

The time-dependent nuclear afterheat for an average fuel rod is plotted in Fig. 12-7. The highest curve, which is the current GCFR decay heat, is from Ref. 12-16; the middle curve is based on Ref. 12-17, and the lowest curve was developed using the RIBD-II computer code (Ref. 12-21) with the ENDF/B-IV fission product data base (Ref. 12-20). The upper curves include the recommended 20% uncertainty through 10^3 s and 10% uncertainty thereafter. The lowest curve includes 3σ uncertainties varying from 36% to 10%, based on Ref. 12-22.

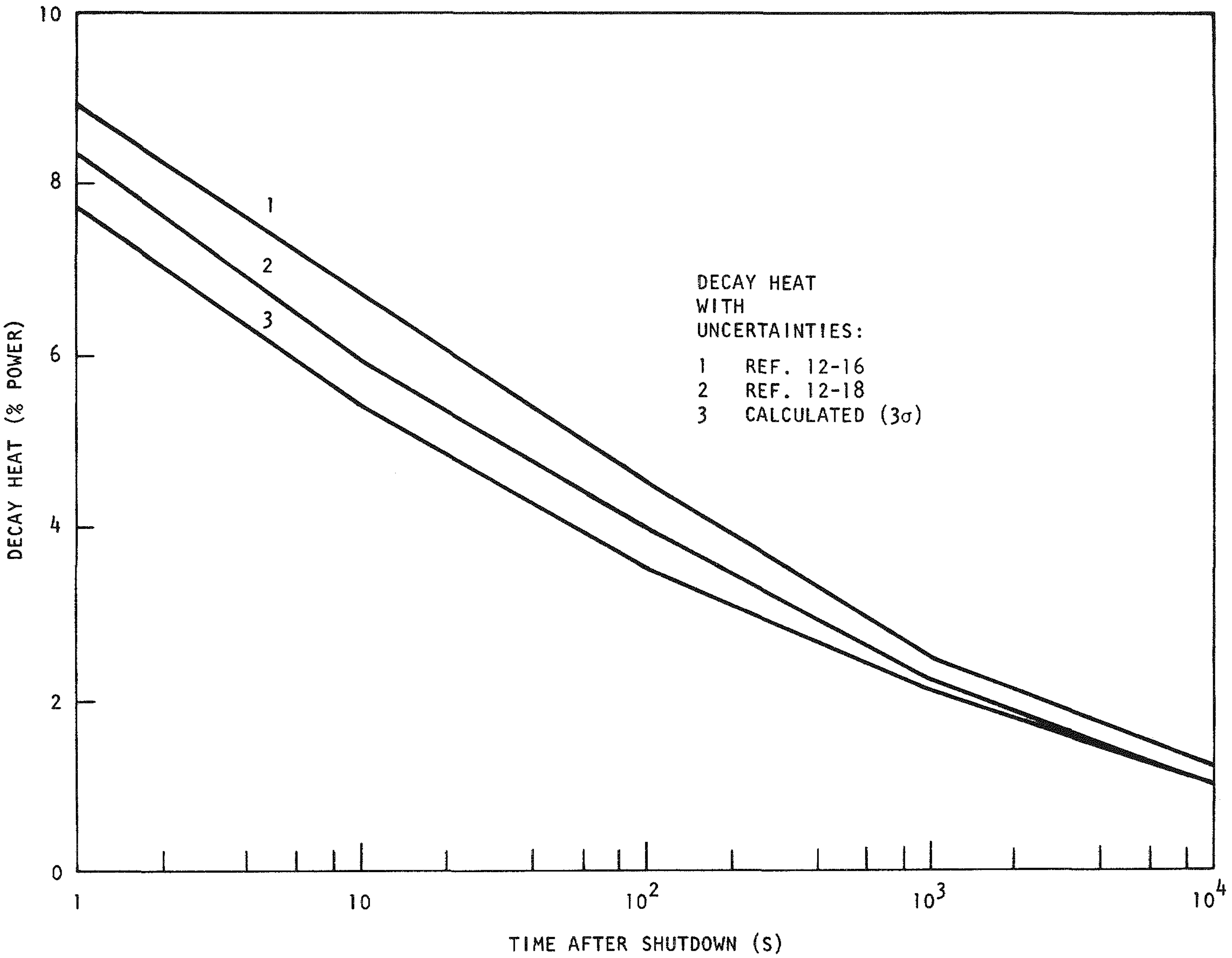

Fig. 12-7. Total decay heat vs time

12.4.3.2. Nuclear Afterheat by PAFC Chemical Groups. Nuclear afterheat sources are frequently grouped into breeding product, fission product, heavy metal, and activated structural material groups. Their classification is made according to their position in the chain of nuclear fission. PAFC is not concerned with the fission process, but with quantification of afterheat within the molten fuel pool and interaction of the pool with the reactor systems. Therefore, four groups were defined (Refs. 12-23, 12-24):

1. Nonvolatile oxide-forming elements.
2. Other nonvolatile elements.
3. Volatile elements.
4. Noble gases.

Group 1 elements are expected to form oxides and remain entrained in the oxide fuel; group 2 elements are preferentially soluble in molten steel. The distinction between groups 3 and 4 involves the potential separation of these elements from the molten pool. Group 4 is expected to separate from the pool independent of pool temperature and to remain in the helium atmosphere; group 3 elements are expected to leave the rod to either form aerosols in the helium phase or deposit on colder structures.

Table 12-2 lists the major elements in the four groups. Breeding products and heavy metals as oxides are in group 1. Activated structural materials, which are mostly metals, are in group 2. Group 4 is not of major significance because it generates only 2% of the afterheat. Fission products are in all four groups and are time dependent. The time dependence of the fission products is plotted in Figs. 12-8 and 12-9 for an average GCFR core assembly in an end of equilibrium cycle core. The curves were developed using the RIBD-II fission product and breeding product evaluation code (Ref. 12-21) and used the corrected ENDF/B-IV fission product yield and decay scheme data for 818 fission product isotopes (Ref. 12-20). The results are in good agreement with the results at 10^2, 10^4, and 10^6 s reported for the FTR in Ref. 12-23. They also agree well with the data in Ref. 12-24 for 85 s after shutdown.

TABLE 12-2
ELEMENTS IN PAFC GROUPS

Group	Elements
1	Heavy metals, fission products, and elements not included in groups 2, 3, and 4
2	Tc, Nb, Mo, Ru, Rh, Pd
3	I, Cs, Rb, Sb, Te, Br, Sn, Ag, Se, In, Cd, As
4	Xe, Kr

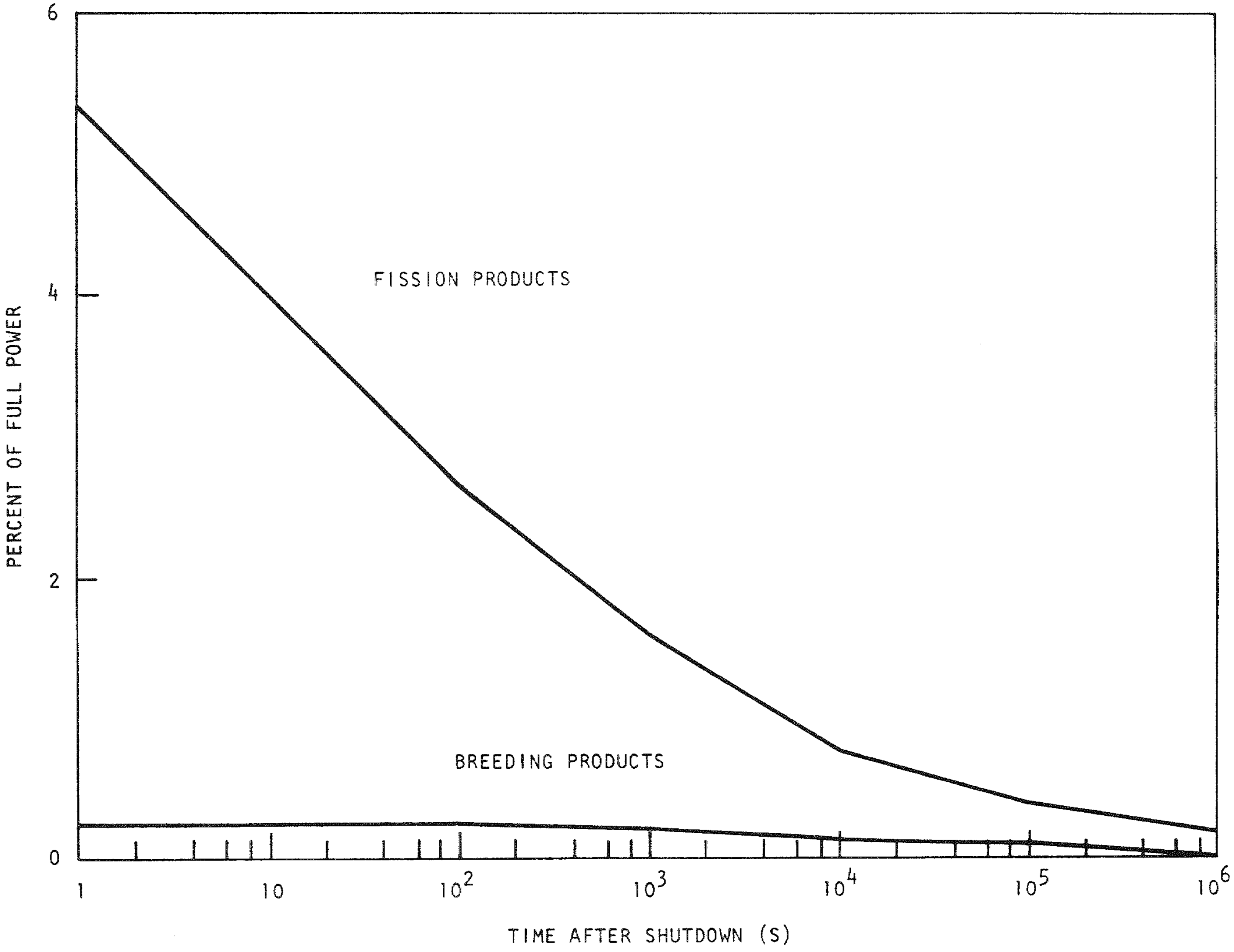

Fig. 12-8. Fission and breeding product decay heat vs time

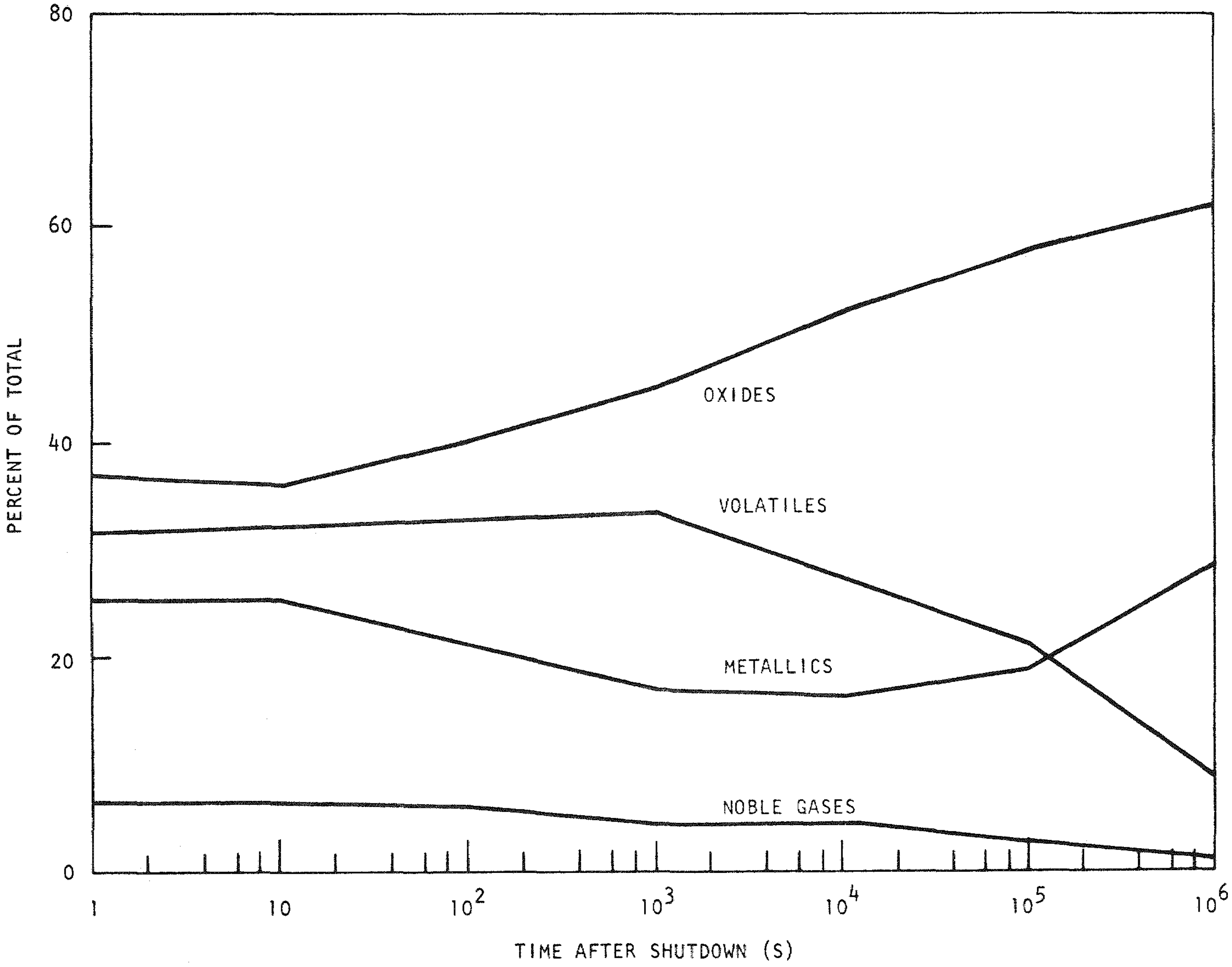

Fig. 12-9. Distribution of PAFC fission product group vs time

During the first days after shutdown, the group 3 and 4 elements generate 20% to 35% of the decay heat. This directly affects postaccident heat removal considerations. Limiting PAFC conditions occur when group 3 and 4 elements have their greatest significance. Thus, there is a large potential reduction in molten pool afterheat to be gained by critical evaluation of the fission product data because some of the decay heat becomes distributed in the primary system and possibly in the containment. PAFC analyses can therefore be used to consider the heating effects of the fission products released from the pool in addition to the upward and downward heat transfer from the molten pool. The dilute form of the released fission products makes it possible to take advantage of the large heat sinks available in the PCRV and the containment.

12.5. LICENSING SUPPORT AND INTEGRATION

As part of the licensing support activity, the CRBR licensing proceedings are being monitored in order to obtain guidance on Nuclear Regulatory Commission (NRC) positions with respect to core disruptive accidents in fast reactors. The CRBR plant safety margin licensing requirements and the types of anlayses needed to establish compliance with these requirements are being evaluated to provide direction for the scope of the analyses necessary for beyond design basis accidents for the GCFR demonstration plant.

12.6. ENGINEERING RELIABILITY INTEGRATION

12.6.1. Introduction

During the first quarter of FY-77, a new subtask was initiated in response to an ERDA request to investigate analytical methods for predicting the reliability of new components and/or systems. The major objective under this subtask is to identify the methods to be used in integrating reliability considerations into the GCFR engineering effort. A secondary objective is to begin applying these methods to a selected safety-related system and component.

12.6.2. Methods Identification

Work continued on identification of engineering reliability integration methods, and a survey of reliability prediction methods has been completed.

REFERENCES

12-1. "GCR Accident Initiation and Progression Analysis - Progress Report for the Period February 1 Through June 30, 1974," USAEC Report GA-A13094, General Atomic, October 8, 1974.

12-2. Kelley, A. P., Jr., "Gas-Cooled Fast Breeder Reactor Accident Initiation and Progression Analysis Progress Report for the Period July 1, 1975 Through June 30, 1976," ERDA Report GA-A14079, March 1977.

12-3. MacNab, D. I., "The CONTEMPT-G Computer Program and Its Application to HTGR Containments," General Atomic Report GA-A12692A, March 1976.

12-4. Buckley, D. W., "TDAC - An Analytical Computer Program to Calculate the Time-Dependent Radiological Effects of Radionuclide Release," General Atomic, unpublished data.

12-5. "Gas-Cooled Fast Breeder Reactor Quarterly Progress Report for the Period February 1, 1977 Through April 30, 1977," ERDA Report GA-A14358, General Atomic, May 1977.

12-6. Spencer, B. W., *et al.*, "Summary and Evaluation of R-Series Loss-of-Flow Safety Tests in TREAT," in *Proceedings of the International Meeting on Fast Reactor Safety and Related Physics, Chicago, October 1976*, American Nuclear Society, to be published.

12-7. Emrich, W. J., Jr., "Duct Melting in the GCFR," General Atomic, unpublished data.

12-8. De Graaf, J. G. A., and E. F. M. Van der Held, "The Relation Between the Heat Transfer and the Convection Phenomena in Enclosed Plane Air Layers," *Appl. Sci. Res., Ser. A*, *3*, 393-410 (1953).

12-9. Mercer, A., and H. Thompson, "An Experimental Investigation of Some Further Aspects of the Buoyancy-Driven Exchange Flow Between Carbon Dioxide and Air Following a Depressurization Accident in a Magnox Reactor. Part 2: The Purging Flow Requirements in Inclined Ducts," *Brit. Nucl. Energy Soc.*, *14*, 335-340 (1975).

12-10. Dalle-Donne, M., and C. A. Goetzmann, "Post-Accident Heat Removal For Gas-Cooled Fast Reactors," in *Proceedings of the International Meeting on Fast Reactor Safety and Related Physics, Chicago, October 1976*, American Nuclear Society, to be published.

12-11. "Gas-Cooled Fast Breeder Reactor Quarterly Progress Report for the Period May 1, 1976 Through July 31, 1976," ERDA Report GA-A13975, General Atomic, August 31, 1976.

12-12. Fieg, G., "Experimental Investigations of Heat Transfer Characteristics in Liquid With Internal Heat Sources," in *Proceedings of the International Meeting on Fast Reactor Safety and Related Physics, Chicago, October 1976*, American Nuclear Society, to be published.

12-13. Kulacki, F. A., A. A. Emara, and J. H. Min, "Natural Convection Heat Transfer in Internally Heated Fluid Layers - PAHR Applications," in *Proceedings of the Second Post-Accident Heat Removal Information Exchange*, Sandia Laboratories Report SAND76-9008, 1975.

12-14. Baker, L., "Models For Internal Heat Generation in Pools - Post-Accident Heat Removal," Argonne National Laboratory Report ANL-RDP48, March 1976, p. 9.4.

12-15. Jahn, M., and H. H. Reineke, "Free Convection Heat Transfer With Internal Heat Sources - Calculations and Measurements," in *Proceedings of the Fifth International Heat Transfer Conference, Tokyo*, v. 3, 1974, p. 72.

12-16. "Decay Energy Release Rates Following Shutdown of Uranium-Fueled Thermal Reactors (Draft)," American Nuclear Society Standard ANS 5.1, October 1971.

12-17. Marr, D. L., and W. L. Bunch, "FTR Fission Product Decay Heat," Hanford Engineering Development Laboratory Report HEDL-TME-71-27, February 1971.

12-18. "Residual Decay Energy for Light Water Reactors for Long Term Cooling," Nuclear Regulatory Commission Branch Technical Position APCSB-9-2, November 24, 1975.

12-19. "Clinch River Breeder Reactor Project Preliminary Safety Analysis Report," Project Management Corporation (NRC Docket 50-537).

12-20. England, T. R., and R. E. Schenter, "ENDF/B-IV Fission Product Files: Summary of Major Nuclide Data," Los Alamos Scientific Laboratory Report LA-6116-MS, October 1975.

12-21. Marr, D. R., "A User's Manual for Computer Code RIBD-II, A Fission Product Inventory Code," Hanford Engineering Development Laboratory Report HEDL-TME-75-26, January 1975.

12-22. Schmittroch, F., and R. E. Schenter, "Uncertainties in Fission-Product Decay-Heat Calculations," to be published in Nucl. Sci. Eng. (1977).

12-23. Baker, L., Jr., et al., "Post-Accident Heat Removal Technology," Argonne National Laboratory Report ANL/RAS 74-12, July 1974.

12-24. Borleon, L., M. Dalle Donne, and S. Dorner, "Temperature and Heat Flux Distribution in the Molten Core Mass of a GCFR After a Hypothetical Melt-Down Accident," EURATOM Report EUR 4852e, November 1972.

13. GCFR SAFETY TEST PROGRAM (189a No. 00588)

It is the responsibility of GA to coordinate the National GCFR Safety Test Program; GA will review and direct the program so that it is responsive to safety test needs and identifies new test needs for which test plans must be proposed and implemented on a time scale which is consistent with GCFR program needs.

13.1. GRIST-2 PROGRAM

The GCFR Safety Program Review Committee has recommended that GCFR fuel tests in a transient facility be undertaken to investigate fuel behavior during unprotected loss of flow and reactivity insertion transients. Therefore, the GRIST program is being developed to complement analytical and experimental programs being conducted under other GCFR and LMFBR programs.

The conceptual design of the GRIST-2 loop system is progressing very well, and the EG&G staff is nearing its FY-77 goal of fixing the major conceptual design parameters. However, several design features still remain unsettled, including the selection of quality design standards, catch cup design, pebble bed heat exchanger design and location, primary-secondary containment arrangement, and handling cask cooling requirements. These items could significantly impact system cost, operation, or safety and will receive attention during the next quarter. Design work on the interface between the in-pile tube and the test train has slowed down owing to manpower limitations at ANL. However, the test train design effort at ANL is expected to increase in the near future.

In response to an ERDA request, the GRIST-2 functional requirements were sent to the SAREF project. The GRIST-2 project objectives and requirements, handling functional requirements, and support facility functional requirements were described.

13.2. DUCT MELTING AND FALLAWAY TEST PROGRAM

LASL has reviewed and commented on the GA objectives, criteria, and requirements for the DMFT program, and the following major conclusions have been reached:

1. The FY-78 DMFT program will concentrate on one full size test simulating a central subassembly. Specific follow-on test specifications will be made dependent upon the evaluation of the first test.

2. Characterization of the heater rod material with respect to thermal properties and vapor evolution over the anticipated temperature range will be necessary to form a basis for test analysis and analytical model verification.

3. Duct instrumentation and power monitoring for each row of fuel rods will be necessary for post-test analysis and analytical model verification.

4. Test bundle preheating with a low coolant flow rate will be necessary to establish the initial bundle condition.

The scope of the first full size DMFT test exceeds the scope originally anticipated by LASL. This will incurr either additional costs to the program during FY-78 or delay completion of the first full-size test until mid-FY-79.

The first cladding melting experiment done for a seven-rod bundle in a 254-mm quartz test fixture was conducted. The test ran very smoothly and cladding melting over a considerable length of each rod occurred.

14. GCFR NUCLEAR ISLAND DESIGN (189a No. 00615)

14.1. GENERAL ARRANGEMENT AND SYSTEMS

The purpose of this subtask is to provide the general arrangement of the nuclear island so that the feasibility of several nuclear island concepts and the major dimensions of the buildings can be established. RECS (Ref. 14-1) has been adopted for the entire GCFR program to integrate planning, scheduling, cost control, and priority identification, and information on the nuclear island general arrangement and systems has been included. The logic diagrams and work sheets have been prepared, all input data have been completed, and initial computer runs have been debugged. The program is considered operational.

The balance of plant requirements (BOPR) have been drafted, and the requirements which the NSS systems impose on the BOP have been defined. The nuclear island and the turbine plant and auxiliaries for the demonstration plant comprise what is normally considered the BOP.

A preliminary list of major mechanical components for nuclear island systems has been prepared for use in the development of conceptual nuclear island arrangements. Development of the nuclear island arrangement has been delayed by a lack of the detailed technical information required. The required information has been identified, but it is anticipated that the design of interfacing systems and components will be further delayed pending major reactor design decisions.

A study was initiated to investigate the feasibility of combining the reactor service building and the reactor auxiliary building to accommodate all fuel handling, storage, and shipping requirements and transfer, storage, and shipment of NSSS components removed from the PCRV.

14.2. STRUCTURAL DESIGN

The purposes of this subtask are to perform the necessary design and arrangement of NSSS equipment and piping, participate in the layout of the equipment within the containment building, and take part in the coordination efforts required for assuring the feasibility of the proposed arrangements.

A feasibility study was made on a PCRV liner cooling system for a PAFC condition. Two separate cooling systems may be required: one for normal operations and the other for PAFC with natural convection to maintain the flow of the coolant. A preliminary analysis to determine the flow requirements for the liner heat transfer is in progress.

A preliminary evaluation has been made of the horizontal circulator mounting and component arrangement.

REFERENCE

14-1. Yensuang, P. K., "Users Guide for Integrated Scheduling Management: RECS - Resource Evaluation and Control System," General Atomic Report GA-A13805, March 1976.

15. GAS-COOLED REACTOR RELIABILITY DATA BANK (189a No. 00617)

The purpose of the reliability data bank task is to obtain, supply, and store the component and system reliability data required as the basic input data for quantifying the event and fault tree models which describe the gas-cooled reactor accident sequences performed under the GCFR and HTGR probabilistic accident and risk analysis tasks.

15.1. EXPANSION OF DATA BASE FOR GAS-COOLED REACTORS

As a result of preliminary probabilistic risk studies on the GCFR, a list of components and subsystems which require reliability data for quantification of RHR system reliability has been generated. Reliability data and estimates from more than 65 sources of data were reviewed and classified for their applicability to gas-cooled reactors. Equipment operating experience for over 2000 yr of fossil experience, over 500 yr of LWR experience, and over 500 yr of gas-cooled reactor experience was studied.

During this quarter data summary tabulations were reviewed, and a new tabulation format was adopted for an internal data bank reference tabulation. This format includes assessed component and system failure rates, repair times, and ranges suggested for use in probabilistic risk assessments.

The reliability data sources were classified into four groups: (1) gas-cooled reactor data, (2) U.S. nuclear, fossil and industrial data, (3) summarized data, and (4) special reliability analysis estimates. The first two groups include information found in the literature describing actual failure incidents for a specified time period and number of components. In addition, most of the sources in groups 1 and 2 give considerable information regarding modes of failure and actual time to restore the system to operation. Groups 3 and 4 include sources of reliability data which report failure rates but do not clearly specify the actual failures or time base experience. Based on the tabulated data, realistically achievable reliability parameters compatible with present-day component production technology have been assessed.

Ranges were obtained which describe the regions within which the reliability parameters associated with HTGR and GCFR equipment have a high probability of lying. The range determination involved data plotting, previous range assessments, and decisions as to the weight and interpretation of data from each data source. As shown by Refs. 15-1 and 15-2, risk calculations are not sensitive to the precise definition of the 90% range definition;* little difference could be detected when the ranges were between 85% to 95%.

15.2. COMMON MODE FAILURE DATA

A preliminary literature review has commenced to examine classification systems which have been employed by others to evaluate common mode or dependent system failures. Information is being gathered on common mode failures, particularly those related to the high risk accident sequences identified in the GCFR risk assessment.

15.3. DOCUMENTATION OF RELIABILITY DATA

Use of the data bank summary tabulation has resulted in the need to refer back to the original source material. The sources are kept on file and indexed. Thus, in a minimum amount of time, an analyst can make an in-depth review of the data and the rationale employed in assessing the recommended failure rate range for any particular component or system.

---

*There is a 90% probability that the data on the actual equipment are in a range bounded by the 5% and 95% lower and upper end points.

REFERENCES

15-1. "HTGR Accident Initiation and Progression Analysis Status Report," v. I through VIII, General Atomic Report GA-A13617, 1975 through 1977.

15-2. "Reactor Safety - An Assessment of Accident Risks in U.S. Commercial Nuclear Power Plants," United States Nuclear Regulatory Commission Report WASH-1400 (NUREG-75/014), October 1975.